Dissertation

submitted to the Combined Faculties
for the Natural Sciences and for Mathematics
of the Ruperto-Carola University of Heidelberg, Germany
for the degree of
Doctor of Natural Sciences

presented by
Dipl.-Math. Nikita Vladimirov
born in Alma-Ata (Kazakhstan)

Date of oral examination: 9.12.2009

Title

Multiscale Modeling of Bacterial Chemotaxis

Referees

Prof. Dr. Victor Sourjik

Priv.-Doz. Dr. Dirk Lebiedz

Summary

One of the central questions of modern systems biology is the role of microscopic parameters of a single cell in the behavior of a cell population. Multiscale models help to address this problem, allowing to understand population behavior from the information about single-cell molecular components and reactions. This goal requires models that are sufficiently detailed to capture central intracellular processes, but at the same time enable simulation of entire cell populations.

In this work a novel multiscale (hybrid) model is presented, which describes chemotactic *Escherichia coli* bacterium by a combination of heterogeneous mathematical approaches in one platform: rapid-equilibrium (algebraic) models, ordinary differential equations, and stochastic processes. The multiscale approach is based on time-scale separation of key reactions. The resulting model of chemotactic bacterium describes signal processing by mixed chemoreceptor clusters (MWC model), adaptation through methylation, running and tumbling of a cell with several flagellar motors. The model is implemented in a program RapidCell. It outperforms the present simulation software in reproducing the experimental data on pathway sensitivity, and simulates bacterial populations in a computationally efficient way.

The model was used to investigate chemotaxis in different gradients. A theoretical analysis of the receptor cluster (MWC) model suggested a new, constant-activity type of gradient to systematically study chemotactic behavior of bacteria *in silico*. Using the unique properties of this gradient, it is shown that the optimal chemotaxis is observed in a narrow range of CheA kinase activity, where concentration of the response regulator CheYp falls into the operating range of flagellar motors. Simulations further confirm that the CheB phosphorylation feedback improves chemotactic

efficiency in a number of gradients by shifting the average CheYp concentration to fit the motor operating range.

Comparative simulations of motility in liquid and porous media suggest that adaptation time required for optimal chemotaxis depends on the medium. In liquid medium, the variability in adaptation times among cells may be evolutionary favourable to ensure co-existence of subpopulations that will be optimally tactic in different gradients. However, in a porous medium (agar) such variability appears to be less important, because agar structure poses mainly negative selection, against subpopulations with low levels of adaptation enzymes.

A detailed model of cell motion predicts existence of an additional mechanism of gradient navigation in *E. coli*. Based on the experimentally observed dependence of cell tumbling angle on the number of clockwise-rotating motors, the model suggests that not only the tumbling frequency, but also the angle of reorientation during a tumble depends on the swimming direction along the gradient. Although the difference in mean tumbling angles up and down the gradient predicted by the model is small, it results in a dramatic enhancement of the cellular drift velocity along the gradient. This result demonstrates a new level of optimization in *E. coli* chemotaxis, which arises from collective switching of several flagellar motors and a resulting fine tuning of tumbling angle. Similar strategy is likely to be used by other peritrichously flagellated bacteria, and indicates a yet another level of evolutionary optimization in bacterial chemotaxis.

Concluding, multiscale models as the one presented here can be an important research instrument for understanding the cell behavior. They reflect the most important experimental knowledge about the biological system, and allow to carry out computational experiments of high complexity, which may be too complicated for experimental trials. Currently, there is abundant experimental data on signal transduction in living organisms, but there is no general mathematical framework to integrate heterogeneous models over the wide range of scales present in most biological systems. This thesis is a new stone in the work aimed to "bridge the scales" in biology.

Kurzfassung

Multi-Skalen Modellierung und Simulation in der Biologie sind notwendig, um zelluläre Funktionalität auf der Basis molekularer Komponenten und Reaktionen zu verstehen. Dazu sind mathematische Modelle erforderlich, die intrazelluläre Prozesse hinreichend detailliert beschreiben, gleichzeitig aber effizient numerische Simulationen von ganzen Zellpopulationen erlauben. Zu diesem Zweck wird in dieser Arbeit ein multiskaliges Hybrid-Modell entwickelt, welches die Chemotaxis bei *Escherichia coli* Bakterien beschreibt. Das Modell vereinigt klassische heterogene mathematische Ansätze zur Modellierung: schnelle Gleichgewichtsannahmen (algebraische Gleichungen) auf der Basis von Zeitskalenseparation, gewöhnliche Differentialgleichungen und stochastische Prozesse. Das resultierende Gesamtmodell der bakteriellen Chemotaxis beschreibt die Signalprozessierung auf der Basis von gemischten Clustern von Chemorezeptoren (MWC Modell), Adaptation durch Rezeptormethylierung, sowie Translationsbewegung und Taumeln der Zellen gesteuert durch mehrere Flagellenmotoren. Das Modell wird im Softwarepaket RapidCell implementiert. Die Software verbessert bestehende Chemotaxis-Modelle signifikant hinsichtlich Reproduzierbarkeit experimenteller Daten und numerischer Effizienz.

Mit Hilfe des in dieser Arbeit entwickelten Multi-Skalen Modells wird die Chemotaxis bei *E. coli* in verschiedenen Gradienten untersucht. Eine theoretische Analyse des Rezeptorclustermodells (MWC) ergibt einen neuartigen Gradienten „konstanter Aktivität“, der sich besonders zur systematischen *in silico* Studie von chemotaktischen Bakterien eignet. Mit Hilfe der speziellen Eigenschaften dieses Gradienten wird gezeigt, dass optimale Chemotaxis in einem engen Aktivitätsbereich der CheA Kinase beobachtet wird, für den die Konzentration des Regulatorproteins CheYp

im Operationsbereich des Flagellenmotors liegt. Simulationen bestätigen weiterhin, dass Feedback-Regulation durch CheB Phosphorylierung die Chemotaxiseffizienz verbessert, indem die mittlere CheYp-Konzentration in den Operationsbereich des Motors verschoben wird.

Vergleichende Simulationen der Bakterienmotilität in Flüssigmedium und porösen Medien deuten darauf hin, dass Zell-zu-Zell-Variabilität in den Adaptationszeiten ein evolutionärer Vorteil ist, der Bakterienpopulationen in flüssigen Medien durch die Koexistenz von Subpopulationen optimale Chemotaxiseffizienz in verschiedenen Gradienten ermöglicht. In porösen Medien (Agar) erweist sich diese Variabilität als weniger bedeutsam, da die Porenstruktur des Mediums eine negativen Selektion von Subpopulationen mit geringem Expressionsniveau von Adaptationsenzymen bewirkt.

Ein detailliertes Modell der Zellfortbewegung durch Flagellenmotorrotation weist auf die Existenz eines zusätzlichen Mechanismus der Navigation von *E. coli* Bakterien in Gradienten hin. Auf der Basis experimenteller Beobachtungen zur Abhängigkeit des Taumelwinkels von der Zahl der CW(clockwise)-rotierenden Flagellenmotoren zeigt das Modell, dass nicht nur die Taumelfrequenz, sondern auch der Reorientierungswinkel nach dem Taumeln von der Orientierung der Translationsbewegung beim Schwimmen im Gradienten abhängt. Obwohl die Differenz der mittleren Taumelwinkel in Aufwärts- bzw. Abwärtsrichtung des Gradienten, die das Modell vorhersagt, klein ist, resultiert ein deutlicher Anstieg der zellulären Driftbewegung entlang des Gradienten. Dieses Ergebnis demonstriert ein neues Optimalitätsprinzip bei der Chemotaxis von *E. coli*, welches auf koordiniertem Schalten mehrerer Flagellenmotoren beruht und eine Feinregulation des Taumelwinkels ermöglicht. Ähnliche Strategien werden sehr wahrscheinlich auch bei anderen peritrichen Flagellenbakterien eine Rolle spielen und weisen auf eine weitere Ebene evolutionärer Optimierung der bakteriellen Chemotaxis hin.

Die vorliegende Arbeit demonstriert, dass Multi-Skalen Modelle vom Typ des hier entwickelten Chemotaxis-Modells ein wichtiges wissenschaftliches Instrument sein können, um zelluläres Verhalten zu studieren. Das Chemotaxis-Modell reflektiert experimentell verfügbares Wissen und ermöglicht *in silico* Experimente hoher Komplexität, welche experimentell aus verschiedensten Gründen ggf. undurchführbar

sind. Gegenwärtig werden in den Biowissenschaften detaillierte und zunehmend quantitative Daten über Signaltransduktionsmechanismen in lebenden Organismen akkumuliert, aber in der Regel gibt es keinen allgemeingültigen mathematischen Rahmen, um heterogene Modellierungsansätze biologischer Systeme über verschiedene Skalen hinweg zu integrieren. Diese Arbeit liefert einen neuen Baustein zur Lösung der Aufgabe dieser Skalenüberbrückung.

Посвящается моей Матери, которая всегда вдохновляла двигаться вперед
(Dedicated to my Mother, who always inspired me to move forward)

Acknowledgements

I would like to say many thanks to my principal supervisor, Prof. Dr. Victor Sourjik, for outstanding attention to all questions, for encouraging ideas, and for his help. In his lab at ZMBH, I had a great experience of working with biologists of highest expertise, sincere and nice people, in a friendly and creative atmosphere.
The project was also supported by my second supervisor, Priv.-Doz. Dr. Dirk Lebiedz, who provided stimulating discussions and computational facilities in IWR, Reactive flows group, where I carried out my simulations and enjoyed a very friendly environment.
Special thanks to my brother Egor Vladimirov, who inspired me to come to Germany and to do a PhD in this beautiful country.
The work was financially supported by the Bioquant Graduate Program 'Molecular machines: mechanisms and functional interconnections' and Landesgraduiertenförderung of Land Baden-Württemberg.

Contents

List of Tables

List of Figures

Chapter 1

Introduction

1.1 Overview of chemotaxis

Many motile unicellular organisms are known to direct their movement toward or away from gradients of specific chemicals – the process called chemotaxis. Chemotactic eukaryotic cells are able to sense shallow gradients across their cell body (Chung et al., 2001), and chemotaxis plays a key role in many physiological processes. Angiogenesis, the blood vessel formation of a growing tumor, is mediated by chemotactic migration of endothelian cells toward the tumor. Immune response involves chemotactic motion of leukocytes to the sources of inflammation (Snyderman and Goetzl, 1981). Another well-studied example of eukaryotic chemotaxis is the slime mold *Dictyostelium discoideum* (Dicty) (Manahan et al., 2004).

While eukaryotic cells are able to sense the gradients by direct comparison of concentrations across the cell body, bacteria employ a more original mechanism – temporal comparisons along their swimming trajectories (Berg and Brown, 1972; Macnab and Koshland, 1972). Theoretical analysis suggested that such a strategy is superior to direct spatial comparisons for objects of bacterial size and swimming speed (Berg and Purcell, 1977). This mechanism plays an important role in the microbial population dynamics. Chemotactic bacteria in a nonmixed environment – that is in presence of nutrient gradients – have significant growth advantage (Kennedy and Lawless, 1985; Kennedy, 1987). Modeling of microbial population dynamics

indicates that motility and chemotactic ability can be as important for evolutionary competition as cell growth rate (Kelly et al., 1988; Lauffenburger, 1991).

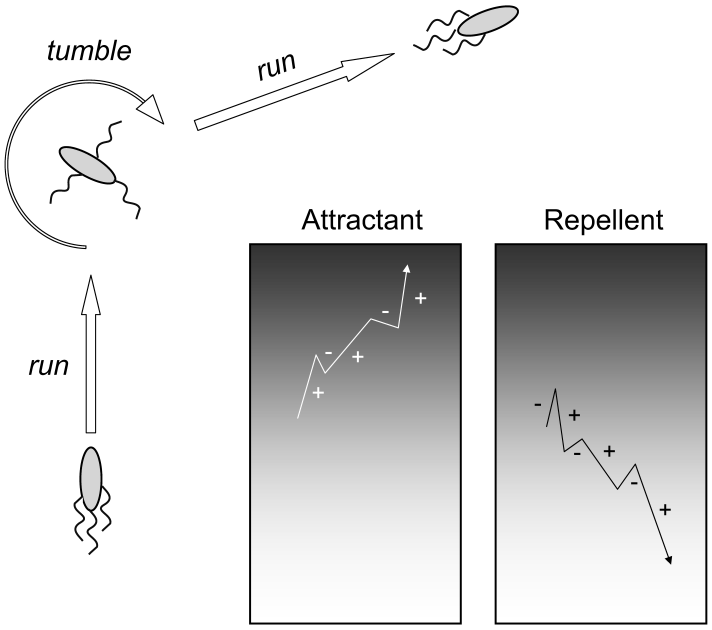

Figure 1: *E. coli* chemotaxis as a biased random walk. The cell moves in a random walk, consisting of long runs (about 1 s) and short tumbles (∼0.1 s). The direction of a new run is assumed to be chosen randomly, while the run length is longer if the cell encounters positive change of attractant concentration, or negative change of repellent concentration. This allows to follow attractant and avoid repellent gradients (insets). Longer runs in a favorable direction are shown by '+', normal (unbiased) runs by '-'.

E. coli bacterium has several flagellar motors distributed in its membrane. Each motor is bound to a long filament (flagellum), which propels or deflects the cell body, depending on the direction of motor rotation. Bacteria have two swimming modes: *runs*, which are periods of long straight swimming, and *tumbles*, in which bacterium stops and abruptly changes its orientation (Figure 1). When all flagellar motors rotate counter-clockwise (CCW), their flagella form a bundle that works like a screw to propel the cell forward, and the cell performs a long run. Switching of one or several flagellar motors to clockwise (CW) rotation results in a tumble. During the tumble, cell rapidly changes its orientation, because one or more CW-rotating flagella

break out of the bundle and rotate as separate rigid screws, deflecting the cell body to a new direction (Turner et al., 2000; Darnton et al., 2007). The runs of a swimming bacterium are interrupted by tumbles, therefore the bacterium moves in a random walk. In response to attractant gradient, this random walk becomes biased: the runs are longer up the gradient, and the cells migrate toward the attractant. On the contrary, in repellent gradient the runs are longer down the gradient (Tsang et al., 1973), allowing the cell to avoid repellent.

1.2 Signal transduction in bacterial chemotaxis

The frequency of tumbles is controlled by the chemotaxis network through switching of individual motors. The CW motor rotation is induced by the phosphorylated protein CheY (CheYp), which binds to the motor protein FliM and changes the motor bias in a highly sensitive mode (Cluzel et al., 2000). CheYp itself is a small molecule which freely diffuses in the cytoplasm between the receptor clusters and flagellar motors. CheY is phosphorylated by the histidine kinase CheA, which is bound to clusters of transmembrane receptors and the adaptor protein CheW (Figure 2). Each receptor can be in either *active* or *inactive* conformation, depending on ligand binding to its outer (periplasmic) domain and the methylation level of its inner (cytoplasmic) domain. The active receptor promotes CheA autophosphorylation, eliciting downstream phosphorylation of the response regulator CheY. CheYp is dephosphorylated by its phosphatase CheZ, which increases the CheYp turnover. Receptors are methylated by the enzyme CheR and demethylated by its counteracting partner CheB, and methylation regulates the receptor activity. For reviews, see (Sourjik, 2004; Wadhams and Armitage, 2004).

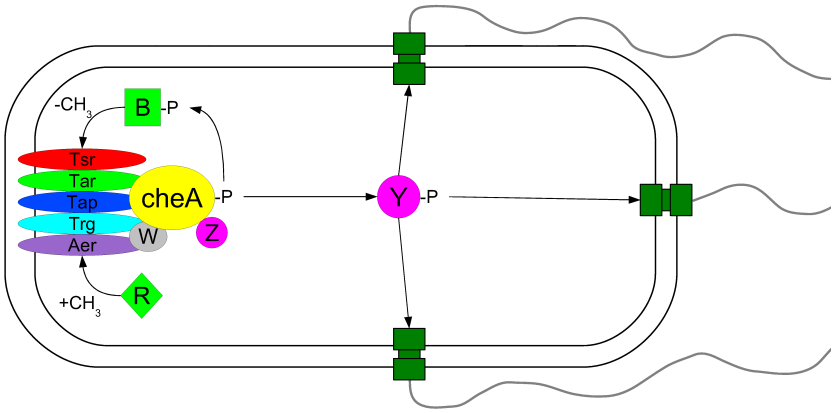

Figure 2: Chemotaxis pathway of *E. coli*. Changes in attractant or repellent concentrations are sensed by a protein complex consisting of transmembrane receptors, an adaptor protein CheW, and a histidine kinase CheA. Transmembrane receptors can be of five types (Tar, Tsr, Tap, Trg, Aer). Autophosphorylation activity of CheA is inhibited by attractant binding and enhanced by repellent binding to receptors. The phosphoryl group is transferred from CheA to the response regulator CheY. Phosphorylated CheY (CheYp) diffuses through the cytoplasm and binds the flagellar motors, thereby changing the direction of motor rotation from counterclockwise to clockwise and promoting tumbles. CheZ phosphatase, localized to sensory complexes through binding to CheA, ensures a rapid turnover of CheYp, which is essential to quickly re-adjust bacterial behaviour. Adaptation is mediated by two enzymes, methyltransferase CheR and methylesterase CheB, which add or remove methyl groups at four specific glutamate residues on each receptor monomer. Receptor modification increases CheA activity and decreases sensitivity to attractants. Feedback is provided by CheB phosphorylation through CheA that increases CheB activity.

1.2.1 Receptor clusters

E. coli can sense a variety of amino acids, sugars and dipeptides, as well as pH, temperature and redox state using five types of receptors. Most abundant and best studied receptors are those for aspartate (Tar) and serine (Tsr). Receptors anchor the complex in the inner membrane and transmit signals from the periplasmic ligand-binding domain to the cytoplasmic part. The cytoplasmic part of the receptor dimer is a four-helix bundle, with highly conserved domain containing four to six specific glutamate residues that are methylated by CheR and demethylated by CheB. The receptor homodimers are organized in trimers by interaction at their helical hairpin

tips, and trimers form the minimum functional units. Receptors are predicted to be organised in large allosteric clusters of about 20 homodimers (Sourjik and Berg, 2004), and these clusters form a high-order structure of thousands of receptors localized at the cell poles. For reviews on function and intracellular organization, see (Sourjik, 2004; Kentner and Sourjik, 2006; Hazelbauer et al., 2008).

The signaling clusters contain receptors, histidine kinase CheA and additional protein CheW (Figure 2). The system functioning can be explained quantitatively by the notion that signaling complexes stay in equilibrium between two conformational states, 'on' and 'off'. In the adapted state, the probabilities of both states are nearly equal. An increase of attractant concentration shifts the equilibrium to 'off' state, decreasing the CheA activity and hence CheYp level. A removal of attractant shifts the system to the 'on' state that activates CheA autophosphorylation and hence the downstream CheY phosphorylation.

The response of clusters with homogeneous (Sourjik and Berg, 2004) and heterogeneous (Mello and Tu, 2005) receptor population is cooperative and can be fitted by the classical Monod-Wyman-Changeux (MWC) model of allosteric proteins (Monod et al., 1965). An alternative Ising model of receptor cluster comprises an extended two-dimensional lattice of interacting receptors (Shimizu et al., 2003). Both models are discussed in detail further in this chapter.

1.2.2 Signal amplification

The sensory system of *E. coli* demonstrates extreme sensitivity. It is able to respond to the addition of as little as 3 nM aspartate (Mao et al., 2003), which corresponds to only several molecules in a volume of a cell. An increase in attractant concentration that changes the receptor occupancy by 0.2% results in a 23% change in the bias of motor rotation (Segall et al., 1986; Sourjik and Berg, 2002a), indicating signal amplification by a factor of ~ 100. This paradox of chemotactic sensitivity was resolved recently by showing that the main signal amplification (~ 35) arises from the cooperative interactions of neighbouring receptors in clusters (Sourjik and Berg, 2002a). Another amplification step is located in the end of pathway, where CheYp binds to FliM molecules in the motor ring in a highly cooperative manner, with a Hill coefficient of about 10 (Cluzel et al., 2000). When combined, these two amplification steps are sufficient to explain the observed gain.

1.2.3 Adaptation

The chemotaxis network has an amazing property of nearly perfect adaptation to stimuli, which means that after addition or removal of an attractant the system gradually returns to its prestimulus values in terms of CheA activity, CheYp concentration, and motor bias. The change in ligand binding is compensated by receptor methylation, which provides the mechanism of adaptation.

The adaptation enzyme CheR consitutively methylates receptors at four glutamate residues located in the cytoplasmic domain. Methylation increases receptor ability to stimulate CheA activity (Borkovich et al., 1992). As a result, when attractant is added and CheA activity rapidly drops down, it then slowly recovers back to the steady state due to methylation of receptors (Figure 3). Methylation also decreases the affinity of the receptor complex to attractants (Borkovich et al., 1992; Li and Weis, 2000; Levit and Stock, 2002), thereby regulating the ligand binding to receptor complexes.

CheB enzyme works in the way opposite to CheR, removing methyl groups from receptors. The outcome of demethylation is inhibition of CheA activity. This allows

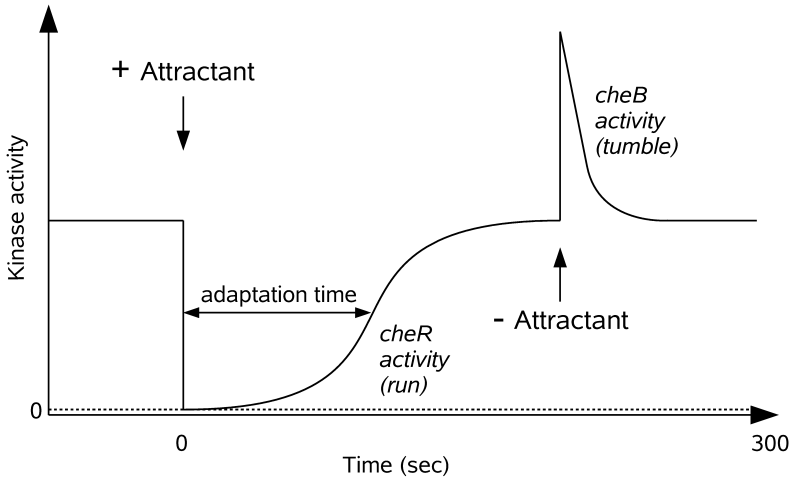

Figure 3: Chemotactic response to step changes of attractant concentration. Step-wise addition of saturating amount of attractant results in an initial fast (less than 0.1 s) decrease in kinase activity that is followed by a slow CheR-dependent adaptation. Adaptation time is proportional to the change in receptor occupancy. Next, removal of attractant results in an initial fast increase in kinase activity followed by CheB-dependent adaptation. Kinase activity below the steady state causes longer runs, above the steady state – frequent tumbling.

adaptation to negative stimuli, such as removal of an attractant or addition of a repellent. Therefore, counteraction of CheR and CheB returns CheA activity to its pre-stimulus value after any type of stimulation, positive or negative.

Adaptation time can span from several seconds to minutes, depending on the strength of a stimulus. The underlying methylation mechanism makes it additive: the adaptation time for a step stimulus from L_1 to L_3 is the sum of the adaptation times for step stimuli from L_1 to L_2 and from L_2 to L_3 (Spudich and Koshland, 1975; Berg and Tedesco, 1975).

Methylation and demethylation occur at much slower time scales than other reactions involved in the network, thereby providing a memory mechanism which allows a cell to remember its recent past state and compare its present situation to the past.

The role of adaptation is crucial. Bacteria retain high sensitivity for some attractants from nanomolar to millimolar concentrations, spanning five to six orders of

magnitude (Berg and Tedesco, 1975; Segall et al., 1986; Kim et al., 2001). To enable high sensitivity over such a wide range, the signal amplification must be coupled with the adaptation. In the absence of adaptation, a 100-fold signal amplification will saturate the system response at 1% receptor occupancy, and the accomplishment of signal amplification with adaptation is a necessary setup of natural signaling systems (Koshland, 1981; Pugh and Lamb, 1990; Kaupp and Koch, 1992; Zufall and Leinders-Zufall, 2000).

Adaptation time depends on the concentration of adaptation enzymes (Alon et al., 1999). Overexpression of CheR decreases the adaptation time to attractant stimuli and increases the steady-state tumbling frequency because of the raised CheYp concentration (CheA activity). Coordinated overexpression of both CheR and CheB decreases the adaptation time alone, without altering of the steady-state tumbling frequency (Kollmann et al., 2005).

1.3 Experimental methods in bacterial chemotaxis

> To follow the ideas of a great man is
> the most exciting science.
> A.S. Pushkin

The first man who discovered motile bacteria was Antonie van Leeuwenhoek. On September 17, 1683, Leeuwenhoek wrote to the Royal Society about his observations of bacteria: '*I then most always saw, with great wonder, that in the said matter there were many very little living animalcules, very prettily a-moving. The biggest sort ... had a very strong and swift motion, and shot through the water (or spittle) like a pike does through the water. The second sort ... oft-times spun round like a top ... and these were far more in number*' (Ford, 1991). However, only in the late XIX century german scientists T.W. Engelmann and W.F. Pfeffer discovered that bacteria are able to move in a certain preferred direction, toward or away from specific chemicals, the process called chemotaxis (Engelmann, 1881; Pfeffer, 1881, 1888).

Capillary assay. The use of a capillary tube was the earliest method to observe chemotaxis. In the 1880s Pfeffer observed bacterial chemotaxis inserting the capillary containing a solution of test chemical into a bacterial suspension and then looking microscopically for accumulation of bacteria at the mouth of and inside the capillary. Many decades later, this procedure was converted by J. Adler into an objective, quantitative assay by measuring the number of bacteria accumulating inside a capillary containing attractant solution (Adler, 1969). The number of cells inside the capillary is counted by serial dilutions. Capillary assays were later improved and parallelized (Berg and Turner, 1990; Bainer et al., 2003), which allowed measuring chemotaxis for many strains and/or under many conditions with high accuracy.

Swarm plate assay. A petri dish containing metabolizable attractant, salts needed for growth, and soft agar (a low enough concentration so that the bacteria can swim) is inoculated in the center with the bacteria. As the bacteria grow, they consume the local supply of attractant, thus creating a gradient, which they follow to form a ring

surrounding the inoculum (Adler, 1966). Measuring the diameter of the swarm ring after a fixed time gives an estimate of chemotactic efficiency of the bacteria.

Defined gradients. Quantitative analysis of bacterial migration has been achieved by making defined gradients of attractant or repellent, and then determining the distribution of bacteria in the gradient by measuring scattering of light by the bacteria (Dahlquist et al., 1972; Tsang et al., 1973; Ford et al., 1991; Lewus and Ford, 2001). The method allows the experimenter to vary the shape and steepness of the gradient.

Imaging. The motion of bacteria can be recorded by microcinematography, or followed as tracks that form on photographic film after time exposure (Macnab and Koshland, 1972; Spudich and Koshland, 1975). An improvement of these methods was delivered by fluorescent labelling of cells and filaments, and usage of CCD camera to follow the flagella transformations and cell movement in high contrast and time resolution (Turner et al., 2000; Darnton et al., 2007).

Tracking microscope. Swimming bacteria move rapidly out of focus plane and viewfield, which makes their behavior difficult to track. A breaking progress was made after invention of an automatic tracking microscope, which allowed objective, quantitative, and much faster observations (Berg, 1971; Berg and Brown, 1972). This method allowed to demonstrate that bacteria migrate in a biased random walk consisting of long runs and short tumbles (originally called 'twiddles'), and that the frequency of tumbles shifts the random walk toward attractants and away from repellents. Despite the long time passed since the construction of tracking microscope in 1971 and its obvious advantages, it did not have successors due to its technical complexity, though the original tracking microscope is still in use (Frymier et al., 1995; Lewus and Ford, 2001).

Tethering experiments. Addition of attractants to *E. coli* cells, tethered to glass by flagella with antibody, results in a counterclockwise rotation of the cell body as viewed from above (Larsen et al., 1974). Addition of repellents causes clockwise rotation of the cells. The response magnitude and adaptation time can be accurately

measured in terms of motor bias. The method is widely used for measuring the behavior of individual cells and single motors (Segall et al., 1986; Alon et al., 1998; Khan et al., 2004; Korobkova et al., 2004).

Microchambers. Modern microfabrication techniques open up the possibilities of making spatially complex habitat landscapes and to investigate how bacteria proliferate and communicate through chemotaxis and quorum sensing (Park et al., 2003; Keymer et al., 2006b). The microfabricated chemostats contain rectangular volumes, corridors or mazes, with input and output channels that supply bacteria with nutrition medium and oxygen, and remove bacterial wastes and excessive biomass, therefore supporting stable conditions of the microenvironment. This technique allows novel approach to study bacterial populations in fabricated ecological environments. Microfluidics experiments have further been used to analyse bacterial responses to well-defined gradient on microscopic scale (Mao et al., 2003; Stocker et al., 2008; Kalinin et al., 2009).

FRET experiments. Fluorescence resonance energy transfer (FRET) is a technique that measures the separation of two fluorescently labelled proteins (and hence their interaction) in cells. It relies on the distance-dependent energy transfer from an excited donor fluorophore to an acceptor fluorophore. Because FRET-based measurements are quantitative and non-invasive, FRET is particularly useful for observing transient protein interactions involved in signal transduction. In the chemotaxis pathway, phosphorylation-dependent interactions of the response regulator CheY fused to YFP (CheY-YFP) with its phosphatase CheZ fused to CFP (CheZ-CFP) were used to monitor the activity of the receptor-kinase complexes (Sourjik and Berg, 2002a, 2004).

1.4 Models of bacterial chemotaxis

From the first quantitative experiments by Julius Adler, chemotaxis always attracted exceptional interest of theoreticians. Depending on the considered scale, the models can be classified as population and individual-scale models. A short introduction into different methods of chemotaxis modeling can be found in (Ritter, 2004). For detailed reviews, refer to (Tindall et al., 2008b,a).

1.4.1 Population-scale models

Keller-Segel model. The motion of bacterial bands in swarm plate and capillary assays is described by the population models in terms of mass conservation law (continuum models). One of the first models of such kind was suggested by Keller and Segel (1971), who were the first to reproduce in model the formation of chemotactic bands observed by Adler (1966). The generalized Keller-Segel (K-S) system consists of two partial differential equations (PDE)

$$\begin{cases} \frac{\partial u}{\partial t} = \underbrace{D_u \Delta u}_{diffusion} \underbrace{-\nabla(\chi(C) u \nabla C)}_{chemotaxis} \underbrace{+g(u,C)}_{growth} \underbrace{-d(u,C)}_{death} \\ \\ \frac{\partial C}{\partial t} = \underbrace{D_c \Delta C}_{diffusion} \underbrace{-h(u,C)}_{consumption} \end{cases} \tag{1}$$

Here $u(\mathbf{x},t)$ is the density of bacteria, $C(\mathbf{x},t)$ is the concentration of chemoattractant, D_u and D_c are diffusion coefficients, $\chi(C)$ is the chemotactic coefficient, while functions $g(u,C), d(u,C)$, and $h(u,C)$ denote cell growth, death, and attractant consumption, respectively. System (1) is solved with appropriate initial and boundary conditions, depending on the assay being modeled. A vast number of studies demonstrated that the Keller-Segel model is quantitatively consistent with chemotaxis experiments, under proper choice of functional forms and coefficients. A good introduction into population models can be found in Chapter 5 of (Murray, 2003). For a detailed review of Keller-Segel system and its applications, refer to (Horstmann, 2003a,b).

The PDE models of Keller-Segel type can be studied analytically, for example, by travelling wave or perturbation analysis. However, numerical simulations are most often employed to solve PDE systems and to compare results with experimental data. To solve PDE systems numerically, method of lines (MOL) can be used (Schiesser, 1991). In this method, spatial domain is discretized, for example, by a regular square grid. Every PDE is substituted by a matrix of ODEs on the grid (one ODE per grid node), and the resulting ODE system is solved numerically.

The Keller-Segel system is widely used not only for bacteria modeling, but also for other biological systems exhibiting chemotaxis (Murray, 2003). For mathematicians, the Keller-Segel system remains a rich source of theoretical insights, in both numerical and analytical aspects. For example, the solution of Keller-Segel equation can be manipulated to form a user-defined pattern, such as Gaussian or parabolic function, by dynamical control of the boundary conditions (Lebiedz and Brandt-Pollmann, 2003; Lebiedz and Maurer, 2004). A number of extensive theoretical works on the theory of partial differential equations were inspired by the Keller-Segel system and bacterial chemotaxis in general (Alt, 1980; Othmer and Stevens, 1997; Hillen and Othmer, 2000). Since its first formulation, the Keller-Segel model became a general framework of population models for more than 30 years, and still remains an actual topic of scientific research because of its complexity.

There were many outstanding theoretical works aimed to couple the microscopic behavior of a single bacterium to the population behavior in terms of Keller-Segel model. One of the first systematic work in this direction was made by Lovely and Dahlquist (1975), who derived expressions for a direction correlation function, diffusion constant, persistence time, and average drift velocity in terms of individual cell parameters. A solid theoretical work was further performed by Alt (1980), who considered a general stochastic chemosensitive system (leukocytes or bacteria) and derived its governing integro-differential equation at the continuum level. Alt carried out asymptotic analysis of the governing equation, and showed that it is approximately described by the Keller-Segel equation. He further derived the diffusion and chemotactic coefficients from microscopic parameters: mean trajectory duration, cell swimming speed and receptor-attractant dissociation constant. Chen et al. (1999)

carried out perturbation analysis of the Alt's governing equation and derived a chemotactic coefficient similar to that obtained previously by Rivero et al. (1989):

$$\chi(C) = \frac{2v}{3} \tanh\left(\frac{\chi_0}{2v} \frac{K_D}{(K_D + C)^2} \frac{\partial C}{\partial x}\right) \tag{2}$$

where $C(x)$ is the chemoattractant concentration at the cell position x, K_D is the receptor-attractant dissociation constant, and v is the cell swimming speed. Note that here ∇C is already included into the chemotactic coefficient. The use of tanh() function is necessary for steep gradients, because it limits possible extreme growth of the chemotactic coefficient. This expression for chemotactic coefficient was used in many macroscopic models, and it fits well the abundant experimental data (Ford and Lauffenburger, 1991; Marx and Aitken, 1999, 2000; Pedit et al., 2002).

Continuing the efforts of bridging the different scales, Erban and Othmer (2004) used a simplified model of excitation and adaptation, described by two ordinary differential equations, to derive a macroscopic description of bacterial chemotaxis in 1D space. Authors incorporated basic parameters of microscopic behavior (excitation and adaptation time) into the evolution equation for the macroscopic density. They derived the following form for chemotaxis sensitivity:

$$\chi(C) = g'(C(x)) \frac{bv^2 t_a}{\lambda_0(1 + 2\lambda_0 t_a)(1 + 2\lambda_0 t_e)} \tag{3}$$

where $g(x)$ is the function that describes the 'cartoon' excitation and adaptation dynamics, λ_0 is the tumbling frequency of unstimulated cells, t_e and t_a are the excitation and adaptation constants, respectively, b is the constant of tumbling sensitivity. These results were further generalized to 2D and 3D cases (Erban and Othmer, 2005). This outstanding theoretical work provides a bridge between simplified microscopic model of signal transduction and the macroscopic population model of Keller-Segel type. However, the microscopic properties of signal transduction model can be included into PDE coefficients only in a form of cartoon model so far, because of enormous complexity of the resulting analytical expressions. Due to this complexity, a single-cell numerical approach seems more promising way to understand bacterial behavior,

aided by the increasing power of modern computers.

1.4.2 Single-cell models

Early models

In parallel to population models, developed mainly by theoreticians, the experimentalists who worked with chemotactic bacteria sought to suggest single-cell models of signal transduction that could account for the observed cell behavior. Macnab and Koshland (1972) were the first to suggest a model of signal transduction mechanism, though most of its molecular details were unknown at that time. In their model, authors considered a response regulator X (essentially CheYp), which is produced from W (CheY) and transformed to Y (also CheY, as was revealed later) by two hypothetical enzymes. Five years later, Koshland extended this model, assuming that covalent modification of receptors by methylation is controlling the activity of response regulator X (Koshland, 1977). In his paper, Koshland suggested a threshold model, in which regulator suppresses tumbling when it rises above the threshold and increases tumbling when it falls below the threshold.

Block, Segall, and Berg studied the response of tethered bacteria to brief pulses of attractant and repellent, and the corresponding times of excitation and adaptation (Block et al., 1982). While the addition of attractant results in almost immediate response (excitation), it disappears with time gradually, even if the attractant is present (adaptation). Analysis of the probability of CCW motor rotation in response to attractant showed that excitation and adaptation occurred at very different timescales, sufficiently different to propose that they are controlled by distinct molecular mechanisms. The timescale of response indicated that bacterium is able to integrate stimuli over several seconds. According to their measurements, the impulse response demonstrates band-pass properties: the cell is maximally sensitive to frequencies at which the low-pass and high-pass contributions overlap. Authors further suggested a two-state model of motor switching. According to the model, switching between CCW and CW is determined by alternate configurations of a regulatory protein or a similar mechanism. The transitions between two states are governed by first order rate

constants, k_r and k_t, which are the probabilities per unit time of terminating a run or a tumble, respectively.

In their next paper, Block et al. (1983) studied response of tethered bacteria to gradual concentration changes (time ramps), which had exponential or sine wave forms. They demonstrated that the change in motor bias is proportional to the change of receptor occupancy dP/dt, therefore bacteria must be able to compare the present level of receptor occupancy to the recent past. Importantly, authors were the first to suggest a model of signal transduction by considering the change in receptor occupancy and adaptation via methylation, which layed the groundwork for the subsequent single-cell models. However, at that time the molecular mechanisms underlying the chemotaxis pathway remained obscure. There were three major challenges to resolve for the next two decades: the mechanism of precise adaptation through receptor methylation, the signal transduction through phosphorylation cascade and the extreme sensitivity of the pathway.

The problem of adaptation was vividly formulated in (Goldbeter and Koshland, 1982): *The phenomenon of adaptation itself places an enormous constraint on mathematical theories. Stated briefly, an absolutely adapting system, which is obtained in the chemotactic and visual systems, requires that the behavior return to normal despite the fact that the stimulus is altered to a new background level.* In their paper, Goldbeter and Koshland analyzed several plausible models of adaptation, and compared them to available experimental data. The resulting four-state model could account for some key system properties observed in experiments: namely, the response times in relation to stimulus changes, the proportionality of receptor modification to receptor occupancy, and the additivity of response times.

An alternative, two-state model was proposed by Asakura and Honda (1984). In their model, receptor exists in a rapid equilibrium between conformations S (from *smooth* swimming) and T (*tumbling*). Methylation shifts the equilibrium to T. Attractant binds only to S, while repellent binds only to T, and both types of ligand shift the S-T equilibrium. Finally, the tumbling frequency is determined by the ratio between S and T. This model has yielded a background for development of many other models. A modified two-state model of receptor is now a standard assumption

in the chemotaxis simulations, starting from (Barkai and Leibler, 1997).

Models of phosphorylation and methylation

The phosphorylation cascade was first simulated by Bray and colleagues (Bray et al., 1993), who implemented their model in a program BCT (Bacterial ChemoTaxis). The authors simulated phosphorylation cascade by a system of ODEs, and correctly reproduced excitation behavior of most known *E. coli* mutants, in which chemotactic genes were deleted and/or overexpressed. The model incorporated CheB phosphorylation, binding of CheYp to a motor, and dephosphorylation of CheYp by CheZ. In their ODE system, Bray et al. used realistic components concentrations and reaction rates from available experimental data. The model was able to correctly reproduce the pathway excitation to aspartate (attractant) and nickel (repellent), but did not include adaptation, which was added in later versions of BCT (Levin et al., 1998). However, the system of ODEs used in BCT was unable to explain the high sensitivity (gain) of the cell response (Bray, 2002). The program BCT is discussed in detail in the section *Simulation Software*.

In the model of Hauri and Ross (1995), authors also simulated the phosphorylation pathway, including the phosphorylation of CheY and CheB and their dephosphorylation. The receptor complex was described in ten states (five attractant-bound and five attractant-free). Due to a lack of experimental data, Hauri and Ross did not include interaction between CheYp and flagellar motor. However, they assumed that frequency of CCW rotation is a Hill function of CheYp, according to experiments of (Kuo and Koshland, 1989). The model was mainly based on known reaction rates and protein concentrations. Whenever possible, rate coefficients were first assigned experimentally measured values. Authors permitted variation in these rate coefficients to obtain values that were sufficient to explain initial response to stimuli (excitation) and an eventual return of behavior to baseline (adaptation). The model simulations agreed well with experiments, in particular the timescale of initial excitation. Also, the model demonstrated exact adaptation for both attractant (aspartate) and repellent (nickel). Authors simulated swimming of model bacteria in a Gaussian gradient of aspartate, but the cells failed to response the applied gradient with given Hill

coefficient of CheYp-motor interaction. A significant increase of it, from 5.5 to 15, allowed the cells to respond to the gradient. The model failed to account for the experimentally observed sensitivity and gain, as well as the timescale of adaptation. Alterations of rate constants changed the adaptation precision, thus the model was not robust.

Spiro and colleagues (Spiro et al., 1997) also incorporated attractant binding, methylation, phosphorylation and CheYp-motor interaction into their model. A minimal number of three methylation states was assumed, and the rate of phosphorylation increased with the methylation state. The rate constants were tuned by trial and error to achieve adaptation over a large range of ligand concentrations. The simulated ramp, step and saturation responses to aspartate showed precise adaptation and a reasonable timescale. The main focus was made on analysis of gain, which was defined as $g = \frac{-db}{d(\ln p)}$, where b is the motor bias, and p is the rate of CheY phosphorylation, in contrast to earlier definition as a change of bias per percent change in receptor occupancy (Segall et al., 1986). Authors argued that a cooperativity in CheYp-motor binding, an activity-dependent dephosphorylation by CheZ, or a receptor-receptor interactions might account for the observed high gain.

A major advance in chemotaxis modeling was achieved by Barkai and Leibler (1997), who suggested a simple and elegant model that exhibited robust adaptation as its generic characteristic. In their model, authors used a two-state model of receptor complex following (Asakura and Honda, 1984): receptor can be either active or inactive, and the probabilities of both states are determined by methylation level and ligand occupancy. The key assumption of this model is that CheB demethylates only active receptors, thus providing a feedback to bring the system to its steady state. The methylating enzyme CheR was assumed to act on both active and inactive receptors. The feedback provided by CheB depends only from the system output A (CheA activity), and therefore the system retains perfect adaptation at various ligand concentrations and methylation levels. Yi et al. (2000) further studied the Barkai-Leibler model analytically, and derived all conditions for perfect adaptation within the Barkai-Leibler model beyond those reported in the original article. Later, Mello and Tu (2003a) performed theoretical analysis of a full ODE system with

phosphorylation cascade included, and formulated conditions necessary for a perfect adaptation and the effects of their violation.

In contrast to deterministic models mentioned above, Morton-Firth and Bray suggested a fully stochastic model of chemotaxis pathway (Morton-Firth and Bray, 1998). The stochastic approach was motivated by necessity to simulate the stochastic nature of motor switching, as reported in (Block et al., 1982, 1983). The receptor model followed the two-state paradigm of (Asakura and Honda, 1984; Barkai and Leibler, 1997). The ligand binding, methylation and phosphorylation reactions were simulated stochastically. The motor bias was defined as a Hill function of CheYp. Authors showed that CheYp fluctuates around an average corresponding to the deterministically calculated concentration. The average duration of fluctuations was found to be 80.7 ms, which is much shorter than the observed alternations between CW and CCW rotations of tethered bacteria (typically 2.6 s). Their results therefore argued against a simple threshold-crossing model for motor switching, and suggested that filtering of the CheYp fluctuations by the motor can produce temporal run and tumble distributions closer to the experimentally observed behaviour.

A principal novelty of the Morton-Firth and Bray model was the use of free energy calculations in respect to ligand binding and methylation of Tar complex, suggesting a unified approach for the undergoing transformations (Morton-Firth et al., 1999). Robust adaptation was achieved by assumption that CheR binds only to inactive receptor complexes and CheBp to active ones. Morton-Firth and colleagues demonstrated close agreement of their model with experimentally observed duration of adaptation response to aspartate over four orders of concentrations, reported by Berg and Tedesco (1975). They also showed that sequential methylation of Tar is important for adaptation. The model was implemented in a StochSim program, which is discussed in the section *Simulation Software*. The first stochastic model failed to reproduce the high sensitivity at low aspartate concentrations, which was addressed in further work (Shimizu et al., 2003).

Models of receptor cooperativity

Apart from models of adaptation and phosphorylation, which were studied in detail by late 1990-s, the problem of high gain remained unresolved. The sensory system of *E. coli* demonstrates extreme sensitivity, with signal amplification by a factor of 100 (see *Signal Amplification* section above). The possible mechanisms of such a strong signal amplification were actively studied by both experimentalists and theoreticians.

Ising model. Cooperativity of receptors as a source of high gain was first suggested by Bray et al. (1998). Shi and Duke (1998) proposed an Ising-type model of receptor-receptor interactions, drawing parallels from a physical problem of magnetic dipoles. A Ising model with two-dimensional lattice of interacting receptors was later merged with stochastic simulator StochSim to give a fully stochastic model of *E. coli* chemotaxis pathway (Shimizu et al., 2003). This spatially resolved model of receptor cluster demonstrated fairly good agreement with FRET dose-response experiments of Sourjik and Berg (2002a).

MWC model. An alternative model of receptor cooperativity was proposed by Sourjik and Berg (2004), who fitted their experimental responses of homogeneous receptor clusters with a classical Monod-Wyman-Changeux (MWC) model of allosteric protein interactions (Monod et al., 1965). The MWC model was further developed in (Mello and Tu, 2005) to fit the experimentally measured responses of heterogeneous receptors. In the MWC model of receptor cluster, there are two key assumptions: (1) the inactive state of a receptor homodimer has a higher affinity to attractant than the active state; and (2) the entire complex exists with all of its N receptor homodimers being either active or inactive. Generally speaking, cooperativity in the MWC model can be characterized by the correlation length of the system, which depends on the strength of the nearest-neighbour interactions in Ising-type models. In the MWC model, the correlation length is effectively set by N, the size of the cluster, therefore bypassing all of the complexity in determining the local interactions between receptors. Also, the MWC model can be solved algebraically, making the analysis easier and more intuitive. A comparative analysis of MWC and Ising models is given in

(Skoge et al., 2006), where MWC is shown to be more consistent with the FRET dose-response data of Sourjik and Berg for wild-type, CheR and CheRCheB mutants. A detailed description of the MWC model for a heterogeneous receptor cluster will be given in section *Methods and Algorithms*.

Endres and Wingreen (2006) simulated the MWC model with an assumption that CheR and CheB can access five to seven receptors when tethered to a particular receptor, as shown experimentally in (Li and Hazelbauer, 2005). Authors stochastically simulate the effect of such an 'assistance neighbourhood', demonstrating that it is necessary for precise adaptation in receptor cluster. For single receptor methylation, authors adopted Barkai-Leibler model with the assumptions that CheR methylates only inactive receptors, while CheBp demethylated only the active receptors. Unlike the original BL model, the methylation level of a single receptor in a cluster is poorly correlated with the overall cluster activity, thus leading to imprecise adaptation. Authors show that their extention of BL model with the assistance neighbourhood yields precise adaptation: assistance neighbourhoods effectively increase the ladder of methylation levels such that CheR and CheB rarely encounter fully methylated or demethylated conditions, which essentially results in perfect adaptation. Endres and Wingreen also predict two distinct limits of adaptation at high attractant concentration: receptors either saturate and hence stop responding, or receptors fully methylate and hence stop adapting.

1.4.3 Robustness and noise

Noise plays an important role in the bacterial world. The cell swims along curly trajectories rather than straight lines because of the Brownian motion causing rotational diffusion (Berg, 1993). The network itself is affected by the noise from receptor-ligand binding, methylation, and variations in protein concentrations (gene noise). The variety of noise sources that disturb the chemotactic navigation poses a question of how this navigation is possible at all, taking into account the relative simplicity of the system. Computer simulations and experimental methods resolved this question.

Variation of *E. coli* network parameters does not break its property of precise adaptation because of its robustness (Barkai and Leibler, 1997; Alon et al., 1999). Later, Morton-Firth et al. (1999), Yi et al. (2000) and Mello and Tu (2003a) demonstrated in their models that precise adaptation is robust if methylation and demethylation rates depend on receptor activity.

Computer analysis of several alternative chemotaxis network topologies demonstrated that *E. coli* has the smallest network which maintains robustness against gene expression noise (Kollmann et al., 2005). In particular, the topology of *E. coli* chemotaxis network ensures robustness of the output (concentration of CheYp) against concerted variations in protein levels, which is the dominant source of gene expression noise. Uncorrelated variations in protein levels, which arise due to noise in protein translation, are further compensated by the translational coupling of neighbouring chemotaxis genes (Løvdok et al., 2009).

While adaptation precision remains robust upon variations in protein concentrations and kinetic parameters, there are two other system properties that are sensitive to perturbations: the steady-state behavior and the adaptation time (Alon et al., 1999). The steady-state behavior variation in live cells is minimized by coupled expression of adaptation enzymes CheR and CheB. When their concentrations change proportionally, the steady-state behavior remains unbiased. However, the adaptation time is sensitive to such changes. This means that even genetically identical cells can have variability in chemotactic behavior (Spudich and Koshland, 1976; Berg and Tedesco, 1975).

Another intrinsic source of noise arises from slow reactions of receptors methylation. Notably, the cells appear to have been selected to maintain low CheR expression levels, which lead to high noise in methylation events and long-term variations in system output. It was shown experimentally that such a noise provides long-term variations in the cellular behavior, with long-term correlations of motor output (up to 20 min) (Korobkova et al., 2004). Such variation in motor behavior, and hence run length, can help the cell to explore the surrounding environment more efficiently, because the runs in adapted state are distributed as Lévy-flights rather than exponential variables. In this case, the noise can be beneficial for individual cells to explore

new areas, also in the presence of gradient (Emonet and Cluzel, 2008).

However, most of the noise factors decrease the efficiency of chemotactic navigation. But the chemotactic network can cope with that. Experiments and simulations of the network input-output properties show that the pathway demonstrates properties of low-pass filter coupled to a differentiator (Block et al., 1982; Andrews et al., 2006; Tu et al., 2008). The system averages the signal over a certain time, and then differentiates it to determine the steepness of the gradient in the current run direction. In this way, the system follows the main signal (gradient) and filters out high-frequency noise. Moreover, Andrews et al. (2006) showed that bacterial signaling system works close to the theoretical limit of precision (Rayleigh limit), demonstrating the characteristics of nearly perfect molecular instrument.

1.4.4 Simulation software

At present, most molecular mechanisms of chemotactic sensing are well understood, and the reaction rates together with concentrations of components are known (http://www.pdn.cam.ac.uk/groups/comp-cell/Data.html). Therefore, the single-cell behavior can be simulated in a quantitative way. The available programs of chemotaxis simulation arise from two main schools of mathematical modeling: ordinary differential equations (ODE) and the stochastic (Monte-Carlo) simulations. The programs of both types are described and discussed below.

BCT

The ODE approach is best represented by Dennis Bray's BCT (Bray et al., 1993; Bray and Bourret, 1995; Levin et al., 1998). BCT was the first program which simulated chemotaxis pathway in a quantitative way. The program numerically solves ODE that govern pre-assembling of ternary signaling complexes, ligand binding, receptor methylation, and the phosphorylation cascade. Currently, the system consists of about 90 differential equations. The most important features of the current version (BCT 4.4) include:

- Detailed simulation of receptor complex preassembling and phosphorylation cascade,
- Exact adaptation to the addition and removal of chemoeffectors,
- Phenotypes of 63 out of 65 bacterial mutants are accurately reproduced,
- Response to two attractants (aspartate and serine), and to a repellent (nickel) can be simulated,
- Individuality in swimming behaviour can be simulated.

The BCT program represented a great advance in the field of chemotaxis modeling. Based on experimentally determined component concentrations and reaction rates, it was carefully analysed and adjusted to reproduce the experimental data on cell

response, including many mutant *E. coli* strains. The main shortcoming of BCT is that it fails to reproduce the high sensitivity (gain) provided by the receptor-receptor cooperative interactions. To obtain the necessary sensitivity, an 'infectivity factor' was introduced, which multiplies the signal strength. For users, the program which is available online has one practical disadvantage: it is compiled and distributed only for Macintosh, which limits its potential usage. The source codes are not web available.

Bray and colleagues used BCT as a core simulator to model individual cell swimming in 2D space (Bray et al., 2007; Zonia and Bray, 2009). The program with detailed graphical representation of a single bacterium (with flagella) is called *E. solo*, while the graphical representation of many bacteria without flagella is called *E. pluribus*.

StochSim

As an alternative approach, stochastic model of chemotaxis pathway was implemented in the program StochSim (Morton-Firth and Bray, 1998; Morton-Firth et al., 1999). The program provides a general-purpose stochastic simulator of biochemical reactions, in which each molecule is represented as an individual software object. Reactions between molecules occur stochastically, according to probabilities computed from known rate constants. The program is able to represent multiple post-translational modifications and conformational states of individual molecules. In particular, the Tar signaling complex is simulated with aspartate binding, methylation at different sites, binding of CheB, CheR and CheY. These reactions are represented by 12 binary flags. Each complex in the program flips between two conformational states with a probability determined by its current combination of binary flags. The most important program features are listed below:

- Implementation of multiple states of individual molecule (for receptor, these include covalent modifications and binding states),
- Implementation of individual molecular reactions and realistic protein copy numbers,
- The model accurately reproduces adaptation time in chemotactic response to different concentrations of aspartate,

- Open-source and well-documented program, with binaries precompiled for Windows, MacOS and Linux.

In the first version of StochSim, the model was non-spatial, so that positions of molecules were not taken into account, assuming uniformly mixed solution. Therefore, StochSim 1.0 failed to reproduce the high sensitivity of chemotactic system. It was addressed in (Shimizu et al., 2003), where authors implemented nearest-neighbour interactions by a two-dimensional Ising model of receptor lattice. This allowed to reproduce the experimental data on high sensitivity. A shortcoming of the purely stochastic approach is its high computational costs. For example, a 500-s simulation of a single bacterium with non-spatial StochSim requires several hours on a modern desktop PC, while the same simulation with spatial StochSim (65x65 lattice) can require up to two days.

AgentCell

StochSim was used as a core simulator in AgentCell (Emonet et al., 2005). AgentCell is designed for simulation of stochastic effects on cellular behavior, and chemotaxis was used as a test system. The program simulates individual chemotactic bacteria swimming in 3D space. The output of StochSim, in number of CheYp molecules, is used to determine the rotation direction of individual flagellar motors. The cell swims or tumbles depending on the state of its flagella: *bundled* or *apart*, corresponding to CCW or CW motor rotation, respectively.

On a single-cell level, AgentCell (StochSim) reproduces chemotactic response to changes of attractant (aspartate). AgentCell is also capable to demonstrate flagellar motor behavior according to power-law rather than exponential distribution, in agreement with the intriguing experiments of Korobkova et al. (Korobkova et al., 2004). On the population level, AgentCell demonstrates reasonable diffusion coefficients of bacterial population in the absence of gradients, and also realistic rate of population drift in presence of attractant gradient. Rotational diffusion as a result of Brownian motion is included into cell motion model.

For researchers, AgentCell provides rich opportunities: its core simulator StochSim

reproduces individual molecular reactions inside every cell, while its main algorithm enables simultaneous tracking of many cells in 3D space in presence of ligand gradients and, potentially, in user-defined spatial geometries. From the programming side, AgentCell is also well-designed: it is open-source, it has a clear and well-documented structure, and it is platform-independent due to Java implementation. For the purpose of large-scale simulations, however, the largest shortcoming of this program is inherited from StochSim, which is computationally demanding. Therefore, simulation of bacterial population requires massive parallel computations, preferably with 1 CPU per bacterium, and such simulations can routinely run only on clusters. However, AgentCell provides a perfect platform for further development of individual-based chemotaxis models, because it is built of inter-changeable modules, and different models can be readily plugged in.

Smoldyn

Yet another level of intracellular modeling is implemented in Smoldyn (Lipkow et al., 2005). Smoldyn is a general-purpose stochastic simulator, which simulates individual molecules stochastically in 3D cell volume, according to Smoluchowski dynamics (Andrews and Bray, 2004). The molecule position is updated at regular time intervals according to its diffusion coefficient, current position and occurring events. Bimolecular reactions are simulated using the proximity of two potential reactants: two suitable molecules that come within each other's binding radius are made to react. When applied to chemotaxis, Smoldyn simulates diffusion of individual CheYp molecules in rectangular cell volume. For the input, Smoldyn uses BCT, which calculates concentration of autophosphorylated CheA molecules at the cell pole. Smoldyn represents a major advance in simulation software, and its features are listed below:

- Spatially resolved simulation of individual molecules and reactions.
- Natural representation of CheYp gradient from signaling complex to flagellar motors.
- Effects of macromolecular crowding in cytoplasm.

- Effect of motor positioning in the cell wall.
- Open-source program.
- 3D graphical representation option.

Smoldyn represents the most detailed model of cytoplasmic events occurring in chemotaxis system. A shortcoming of the current version is the usage of BCT module – a use of spatially resolved StochSim would be probably more reasonable. Because of their focus on single-molecule level, spatially-resolved models of signaling pathway are also computationally expensive for simulation of bacterial populations. However, such programs as Smoldyn and StochSim provide insights into molecular mechanisms of the signal transduction, and therefore they can be very helpful for detailed analysis of the system behavior on a molecular level.

1.4.5 Multiscale models

Multiscale problems arise naturally from a certain level of understanding of a particular system, when its building blocks are already well understood, but the whole system behavior over multiple levels of complexity remains obscure. Currently, there is no general mathematical framework to integrate heterogeneous models over the wide range of scales present in most biological, physical and engineering problems (Colella et al., 2004). New ways of thinking in mathematics and computation are required to "bridge the scales."

There exist three major approaches to the multiscale problems: *multiresolution discretization methods*, which resolve multiple scales within a single model system by dynamically adjusting the resolution as a function of space, time, and data; *closure methods*, which provide analytical representations from detailed microscopic models; and *hybrid methods*, which couple different models and numerical representations that represent different scales.

Multiresolution numerical methods include adaptive timestep methods for stiff ordinary differential equations, differential-algebraic systems, and stochastic differential equations; adaptive mesh refinement (AMR) and front-tracking methods for partial differential equations; and adaptive analysis-based methods for integral equations. These methods are widely used in physics, from quantum chemistry to supernova simulations. In simulation of biochemical networks, a coarse-grained method called tau-leaping has been proposed for acceleration of discrete stochastic simulations (Gillespie, 2001; Cao et al., 2006).

Closure methods are derivation of macroscopic models from more detailed microscopic models. Such problems include those that lack a strong separation of scales, rare-event problems, and problems involving the reduction of high-dimensional state spaces to a small number of degrees of freedom. The closure methods are used, for example, in hydrodynamics of a multifluid medium, material science and chemistry of combustion. In biology closure methods are used to find the first two central moments (mean and covariance) in stochastic models of noisy biochemical networks (Gadgil et al., 2005; Lee et al., 2009).

Hybrid methods typically start from an analysis of a general mathematical model

that describes the system at all relevant scales. Such an analysis yields either a hierarchy of models that describe the system behavior on different spatial scales (with overlap in the range of validity), or a splitting of the unknowns into components corresponding to slow and fast dynamics. Hybrid methods are used in physics, chemistry and earth science, e.g. for simulation of plasma in tokamaks, catalytic surface reactions, and climate modeling. In biology hybrid models can be used, for example, in simulation of intracellular reaction-diffusion systems using hybridization of stochastic and deterministic methods, with appropriate spatial mesh discretization (Chiam et al., 2006; Kalantzis, 2009).

Separation of system reactions into slow and fast components allows to perform efficient model reduction, which is especially relevant for high-dimensional systems in physics, chemistry and biochemistry. Such a model reduction can be made automatically using mathematical analysis of the underlying system of ordinary differential equations. The model reduction methods include analysis of system eigenvalues or computing the system trajectories that are close to slow attracting manifolds (Lebiedz, 2004; Lebiedz et al., 2008; Reinhardt et al., 2008).

Some specific hybrid models were proposed for bacterial chemotaxis. Setayeshgar et al. (2005) described the chemotactic excitation and adaptation with a simplified model of two ODEs. The motor is described by a two-state model, switching between CCW and CW with rates depending on CheYp. The 'voting rule' of tumbling is used: when the majority of motors rotate CW, the cell tumbles, as suggested in (Ishihara et al., 1983; Segall et al., 1986). The simplified model of signal transduction coupled with voting model of tumbling is simulated using a Monte-Carlo scheme, with the cells moving in 1D space. Authors apply a coarse integration scheme to compute the bacterial density at given timepoints. The key assumption is that the system 'closes' on the spatial density, that is it can be described on long time scales solely by the spatial cell density distribution. The spatial distribution is thus extrapolated over long time using short local full-scale Monte-Carlo simulations.

The model of Setayeshgar et al. (2005) was used by Erban and Othmer (2004, 2005) to incorporate the microscopic network dynamics to the coefficients of Keller-Segel equation, as described above in section *Population-scale models*.

Multiscale problems can be addressed by a specific design of simulation software, by using high-thoughput methods of data processing and storage. The program AgentCell, discussed above, is designed with powerful methods to scale it up to populational simulations: high performance Java-based results logging system, Hierarchical Data Format 5 (HDF5) data storage system, and parallelization of computations among many computers within a computing cluster.

Another multiscale platform for bacterial simulation is BacSim (Kreft et al., 1998), which is an individual-based model of bacterial growth including substrate uptake, metabolism, maintenance, cell division and death. The model quantitatively simulates *E. coli* population growing in defined medium, with spatially-resolved individual cells and surrounding medium. Though it does not include chemotaxis network, this model shows a significant step toward construction of multiscale platforms, aimed at individual-based simulations of bacterial populations and multi-species biofilms.

1.5 Motivation

During the last 40 years of extensive research, bacterial chemotaxis became the best described signaling system in biology. Most molecular interactions, protein copy numbers and reaction rates are known in detail. A number of mathematical models was suggested to study the system properties of chemotaxis signaling network, to reproduce its input-output behavior, and to simulate swimming of bacteria in artificial gradients *in silico*. It was a large effort in the area of modeling during the recent 15 years that brought us to the quantitative understanding of bacterial chemotaxis from elementary reactions. The next challenge is to quantitatively understand the behavior of bacterial populations in their environment, and the roles of particular system properties in different spatial and temporal scales.

The overview of existing models demonstrates a lack of individual-based models for simulation of bacterial populations. The available models are strongly focused on molecular details of signal transduction in a single cell. They are either too detailed and computationally demanding (AgentCell) or lack an accurate description of receptor clusters (*E. pluribus*) to simulate bacterial populations quantitatively. This has a methodological reason, because these models are based either on purely stochastic methods, which are aimed to simulate individual molecules, or on ODE approach, which is based on assumption of well-mixed system and mass action law. Multiscale modeling requires combination of stochastic and deterministic methods to simulate bacterial populations using quantitative models of individual cells.

To address this problem, in this work different mathematical approaches are combined into a hybrid model. The receptor cluster activity is described algebraically by a mean-field approximation (MWC), the methylation is described by ODE, the phosphorylation cascade is described algebraically assuming its rapid equilibrium, and the flagellar motors are modeled as stochastic switches. Combination of different methods allowed to construct a highly efficient and up-to-date model, which is described in detail in the following section *Methods and Algorithms*. Based on this model, simulations of bacterial populations allowed to reveal novel system properties of *E. coli* chemotaxis, which are described in section *Results*.

Chapter 2

Methods and Algorithms

> Everything must be made as simple as possible. But not simpler.
>
> Albert Einstein

2.1 Hybrid model of chemotaxis pathway in *E. coli*

2.1.1 MWC model of mixed receptor cluster

In order to simulate the receptor complex activity, a Monod-Wyman-Changeux (MWC) model for a mixed receptor cluster was applied (Mello and Tu, 2005; Endres and Wingreen, 2006; Keymer et al., 2006a). This model accounts for the observed experimental dose-response curves of adapted cells measured *in vivo* by FRET technique (Sourjik and Berg, 2002a). According to the model, individual receptor homodimer of type r ($r = a$ for Tar, s for Tsr) is described as a two-state receptor, which can be either 'on' or 'off'. Receptors form clusters with all receptors in a cluster either 'on' or 'off' together (Figure 4). The clusters are composed of mixtures of Tar and Tsr receptors. At equilibrium, the probability that a cluster will be active is

$$A = \frac{1}{1 + e^{F}} \tag{4}$$

where $F = F^{on} - F^{off}$ is the total free energy of the cluster, and $F^{on/off}$ is the free energy of the cluster in the on/off state, respectively. For a cluster composed of n_a Tar and n_s Tsr receptors, the total free-energy difference is, in the mean-field approximation, $F = n_a f_a(m) + n_s f_s(m)$, which is the sum of the individual free-energy differences between the two receptor states

$$f_r(m) = f_r^{on}(m) - f_r^{off} = \varepsilon_r(m) + \log\left(\frac{1 + [S]/K_r^{off}}{1 + [S]/K_r^{on}}\right) \tag{5}$$

where $[S]$ is the ligand concentration, $K_r^{on/off}$ is the dissociation constant for the ligand in the on and off state, respectively. The methylation state of the receptor enters via the 'offset energy' $\varepsilon_r(m)$, which is described below in detail.

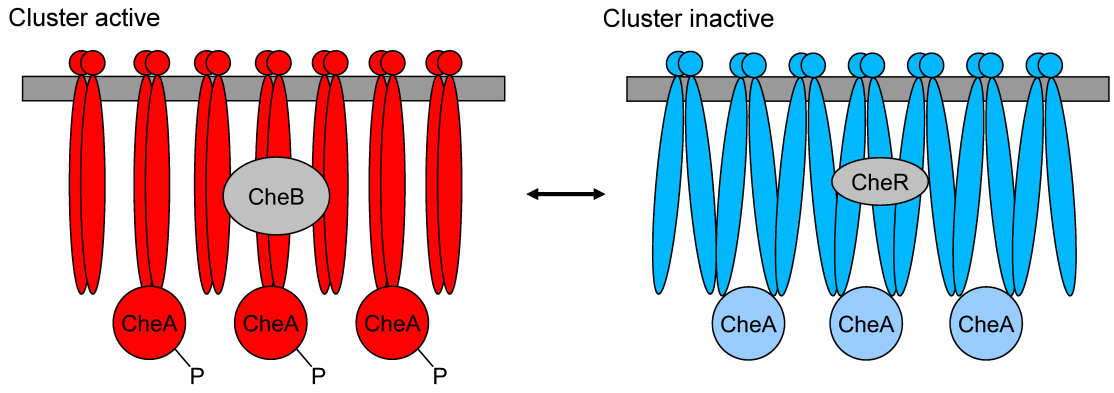

Figure 4: The MWC model of receptor cluster. Each receptor homodimer is described by a two-state model. The inactive state of a receptor has a higher affinity to attractant than the active state. The entire complex exists with all of its receptor homodimers either active or inactive. As in the two-state model, the receptor and the kinase are tightly coupled, so that the kinase is active when the receptor is active. The probability A that receptor cluster is active is dependent on ligand concentration and the methylation state of the receptors. CheB is assumed to demethylate only active receptors, while CheR methylates only inactive ones.

2.1.2 Adaptation model

Adaptation is modeled according to the mean-field theory of MWC model (Mello et al., 2004; Endres and Wingreen, 2006). CheB demethylates only active receptors, CheR methylates only inactive receptors, and both enzymes work at saturation. Each bound CheR adds methyl groups at a rate $a(1-A)$, and each bound CheB removes methyl groups at a rate bA. Under these assumptions, the methylation rate is given by

$$\frac{dm}{dt} = a(1-A)[CheR]\frac{[MCP]}{K_R + [MCP]} - bA[CheB]\frac{[MCP]}{K_B + [MCP]} \tag{6}$$

We further assume that both enzymes work at saturation:

$$\frac{dm}{dt} \approx a(1-A)[CheR] - bA[CheB] \tag{7}$$

Note that this equation does not imply a first-order reaction mechanism between the adaptation enzymes and receptors – the enzymes work in the zero-order regime. The linear products $a(1-A)[CheR]$ and $bA[CheB]$ mean that a bound CheR and CheB can only act if the receptor cluster is inactive (CheR) or active (CheB), with probability $(1-A)$ and A, respectively (Endres and Wingreen, 2006; Hansen et al., 2008).

A *relative adaptation rate* is defined by parameter k in equation

$$\frac{dm}{dt} = k(a[CheR](1-A) - b[CheB]A) \equiv kV_0 \tag{8}$$

Parameter k denotes the adaptation rate relative to the wild-type adaptation rate V_0. In the cells with normal steady-state activity ($A^* = 1/3$), the rates and concentrations of the adaptation enzymes are equilibrated by assuming $b[CheB] = 2a[CheR]$. The catalytic rates a and b remain unchanged, and the cell-to-cell variability in adaptation rate k is caused by variability in their $[CheR, CheB]$, provided that they change in a coordinated manner with the fixed ratio: $[CheR] : [CheB] = 0.16 : 0.28$ (Li and Hazelbauer, 2004). The latter ODE for methylation is integrated using the explicit

Euler method, so that the average methylation level evolves in time as

$$m(t + \Delta t) = m(t) + kV_0\Delta t \tag{9}$$

To achieve high computational efficiency in the model, the average methylation level m is assumed a continuously changing variable within the interval $[0, 8]$, with linear interpolation between the key offset energies: $\varepsilon_r(0), 1.0$; $\varepsilon_r(1), 0.5$; $\varepsilon_r(2), 0.0$; $\varepsilon_r(3), -0.3$; $\varepsilon_r(4), -0.6$; $\varepsilon_r(5), -0.85$; $\varepsilon_r(6), -1.1$; $\varepsilon_r(7), -2.0$; $\varepsilon_r(8), -3.0$, following (Endres and Wingreen, 2006; Hansen et al., 2008).

2.1.3 Kinase activity and CheY phosphorylation

CheA kinase activity (Ap) is assumed to be equal to the activity of the receptor complex (A). The differential equation for CheY phosphorylation is (Kollmann et al., 2005)

$$\frac{dYp}{dt} = k_Y Ap(Y^T - Yp) - k_Z YpZ - \gamma_Y Yp \tag{10}$$

Here Yp is [CheYp], Y^T – total $[CheY]$, Z^T – total $[CheZ]$, Ap – active $[CheA]$, and $k_y = 100\ \mu M^{-1}s^{-1}, k_Z = 30/[CheZ]\ s^{-1}, \gamma_Y = 0.1$ are the rate constants according to (Kollmann et al., 2005; Stewart et al., 2000; Sourjik and Berg, 2002b). The rate of phosphotransfer from active CheA to CheY is much faster than the rate of CheA autophosphorylation (Table 1). Therefore, the concentration of CheYp is obtained as a function of active CheA from the steady-state equation:

$$Yp = \frac{k_Y ApY^T}{k_Y Ap + k_Z Z + \gamma_Y} \tag{11}$$

In relative units, $[CheYp] = 3\frac{k_Y k_s A}{k_Y k_s A + k_Z Z + \gamma_Y}$, where $k_s = 0.45$ is a scaling coefficient.

In this scaling, relative $[CheYp] = 0, 1, 3$ correspond to fully inactive, adapted and fully active receptor cluster, respectively. The absolute concentration relates to the relative as $[CheYp]_{abs} = 3.1[CheYp]$ (μM), following (Cluzel et al., 2000).

2.1.4 CheB phosphorylation

To study the effect of kinase-dependent CheB phosphorylation, the concentration of phosphorylated (active) CheB was assumed to follow the steady-state equation (Kollmann et al., 2005; Mello and Tu, 2003b):

$$[CheB] = [CheB]_{tot} \frac{A}{A + k_{0.5}} \tag{12}$$

where $[CheB]_{tot}$ is the total relative concentration of CheB, and A is the kinase activity.

It was assumed that 100%, 50%, or 25% of CheB can be phosphorylated in the steady state $A^* = \frac{1}{3}$, corresponding to $[CheB]_{tot} = 1, 2, 4$ and $k_{0.5} = 0, \frac{1}{3}, 1$, respectively. Note that at maximum kinase activity $A = 1$, the active $[CheB]$ increases 1, 1.5 and 2 times compared to $[CheR]$; at steady state $A = \frac{1}{3}$ both enzymes always have equal levels, whereas at positive chemotactic signal $A < \frac{1}{3}$ $[CheB]$ is equal to $[CheR]$ ($k_{0.5} = 0$) or lower than $[CheR]$ ($k_{0.5} = \frac{1}{3}, 1$).

2.1.5 Time-scale separation

It is assumed that the rates of ligand binding t_l, rates of receptor-cluster conformational changes t_k and receptor covalent modification t_m are well separated in scales: $t_l \ll t_k \ll t_m$. On our scale ($\sim$ 1 s) the reactions of CheA autophosphorylation, phosphotransfer from CheA to CheY and CheB can be described as a rapid equilibrium state by algebraic equations (11) and (12). The slowest reactions – methylation by CheR and demethylation by CheB – are described by the ODE (8) to reproduce the time scales of seconds and minutes required for adaptation. Table 1 shows the comparative rates of the main reactions.

2.1.6 Motor switching

The motor is modeled according to the two-state model (Block et al., 1983)

$$CCW \underset{k_-}{\overset{k_+}{\rightleftharpoons}} CW \tag{13}$$

Description	Value [1/s]		
	ref. (1)	ref. (2)	ref. (3)
CheR catalytic rate	0.819	0.39	0.75
CheB catalytic rate	0.155	6.3	0.6
CheA autophosphorylation rate	15.5	50	23.5
CheY phosphorylation rate	15	530	530
CheB phosphorylation rate	15	15.9	53
CheY dephosphorylation rate	14.5	30.1	30

Table 1: Rates of reactions involved in the signaling pathway, according to (1) Morton-Firth et al., 1999; (2) Kollmann et al., 2005; (3) Emonet and Cluzel, 2008.

The CCW motor bias (the fraction of time motor spins CCW) is related to the switching rates as (Scharf et al., 1998)

$$mb = \frac{k_-}{k_- + k_+} \tag{14}$$

The CCW motor bias depends on CheYp concentration as a Hill function in the following form (Cluzel et al., 2000; Shimizu et al., 2003)

$$mb = \frac{mb_0}{\left(\frac{CheYp}{CheYp_0}\right)^H (1 - mb_0) + mb_0} \tag{15}$$

In this work, CheYp is already normalized to its steady-state value, so $CheYp_0 = 1$.

The frequency of switching CW→CCW is taken $k_- = 1/T_{cw} = 0.83\ s^{-1}$ and assumed to be constant, because its relative change upon stimulus is small compared to change of k_+ (Block et al., 1983). Equation

$$k_+ = k_- \left(\frac{1}{mb(CheYp)} - 1\right) \tag{16}$$

gives the frequency of CCW→CW motor switching. This model of motor switching was used in (Vladimirov et al., 2008). For a more detailed model of motor switching, see Appendix B.

In simulation algorithm, at every time step Δt the motor can switch its direction

according to the switching frequency $k_{+(-)}$, with probability $P_{+(-)} = k_{+(-)}\Delta t$.

2.1.7 Model verification

A summary of the parameters used in the model is given in Table 2, and a summary of sub-models and underlying assumptions is shown in Table 3. Along the lines of the MWC model for a mixed receptor cluster (Endres and Wingreen, 2006), a cluster of 18 receptors is considered, composed of 6 Tar and 12 Tsr receptors. The catalytic rates a and b were chosen to achieve the proper time scale of adaptation according to *in vivo* FRET dose-response curves. The model was implemented in a program RapidCell, which is described in the corresponding section.

Parameter	Value	Reference
K_a^{on}	$12\ \mu M$	Diss. constant of Tar to Asp (Morton-Firth et al., 1999)
K_a^{off}	$1.7\ \mu M$	Diss. constant of Tar to Asp (Morton-Firth et al., 1999)
$K^*(K_D)$	$4.52\ \mu M$	Apparent diss. constant of Tar to Asp (Shimizu et al., 2003), this work
K_s^{on}	$10^6\ \mu M$	Diss. constant of Tsr to MeAsp (Endres and Wingreen, 2006)
K_s^{off}	$100\ \mu M$	Diss. constant of Tsr to MeAsp (Endres and Wingreen, 2006)
n_a	6	Number of Tar receptors in a cluster (Endres and Wingreen, 2006)
n_s	12	Number of Tar receptors in a cluster (Endres and Wingreen, 2006)
$[CheR]$	$0.16\ \mu M$	Wild-type concentration (Li and Hazelbauer, 2004)
$[CheB]$	$0.28\ \mu M$	Wild-type concentration (Li and Hazelbauer, 2004)
a	0.0625	Catalytic rate of methylation, fitted
b	0.0714	Catalytic rate of demethylation, fitted
$[CheY]_{tot}$	$9.7\ \mu M$	Total CheY concentration (Li and Hazelbauer, 2004)
A^*	$1/3$	Steady-state cluster activity (Endres and Wingreen, 2006)
CCW mb_0	0.65	Steady-state motor bias (Cluzel et al., 2000; Segall et al., 1986)
H	10.3	Hill coefficient of CheYp-motor interaction (Cluzel et al., 2000)
v_0	$20\ \mu m s^{-1}$	Cell swimming speed (Staropoli and Alon, 2000)
D_r	$0.062\ rad^2 s^{-1}$	Rotational diffusion coefficient (Berg and Brown, 1972; Berg, 1993)
Δt	$0.01\ s$	Time step in the model

Table 2: Parameters used in RapidCell-1.0

As shown previously in (Mello and Tu, 2005; Endres and Wingreen, 2006; Keymer et al., 2006a; Skoge et al., 2006), the MWC model for a mixed receptor cluster correctly reproduces the *in vivo* FRET response amplitudes to step-wise addition and removal

Model	Reference
Receptor free energy: $f_r(m) = f_r^{on}(m) - f_r^{off}$ $f_r^{on}(m) = \varepsilon_r(m)$ $f_r^{off} = \log\left(\frac{1+[S]/K_r^{off}}{1+[S]/K_r^{on}}\right)$	(Mello and Tu, 2005; Endres and Wingreen, 2006)
Cluster free energy: $F = n_a f_a(m) + n_s f_s(m)$	(Mello and Tu, 2005; Endres and Wingreen, 2006)
Cluster activity: $A = \frac{1}{1+e^F}$	(Mello and Tu, 2005; Endres and Wingreen, 2006)
Receptor methylation: $\frac{dm}{dt} = a(1-A)[CheR] - bA[CheB]$	(Endres and Wingreen, 2006; Hansen et al., 2008)
Steady-state CheYp concentration $[\text{CheYp}] = 3\frac{k_Y k_s A}{k_Y k_s A + k_Z Z + \gamma_Y}$	(Kollmann et al., 2005) CheYp is normalized to CheYp_0
CCW motor bias $mb = \frac{k_-}{k_- + k_+} = \frac{mb_0}{Y^H(1-mb_0)+mb_0}$	(Scharf et al., 1998; Shimizu et al., 2003) Y is CheYp normalized to CheYp_0
Motor switching freq. (CW→CCW) $k_- = 0.83\ s^{-1}$	(Block et al., 1983), assumed to be constant
Motor switching freq. (CCW→CW) $k_+ = k_-\left(\frac{1}{mb(CheYp)} - 1\right)$	follows from mb equation
Distribution of tumbling angle (isotropic) $f(\Theta) = 0.5(1 + cos\Theta)sin\Theta,\ 0 < \Theta < \pi$	(Chen et al., 1998, 2003)

Table 3: Models used in RapidCell-1.0.

of MeAsp (Sourjik and Berg, 2002a, 2004). The model output was further compared to FRET response in time (Figure 5A), showing agreement between simulation and experiment both for amplitude and duration of the chemotactic response. However, the steepness of the adaptation curve after attractant removal can only be roughly

described by the existing model of CheB activity, a deficiency which needs to be addressed for more precise modeling in future. This discrepancy lays in CheYp region above the adapted state, and it may change the duration of tumbles upon steep negative responses. As a result, it may affect cell behavior in gradients of repellents. However, the results presented in this work should not be affected by this discrepancy, because simulations are performed in gradients of attractants, where actual CheYp concentrations stay below the adapted state. Comparison of RapidCell and spatially

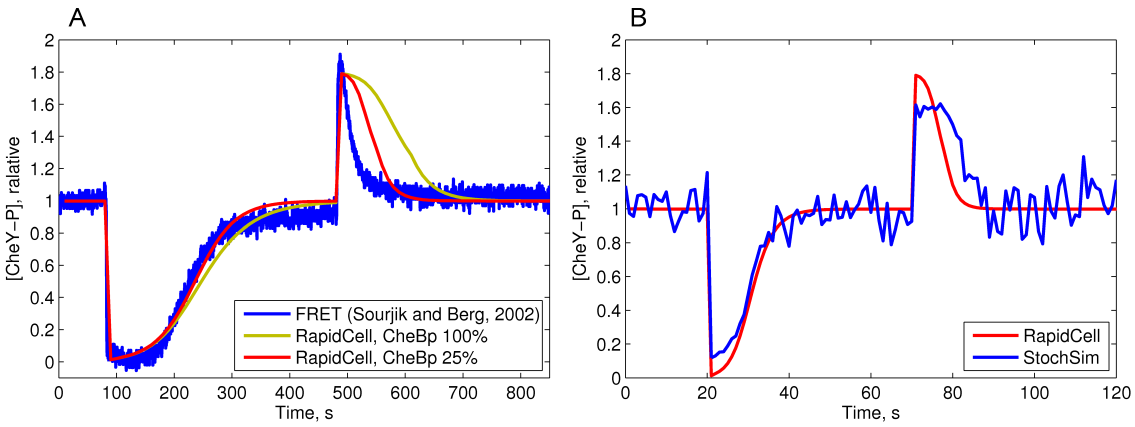

Figure 5: Verification of RapidCell using FRET experiments and StochSim simulations. (A) FRET response curve and RapidCell simulation of cell response to a step-wise stimulus of MeAsp. Initial ambient concentration is zero, at point $t = 80$ sec 30 μM MeAsp is added, at 480 s removed. The best fit by RapidCell is obtained with the adaptation rate $k = 0.5$, that corresponds to the temperature $T = 20^o$, at which the FRET experiments were carried out. At $T = 30^o$ the fitting adaptation rate is $k = 1.0$ (V.Sourjik, unpublished data). (B) StochSim and RapidCell simulation of cell response to a step-wise stimulus of Asp. Initial ambient concentration is zero, at $t = 20$ sec $3.5\,\mu M$ Asp is added, then at 70 s removed. The best fit by RapidCell is obtained with the adaptation rate $k = 8$, which tends to be a very rapid adaptation. The StochSim simulations were carried out with a coupled model (Shimizu et al., 2003), 65×65 square receptor lattice with coupling energy $E_J = -3.1kT$.

extended StochSim responses to addition and removal of Asp is shown in Figure 5B. The adaptation rate of StochSim seems very high compared to FRET experiments and RapidCell simulations ($k = 8$ is the best fitting adaptation rate), which suggests that RapidCell will be much more sensitive to gradients than AgentCell. StochSim gives lower response amplitudes compared to FRET experiments (Shimizu et al.,

2003).

RapidCell correctly reproduces experimental data on tethered cell stimulation with pulse and step changes of Asp concentration (Segall et al., 1986) (Figure 6A,B). The adaptation times after a step increase of α-methylaspartate (MeAsp) concentration over three orders of magnitude agree with experimental data reported in (Berg and Tedesco, 1975) (Figure 6C).

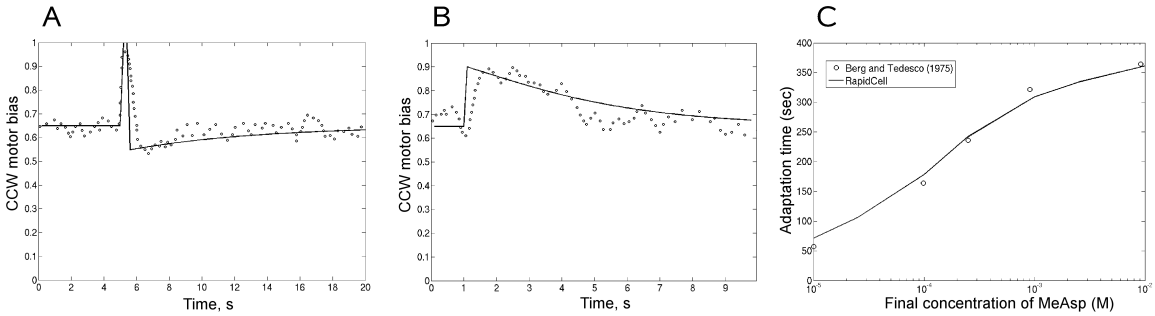

Figure 6: Verification of RapidCell using experiments on tethered cells. (A) Simulation of CCW motor bias response to a short pulse of attractant. Initial ambient concentration is zero, at $t = 5$ sec $1.0\,mM$ Asp is added for 0.35 sec interval; solid line - simulations (the best fit is obtained at with the adaptation rate of 2.0), circles - experimental data (Segall et al., 1986). (B) Simulation of CCW motor bias response to a step-wise stimulus. Initial ambient concentration is zero, at $t = 1$ sec $0.075\,\mu M$ Asp is added; solid line - simulations, circles - experimental data (Segall et al., 1986). The best fit is obtained with the adaptation rate of 5.0, which is still in physiological limits (different cell cultures and/or growth conditions). (C) Adaptation times to a step increase of α-methylaspartate (MeAsp) from zero ambient level, obtained in simulations (solid line) and in experiments (Berg and Tedesco, 1975) (circles). In simulations, dissociation constants were taken $K_a^{off} = 0.02\,mM$ and $K_a^{on} = 0.5\,mM$ (Keymer et al., 2006a); the best fit is obtained with the adaptation rate of 1.3.

2.2 Bacterial motion

The cells are simulated in continuous 2D space, and their motion is described by coordinates (x, y), speed v orientation α and tumbling angle Θ (Figure 7). The cell coordinates change every time step

$$\begin{aligned} x(t + \Delta t) &= x(t) + v\Delta t \cos(\alpha) \\ y(t + \Delta t) &= y(t) + v\Delta t \sin(\alpha) \end{aligned} \tag{17}$$

Here, v is the cell speed and α is the cell body orientation (angle between swimming direction and **X** axis). Orientation is affected by rotational diffusion (Berg and Brown, 1972; Berg, 1993): at every time step, the running direction is changed by adding a stochastic component

$$\alpha(t + \Delta t) = \alpha(t) + \xi \tag{18}$$

Here, ξ is a stochastic variable with normal distribution $N(m, \sigma) = N(0, \sqrt{2D_r\Delta t})$. The diffusion coefficient $D_r = 0.062\, rad^2 s^{-1}$ (Berg, 1993). After a tumble, the cell orientation changes by the tumbling angle Θ, with randomly chosen sign.

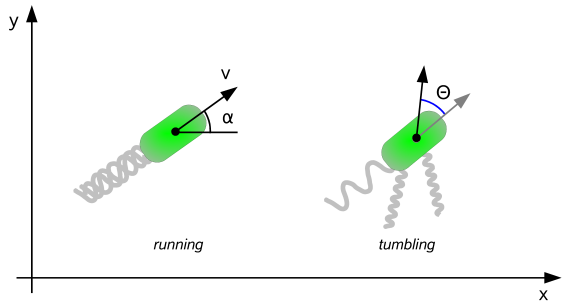

Figure 7: Swimming orientation α and tumbling angle Θ.

Run and tumble events include a complex interplay of filaments in a bundle, the details of which have been investigated experimentally (Darnton et al., 2007; Turner et al., 2000). To simulate the run and tumble behavior of a cell with several motors ($N = 3-7$), two alternative models were considered, simplified and detailed. The first model takes into account only the number of CW-rotating motors at each moment

of time, while the second considers also the 'history' of each CW-rotating motor, i.e. how long it rotates CW. Both models are described below.

2.2.1 Running and tumbling: Model 1

Running. During a run, the cell is assumed to move with constant speed $v_0 = 20\,\mu m/s$. At each moment of time, the number of CW-rotating motors is counted for run-tumble switching decision.

Tumbling: Voting motors. The cell has $N = 5$ motors switching independently, and the run-tumble state of the cell is determined according to a voting model (Ishihara et al., 1983; Turner et al., 2000; Andrews et al., 2006). The cell switches from 'Run' to 'Tumble', if at least 3 of its 5 motors rotate CW, and from 'Tumble' to 'Run', if at least 3 of the 5 rotate CCW. The choice of $N = 5$ is arbitrary, and similar results are obtained for $N = 3, 7$ under the condition of majority voting.

For model validation, simulations of cells with $N = 3, 5, 7$ motors were carried out. The simulated run times (1.04-1.11 s, Table 4) agree with the experimental value of 1.24 ± 1.16 s (Lewus and Ford, 2001). The simulated tumble times (0.26-0.44 s) are higher than the measured 0.14 ± 0.08 s (Berg and Brown, 1972; Turner et al., 2000). However, the latter study (Turner et al., 2000) shows that the time from bundle breaking in the old run to bundle consolidation in the new is 0.43 ± 0.27 s. Therefore, this model was used initially (Vladimirov et al., 2008), but after discussion with Howard Berg is was changed to Model 2 as described further in this section.

2.2.2 Tumbling angle distribution (isotropic)

The tumbling angle is distributed according to the probability density function (Chen et al., 1998, 2003)

$$f(\Theta) = 0.5(1 + cos\Theta)sin\Theta,\ 0 < \Theta < \pi \tag{19}$$

with mean $M(\Theta) = 67.5^o$ which is close to the experimental measurement of 68^o (Berg and Brown, 1972), and the corresponding shape of the function (Figure 8).

In Model 2, this tumbing angle distribution is called *isotropic*, because it does not depend on any external factors, such as swimming direction.

N motors	Voting threshold	T_{run}	T_{tumble}
3	2	1.11	0.44
5	3	1.09	0.33
7	4	1.04	0.26

Table 4: Simulated run and tumble times for cells with voting model of tumbling, at different number of motors. Parameters: $T_{ccw} = 1.33$ s, $T_{cw} = 0.72$ s, $mb = 0.65$, $n = 10000$.

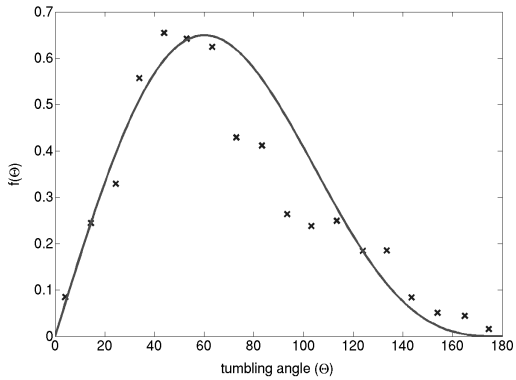

Figure 8: Probability density function of tumbling angles $f(\Theta) = 0.5(1 + Cos\Theta)Sin\Theta$, in the isotropic model of tumbling (solid line), and experimental measurements (cross markers) from (Berg and Brown, 1972).

2.2.3 Running and tumbling: Model 2

To simulate the experimentally observed hydrodynamics of bacterial swimming and tumbling in simple terms, a *distortion* factor d_{cw} is introduced, which reflects how one CW-rotating flagellum influences the speed and angular deviation of the swimming cell

$$d_{cw} = \begin{cases} t_{cw}/t^0_{cw}, & t_{cw} \leq t^0_{cw} \\ e^{-20(t_{cw} - t^0_{cw})}, & t_{cw} > t^0_{cw} \end{cases} \tag{20}$$

This functional form implies that the distortion rises proportionally to the CW rotation time t_{cw} as long as it is below the threshold t^0_{cw} (the first period). After this threshold is reached, the distortion exponentially decays (the second period). The first period corresponds to unwinding of a flagellum from the bundle and its rotation in the right-handed semicoiled form, which initiates a tumble. In the second period, when the flagellum rotates CW longer than the threshold time, a rapid transformation from semicoiled to curly 1 form occurs, and the flagellum twists around the bundle during the new run, due to high flexibility of the latter form (Darnton et al., 2007). Parameters are shown in Table 5.

The collective influence of several simultaneously CW-rotating motors is assumed to be proportional to the sum of their distortion factors

$$D_{cw} = \sum_{i=1}^{i_{cw}} d^i_{cw} \tag{21}$$

This implies that the tumble can occur if a single motor rotates CW for at least t^0_{cw} period, or if two or more motors rotate CW together for a shorter time. Formally, a tumble occurs when $D_{cw} \geq D^0_{cw}$, where D^0_{cw} is a threshold value. In principle, the threshold depends on the total number of motors: the larger N, the higher D^0_{cw} is required to generate a tumble. This is consistent with experimental data in Fig. 12 of (Turner et al., 2000), where switching of 1 motor is sufficient for a tumble at $N = 2-4$, but for $N = 5$ at least 2 motors are necessary for a tumble. However, we keep the same $D^0_{cw} = 1$ for $N = 2, 3, 4, 5$ for simplicity, to avoid additional arbitrarily chosen thresholds. The simulated run lengths in a ligand-free medium have distribution close to exponential, and their mean values are about 1 s.

Parameter	Value	Reference
t^0_{cw}	0.15 s	Max. time flagellum rotates CW in semicoiled form
D^0_{cw}	1.0	Threshold of total distortion to initiate a tumble
V_{max}	20 $\mu m s^{-1}$	Max. swimming speed

Table 5: Additional parameters used in RapidCell-1.1 with anisotropic tumbling. Other model parameters are the same as described in Table 2.

The cellular swimming speed linearly decreases with the distortion

$$v = \begin{cases} v_0(D_{cw}^0 - D_{cw}), & D_{cw} < D_{cw}^0 \\ 0, & D_{cw} \geq D_{cw} \end{cases} \quad (22)$$

In this model, only 'complete' tumbles are considered, which occur when D_{cw} reaches D_{cw}^0 and the swimming speed falls to zero: at this time point the cell instantly changes its orientation by the tumbling angle Θ, which is determined by two alternative models, isotropic and anisotropic. The mean length of complete tumbles is now very short ($\sim$0.01 s), but the efficient tumble length is about 0.1 s due to the drop of speed. For simplicity, it is assumed that if the distortion D_{cw} does not reach D_{cw}^0, it causes only a drop of speed.

2.2.4 Anisotropic tumbling

The tumbling angle Θ is determined by the number of CW-rotating motors n_{cw} involved in the tumble, and the total number of motors N. For each pair of (n_{cw}, N), the cell swimming in a ligand-free medium was simulated, and the frequency p_i of the tumbles which are caused by i CW-rotating motors was calculated for each $i = n_{cw}$. Using the frequency p_i, we chose the turning angle Θ_i close to the experimental values (Turner et al., 2000), while keeping the average turning angle constant in all models,

$$\sum_{i=1}^{N} p_i \Theta_i = 67.5^o \quad (23)$$

The actual Θ_i and p_i values used in simulations are shown in Results, Figure 24C,D.

2.3 Model of the environment

The virtual cells are swimming in a 2D environment with a predefined attractant concentration field $S(x, y, t)$. The domain geometry is either rectangular $(0, x_{max}) \times (0, y_{max})$ or circular $(0, r_{max})$, with reflecting walls. The simulation time T_{max} was chosen to be short enough to avoid boundary effects. An extension to 3D motion

is given in the Appendix with necessary mathematical background. However, simulation in three-dimensional space is not expected to bring novel system properties in the chemotactic behavior, and in this work all simulations are carried out in two dimensions.

2.3.1 Constant-activity gradient

The gradients used in chemotaxis modeling are usually linear, Gaussian or exponential (Emonet et al., 2005; Bray et al., 2007). However, in these gradients the signal is non-constant, which means it is strong at low attractant concentrations, and weak at high concentrations due to receptors saturation. Such a non-uniform shape of signal makes it difficult to estimate chemotactic efficiency over long time intervals – cells soon become 'blind' because receptors are saturated, and chemotactic drift decreases. In this work, a formula of "ideal" gradient that provides constant network excitation was derived from the MWC model (see Appendix for mathematical details). The chemoattractant function of such a constant-activity gradient is

$$S(x) = K^* \frac{Cx}{\frac{K^{on} - K^{off}}{K^*} - Cx} \tag{24}$$

where x is the space variable, C is a parameter of gradient steepness, $K^* = \sqrt{K^{on} K^{off}}$, i.e. the geometric mean of ligand-receptor dissociation constants K^{on} and K^{off}.

Gradient steepness. A cell swimming with speed v along the axis X from the point $(x = 0)$ senses the monotonically increasing function $S(x)$ and a constant change in receptor free energy per second

$$dE/dt = Cdx/dt = Cv \tag{25}$$

(see Appendix C for details). This value is defined as *steepness* of the constant-activity gradient.

Limiting condition. Note the necessary condition ($\frac{K^{on}-K^{off}}{K^*} - Cx > 0$) for Eqn. 24 to avoid singularity and negative concentrations. It sets the upper limit $C < C_{max} = \frac{K^{on}-K^{off}}{K^*}\frac{1}{x_{max}}$ for the gradient steepness C within the domain $(0, x_{max})$. For example, within a domain of size $x_{max} = 10\,mm$, the maximum steepness of a gradient of aspartate is $Cv = 2.28/x_{max}v = 4.56 \times 10^{-3}$.

2.3.2 Constant-activity and exponential time ramps

In contrast to spatial gradients, which direct the cellular motility in space, time ramps are used to study the chemotactic response of tethered cells (Block et al., 1983; Segall et al., 1986).

The constant-activity ramp of Asp was simulated according to Eqn. 24:

$$S(t) = K^* \frac{Ct}{\frac{K^{on}-K^{off}}{K^*} - Ct},\; C = \frac{K^{on} - K^{off}}{K^*} \cdot 0.9999/T_{max} \tag{26}$$

with simulation time $T_{max} = 1000$ seconds. The resulting value of C gives the maximum ligand concentration $S(T_{max}) = 9999K^*$.

The exponential ramp was simulated as:

$$S_e(t) = 0.31K_D \exp(0.005(t - 200)),\; (t \geq 200) \tag{27}$$

after 200 s of adaptation to the initial stimulus $0.31K_D$, following the model and experiments of (Block et al., 1983). The concentration profiles are shown in Figure 11A.

2.3.3 Simulations in constant-activity and other gradients

The constant-activity gradient (Eqn. 24) has an intensity $C = \frac{K^{on}-K^{off}}{K^*}\frac{0.999}{x_{max}}$, and the domain has a rectangular $(0, x_{max}) \times (0, y_{max})$ or circular $(0, r_{max})$ shape. The gradient has its minimum $S(0) = 0$ and reaches its maximum $S(x_{max}) = 999K^*$ (Figure 12A). The circular gradient shape was used to simulate radially symmetric gradient created by cells consuming the attractant in swarm plate experiments.

Comparative set of constant-activity gradients (N0, N1, N2, N3). The circular constant-activity gradient ($r_{max} = 10mm$) has steepness $dE/dt = Cv = 4.56 \times 10^{-3}$. A set of other constant-activity gradients was obtained by changing the steepness by a factor of two: (1.14, 2.28, 4.56, 9.11, 18.22, 36.44, 72.88)$\times 10^{-3}$. The chemotactic efficiency is studied in four of them with moderate steepness (1.14, 2.28, 4.56, 9.11)$\times 10^{-3}$. These gradients are referred to as constant-activity gradients N0, N1, N2, and N3. In simulations, gradients were used in either radially symmetric form (circular domain), or in one-dimensional form along X axis (rectangular domain).
In radially symmetric form, they are described by formula

$$S(r) = K^* \frac{Cr}{\frac{K^{on}-K^{off}}{K^*} - Cr},\ C = \frac{K^{on} - K^{off}}{K^*} \cdot \frac{0.999}{r_{max}} \tag{28}$$

with $r_{max} = 40, 20, 10, 5$ mm for N0, N1, N2, and N3, respectively. Here, r_{max} is the radius of the circular domain.
In one-dimensional form along X axis, they are described as

$$S(x) = K^* \frac{Cx}{\frac{K^{on}-K^{off}}{K^*} - Cx},\ C = \frac{K^{on} - K^{off}}{K^*} \cdot \frac{0.999}{x_{max}} \tag{29}$$

with $x_{max} = 40, 20, 10, 5$ mm for N0, N1, N2, and N3, respectively. Here, x_{max} is the width of the rectangular domain.

Chemotactic efficiency. Chemotactic efficiency was estimated as the average drift velocity of a cell population, measured between 200 and 500 s of model time, in the basic constant-activity gradients. As shown in Figure 13, within this interval the average CheYp level of cells is constant, and the drift velocity can be accurately measured by a linear fit.

Linear gradient. A linear gradient used in simulations has a form of $S(x) = Kx$, $x \in$(0,10 mm) with coefficient $K = 10^{-2}\, mM\, mm^{-1}$ (Figure 12A).

Gaussian gradient. Another form of gradient used in simulations is Gaussian $S(x) = 10K \exp(-(x-10)^2/(2\sigma^2))$, with shape parameter $\sigma = 3.33$ and coefficient $K = 10^{-2}\, mM\, mm^{-1}$ (Figure 12A).

2.4 RapidCell program

RapidCell is a platform-independent console application (Windows, Linux, MacOS). The source codes are available online on the program website (`http://rapidcell.vladimirov.de`). The output files contain the key characteristics of the intracellular state (CheYp level, CheA activity, methylation state, motor bias) and the positions of cells. The principal algorithm of the program is shown in Figure 9 in a form of pseudo-code. The model was implemented using Java classes similar to AgentCell (Emonet et al., 2005), but with simplified architecture. The algorithm implements a discrete-time Monte Carlo scheme with time step $\Delta t = 0.01s$. For random-number generation, external Java libraries were used (Flanagan, 2007; Matsumoto and Nishimura, 1998). The code was written using Eclipse SDK (`www.eclipse.org`). The output data were analyzed with MATLAB (The MathWorks, MA). See Appendix A or the RapidCell website for instructions on running RapidCell and analysis of the output files.

2.4.1 Java class files

`Run.java` This class creates a model instance and starts simulation.

`Model.java` The class contains parameters of simulation and domain geometry. Methods `tryTumbleNmotors()`, `tryRunNmotors()`, `updateMotorStates()` implement the Poisson processes for random switching between run and tumble for a single cell, and the CCW/CW switching for its motors. Method `tryStop(Cell)` implements the Poisson statistics for random traps during runs (in simulations of porous medium).

`Cell.java` The abstract class containing general attributes of the cell - `RunTumbleState, chemotaxisNetwork, flagellarMotors`. Class `Cell2D` extends `Cell` with corresponding attributes `PositionX, PositionY, Orientation` and method of reorientation `tumble()`. The class `Cell` contains an array `flagellarMotors[]` of N motors.

`Network.java` The class contains attributes and methods for chemotaxis network simulation, for example method `updateMWCmodel()`, which updates the methylation

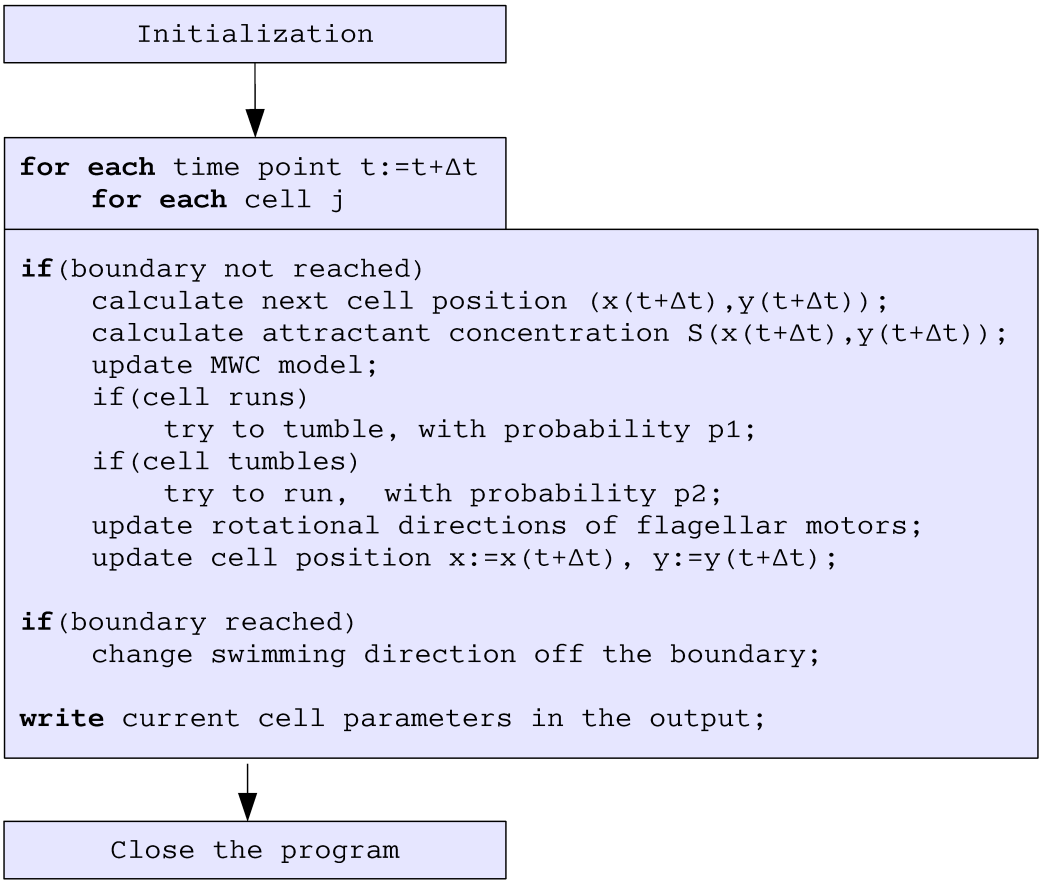

Figure 9: The scheme of RapidCell algorithm as a pseudo-code. The initialization part includes setting up all necessary variables and parameters, creation of cells with defined initial states of their networks in certain space positions, etc. The two `for each` statements denote the two main loops, along the time and across the cell population. The `try to tumble` statement means that the run will be ended and the cell state will be changed to *tumble* starting from the next time step. The `try to run` statement means that the tumble is finished, and the cell will start to run from the next time step.

level and cluster activity. An instance `chemotaxisNetwork` of class `Network` is a member of class `Cell`.

`Motor.java` The class contains parameters of flagellar motor and methods for calculating the switching frequencies of a motor.

2.4.2 Computational costs

Expensive simulations of the signaling pathway are avoided in RapidCell due to the hybrid description of the network. This leads to a dramatic drop in computational costs. Simulation of 1000 s long walk of a single cell in a ligand gradient takes about 1 second to run in RapidCell. The same simulation requires 133 minutes for AgentCell (StochSim without receptor coupling), while the spatially extended version of StochSim requires several days on the same hardware (Intel Pentium 4, 2.40GHz, RAM 1GB, OS Linux Suse 10.2). A 1000 s long series of step responses with the BCT program takes 100 s under comparable conditions (PowerPC G5, 1.8GHz, RAM 1GB, MacOS X). Therefore, RapidCell provides a computational speedup of 8000 times compared to AgentCell (based on StochSim without receptor coupling), and approximately 100 times compared to BCT. It enables simulations of up to 100,000 cells to be completed within several hours using a single desktop computer.

The computational time of RapidCell rises linearly with the number of simulated cells and with the simulation time, as shown in Table 6.

a) N(cells):	1	10	100	1000
Computation time (s):	1	6	62	636
b) T_{max}(s):	1	10	100	1000
Computation time (s):	1	6	66	623

Table 6: Computational time of RapidCell-1.0 at a) fixed simulation time $T_{max} = 1000$ s and variable number of cells; b) fixed number of cells $N = 1000$ and variable simulation time. Simulations were run on PC of the following configuration: Intel Pentium 4, 2.40GHz, RAM 1GB, OS Linux Suse 10.2.

Chapter 3

Results

The constructed multiscale model of chemotactic *E. coli* (Figure 10A) has several important features, which distinguish it from other models. First, the receptor cluster is described by a mean-field approximation of the MWC model, with heterogeneous receptor composition (Tar and Tsr). The methylation is described by a simple ODE, which allows to reproduce the time course of adaptation in agreement with the recent FRET experiments. The relatively rapid reactions of ligand binding, conformational changes and phosphotransfer are described by rapid-equilibrium algebraic equations. The probabilistic nature of motor switching is reproduced by stochastic model of CW-CCW switching motor, with the motor bias depending on current CheYp concentration. Though all these components were in some forms used in other models of bacterial chemotaxis, they are here combined in the same model with fine time discretization, allowing to bind these heterogeneous mathematical methods in a single platform. The model is implemented in a program RapidCell, which is available for use and supplemented with instructions, as described in Appendix. These methodological results are described in detail in section *Methods and Algorithms*, and hereafter simulations of chemotactic *E. coli* populations performed with RapidCell are described.

3.1 Chemotaxis in gradients of different shape and steepness

After validation of the model using different sources of experimental data (see *Methods and Algorithms*), the cellular behavior was studied in the proposed universal constant-activity gradient and compared with behavior in Gaussian and linear gradients. In simulations, both single cell swimming (Figure 10B) and the behavior of populations were analysed. The key characteristics that were considered are CheYp concentration, cell position, and the population drift velocity along the gradient.

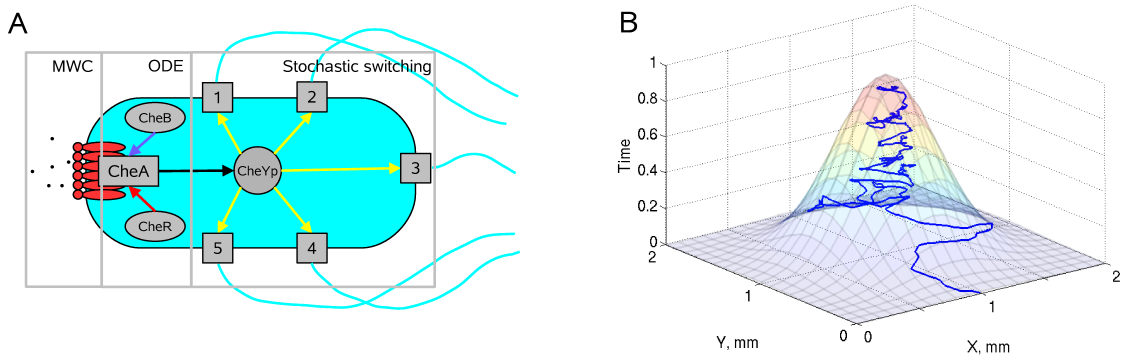

Figure 10: Model of chemotactic *E. coli*. (A) Scheme of the hybrid model. The activity of receptor cluster depends on the local ligand concentration and the methylation level according to the MWC model. Methylation (red arrow) and demethylation (blue arrow) are performed by CheR and CheB. The phosphate group is transferred from active CheA to the response regulator CheY (black arrow). The concentration of CheYp modulates the motor bias of 5 independent motors (yellow arrows), and their collective behavior makes the cell run or tumble. Ligand binding, receptors cluster switching, CheY phosphorylation and motor switching are considered to be in rapid equilibrium and are described by algebraic equations, while the methylation and demethylation kinetics are relatively slow and simulated using an ODE. Motor switching is simulated stochastically. (B) The model reproduces swimming of *E. coli* cells up gradients of attractants, taking into account the effect of rotational diffusion. A typical path of a swimming virtual cell is shown in 2D space, with the relative time course shown along the Z axis, demonstrating how the cell finds the maximum attractant concentration and stays in its vicinity. The attractant concentration profile is overlayed.

3.1.1 Response of the MWC model to time ramps of Asp

Block et al. (1983) showed experimentally that tethered cells respond with constant strength to an exponentially rising gradient of MeAsp, in the range between 0.31 and $3.2K_D$. Here, the response of the MWC model to increasing ramps of Asp in the exponential and constant-activity form was simulated (Figure 11A). Indeed, the exponential ramp gives nearly constant response between 0.5 and $3.0K^*$, consistent with the model of (Block et al., 1983). However, the constant-activity ramp results

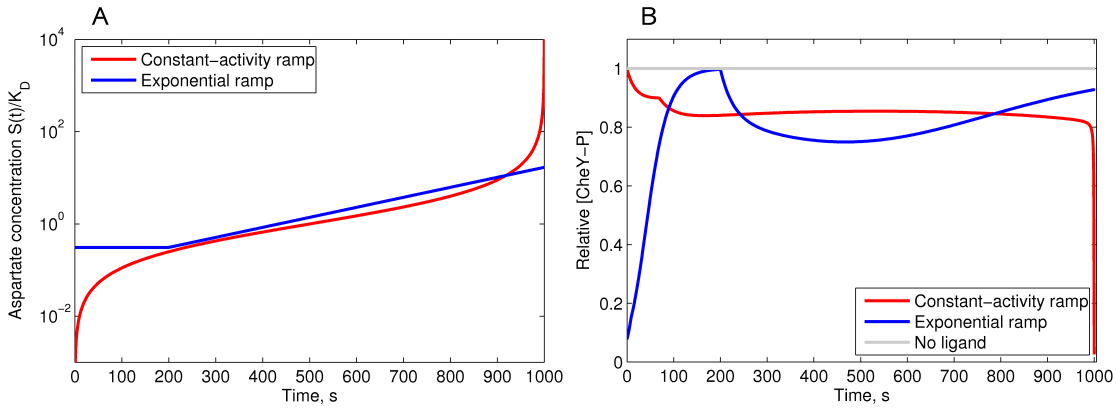

Figure 11: MWC model response to the constant-activity and exponential ramps of aspartate. (A) The concentration profiles of constant-activity and exponential ramps of aspartate, relative to $K_D = 4.52\ \mu M$ (logarithmic scale). (B) The response of the MWC model to the applied constant-activity and exponential ramps. Upon stimulation with the constant-activity ramp, the [CheYp] rapidly goes down during initial excitation. The single non-smooth point on the slope is the result of the piece-wise linearity of the methylation energy function. The constant-activity ramp produces a long flat response up to a concentration of $100K_D$, above which Tsr receptors become sensitive to the ligand and the cluster activity falls. Upon stimulation with the exponential ramp, the cell initially adapts to the minimum concentration $C_{min} = 0.31K_D$, and after 200 s the exponential ramp begins. After 700 s, adaptation overcomes excitation and [CheYp] slowly returns to the steady state. Relative adaptation rate $k = 1$.

in a chemotactic response that remains approximately constant over three orders of ligand concentration – between 0.1 and $100K_D$ (Figure 11B). If Tsr is non-sensitive to the ligand, constant activity remains up to $1000K_D$. However, since Tsr receptors are able to respond to aspartate non-specifically, the activity drops to zero, as previously

shown for a mixed-receptor cluster (Sourjik and Berg, 2002a; Endres and Wingreen, 2006).

3.1.2 Chemotactic efficiency of populations in different gradients

To study chemotactic efficiency in common gradients that arise from general diffusion models, the chemotactic drift was simulated in linear and Gaussian gradients (Figure 12A), and compared with drift in the constant-activity gradient. Chemotactic efficiency was estimated by the average drift velocities of populations consisting of 1000 identical cells. In Figure 12B, one can see that in the linear and Gaussian gradients the drift velocity decays after about 400 and 800 s, respectively, indicating that cells loose sensitivity due to receptor saturation. In contrast, the constant-activity gradient keeps the drift velocity constant at any point (Figure 12B), as expected from theory. This population behavior can be explained by the intracellular CheYp levels

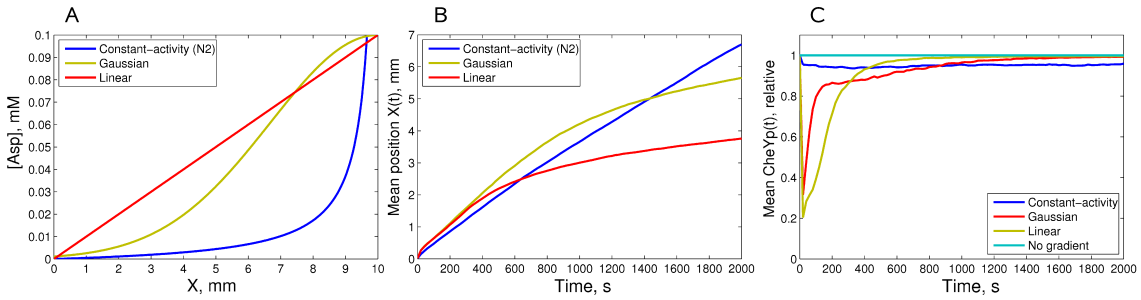

Figure 12: Simulations of chemotactic population in gradients of different shape. (A) Concentration profiles of the gradients used in the simulations. (B) Chemotactic drift of cells in these gradients. The average position $\langle X \rangle$ of the cells is shown as a function of time. A population of 2000 cells starts moving from the left wall ($x_0 = 10\,\mu m$, y_0 randomly distributed in $(0, y_{max})$), and swims for 2000 s. (C) Relative CheYp concentration as a function of time, averaged over 2000 cells in the same gradients. The gray line indicates the fully adapted state $[CheYp] = 1.0$ in a medium without attractant. Relative adaptation rate $k = 1$. All cellular parameters are as described in Table 2.

of the cells in these gradients. Gaussian and linear gradients result in a strong excitation at low attractant concentrations, and poor excitation at high concentrations

(Figure 12C). In contrast, the constant-activity gradient produces an approximately constant level of CheY phosphorylation across the cell population. These two unique properties of the constant-activity gradient – constant drift velocity and constant average CheYp – favour this gradient as a reliable *in silico* assay to study the chemotactic motility of cells.

Average CheYp level in the constant-activity gradients Simulation of cell populations in the constant-activity gradients N1, N2 and N3 demonstrate that the average CheYp level depends on gradient steepness and remains stable over long time intervals (Figure 13). These three gradients were used further to measure chemotactic efficiency under different test conditions.

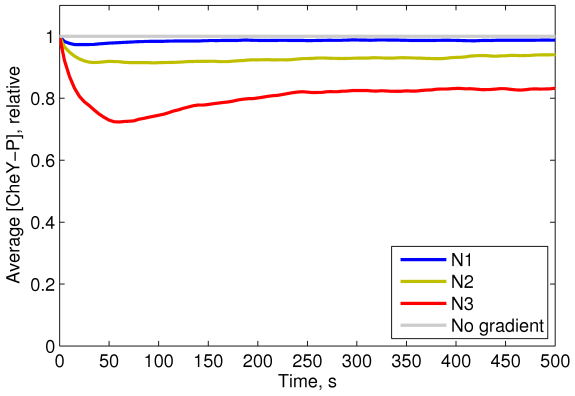

Figure 13: Average CheYp levels in three constant-activity gradients. The CheYp levels of 5000 cells swimming in the constant-activity gradients N1 (blue), N2 (green) and N3 (red) are shown. Relative adaptation rate $k = 1$. The cell parameters are as described in Table 2.

3.2 Optimal adaptation rates (in a liquid medium)

The constant-activity gradient was used to study the effect of adaptation rate on chemotactic efficiency. For this purpose, homogeneous populations consisting of cells with the same adaptation rate were simulated. In a fixed constant-activity gradient, the population drift velocity depends on adaptation rate in a unimodal manner

(Figure 14A). A zero level of adaptation enzymes (non-adapting cells) results in a low drift velocity, though it is clearly distinguishable from non-chemotactic behavior. A proportional increase of adaptation rate improves cellular drift velocity up to a certain maximum, after which it slowly declines again. Extremely high adaptation rates, more than 100 times higher than wild-type, make the cells non-chemotactic (Figure 14A).

To study chemotactic efficiency as a function of gradient steepness, cells were simulated in seven constant-activity gradients with the steepness changing 64-fold, from 1.14 to 72.88×10^{-3}, (Figure 14B). In each gradient, the optimal adaptation rate was determined, at which cellular drift velocity reaches its maximum. The simulated drift velocities are in the same range as those measured experimentally for *E.coli* in steep gradients ($7\,\mu m\ s^{-1}$) (Berg and Turner, 1990). Interestingly, the optimal adaptation rate rises in proportion with the gradient steepness (Figure 14B).

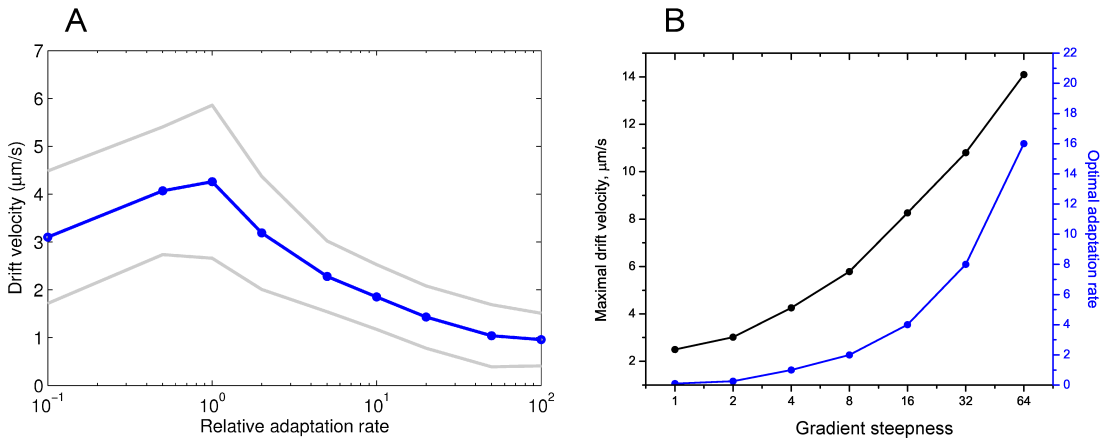

Figure 14: Chemotactic properties of cells at different adaptation rates in constant-activity gradients. (A) Drift velocity of cells in the constant-activity gradient N2 as a function of adaptation rate. The horizontal axis shows the adaptation rate k relative to the wild type (logarithmic scale). Gray lines show standard deviations. (B) Maximal drift velocities (black) and the corresponding optimal adaptation rates (blue) as a function of gradient steepness. The steepness of the constant-activity gradients was changed over a 64-fold range, as described in *Methods and Algorithms*.

To investigate the latter effect in more detail, the adaptation rate was varied from

0 to 10-fold relative to the wild-type. In steeper gradients, the optimal adaptation rate is indeed higher (Figure 15A), and the peak of the drift velocity becomes less sharp. To find the reason for the observed dependence between the gradient steepness and optimal adaptation rate, the average CheYp of the cells was analysed. As one can see in Figure 15B, in all gradients the 90%-intervals around the velocity peaks correspond to adaptation rate intervals $[0.1, 0.5]$, $[0.4, 1.5]$, $[1, 3]$, respectively. These three intervals are projected to the same interval $[0.80 \leq CheYp \leq 0.97]$, within the error of estimation. The optimal adaptation rates which give maximal drift velocities correspond to an average $[CheYp] \sim 0.9$. In steep gradients, the profile of average CheYp flattens, and the optimal adaptation rate becomes higher (Figure 15B). The

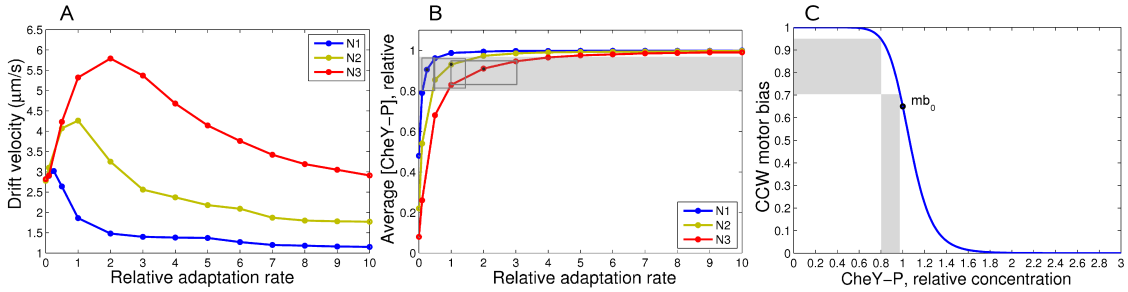

Figure 15: Optimal chemotactic behavior at different adaptation rates. (A) Drift velocities of cells as a function of adaptation rate, in the constant-activity gradients N1 (blue), N2 (green), N3 (red). For each adaptation rate, the drift velocity was estimated from the simulation of 1000 cells, with standard error of mean 0.05. (B) Average CheYp levels of cells in the same simulations. Black dots indicate the adaptation rate at which drift velocity is maximal. Gray rectangles show the intervals of optimal adaptation rates, defined by taking the 90%-interval from the drift velocity maximum. The width of each rectangle indicates the optimal adaptation-rate interval, and height shows the corresponding CheYp interval. All three intervals of adaptation rates fall into the same CheYp interval: $[0.80, 0.97]$, shown by the gray band. (C) The CCW motor bias as a function of CheYp. Gray bands indicate the optimal CheYp interval and the corresponding operating range of the motor. The cell parameters are as described in Table 2.

reason why the interval $[0.80 \leq CheYp \leq 0.97]$ corresponds to optimal chemotaxis is evident from the profile of motor bias as a function of CheYp (Figure 15C). The interval $[0.80 \leq CheYp \leq 0.97]$ corresponds to the operating range of the motor $[0.95 \geq mb \geq 0.72]$, where the dependence between mb and $CheYp$ is approximately

linear. In this interval, chemotactic behavior is most efficient in liquid media. The optimal adaptation rate therefore sets the CheYp level to fit the motor operating range. In steep gradients, the adaptation rate must be high enough to balance the strong excitation and set CheYp within this optimal interval. In shallow gradients, adaptation must be slow enough to allow excitation, otherwise the cells become adapted before they are able to respond.

3.2.1 Effect of [CheR]/[CheB] ratio on chemotactic efficiency

The effect of varying the $[CheR]$ to $[CheB]$ ratio was studied at fixed $[CheB]$ in three constant-activity gradients N1, N2, and N3 in a liquid medium. The chemotactic efficiency dramatically decreases at $[CheR] > 1$ (Figure 16), because the resulting higher steady-state CheYp level produces tumbling behavior. At $[CheR] < 1$, chemotactic efficiency decreases slowly for N3, or goes up for the N1 and N2 gradients. The latter effect is caused by a shift of average CheYp level to the optimal interval, where chemotactic sensitivity is the highest due to a more optimal fit to the motor operating range.

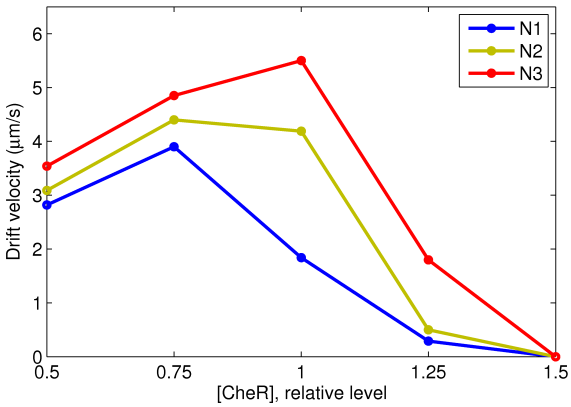

Figure 16: Effect of altered $[CheR]$ on chemotactic efficiency. The vertical axis shows drift velocities. The level of $[CheB]$ is fixed at the wild-type value (0.28 μM), while $[CheR]$ is varied relative to wild type (0.16 μM). Note the steep fall in the drift velocities for $[CheR] > 1$, where the steady-state CheYp produces tumbling behavior.

3.2.2 Effect of CheB phosphorylation on chemotactic efficiency

The effect of CheB phosphorylation feedback on chemotactic efficiency in a liquid medium was studied. Under the assumption that $[CheR]$ and $[CheB]$ perfectly match each other ($A^* = 1/3$), the CheBp-effect is positive when the adaptation rate is lower than the optimum, and negative when the adaptation rate is higher, in the given gradient (Figure 17A). This effect is caused by the reduction of CheB activity relative to CheR when the kinase activity A is below the steady-state level ($A^* = 1/3$), as described in *Methods and Algorithms*. The average CheYp level is thus shifted up, which results in a positive or negative effect of CheB phosphorylation, depending on the rate of adaptation (Figure 17B).

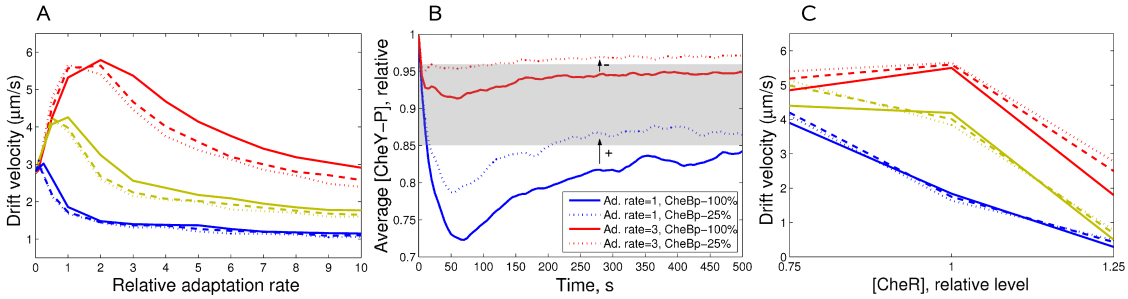

Figure 17: Effect of CheB phosphorylation on chemotactic efficiency. (A) Drift velocity as a function of adaptation rate in the constant-activity gradients N1 (blue), N2 (green), N3 (red). The ratio of [CheR] to active [CheB] at steady state is the same as in the wild type (0.16/0.28), ensuring the same steady-state activity $A^* = 1/3$ in all cases. Solid lines correspond to cells with 100%-active CheB at steady state, dashed lines - 50%-active, finely dashed - 25%-active CheB. (B) The average [CheYp] resulting from the balance between CheR and CheB activity determines the positive or negative role of CheB phosphorylation. Cells are simulated in the gradient N3, at adaptation rates of 1.0 and 3.0. Kinase-dependent CheB activity means that CheB works more weakly at $A < 1/3$, and thus the average [CheYp] is higher than the level obtained for constantly active CheB. Such a shift improves chemotaxis at low adaptation rates, but reduces it at high rates. The optimal range of CheYp is shown by the gray band. (C) Drift velocities at variable $[CheR]$ and variable CheB activity and fixed $[CheB]$ (0.28 μM, wild type). Solid, dashed and finely dashed lines indicate 100%, 50% and 25% active CheB, respectively. Adaptation rate $k = 1$, other cell parameters as described in Table 2.

The positive role of phosphorylation can be significantly increased when the ratio

of $[CheR]$ to $[CheB]$ is non-perfect (Figure 17C). For example, 25%-active CheB can significantly counteract the strong negative effect of $[CheR] = 1.25$ in the N3 gradient – the drift velocity rises from 1.8 to 2.8 $\mu m\, s^{-1}$ (55%). At $[CheR] = 0.75$ the effect is not so dramatic, but remains significant – the average drift velocities increase by about 10-15% in all three gradients. This suggests that CheB phosphorylation helps to maintain chemotaxis at fluctuating concentrations of CheR and CheB, when their ratio is not perfect due to gene-expression noise.

3.3 Chemotaxis in a porous medium (agar)

3.3.1 Swarm plate model

In the swarm assay in soft agar, bacteria consume an attractant, thereby creating a local gradient, and follow it in the form of a growing ring (Adler, 1966; Wolfe and Berg, 1989). The intensity of the moving gradient is assumed constant, and the radial constant-activity gradient is used as a simple model of environment for the swarm assay simulation. The radial constant-activity gradient provides a constant cellular-drift velocity at any distance from the center of the plate. This property allows using it as a stationary model of the real moving gradient of attractant.

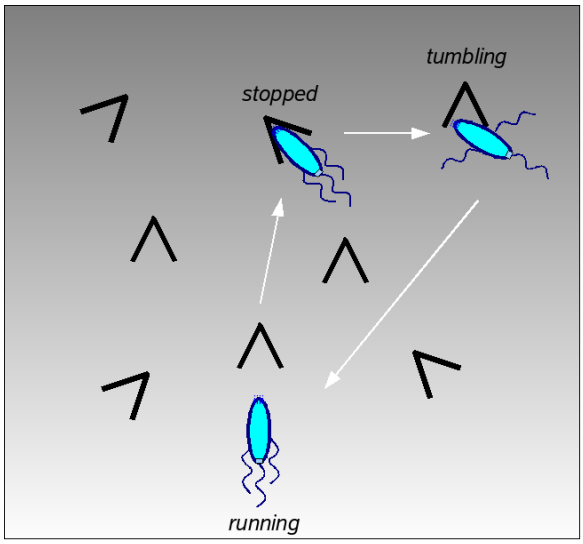

Figure 18: Model of motility in a porous medium (agar). A cell encounters traps along its run, and stops in the traps. It stays in the trapped state until the first tumble occurs, then normal run and tumble behavior resumes. The trap positions are not fixed in the 2D space - instead, it is assumed that each cell encounters traps in a series of randomly distributed time intervals.

In swarm assays, bacteria move in a labyrinth of agar filaments, with obstacles and traps along the cell's path. The cell can encounter traps during its run, and stays trapped until it makes the next tumble, as observed by Wolfe and Berg (1989). Therefore, non-adapting cells and non-tumbling mutants form the smallest rings. To

simulate motility in agar, a new state of the cell was introduced, corresponding to a stop in a trap during a run (Figure 18). The positions of traps are not fixed in space. Instead, it is assumed that each cell encounters traps in an exponentially distributed time series, which mimics the random collisions of the cell with agar filaments. The mean free time between traps is set to 2.0 s to achieve biologically realistic drift velocities (about 1 $\mu m\, s^{-1}$). While it is trapped, the cell remains stationary until it makes a tumble, whereupon normal run and tumble behavior resumes until the next stop occurres (Wolfe and Berg, 1989).

3.3.2 Optimal [CheR,CheB] in agar – experiments and simulations

In the model, the levels of the adaptation enzymes CheR and CheB are assumed to vary in a coordinated manner, leaving the $[CheR] : [CheB]$ ratio the same as in the wild type. The ratio of CheR to CheB remains largely fixed because their genes are adjacent and transcriptionally coupled in the *meche* operon (Løvdok et al., 2009). The adaptation rate in the model is thus proportional to the level of co-expression of CheR and CheB, which will be denoted as $[CheR, CheB]$.

In order to study chemotactic efficiency at different adaptation rates in agar, L. Løvdok experimentally measured chemotactic efficiency on swarm plates. In these experiments, CheR and CheB-YFP were co-expressed from one operon under control of a pBAD promoter and native ribosome-binding sites. The pBAD promoter gives expression levels lower or higher than the wild-type value, depending on the strength of arabinose induction. Mean protein levels in the population at a given induction were determined as described in (Vladimirov et al., 2008).

Experiment and simulations show that cells with $[CheR, CheB]$ above a certain threshold perform chemotaxis equally efficiently. However, the cells with $[CheR, CheB]$ below the threshold have severely impaired chemotactic behavior (Figure 19A,B). According to the simulations, cells with low $[CheR, CheB]$ tend to run without tumbling and stay trapped most of the time.

The limits of motor bias for optimal chemotaxis in agar are different from those in

liquid media. As one can see in Figure 19C, the average CCW motor bias of successful cells is just slightly higher than the steady-state mb_0. Cells with higher motor bias would drift faster in liquid media, but not in agar, because the period of time they remain trapped also increases with CCW motor bias.

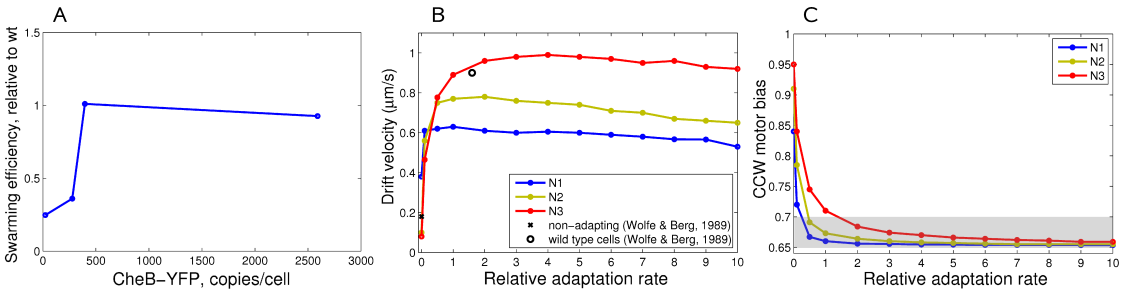

Figure 19: Swarm-plate assay at different $[CheR, CheB]$. (A) Experimentally measured chemotactic efficiency at different expression levels of the *cheR cheB-eyfp* operon under the control of a pBAD promoter. The applied arabinose concentrations were 0.0, 0.0005, 0.001, 0.01 %, respectively. The CheB-YFP level reflects the concerted [CheR,CheB-YFP] due to strong translational coupling. For scale conversion, the wild-type level of CheB can be taken as 240 copies/cell (Li and Hazelbauer, 2004). (B) Simulated chemotactic efficiency as a function of $[CheR, CheB]$. Cells are simulated in the constant-activity gradients N1 (blue), N2 (green), N3 (red). The black open circle shows the experimentally observed drift velocity of wild-type cells, estimated from Fig. 4 of (Wolfe and Berg, 1989). The cross shows the drift velocity of non-adapting cells, from Fig. 6 of (Wolfe and Berg, 1989). The cell parameters are as described in Table 2. (C) Average motor bias of cells as a function of $[CheR, CheB]$. The steady-state motor bias is 0.65, with the gray band indicating the region of optimal motor bias for chemotaxis in agar.

3.3.3 Population in liquid medium and in agar

To model swarm assays more realistically, cell populations with a log-normal distribution of $[CheR, CheB]$ were simulated. The mean (1.6) and standard deviation (0.48) were fitted to reproduce the variability of adaptation times observed for wild-type cells (Berg and Tedesco, 1975): $T_{ad} = 311 \pm 150$ s in response to a $0 - 10^{-3}$ M MeAsp step.

The scatter plot of distances travelled by cells along the radial gradient N2 in a liquid medium shows that a subpopulation with optimal $[CheR, CheB]$ levels drifts

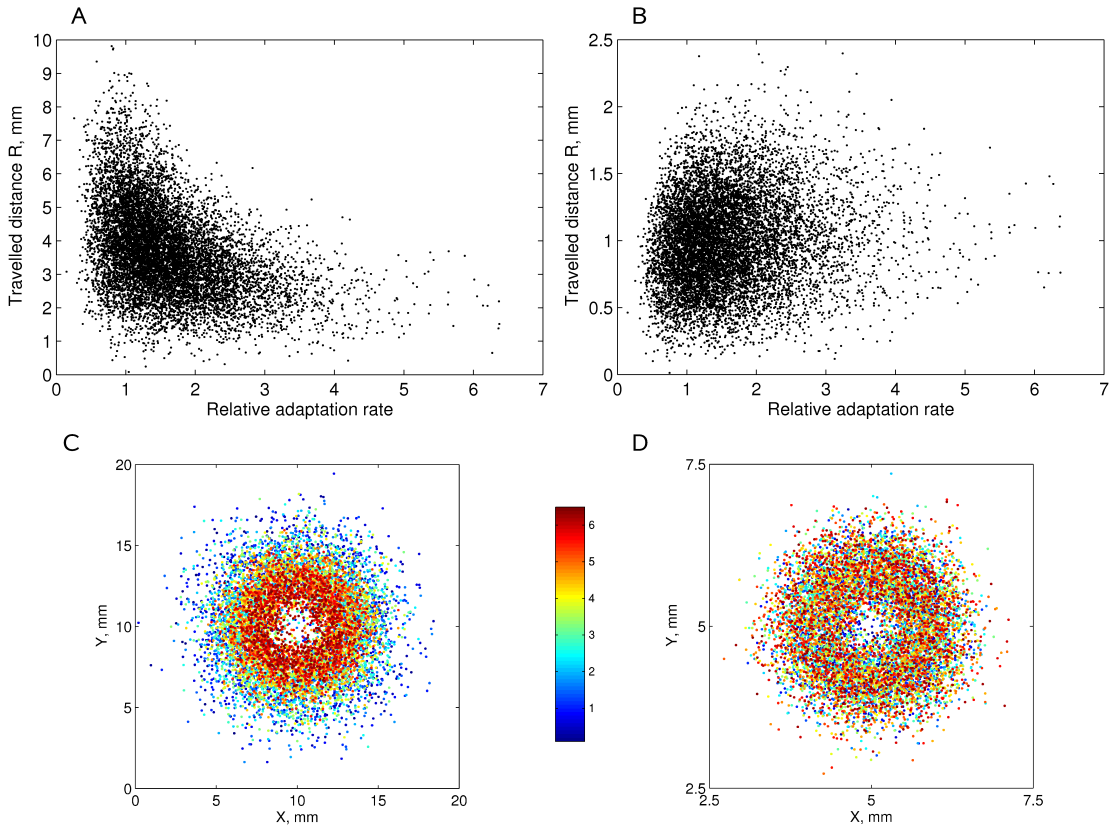

Figure 20: Simulation of a population in a liquid medium and agar with a physiological $[CheR, CheB]$ distribution. The distances R travelled by 10^4 cells after 1000 s of simulation time in (A) the liquid medium, N2 gradient; (B) agar, N3 gradient. The (x,y)-positions of cells colored from deep blue to red, according to their $[CheR, CheB]$, are shown in (C) for the liquid medium, (D) for agar. The smallest $[CheR, CheB]$ values correspond to deep blue, the highest values correspond to red. Note the different scales of the figures. The cell parameters are as described in Table 2.

more rapidly than other cells (Figure 20A). Simulations in the N3 gradient in agar show that cells with low $[CheR, CheB]$ levels are hindered by agar traps, while other cells drift successfully (Figure 20B).

In Figure 20C,D these cells are colored from deep blue to red, according to their $[CheR, CheB]$. The outer edge of the bacterial ring in a liquid medium contains many blue cells with $[CheR, CheB]$ between 0.5 and 2. In contrast, the outer edge in the agar contains a uniform mixture of cells with different $[CheR, CheB]$ levels, while

deep blue cells with low $[CheR, CheB]$ tend to be left behind.

These results suggest that in a liquid medium there can be a positive selection for cells with optimal $[CheR, CheB]$ – such cells can reach the nutrient source faster and have more available substrates for growth. In contrast, swimming in agar poses mainly negative selection – cells with low $[CheR, CheB]$ are filtered out from the chemotactic population.

3.3.4 Experimental measurement of [CheR,CheB] in individual cells in different parts of swarm rings

To confirm that chemotactic cells are selected for their $[CheR, CheB]$ levels in swarm plates, cells expressing CheR and CheB-YFP from one operon were taken from two positions in the swarm ring – at the center and at the outer edge – and protein levels in individual cells were determined using fluorescence imaging (experiments were performed by L. Lovdok). The cells collected near the center at a standard agar concentration (0.27%) have on average lower copy numbers of adaptation enzymes than cells at the outer edge, confirming the predicted selection against low copy numbers (Figure 21A). As expected, in the swarm plates with a reduced agar concentration (0.20%), the difference between center and outer edge is much smaller (Figure 21B), suggesting that there is no strong selection against low copy numbers in liquid media. It should be noted that agar concentrations below 0.20% do not produce a stable gel structure, and therefore that is probably the most liquid agar that can be used for swarm plate experiments.

Simulations and additional experiments with a pTrc promoter, which gives much higher basal expression level of $[CheR, CheB]$, show that very high levels of the adaptation enzymes, over 20-fold, can again decrease chemotactic efficiency in agar (Figure 22, 23).

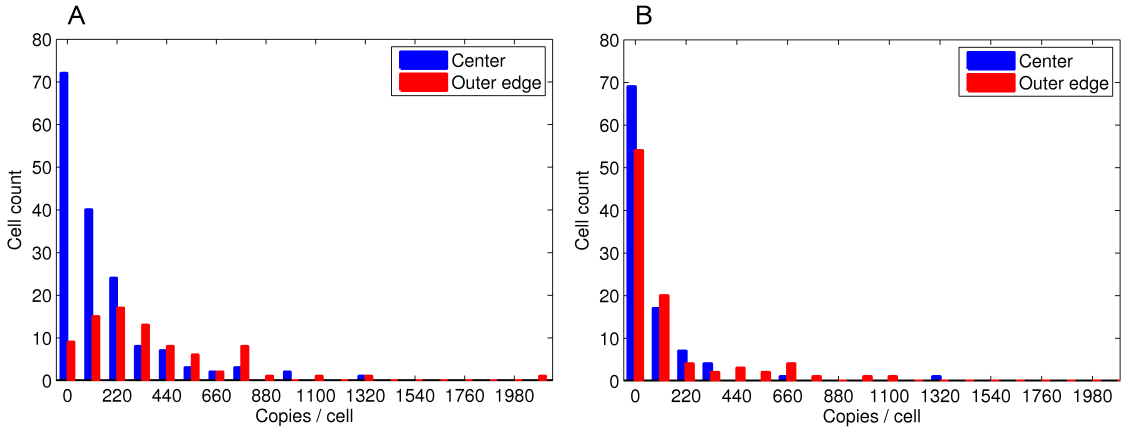

Figure 21: Experimental measurement of [CheR,CheB-YFP] in individual cells at different points in the swarm ring, for plates with (A) normal agar (0.27%); (B) liquid agar (0.20%). Blue columns show the least swarming cells in the center of the swarm plate, and the red ones – the best swarming cells from the outer edge. The expression of *cheR cheB-yfp* was under the control of a pBAD promoter, which gives a basal expression level close to wild-type. The bin size is 110 copies/cell.

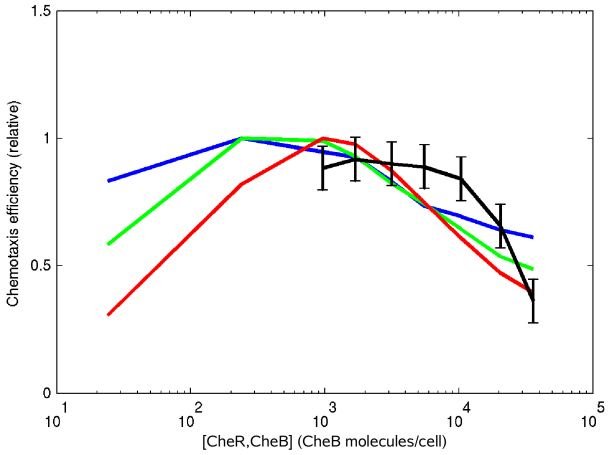

Figure 22: Chemotactic efficiency in agar as a function of highly over-expressed $[CheR, CheB]$, observed in experiments and simulations: (black line) swarm plates efficiency of cells with CheR and CheB-YFP expression under control of pTrc promoter. The chemotaxis efficiency was estimated as diameters of swarm rings divided by diameters of wild-type swarm rings. Color lines denote simulated chemotaxis efficiency in three isotropic gradients N1 (blue), N2 (green), N3 (red). The chemotaxis efficiency in simulations was estimated as the average distance travelled by cells, divided by the distance at the optimal $[CheR, CheB]$. Error bars indicate standard deviations.

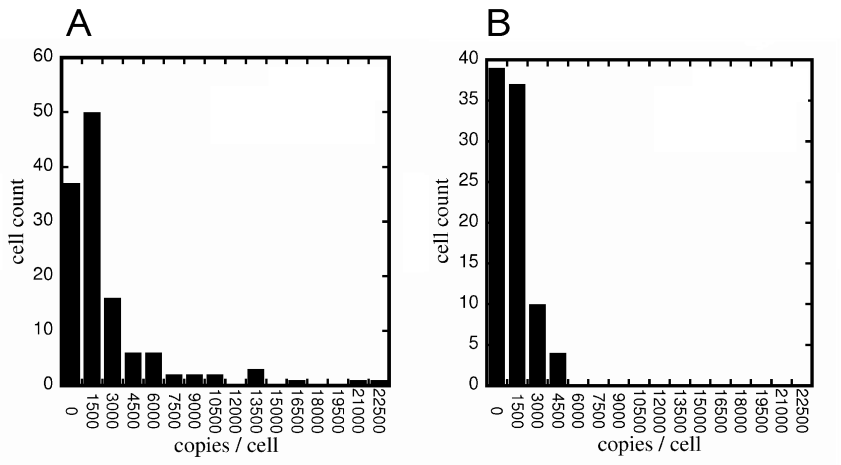

Figure 23: Experimental measurement of [CheR,CheB-YFP] in individual cells at different points of the swarm ring, for cells with (A) the least, and (B) the best swarming efficiency. The cells with the highest [CheR,CheB-YFP] have the least chemotactic efficiency. CheR and CheB-YFP were expressed from one operon under control of pTrc promoter and native ribosome-binding sites. The pTrc promoter gives high basal expression relatively to the wild-type level. The least swarming cells were taken from the center of the swarm plate, and the best swarming - from the outer edge of the swarm ring. The mean protein levels were determined as described in (Vladimirov et al., 2008).

3.4 Fine-tuning of tumbling angle and its effect on drift velocity

Dependence of tumbling angle on the number of CW-rotating motors. The tumbling angle dependence on the number of switching motors was investigated by extending the RapidCell model from the version used in (Vladimirov et al., 2008). First, a more detailed model of tumbling was developed to bring the model in a closer agreement with the tracking experiments of Berg and Brown (1972). While previous version of the model relied on a simple voting model of tumbling, which started the tumble as soon as the majority of motors rotate CW, the new model takes into account the duration of CW-rotation of every motor (Figure 24A). The complex hydrodynamics of multiple flagella is described in simplified form, through a *distortion factor* which is a function of t_{cw} of each motor (see Methods and Algorithms). Despite this simplification, the simulated swimming of *E. coli* is in a very good agreement with the original tracking experiments of Berg and Brown (1972). The model realistically reproduces nearly all data provided by tracking experiments: mean cellular speed, run times, tumbling angles (Table 7), as well as individual motor switching and gradua recovery of cellular speed after a tumble.

Second, a dependence of tumbling angle on the number of CW-rotating motors that cause the tumble was introduced (Figure 24B). This was done by fitting the experimental data of Turner et al. (2000) with a realistic choice of discrete tumbling angles at each number of CW-switched motors (Figure 24C). To ensure consistency with experimental data, a dependence of tumbling angle on the total number of motors was also assumed. The resulting model was called *anisotropic*, and it was compared to a conventional model of tumble (*isotropic*), which chooses the tumbling angle stochastically. In simulations without a gradient, both models produce equal cellular drift velocities, with the accuracy of estimation error. To keep the mean angles of both models consistent, the frequencies of the discrete angles in the anisotropic model were defined as shown in Figure 24D.

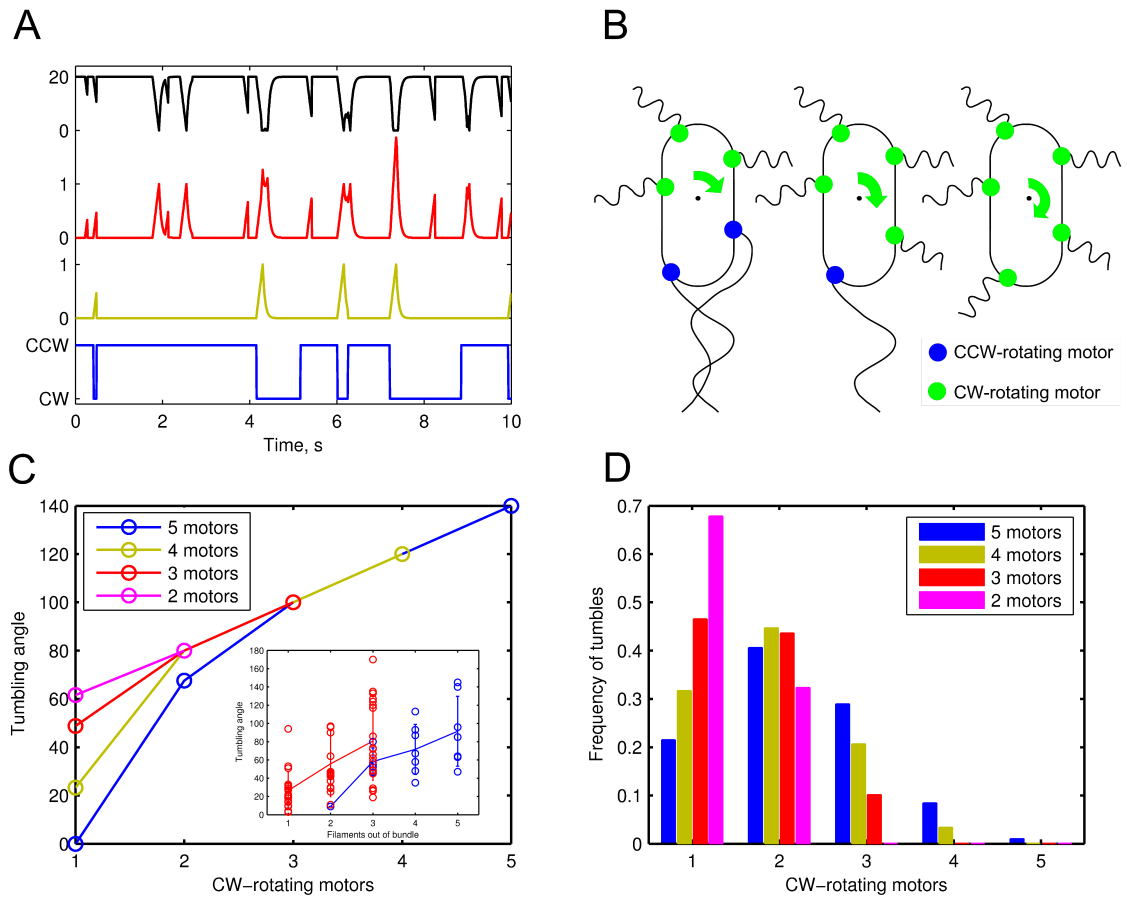

Figure 24: Anisotropic model of *E. coli* tumbling. (A) The output series for a single swimming cell (from bottom to top): switching of a single motor (blue), its distortion d_{cw} (green), the sum of distortions of 3 motors D_{cw} (red), the resulting falls of swimming speed during tumbles (black). (B) The schematic illustration of tumbling angle (green arrow) dependence on the number of CW-rotating motors (green circles). (C) Anisotropic model of tumbling. The tumbling angle Θ_i at different number of CW-rotating motors n_{cw}. *Inset.* Experimental data sets reproduced from Fig. 12 of (Turner et al., 2000). Solid lines show means, error-bars show standard deviations, circles correspond to individual tumbles. Color code of the inset is the same as in the main panel. (D) Frequencies p_i of tumbles which involve n_{cw} CW-rotating motors out of the total number of motors $N = 2..5$.

Dependence of tumbling angle on swimming direction. Simulations of cells with anisotropic model show that tumbling angle depends on the swimming direction prior to a tumble (Figure 25A). This dependence naturally arises from the dependence

Parameter	Isotropic model	Anisotropic model	Experiment
Tumbling angle, control (^{o})	67.5	67.5	68
Run length, control (s)	0.81 ± 0.63	0.81 ± 0.63	0.86 ± 1.18
Run length, gradient (s)	0.89 ± 0.77	0.92 ± 0.86	0.90 ± 1.56
Run length, up gradient (s)	0.93 ± 0.83	0.98 ± 0.95	1.07 ± 1.80
Run length, down gradient (s)	0.83 ± 0.69	0.86 ± 0.75	0.80 ± 1.38
Swimming speed, control (μms^{-1})	17 ± 5.4	17 ± 5.4	14.2 ± 3.4
Drift velocity, control (μms^{-1})	0.36 ± 0.03	0.39 ± 0.03	–
Drift velocity, gradient (μms^{-1})	0.92	1.40	0.90

Table 7: Comparison of the RapidCell-1.1 output and the tracking data from Berg and Brown, 1972. The main model parameters are the same as described in Table 2, with additional model parameters shown in Table 5. The number of motors $N = 3$, the aspartate gradient is N1. Values are estimated from 1000 cells simulated for 500 s. Controls correspond to a ligand-free medium. Means and std (where relevant) are shown.

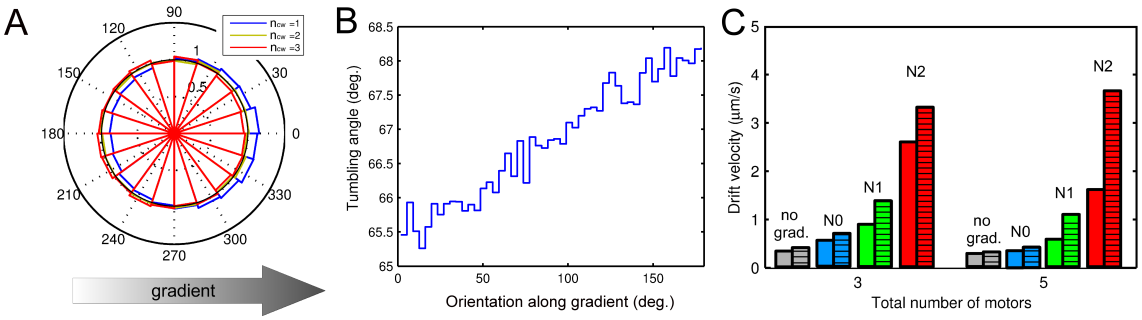

Figure 25: Behavior of cells with anisotropic tumbling model. (A) Distribution of cellular orientations prior to tumbles. The tumbling events are divided into 3 groups, by the number of CW-rotating motors involved in a tumble. The rose histograms are normalized by the number of counts. The inner black circle shows unbiased (isotropic) distribution as a reference. Cell orientation is given relative to the gradient. The gradient steepness is N1. (B) Average tumbling angle as a function of orientation along the gradient prior to tumbles. (C) Chemotactic drift velocity of cells in gradients of different steepness. Bars show the drift velocities of cells with 3 motors (left group) or 5 motors (right group) in the medium without a gradient (gray), in gradient N0 (blue), N1 (green) and N2 (red). Left bars show the isotropic model, right (hatched) bars – anisotropic model of tumbling. In the absence of gradient, the difference is within the error of estimation. Standard error of the mean is about 0.03. Cells in (A) and (B) have 3 motors, other parameters are as described in Methods and Algorithms, Tables 2,5. The number of simulated cells is 10^3 in each case.

of tumbling angle on the number of CW-rotating motors. The cells which turned with the smallest n_{cw} were swimming in slightly skewed directions up the gradient before the tumble, whereas the cells which turned with the highest n_{cw} were swimming with even smaller skew down the gradient before the tumble. A more detailed analysis shows that the total angular difference between tumbling angles that correspond to the movement up and down a gradient is only about 3^o (Figure 25B). Such a small difference is within the error of the early tracking experiments, about 5^o (Brown, 1974), which explains why it remained undetected.

Effect of anisotropic model on cell drift velocity. Despite such a small difference of mean angles, it can significantly increase the chemotactic performance, with the mean drift velocity being up to two times higher for anisotropically tumbling cells (Figure 25C). The positive effect of anisotropic tumble becomes more visible in steeper gradients and for higher number of motors, which suggests that highly flagellated cells can adjust their tumbling angle more precisely.

In the case of $N = 3$ motors and moderate gradient (N1), the mean tumbling angle is $M(\Theta) = 67.0^o$. This value is only 0.5^o smaller than the angle in ligand-free simulations, so the increase of the drift velocity in the anisotropic model cannot be attributed to the change of the total mean tumbling angle. The mean tumbling angle up the gradient $\Theta(cos(\alpha > 0)) = 66.4^o$, while down the gradient it is $\Theta(cos(\alpha < 0)) = 67.6^o$. Therefore, the 1.2^o difference in mean tumbling angles causes a 52% increase in the population drift velocity, from 0.92 to 1.4 μms^{-1} (Figure 25C).

Dependence of anisotropic model effect on the magnitude of angle adjustment and on rotational diffusion. As a control, chemotactic cells that tumble with a constant angle (67.5 deg.) were simulated and compared to cells that tumble with slightly higher angle (67.5-Δ), when they swim up the gradient, and with slightly lower angle (67.5+Δ), when they swim down the gradient. Here, the Δ was a constant parameter changed from 1 to 5 deg. A difference of $\Delta = 5$ degrees increased the drift velocity by about 100% in the gradient N1, and by $\sim$ 50% in the gradient N2 (Figure 26A). This confirms that the observed increase in drift velocity shown in

Figure 25C is due to small changes in tumbling angles of up- and down-swimming cells, and does not arise from model-specific parameters.

Bacterial movement in gradients is further affected by the Brownian motion for both isotropic and anisotropic tumbling models (Figure 26B). In simulations the default rotational diffusion coefficient was 0.062 $rad^2 s^{-1}$. At lower coefficients of rotational diffusion, both models demonstrate better chemotaxis, and the advantage of the anisotropic tumbling is most pronounced, which is due to lower noise factor arising from rotational diffusion (Andrews et al., 2006). Since rotational diffusion depends on the cells size, flagellar length, media viscosity and temperature (Berg, 1993; Mitchell, 1991), predicted effects of anisotropic tumbling can be even more pronounced for other bacteria or under different environmental conditions.

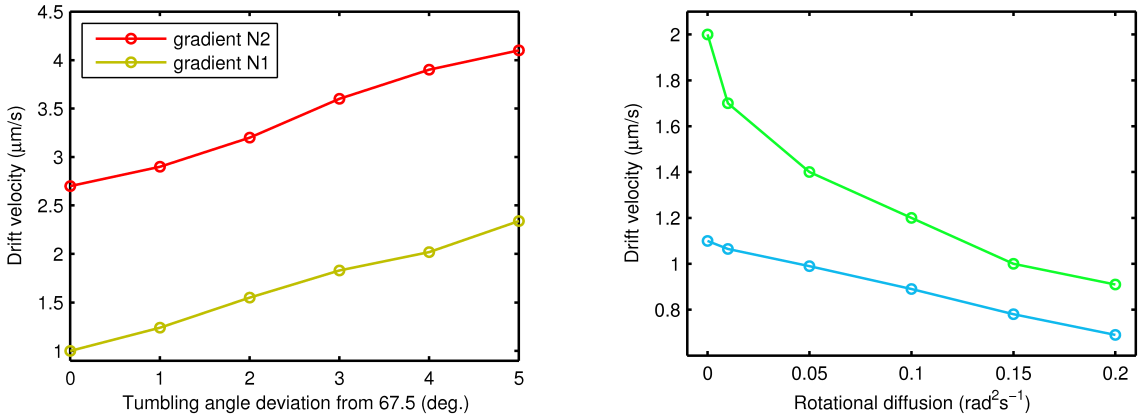

(a) (b)

Figure 26: Effects of tumbling angle adjustment and rotational diffusion on chemotactic efficiency. (A) Dependence of chemotactic drift velocity on fixed tumbling angle deviation Δ in a simplified tumbling model. The cells swimming up the gradient tumble with a smaller angle $67.5 - \Delta$, while cells swimming down the gradient tumble with higher angle $67.5 + \Delta$. Cells with $\Delta = 0$ tumble with a fixed angle 67.5^o, i.e. isotropically. (B) Dependence of chemotactic drift on rotational diffusion coefficient for cells with isotropic (blue) and anisotropic (green) models of tumbling. The number of simulated cells is 10^3 in each case, the gradient is N1. Cells in (A) and (B) have 3 motors, other parameters are as described in Methods and Algorithms, Tables 2,5.

Taken together, these results suggest that in addition to extending the run length

while swimming up the gradient, *E. coli* uses an auxiliary mechanism of tumbling angle tuning according to the swimming direction. This fine tuning of tumble is mediated by the same adjustment of tumbling frequency that underlies the conventional chemotaxis strategy of bacteria (Figure 27). This previously unrecognized feature is expected to be shared by other peritrichously flagellated bacteria and seems to represent yet another level of evolutionary optimization of the chemotaxis system.

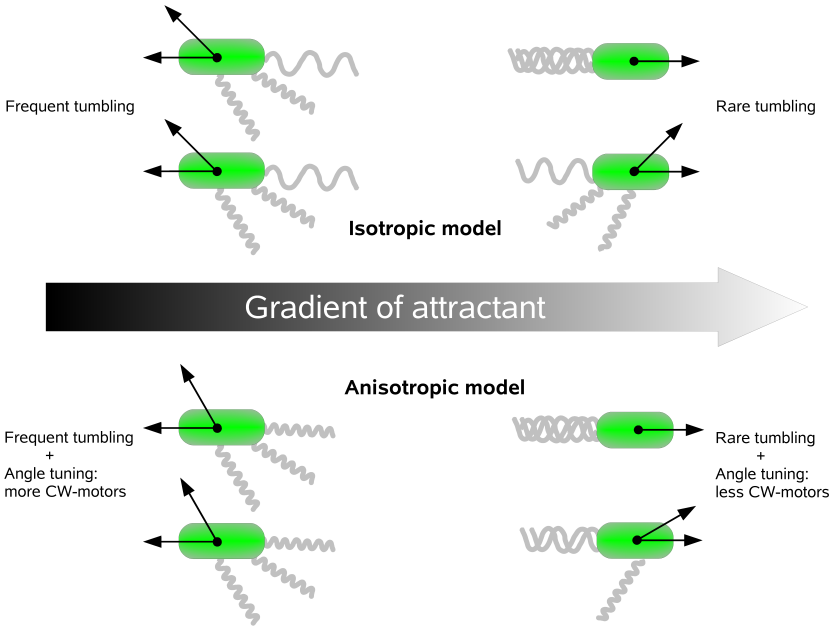

(a)

Figure 27: Enhancement of chemotactic efficiency due to anisotropic tumbling. In the isotropic model (top), cells have lower CW bias and tumble less frequently up the gradient, but their average tumbling angle is the same in all directions. In the anisotropic model (bottom), the same lowering of CW motor bias additionally leads to the reduction of tumbling angles below average for cells swimming up the gradient. Cells swimming down the gradient have tumbling angles larger than the average. Directional dependence of the tumbling angle enhances average drift up the gradient. The difference of tumbling angles is exaggerated for illustration purposes.

Chapter 4

Discussion

The constructed model of chemotactic *E. coli* (RapidCell) allowed to carry out large-scale numerical experiments to study the effects of microscopic network parameters on population behavior. RapidCell employs a hybrid model for pathway simulation, with mixed algebraic, ODE and stochastic components instead of a fully stochastic model, AgentCell (Emonet et al., 2005), or a complete system of ordinary differential equations, *E. pluribus* (Bray et al., 2007). The proposed approach of modeling allowed to dramatically decrease in computational costs of simulations. Though many molecular details are skipped or modeled in a rapid-equilibrium (algebraic) approximation based on time-scale separation, the key steps of the network are reproduced in agreement with up-to-date experimental data.

For the receptor complex simulation, the mixed-receptor cluster MWC model was applied (Mello and Tu, 2005; Endres and Wingreen, 2006; Hansen et al., 2008), which accounts for the observed broad range of sensitivity and reproduces the recent *in vivo* FRET experiments (Sourjik and Berg, 2002a). The adaptation is modeled according to the mean-field approximation of the MWC model, with the assumption that the average methylation level of multiple receptors can be represented as a continuous rather than a discrete variable. In contrast to other reactions, methylation and demethylation are relatively slow and therefore described by an ODE. The ODE is integrated by the first-order explicit Euler scheme to ensure high computational speed of the program, while the time step is chosen as 0.01 s to keep the simulation error

low.

In contrast to detailed single-cell simulations which reproduce the noisy behavior of individual cells (Korobkova et al., 2004; Emonet et al., 2005), RapidCell is aimed at predicting the averaged behavior of bacterial populations, and to investigate how it is affected by the signaling network parameters, neglecting the intrinsic noise coming from molecular reactions. However, artificial sources of noise can be further added in the deterministic model of the signaling pathway. In the present version of RapidCell, the noise arises only from rotational diffusion and stochastic switching of the motors.

To capture the essential features of cellular behavior but avoid significant increase of computation time, the cells are simulated in 2D space instead of 3D. The mathematical background of 3D cell motion is given in Appendix D. However, the 3D case is not expected to provide qualitatively new effects in the considered problems. The 2D model of motion was chosen for its simplicity and significant reduction of computational requirements for large-scale simulations.

Taking into account the available experimental studies on tumble mechanics (Darnton et al., 2007; Turner et al., 2000), a voting model of run-tumble switching (Ishihara et al., 1983; Turner et al., 2000; Andrews et al., 2006) was used as a first approximation for the tumbling. This model was used to study the effect of adaptation rate in gradients of different steepness (Vladimirov et al., 2008).

Constant-activity gradient. There are several types of gradients usually applied in computer models of chemotaxis. The linear gradient arises between stationary source and adsorber, and can often be observed under natural conditions. The Gaussian, another commonly used gradient, appears when a limited amount of molecules is injected into the medium from a micropipette or a similar source (Berg, 1993). Other gradients that arise from general models of diffusion have hyperbolic or exponential shapes. However, all commonly used gradients have a 'blind' zone where receptors are saturated and cells do not respond. When cells drift along these gradients, the average profile of CheYp changes dramatically, from a steep fall at low concentrations to a weakly stimulated state at high concentrations (Figure 12C). This makes it difficult to compare long-term chemotactic efficiency, because the average CheYp and

drift velocity are non-stable along the gradient.

To study chemotaxis systematically, a new – constant-activity – type of gradient was proposed. This gradient has unique properties of providing the same CheYp level and cellular-drift velocity over a wide range of ligand concentrations. The stability of the CheYp level allows studying properties of virtual chemotactic cells systematically, and to compare chemotactic behavior over long time periods and concentration ranges.

The form of the constant-activity gradient is derived from the MWC model, by formulating the differential equation for the gradient shape which gives a constant rate of receptor free energy change per unit time. In earlier work, the condition of constant chemotactic response was studied using a phenomenological model of ligand binding, with a single dissociation constant K_D (Block et al., 1983). The study of Block and co-authors showed that such a model can be simplified, and as a result an exponential ramp of ligand should give a constant response in the range between $C_{min} = 0.31K_D$ and $C_{max} = 3.2K_D$, a prediction that was supported by their experiments (Block et al., 1983).

In this work it is shown that the differential equation for the constant-response gradient proposed in (Block et al., 1983) can be derived directly from the MWC model of receptor cluster. The mentioned differential equation is solved here analytically, and the exact form of the constant-activity gradient is found. The constant-activity gradient grows similarly to the exponential function at moderate ligand concentrations, and increases faster than exponential at low and high concentrations (Figure 11A).

Numerical simulations show that the chemotactic response of the MWC model in the constant-activity gradient remains stable over four orders of ligand concentration – between 0.1 and $1000K_D$, in the case when Tsr receptors are fully insensitive to the ligand. In the case of (Me)-Asp, the Tsr receptors are able to respond non-specifically to high ligand concentrations, therefore above $100K_D$ the cluster activity drops to zero in a mixed-receptor cluster (Endres and Wingreen, 2006; Sourjik and Berg, 2002a). In simulations of population behavior only moderate Asp concentrations were applicable, so the cluster activity remains nearly constant in all observed cases.

The exponential ramp also gives nearly constant response in the MWC model, but over a much smaller range – between 0.5 and $3.0K_D$, in agreement with (Block

et al., 1983) and the recent study of Tu et al. (2008).

It is shown analytically that the apparent dissociation constant K_D can be estimated by either the arithmetic or geometric mean of K^{off} and K^{on}, but the geometric mean gives a better approximation over a wide range of ligand concentrations.

The shape of the constant-activity gradient can be approximated not only by exponential, but also by a hyperbolic function. A change of variables gives $K_D Cx/(1-Cx) = K_D(1/y - 1) \sim K_D/y$, $(y = 1 - Cx,\ K_D \ll 1)$. The hyperbolic gradient arises from simple models of diffusion, when ligand molecules are emitted from a spherical source into the surrounding medium. In nature, such conditions can be observed, for example, in aquatic ecosystems where microalgae leak organic matter attractive for bacteria (Jackson, 1987). This suggests that hyperbolic and exponential gradients with appropriate parameters can be good approximations of the constant-activity gradient.

Effect of adaptation rate on chemotaxis efficiency. In the proposed model, the *adaptation rate* is assumed to be proportional to the co-varied concentration of the adaptation enzymes [CheR,CheB], and through the text both terms are used to denote the rate of adaptation. However, increasing expression of the adaptation enzymes may lead to saturation of the adaptation rate at some point, because the enzymes will start working out of saturation kinetics. For these reasons, it is more correct to consider the presented results in terms of adaptation-rate effects on chemotaxis, whatever the origins of adaptation-rate variability may be.

The effect of adaptation rate on chemotaxis agrees in many respects with the results reported in (Andrews et al., 2006) for optimal noise filtering of the chemotaxis signaling system. In their work, authors demonstrated the existence of an optimal cutoff frequency for efficient chemotaxis, an analog of the adaptation rate in our study. For a fixed linear gradient, they show the same shape of chemotactic efficiency as a function of cutoff frequency (Fig. 3B in (Andrews et al., 2006)) as found in this work (Figure 14A). Authors also show that the optimal cutoff frequency depends on gradient steepness in a linear manner (Fig. 5A in (Andrews et al., 2006)), consistent with simulations presented here (Figure 14B).

Simulations of bacteria in the constant-activity gradient suggest a simple biological mechanism that determines the optimal adaptation rate for a given gradient steepness. Different optimal adaptation rates correspond to a single CheYp interval, which fits the linear range of the motor response function. This means that the highest drift velocity in liquid media is observed when the CheYp level is in the narrow interval fitting the operating range of the motor. In this range, the dependence between CheYp and motor bias is approximately linear (Figure 15C).

The CheB phosphorylation feedback is found to have either a positive or negative effect on chemotactic efficiency, depending on how it shifts the average CheYp level relative to the region of linear motor response. In the case of non-perfect ratio of CheR to CheB, the CheB phosphorylation mechanism can partially counteract the negative effect of unbalanced [CheR]/[CheB] ratio, by shifting the average CheYp towards the optimal region. This confirms that CheB phosphorylation can improve the chemotactic properties of cells with deviations in the ratio of [CheR]/[CheB], as well as in the ratios of other proteins, from the optimum (Kollmann et al., 2005).

Chemotaxis in agar. Chemotactic behavior in liquid media differs from that in agar. The agar medium was simulated using traps that are randomly distributed in time – a cell can encounter traps during its run, and stays trapped until it makes the next tumble, as observed by Wolfe and Berg (1989). This restricts cellular motility – cells that are highly biased towards running remain in traps longer. In agar, the region of optimal motor bias is very narrow and is just above the unstimulated state mb_0, because higher bias increases the period of time cells remain in traps. Subdiffusion in porous media and the treatment of a trapped situation as an additional state have been analyzed mathematically in a general setting, see e.g. (Mommer and Lebiedz, 2009).

The growth of a bacterial population was not considered in the model. The typical swarm plate experiments last several hours, and cells grow and divide during the experiment, leading to variations in protein levels and to redistribution of proteins from generation to generation. However, the effect of different adaptation rates in simulations is clearly visible already within one cell generation after 1000 s of model

time (Figure 20B). The selection thus works on a time scale that is shorter than the generation time, which justifies using a fixed protein distribution. Therefore, the addition of cell growth should not change the results qualitatively. In experiments, daughter cells with sub-optimal levels of CheR and CheB will rapidly fall behind the spreading swarm ring in the vicinity of the division site, while the subpopulation with optimal adaptation rates will be always at the front edge of the ring.

In most simulations, the CheR and CheB ratio is assumed constant due to the genetic coupling between the two respective genes (Løvdok et al., 2009), and that cell-to-cell variation in adaptation rates arises from concerted variation in the levels of both enzymes (Kollmann et al., 2005). The effects of variation in the $[CheR]/[CheB]$ ratio was also studied. Such a variation results from translational noise, and affects both the adaptation rate and the steady-state motor bias. In addition to these investigated sources of noise, there is an intrinsic noise in the pathway activity which arises from the stochastic nature of (de-)methylation events. The latter sort of noise can also have positive effects on the spreading of cells in a ligand-free medium (Korobkova et al., 2004), and even on chemotactic drift in weak gradients (Emonet and Cluzel, 2008). Superposition of variable noise effects on chemotactic efficiency in variable gradients would be an interesting issue for further study.

The variability in concerted CheR and CheB concentrations was estimated using available experimental data on cell-to-cell variability in adaptation times (Berg and Tedesco, 1975). A log-normal distribution for protein concentrations was assumed, which also gives a log-normal distribution of adaptation times to a step-wise stimulus from 0 to $10^{-3}M$ MeAsp (Berg and Tedesco, 1975). There are also other experimental estimates of cell-to-cell variation in adaptation times (Spudich and Koshland, 1976) and related simulations (Levin, 2003), but the adaptation rates observed in those experiments were several times higher, presumably due to different culture growth conditions.

The results presented in this part suggest some evolutionary implications. In liquid media with variable food sources and gradient intensities, variability in adaptation times (protein levels) among cells can help the whole population to respond to different gradients more readily, due to positive selection of cells with optimal $[CheR, CheB]$.

In other words, for any given gradient steepness, there will be a subpopulation which has the best [CheR,CheB] to follow this gradient. In contrast, agar poses mainly negative selection on cell populations - cells with low $[CheR, CheB]$ are filtered out from competition, while all other cells travel with approximately equal efficiency.

Anisotropic tumbling. Another issue addressed in this work is a more detailed model of cell swimming and tumbling, and possible consequences of motion with several flagellar motors. To study the fine effects of tumbling in more detail, a novel model of tumbling was constructed, called anisotropic because the tumbling angle depends on the swimming direction through the number of CW-switching motors. The model brought RapidCell closer to single-cell tracking experiments of Berg and Brown (1972), and allowed to reveal a novel auxiliary navigation mechanism of *E. coli*. Simulations suggest that in addition to extending the run length while swimming up the gradient, *E. coli* uses a mechanism of tumbling angle tuning according to the swimming direction. This previously unrecognized feature is expected to be shared by other peritrichously flagellated bacteria and seems to represent another level of evolutionary optimization of the chemotaxis system.

Hybridization of models. In this work, a hybrid model was constructed using the time scale separation between ligand binding, receptor-cluster conformational changes and receptor covalent modification. The heterogeneous models of receptor cluster, (de-)methylation, CheY phosphorylation and motor switching were merged by sufficiently fine time discretization, under the assumption of well-mixed cytoplasmic components and negligible times of CheYp diffusion through cytoplasm. The bacterial cells are represented as individual objects swimming in space with defined gradient of attractant. The model can be potentially developed further to include consumption and secreting of chemicals from and into the medium by the bacterial population. Such model improvement demands already spatial merging of discrete-particle population model and continuous PDE model of the medium, which would represent another scale of system complexity, laying beyond the scope of this work. However, this can be a promising direction of future studies.

Chapter 5

Conclusions

In this work, a multiscale model of chemotactic bacteria was constructed. The model is focused on central events in signal transduction on a single-cell level, but at the same time it enables simulation of bacterial populations in a computationally efficient way. This goal was achieved by combining three different modeling approaches: algebraic models (rapid equilibrium interactions), ordinary differential equations (slow reactions), and stochastic components (motor switching). The constructed model reflects the most up-to-date experimental data on the system properties, it is computationally efficient, and it was used for *in silico* studies of *E. coli* behavior. Simulations of bacterial populations in gradients of defined steepness revealed several important issues of chemotactic behavior. First, there is an optimal adaptation rate in every gradient, and the optimum is determined by a balance of the network excitation and adaptation, in which the signal transmitting molecule CheYp fits the narrow working range of the flagellar motor. Variability of adaptation rates may be beneficial for a population to fit the variability in gradients. Second, motility in porous media poses significant restrictions on cellular behavior, and changes the criteria for optimal chemotaxis. Low excitation due to shallow gradient and rapid adaptation is preferential in porous medium. Third, bacteria like *E. coli* with several flagellar motors are predicted to have an additional navigation mechanism by fine-tuning of the tumbling angle. This previously unknown effect is the result of different average number of motors that cause tumbles up and down the gradient, and it is predicted to have a

significant impact on the chemotaxis efficiency. This fine tuning of tumble is mediated by the same adjustment of tumbling frequency that underlies the conventional chemotaxis strategy of bacteria. This feature is expected to be shared by other peritrichously flagellated bacteria and seems to represent another level of evolutionary optimization of the chemotaxis system.

In general, such multiscale models as presented here can be an important research instrument for understanding the cell behavior. They reflect the most important experimental knowledge on bacterial behavior, and allow to carry out computational experiments of high complexity, which would be too complicated or expensive for experimental trials. The multiscale description of cell poses challenges in mathematics, physics, computer science and biology, which should work in intimate collaboration to understand the cell behavior at different scales. Even though we know the molecular mechanisms of chemotaxis in detail, there is a vast *terra incognita* in our understanding how bacteria interact with their environment. The issues of evolution and environment, individual versus collective behavior, and chemotaxis of more complex organisms come to the foreground of modern research.

Bibliography

Adler, J. (1966). Chemotaxis in bacteria. Science *153*(3737), 708–716.

Adler, J. (1969). Chemoreceptors in bacteria. Science *166*(3913), 1588–1597.

Alon, U., Camarena, L., Surette, M. G., Aguera y Arcas, B., Liu, Y., Leibler, S., and Stock, J. B. (1998). Response regulator output in bacterial chemotaxis. The EMBO Journal *17*(15), 4238–4248.

Alon, U., Surette, M. G., Barkai, N., and Leibler, S. (1999). Robustness in bacterial chemotaxis. Nature *397*(6715), 168–171.

Alt, W. (1980). Biased random walk models for chemotaxis and related diffusion approximations. Journal of Mathematical Biology *9*(2), 147–177.

Andrews, B. W., Yi, T.-M., and Iglesias, P. A. (2006). Optimal noise filtering in the chemotactic response of Escherichia coli. PLoS Computational Biology *2*(11), 1407–1418.

Andrews, S. S. and Bray, D. (2004). Stochastic simulation of chemical reactions with spatial resolution and single molecule detail. Physical Biology *1*(3-4), 137–151.

Asakura, S. and Honda, H. (1984). Two-state model for bacterial chemoreceptor proteins: the role of multiple methylation. Journal of Molecular Biology *176*(3), 349–367.

Bainer, R., Park, H., and Cluzel, P. (2003). A high-throughput capillary assay for bacterial chemotaxis. Journal of Microbiological Methods *55*(1), 315–319.

Barkai, N. and Leibler, S. (1997). Robustness in simple biochemical networks. Nature *387*(6636), 913–917.

Berg, H. C. (1971). How to track bacteria. The Review of Scientific Instruments *42*(6), 868–871.

Berg, H. C. (1993). Random Walks in Biology (Princeton University Press).

Berg, H. C. and Brown, D. A. (1972). Chemotaxis in Escherichia coli analysed by three-dimensional tracking. Nature *239*(5374), 500–504.

Berg, H. C. and Purcell, E. M. (1977). Physics of chemoreception. Biophysical Journal *20*(2), 193–219.

Berg, H. C. and Tedesco, P. M. (1975). Transient response to chemotactic stimuli in Escherichia coli. Proc. Natl. Acad. Sci. USA *72*(8), 3235–3239.

Berg, H. C. and Turner, L. (1990). Chemotaxis of bacteria in glass capillary arrays. Escherichia coli, motility, microchannel plate, and light scattering. Biophysical Journal *58*(4), 919–930.

Block, S., Segall, S., and Berg, H. (1982). Impulse responses in bacterial chemotaxis. Cell *31*(1), 215–226.

Block, S. M., Segall, J. E., and Berg, H. C. (1983). Adaptation kinetics in bacterial chemotaxis. Journal of Bacteriology *154*(1), 312–323.

Borkovich, K. A., Alex, L. A., and Simon, M. I. (1992). Attenuation of sensory receptor signaling by covalent modification. Proc. Natl. Acad. Sci. USA *89*(15), 6756–6760.

Bray, D. (2002). Bacterial chemotaxis and the question of gain. Proc. Natl. Acad. Sci. USA *99*(1), 7–9.

Bray, D. and Bourret, R. B. (1995). Computer analysis of the binding reactions leading to a transmembrane receptor-linked multiprotein complex involved in bacterial chemotaxis. Molecular Biology of the Cell *6*(10), 1367–1380.

Bray, D., Bourret, R. B., and Simon, M. I. (1993). Computer simulation of the phosphorylation cascade controlling bacterial chemotaxis. Molecular Biology of the Cell *4*(5), 469–482.

Bray, D., Levin, M. D., and Lipkow, K. (2007). The chemotactic behavior of computerbased surrogate bacteria. Current Biology *17*(1), 12–19.

Bray, D., Levin, M. D., and Morton-Firth, C. J. (1998). Receptor clustering as a cellular mechanism to control sensitivity. Nature *393*(6680), 85–88.

Brown, D. A. (1974). Chemotaxis in Escherichia coli: a biased random walk. Ph.D. Thesis. Dissertation, University of Colorado, Department of Physics and Astrophysics.

Cao, Y., Gillespie, D. T., and Petzold, L. R. (2006). Efficient step size selection for the tau-leaping simulation method. The Journal of Chemical Physics *124*(4), 044109+.

Chen, K. C., Ford, R. M., and Cummings, P. T. (1998). The global turning probability density function for motile bacteria and its applications. Journal of Theoretical Biology *195*(2), 139–155.

Chen, K. C., Ford, R. M., and Cummings, P. T. (1999). Perturbation expansion of Alt's cell balance equations reduces to Segel's one-dimensional equations for shallow chemoattractant gradients. SIAM Journal of Applied Mathematics *59*(1), 35–57.

Chen, K. C., Ford, R. M., and Cummings, P. T. (2003). Cell balance equation for chemotactic bacteria with a biphasic tumbling frequency. Journal of Mathematical Biology *47*(6), 518–546.

Chiam, K.-H. H., Tan, C. M. M., Bhargava, V., and Rajagopal, G. (2006). Hybrid simulations of stochastic reaction-diffusion processes for modeling intracellular signaling pathways. Physical review. E, Statistical, nonlinear, and soft matter physics *74*(5 Pt 1).

Chung, C. Y., Funamoto, S., and Firtel, R. A. (2001). Signaling pathways controlling cell polarity and chemotaxis. Trends in Biochemical Sciences *26*(9), 557–566.

Cluzel, P., Surette, M., and Leibler, S. (2000). An ultrasensitive bacterial motor revealed by monitoring signaling proteins in single cells. Science *287*(5458), 1652–1655.

Colella, P., Hou, T., and Petzold, L., eds. (2004). Report of the First Multiscale Mathematics Workshop: first steps toward a roadmap.

Dahlquist, F. W., Lovely, P., and Koshland, D. E. (1972). Quantitative analysis of bacterial migration in chemotaxis. Nature: New biology *236*(65), 120–123.

Darnton, N. C., Turner, L., Rojevsky, S., and Berg, H. C. (2007). On torque and tumbling in swimming Escherichia coli. Journal of Bacteriology *189*(5), 1756–1764.

Emonet, T. and Cluzel, P. (2008). Relationship between cellular response and behavioral variability in bacterial chemotaxis. Proc. Natl. Acad. Sci. USA *105*(9), 3304–3309.

Emonet, T., Macal, C. M., North, M. J., Wickersham, C. E., and Cluzel, P. (2005). AgentCell: a digital single-cell assay for bacterial chemotaxis. Bioinformatics *21*(11), 2714–2721.

Endres, R. G. and Wingreen, N. S. (2006). Precise adaptation in bacterial chemotaxis through "assistance neighborhoods". Proc. Natl. Acad. Sci. USA *103*(35), 13040–13044.

Engelmann, T. W. (1881). Neue Methoden zur Untersuchung der Sauerstoffausscheidung pflanzlicher und tierischer Organismen. Pflüger's Archiv Gesamte Physiol. (25), 285–292.

Erban, R. and Othmer, H. G. (2004). From individual to collective behavior in bacterial chemotaxis. SIAM Journal of Applied Mathematics *65*(2), 361–391.

Erban, R. and Othmer, H. G. (2005). From signal transduction to spatial pattern formation in E. coli: A paradigm for multiscale modeling in biology. Multiscale Modeling & Simulation *3*(2), 362–394.

Flanagan, M. (2007). Java Scientific Library. http://www.ee.ucl.ac.uk/~mflanaga/java/index.html .

Ford, B. (1991). The Leeuwenhoek legacy (Farrand Press).

Ford, R. M. and Lauffenburger, D. A. (1991). Measurement of bacterial random motility and chemotaxis coefficients: II. Application of single-cell-based mathematical model. Biotechnology and Bioengineering *37*(7), 661–672.

Ford, R. M., Phillips, B. R., Quinn, J. A., and Lauffenburger, D. A. (1991). Measurement of bacterial random motility and chemotaxis coefficients: I. Stopped-flow diffusion chamber assay. Biotechnology and Bioengineering *37*(7), 647–660.

Frymier, P. D., Ford, R. M., Berg, H. C., and Cummings, P. T. (1995). Three-dimensional tracking of motile bacteria near a solid planar surface. Proc. Natl. Acad. Sci. USA *92*(13), 6195–6199.

Gadgil, C., Lee, C., and Othmer, H. (2005). A stochastic analysis of first-order reaction networks. Bulletin of Mathematical Biology *67*(5), 901–946.

Gillespie, D. T. (2001). Approximate accelerated stochastic simulation of chemically reacting systems. The Journal of Chemical Physics *115*(4), 1716–1733.

Goldbeter, A. and Koshland, D. (1982). Simple molecular model for sensing and adaptation based on receptor modification with application to bacterial chemotaxis. Journal of Molecular Biology *161*(3), 395–416.

Hansen, C. H., Endres, R. G., and Wingreen, N. S. (2008). Chemotaxis in Escherichia coli: a molecular model for robust precise adaptation. PLoS Computational Biology *4*(1), 14–27.

Hauri, D. C. and Ross, J. (1995). A model of excitation and adaptation in bacterial chemotaxis. Biophysical Journal *68*(2), 708–722.

Hazelbauer, G. L., Falke, J. J., and Parkinson, J. S. (2008). Bacterial chemoreceptors: high-performance signaling in networked arrays. Trends in Biochemical Sciences *33*(1), 9–19.

Hillen, T. and Othmer, H. G. (2000). The diffusion limit of transport equations derived from velocity-jump processes. SIAM Journal on Applied Mathematics *61*(3), 751–775.

Horstmann, D. (2003a). From 1970 until present: the Keller-Segel model in chemotaxis and its consequences I. Jahresber. DMV *105*(3), 103–165.

Horstmann, D. (2003b). From 1970 until present: the Keller-Segel model in chemotaxis and its consequences II. Jahresber. DMV *106*(2), 51–69.

Ishihara, A., Segall, J. E., Block, S. M., and Berg, H. C. (1983). Coordination of flagella on filamentous cells of Escherichia coli. Journal of Bacteriology *155*(1), 228–237.

Jackson, G. A. (1987). Simulating Chemosensory Responses of Marine Microorganisms. Limnology and Oceanography *32*(6), 1253–1266.

Kalantzis, G. (2009). Hybrid stochastic simulations of intracellular reaction-diffusion systems. Computational Biology and Chemistry *33*(3), 205–215.

Kalinin, Y. V., Jiang, L., Tu, Y., and Wu, M. (2009). Logarithmic sensing in Escherichia coli bacterial chemotaxis. Biophysical Journal *96*(6), 2439–2448.

Kaupp, U. B. and Koch, K. W. (1992). Role of cGMP and Ca2+ in vertebrate photoreceptor excitation and adaptation. Annual Review of Physiology *54*, 153–175.

Keller, E. F. and Segel, L. A. (1971). Traveling bands of chemotactic bacteria: a theoretical analysis. Journal of Theoretical Biology. *30*(2), 235–248.

Kelly, F. X., Dapsis, K. J., and Lauffenburger, D. A. (1988). Effect of bacterial chemotaxis on dynamics of microbial competition. Microbial Ecology *16*(2), 115–131.

Kennedy, M. J. (1987). Role of motility, chemotaxis, and adhesion in microbial ecology. Annals of the New York Academy of Sciences *506*(1), 260–273.

Kennedy, M. J. J. and Lawless, J. G. G. (1985). Role of chemotaxis in the ecology of denitrifiers. Applied and Environmental Microbiology *49*(1), 109–114.

Kentner, D. and Sourjik, V. (2006). Spatial organization of the bacterial chemotaxis system. Current Opinion in Microbiology *9*(6), 619–624.

Keymer, J. E., Endres, R. G., Skoge, M., Meir, Y., and Wingreen, N. S. (2006a). Chemosensing in Escherichia coli: two regimes of two-state receptors. Proc. Natl. Acad. Sci. USA *103*(6), 1786–1791.

Keymer, J. E., Galajda, P., Muldoon, C., Park, S., and Austin, R. H. (2006b). Bacterial metapopulations in nanofabricated landscapes. Proc. Natl. Acad. Sci. USA *103*(46), 17290–17295.

Khan, S., Jain, S., Reid, G. P., and Trentham, D. R. (2004). The fast tumble signal in bacterial chemotaxis. Biophysical Journal *86*(6), 4049–4058.

Kim, C., Jackson, M., Lux, R., and Khan, S. (2001). Determinants of chemotactic signal amplification in Escherichia coli. Journal of Molecular Biology *307*(1), 119–135.

Kollmann, M., Lovdok, L., Bartholome, K., Timmer, J., and Sourjik, V. (2005). Design principles of a bacterial signalling network. Nature *438*(7067), 504–507.

Korobkova, E., Emonet, T., Vilar, J. M., Shimizu, T. S., and Cluzel, P. (2004). From molecular noise to behavioural variability in a single bacterium. Nature *428*(6982), 574–578.

Koshland, D. E. (1977). A response regulator model in a simple sensory system. Science (New York, N.Y.) *196*(4294), 1055–1063.

Koshland, D. E. (1981). Biochemistry of sensing and adaptation in a simple bacterial system. Annual Review of Biochemistry *50*, 765–782.

Kreft, J. U., Booth, G., and Wimpenny, J. W. (1998). BacSim, a simulator for individual-based modelling of bacterial colony growth. Microbiology *144 (Pt 12)*, 3275–3287.

Kuo, S. C. and Koshland, D. E. (1989). Multiple kinetic states for the flagellar motor switch. Journal of Bacteriology *171*(11), 6279–6287.

Larsen, S. H., Reader, R. W., Kort, E. N., Tso, W. W., and Adler, J. (1974). Change in direction of flagellar rotation is the basis of the chemotactic response in Escherichia coli. Nature *249*(452), 74–77.

Lauffenburger, D. (1991). Quantitative studies of bacterial chemotaxis and microbial population dynamics. Microbial Ecology *22*(1), 175–185.

Lebiedz, D. (2004). Computing minimal entropy production trajectories: an approach to model reduction in chemical kinetics. The Journal of Chemical Physics *120*(15), 6890–6897.

Lebiedz, D. and Brandt-Pollmann, U. (2003). Manipulation of self-aggregation patterns and waves in a reaction-diffusion system by optimal boundary control strategies. Physical Review Letters *91*(20), 208301+.

Lebiedz, D. and Maurer, H. (2004). External optimal control of self-organisation dynamics in a chemotaxis reaction diffusion system. Systems Biology, IEE Proceedings *1*(2), 222–229.

Lebiedz, D., Skanda, D., and Fein, M. (2008). Automatic complexity analysis and model reduction of nonlinear biochemical systems. In M. Heiner and A. Uhrmacher, eds., Computational Methods in Systems Biology. Lecture Notes in Bioinformatics, vol. 5307, pp. 123–140.

Lee, C. H., Kim, K. H., and Kim, P. (2009). A moment closure method for stochastic reaction networks. The Journal of Chemical Physics *130*(13), 134107+.

Levin, M. D. (2003). Noise in gene expression as the source of non-genetic individuality in the chemotactic response of Escherichia coli. FEBS Letters *550*(1-3), 135–138.

Levin, M. D., Morton-Firth, C. J., Abouhamad, W. N., Bourret, R. B., and Bray, D. (1998). Origins of individual swimming behavior in bacteria. Biophysical Journal *74*(1), 175–181.

Levit, M. N. and Stock, J. B. (2002). Receptor methylation controls the magnitude of stimulus-response coupling in bacterial chemotaxis. Journal of Biological Chemistry *277*(39), 36760–36765.

Lewus, P. and Ford, R. M. (2001). Quantification of random motility and chemotaxis bacterial transport coefficients using individual-cell and population-scale assays. Biotechnology and Bioengineering *75*(3), 292–304.

Li, G. and Weis, R. M. (2000). Covalent modification regulates ligand binding to receptor complexes in the chemosensory system of Escherichia coli. Cell *100*(3), 357–365.

Li, M. and Hazelbauer, G. L. (2004). Cellular stoichiometry of the components of the chemotaxis signaling complex. Journal of Bacteriology *186*(12), 3687–3694.

Li, M. and Hazelbauer, G. L. (2005). Adaptational assistance in clusters of bacterial chemoreceptors. Molecular Microbiology *56*(6), 1617–1626.

Lipkow, K., Andrews, S. S., and Bray, D. (2005). Simulated diffusion of phosphorylated CheY through the cytoplasm of Escherichia coli. Journal of Bacteriology *187*(1), 45–53.

Løvdok, L., Bentele, K., Vladimirov, N., Müller, A., Pop, F. S., Lebiedz, D., Kollmann, M., and Sourjik, V. (2009). Role of translational coupling in robustness of bacterial chemotaxis pathway. PLoS Biology *7*(8), e1000171+.

Lovely, P. S. and Dahlquist, F. W. (1975). Statistical measures of bacterial motility and chemotaxis. Journal of Theoretical Biology *50*(2), 477–496.

Macnab, R. M. and Koshland, D. E. (1972). The gradient-sensing mechanism in bacterial chemotaxis. Proc. Natl. Acad. Sci. USA *69*(9), 2509–2512.

Manahan, C. L., Iglesias, P. A., Long, Y., and Devreotes, P. N. (2004). Chemoattractant signaling in Dictyostelium discoideum. Annual Review of Cell and Developmental Biology *20*, 223–253.

Mao, H., Cremer, P. S., and Manson, M. D. (2003). A sensitive, versatile microfluidic assay for bacterial chemotaxis. Proc. Natl. Acad. Sci. USA *100*(9), 5449–5454.

Marx, R. B. and Aitken, M. D. (1999). Quantification of chemotaxis to naphthalene by Pseudomonas putida G7. Applied and Environmental Microbiology *65*(7), 2847–2852.

Marx, R. B. and Aitken, M. D. (2000). A material-balance approach for modeling bacterial chemotaxis to a consumable substrate in the capillary assay. Biotechnology and Bioengineering *68*(3), 308–315.

Matsumoto, M. and Nishimura, T. (1998). Mersenne Twister: A 623-dimensionally equidistributed uniform pseudo-random number generator. ACM Transactions on Modeling and Computer Simulation *8*(1), 3–30.

Mello, B. A., Shaw, L., and Tu, Y. (2004). Effects of receptor interaction in bacterial chemotaxis. Biophysical Journal *87*(3), 1578–1595.

Mello, B. A. and Tu, Y. (2003a). Perfect and near-perfect adaptation in a model of bacterial chemotaxis. Biophysical Journal *84*(5), 2943–2956.

Mello, B. A. and Tu, Y. (2003b). Quantitative modeling of sensitivity in bacterial chemotaxis: the role of coupling among different chemoreceptor species. Proc. Natl. Acad. Sci. USA *100*(14), 8223–8228.

Mello, B. A. and Tu, Y. (2005). An allosteric model for heterogeneous receptor complexes: understanding bacterial chemotaxis responses to multiple stimuli. Proc. Natl. Acad. Sci. USA *102*(48), 17354–17359.

Mitchell, J. (1991). The influence of cell size on marine bacterial motility and energetics. Microbial Ecology *22*(1), 227–238.

Mommer, M. S. and Lebiedz, D. (2009). Modeling subdiffusion using reaction diffusion systems. SIAM Journal on Applied Mathematics *70*(1), 112–132.

Monod, J., Wyman, J., and Changeux, J. P. (1965). On the nature of allosteric transitions: a plausible model. Journal of Molecular Biology *12*, 88–118.

Morton-Firth, C. J. and Bray, D. (1998). Predicting temporal fluctuations in an intracellular signalling pathway. Journal of Theoretical Biology pp. 117–128.

Morton-Firth, C. J., Shimizu, T. S., and Bray, D. (1999). A free-energy-based stochastic simulation of the Tar receptor complex. Journal of Molecular Biology *286*(4), 1059–1074.

Murray, J. D. (2003). Mathematical Biology II: Spatial Models and Biomedical Applications (Springer).

Othmer, H. G. and Stevens, A. (1997). Aggregation, blowup, and collapse: the abc's of taxis in reinforced random walks. SIAM Journal of Applied Mathematics *57*(4), 1044–1081.

Park, S., Wolanin, P. M., Yuzbashyan, E. A., Silberzan, P., Stock, J. B., and Austin, R. H. (2003). Motion to form a quorum. Science *301*(5630), 188.

Pedit, J. A., Marx, R. B., Miller, C. T., and Aitken, M. D. (2002). Quantitative analysis of experiments on bacterial chemotaxis to naphthalene. Biotechnology and Bioengineering *78*(6), 626–634.

Pfeffer, W. (1881). Locomotorische Richtungsbewegungen durch chemischen Reize. Untersuch. Botan. Inst., Tubingen (1), 363–482.

Pfeffer, W. (1888). Über chemotaktische Bewegungen von Bakterien, Flagellaten und Volvocineen. Untersuch. Botan. Inst., Tubingen (2), 582–661.

Pugh, E. N. and Lamb, T. D. (1990). Cyclic GMP and calcium: the internal messengers of excitation and adaptation in vertebrate photoreceptors. Vision Research *30*(12), 1923–1948.

Reinhardt, V., Winckler, M., and Lebiedz, D. (2008). Approximation of slow attracting manifolds in chemical kinetics by trajectory-based optimization approaches. The Journal of Physical Chemistry. A *112*(8), 1712–1718.

Ritter, L. R. (2004). A short course in the modeling of chemotaxis. Texas A & M University .

Rivero, M. A., Tranquillo, R. T., Buettner, H. M., and Lauffenburger, D. A. (1989). Transport models for chemotactic cell populations based on individual cell behavior. Chemical Engineering Science *44*(12), 2881–2897.

Scharf, B. E., Fahrner, K. A., Turner, L., and Berg, H. C. (1998). Control of direction of flagellar rotation in bacterial chemotaxis. Proc. Natl. Acad. Sci. USA *95*(1), 201–206.

Schiesser, W. E. (1991). The numerical method of lines: Integration of partial differential equations (Academic Press, New York).

Segall, J. E., Block, S. M., and Berg, H. C. (1986). Temporal comparisons in bacterial chemotaxis. Proc. Natl. Acad. Sci. USA *83*(23), 8987–8991.

Setayeshgar, S., Gear, C. W., Othmer, H. G., and Kevrekidis, I. G. (2005). Application of coarse integration to bacterial chemotaxis. Multiscale Modeling and Simulation *4*(1), 307–27.

Shi, Y. and Duke, T. (1998). Cooperative model of bacterial sensing. Physical Review E *58*(5), 6399–6406.

Shimizu, T. S., Aksenov, S. V., and Bray, D. (2003). A spatially extended stochastic model of the bacterial chemotaxis signalling pathway. Journal of Molecular Biology *329*(2), 291–309.

Skoge, M. L., Endres, R. G., and Wingreen, N. S. (2006). Receptor-receptor coupling in bacterial chemotaxis: evidence for strongly coupled clusters. Biophysical Journal *90*(12), 4317–4326.

Snyderman, R. and Goetzl, E. J. (1981). Molecular and cellular mechanisms of leukocyte chemotaxis. Science *213*(4510), 830–837.

Sourjik, V. (2004). Receptor clustering and signal processing in E. coli chemotaxis. Trends Microbiology *12*(12), 569–576.

Sourjik, V. and Berg, H. (2002a). Receptor sensitivity in bacterial chemotaxis. Proc. Natl. Acad. Sci. USA *99*(1), 123–127.

Sourjik, V. and Berg, H. C. (2002b). Binding of the Escherichia coli response regulator CheY to its target measured in vivo by fluorescence resonance energy transfer. Proc. Natl. Acad. Sci. USA *99*(20), 12669–12674.

Sourjik, V. and Berg, H. C. (2004). Functional interactions between receptors in bacterial chemotaxis. Nature *428*(6981), 437–441.

Spiro, P. A., Parkinson, J. S., and Othmer, H. G. (1997). A model of excitation and adaptation in bacterial chemotaxis. Proc. Natl. Acad. Sci. USA *94*(14), 7263–7268.

Spudich, J. L. and Koshland, D. E. (1975). Quantitation of the sensory response in bacterial chemotaxis. Proc. Natl. Acad. Sci. USA *72*(2), 710–713.

Spudich, J. L. and Koshland, D. E. (1976). Non-genetic individuality: chance in the single cell. Nature *262*(5568), 467–471.

Staropoli, J. F. and Alon, U. (2000). Computerized analysis of chemotaxis at different stages of bacterial growth. Biophysical Journal *78*(1), 513–519.

Stewart, R. C., Jahreis, K., and Parkinson, J. S. (2000). Rapid phosphotransfer to CheY from a CheA protein lacking the CheY-binding domain. Biochemistry *39*(43), 13157–13165.

Stocker, R., Seymour, J. R., Samadani, A., Hunt, D. E., and Polz, M. F. (2008). Rapid chemotactic response enables marine bacteria to exploit ephemeral microscale nutrient patches. Proc. Natl. Acad. Sci. USA *105*(11), 4209–4214.

Tindall, M., Maini, P., Porter, S., and Armitage, J. (2008a). Overview of mathematical approaches used to model bacterial chemotaxis II: Bacterial populations. Bulletin of Mathematical Biology *70*(6), 1570–1607.

Tindall, M., Porter, S., Maini, P., Gaglia, G., and Armitage, J. (2008b). Overview of mathematical approaches used to model bacterial chemotaxis I: The single cell. Bulletin of Mathematical Biology *70*(6), 1525–1569.

Tsang, N., Macnab, R., and Koshland, D. E. (1973). Common mechanism for repellents and attractants in bacterial chemotaxis. Science *181*(4094), 60–63.

Tu, Y., Shimizu, T. S., and Berg, H. C. (2008). Modeling the chemotactic response of Escherichia coli to time-varying stimuli. Proc. Natl. Acad. Sci. USA *105*(39).

Turner, L., Ryu, W. S., and Berg, H. C. (2000). Real-time imaging of fluorescent flagellar filaments. Journal of Bacteriology *182*(10), 2793–2801.

Vladimirov, N., Lebiedz, D., and Sourjik, V. (2009). Auxiliary navigation mechanism of peritrichously flagellated chemotactic bacteria. (submitted) .

Vladimirov, N., Løvdok, L., Lebiedz, D., and Sourjik, V. (2008). Dependence of bacterial chemotaxis on gradient shape and adaptation rate. PLoS Computational Biology *4*(12), e1000242+.

Wadhams, G. H. and Armitage, J. P. (2004). Making sense of it all: bacterial chemotaxis. Nature Reviews Molecular Cell Biology *5*(12), 1024–1037.

Wolfe, A. J. and Berg, H. C. (1989). Migration of bacteria in semisolid agar. Proc. Natl. Acad. Sci. USA *86*(18), 6973–6977.

Yi, T. M., Huang, Y., Simon, M. I., and Doyle, J. (2000). Robust perfect adaptation in bacterial chemotaxis through integral feedback control. Proc. Natl. Acad. Sci. USA *97*(9), 4649–4653.

Zonia, L. and Bray, D. (2009). Swimming patterns and dynamics of simulated Escherichia coli bacteria. Journal of the Royal Society Interface *6*(40), 1035–1046.

Zufall, F. and Leinders-Zufall, T. (2000). The cellular and molecular basis of odor adaptation. Chemical Senses *25*(4), 473–481.

Appendix A

Running the RapidCell program

To run RapidCell, make sure that you have the Java SE Development Kit 6 (JDK 6), or download the latest version from http://java.sun.com/javase/6/download.jsp (Make sure you download the JDK, *not* the JRE.)
Open the terminal window. In Windows, you can do this from the **Start** menu by choosing **Command Prompt** (Windows XP), or by choosing **Run...** and then entering `cmd`. Make sure that `javac` command works in your current directory. If not, set up the PATH variable to include your JDK binaries folder. See more information about setting PATH at http://java.sun.com/docs/books/tutorial/essential/environment/paths.html

Unpack RapidCell into your home folder.

Use the terminal window: change to the RapidCell directory

```
cd YOUR_HOME_FOLDER/RapidCell1.1;
```

(Windows users: `cd /D C:\YOUR_HOME_FOLDER\RapidCell1.1`)

Compile the program

```
javac *.java
```

Run the program

```
java -cp .  Run
```

After RapidCell is complete, the output is written into 2 txt-files (tab-delimited):

`individuals.out` (states of each cell at defined time points)
`averages.out` (the most important characteristics of cell behavior, averaged over the population)

A.0.1 Analysis of individual cell behavior in Matlab

To open the output file in Matlab, use the following Matlab script:

```
cd YOUR_HOME_FOLDER/RapidCell1.1
DATA=load('individuals.out');
X=DATA(:,1:7:length(DATA(1,:)));
Y=DATA(:,2:7:length(DATA(1,:)));
R=DATA(:,3:7:length(DATA(1,:)));
CheA=DATA(:,4:7:length(DATA(1,:)));
CheY=DATA(:,5:7:length(DATA(1,:)));
meth=DATA(:,6:7:length(DATA(1,:)));
mb=DATA(:,7:7:length(DATA(1,:)));
```

The code above reads data from file `individuals.out`. Each line of the file corresponds to a single timepoint, and the seven main parameters of every cell are written one after another delimited by tabs. Thus, first seven entries of a line correspond to the first cell, second seven – to the second cell, etc.

Basic examples of analysis

To plot the mean X(t) positions of all cells

```
mX=mean(X,2);
plot((0:100)*5,mX)
```

Here, the time is represented by 101 points from 0 to $Tmax = 500s$.
To estimate the drift velocity of cells up the gradient, type

```
plot((40:100)*5,mean(X(41:101,:),2))
```

Then use `Tools->Basic Fitting->Linear (show equations)` in the main Matlab menu. It will give the slope of the plot, which is the population drift velocity (mm/s),

measured between 200 and 500 s of model time. Use `R` insead of `X`, if gradient is radial.
To plot mean CheY(t) level of all cells

```
mCheY=mean(CheY,2);
plot((0:100)*5,mCheY)
```

To plot X(t) and Y(t) trajectory of a single cell, say, the cell #1

```
plot(X(:,1),Y(:,1))
```

To get a scatterplot of positions of all cells at timepoint 101 (500 sec):

```
plot(X(101,:),Y(101,:),'.')
```

A.0.2 Changing the parameters of simulation

By default, the parameters are defined in file `PARAM.INI`. Alternatively, you can define parameters in the source file `Model.java`, lines 125-128. To do this, simply set the variable

```
private boolean ReadFromINIfile=true;
```

to `'false'` in line 8 of `Model.java`, and change the parameters therein.

Other parameters (network, motor behavior, etc.) can be changed in the corresponding files `Network.java`, `Motor.java`, etc.

Appendix B

Versions of RapidCell program

Version 1.0 Basic model with isotropic tumbling angle, model of voting motors for run-tumble switching, constant cell swimming speed. Used in (Vladimirov et al., 2008).

Version 1.1 Anisotropic tumbling angle is added. The run-tumble switching depends on the time of motors CW-rotation (distortion factor). The swimming speed is also affected by the distortion factor. Used in (Vladimirov et al., 2009).

Version 1.2 The motor switching frequencies λ_+ and λ_- depend on motor bias *and* motor reversal frequency, which is proportional to derivative of motor bias, as described below.

B.1 Detailed model of motor switching: version 1.2

In the first version of RapidCell, a simplified model of motor switching was used, which assumes a constant switching frequency k_-. This model was used in (Vladimirov et al., 2008, 2009). To avoid this simplification in future, a more general model of motor switching is introduced, as described below. This model update does not change the cell behavior qualitatively, but may reduce the population drift velocity by about 30% due to shorter runs.

The CCW motor bias (the fraction of time motor spins CCW) is related to the switching rates as (Scharf et al., 1998)

$$mb = \frac{k_-}{k_- + k_+} \tag{30}$$

The motor reversal frequency is related to the switching rates as their harmonic mean (Scharf et al., 1998)

$$\omega = \frac{2k_-k_+}{k_- + k_+} \tag{31}$$

Equations 30, 31 allow to express the switching rates using motor bias and reversal frequency

$$k_+ = \frac{\omega}{2mb} \tag{32}$$

$$k_- = \frac{\omega}{2(1-mb)} \tag{33}$$

It was shown by Cluzel et al. (2000) that the reversal frequency is well fitted by the derivative of CW motor bias with respect to CheYp (y) with a scaling coefficient of about 0.5

$$\omega = 0.5\frac{d(1-mb)}{dy} = \frac{0.5H(1/mb_0 - 1)y^{H-1}}{(1 + (1/mb_0 - 1)y^H)^2} \tag{34}$$

The final formulae for switching frequencies are

$$k_+ = \frac{\omega}{2mb} = \frac{0.5H(1-mb_0)y^{H-1}}{2(1 + (1/mb_0 - 1)y^H)} \tag{35}$$

$$k_- = \frac{\omega}{2(1-mb)} = \frac{0.5Hmb_0}{2y(y^H(1-mb_0) + mb_0)} \tag{36}$$

The summary of motor model changes is given in Table 8.

Model	Reference
Motor reversal frequency $\omega = \frac{2k_-k_+}{k_-+k_+} \sim 0.5\frac{d(1-mb(Y))}{dY}$	(Scharf et al., 1998; Cluzel et al., 2000), coefficient 0.5 estimated in this work
Motor switching freq. (CCW→CW) $k_+ = \frac{\omega}{2mb}$	(Scharf et al., 1998; Setayeshgar et al., 2005)
Motor switching freq. (CW→CCW) $k_- = \frac{\omega}{2(1-mb)}$	(Scharf et al., 1998; Setayeshgar et al., 2005)

Table 8: Changes in RapidCell-1.2.

Appendix C

Derivation of the formula for constant-activity gradient

According to the MWC model, an increase in ligand concentration ΔS causes an initial rise in receptor free-energy difference

$$\Delta f = log\left(1 + \frac{\Delta S}{S + K^{off}}\right) - log\left(1 + \frac{\Delta S}{S + K^{on}}\right) \tag{37}$$

Using the Taylor-series approximation,

$$\Delta f \approx \frac{\Delta S}{S + K^{off}} - \frac{\Delta S}{S + K^{on}} \tag{38}$$

leads to the following approximation for free energy per concentration change:

$$\Delta f \approx \Delta S \frac{K^{on} - K^{off}}{(S + K^{on})(S + K^{off})} \tag{39}$$

Simplified solution. The denominator in Eqn. 39 can be simplified by assuming

$$(S + K^{on})(S + K^{off}) \approx (S + K^{*})^2 \tag{40}$$

and the unknown K^* can be found from equation

$$(S + K^{on})(S + K^{off}) = (S + K^*)^2 \tag{41}$$

$$S^2 + SK^{on} + SK^{off} + K^{on}K^{off} = S^2 + 2SK^* + (K^*)^2 \tag{42}$$

$$S(K^{on} + K^{off}) + K^{on}K^{off} = 2SK^* + (K^*)^2. \tag{43}$$

which gives two alternative estimates for K^*:
$K^* = \frac{K^{on}+K^{off}}{2}$ and $K^* = \sqrt{K^{on}K^{off}}$, i.e. the arithmetic and geometric means of K^{on} and K^{off}.

At zero or relatively low ligand concentrations, the geometric mean has a high impact in Eqn. 43, and is preferable as an estimate. Indeed, in earlier works it was referred to as the apparent dissociation constant K_D of ligand binding (Shimizu et al., 2003). However, at high concentrations, the arithmetic mean will have a higher impact in Eqn. 43, so it can be used as an alternative estimate. Simulations indicate that within four orders of aspartate concentration the geometric mean serves as the best estimate of K^* (Fig 28).

Taken together, the energy difference is approximated by $\Delta S \frac{K^{on}-K^{off}}{(S+K^*)^2}$. The differential equation

$$\frac{S'(K^{on} - K^{off})}{(K_D + S)^2} = C \tag{44}$$

describes the unknown function $S(x)$, which will give the 'constant-activity' gradient shape. The function $S(x)$ will give a constant change of energy difference C per length unit dx of cellular path along the gradient. In other words, such a shape of gradient will give a constant cluster activity at any ligand concentration.

Within the accuracy of a constant term, the latter differential equation was previously used in (Block et al., 1983), where authors derived it assuming that receptor occupancy is proportional to $S/(S + K_D)$, with a single K_D for active and inactive receptors. Authors assumed that the chemotactic response is proportional to the change in receptor occupancy (Block et al., 1983; Sourjik and Berg, 2002a). They simplified this equation to reduce the variability of the $\frac{1}{(K_D+S)^2}$ term, leading to the

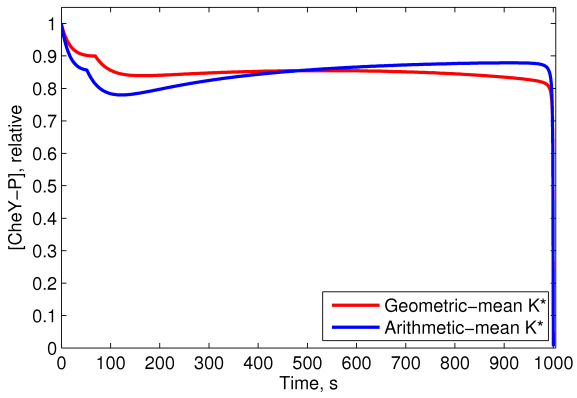

Figure 28: The CheYp response of MWC model to the constant-activity ramp of aspartate from 0.1 to $10000K_D$. The ramp is simulated as $S(t) = K^*Ct/\left(\frac{K^{on}-K^{off}}{K^*} - Ct\right)$ in two forms, with $K^* = 0.5(K^{on} + K^{off})$ (arithmetic mean), or $K^* = (K^{on}K^{off})^{0.5}$ (geometric mean). The MWC model shows approximately constant response for both approximations, but the geometric mean gives more stable response over wider range of concentrations.

exponential form of the solution.

However, one can solve Eqn. 44 analytically:

$$S(x) = (K^{on} - K^{off})\left(\frac{1}{C(C_1 - x)}\right) - K^* \tag{45}$$

where $C_1 = \frac{(K^{on}-K^{off})}{C(S(0)-K^*)}$ is the constant of integration, determined by the initial condition $S(0)$. The condition $S(0) = 0$ gives the following chemoattractant function:

$$S(x) = K^* \frac{Cx}{\frac{K^{on}-K^{off}}{K^*} - Cx} \tag{46}$$

Appendix D

Mathematics of cell motion in 3D space

Swimming of a cell in 3D space requires more complicated mathematics to calculate orientation, compared to 2D case. The orientation of cell is described by direction of motion $\mathbf{n} = (n_x, n_y, n_z)$, a vector of unit length in 3D Cartesian coordinates. The orientation of $\mathbf{n}$ is determined by two angles: β is the angle between $\mathbf{n}$ and $\mathbf{Z}$ axis, and α is the angle between projection of $\mathbf{n}$ on $\mathbf{XY}$ plane and $\mathbf{X}$ axis (in the 2D case, only α was taken into account). The vector coordinates are related to orientation angles as

$$\begin{aligned} n_x &= \sin(\beta)\cos(\alpha) \\ n_y &= \sin(\beta)\sin(\alpha) \\ n_z &= \cos(\beta) \end{aligned} \tag{47}$$

The angles related to coordinates as

$$\begin{aligned} \alpha &= \arctan(n_y/n_x) \\ \beta &= \arccos(n_z) \end{aligned} \tag{48}$$

Cell running. In the case of straight swimming, the position $\mathbf{x}$ of the cell in the next simulation step is calculated from the previous step according to direction of

motion and speed

$$\mathbf{x}(t+\Delta t) = \mathbf{x}(t) + \mathbf{n}v_0 dt \tag{49}$$

where v_0 is the absolute magnitude of cell speed. In scalar form this reads

$$\begin{aligned} x(t+\Delta t) &= x(t) + v_x v_0 dt \\ y(t+\Delta t) &= y(t) + v_y v_0 dt \\ z(t+\Delta t) &= z(t) + v_z v_0 dt \end{aligned} \tag{50}$$

Mathematics of rotational diffusion in 3D can be found in supplementary information to (Emonet et al., 2005), and it includes multiplication of three rotational matrices (for x, y and z components) at each time step.

Cell tumbling. Tumbling in 3D space is determined by angle Θ, which is the difference between the old and the new direction (similar to 2D case), and angle ϕ, which is an arbitrary rotation around the old direction. In the coordinate system of cell, the old velocity vector $\mathbf{v}$ is directed along the $\mathbf{Z}_{cell}$ axis. In the cell coordinates, the tumble is described by rotation of cell body by angle Θ along $\mathbf{Y}_{cell}$ or $\mathbf{X}_{cell}$ axis (we take $\mathbf{Y}_{cell}$), and a rotation around the $\mathbf{Z}$ axis by angle ϕ. These transformations are described mathematically by multiplication of rotational matrices and the velocity vector $(0, 0, 1)$ in the cell coordinates

$$\mathbf{v}(t+\Delta t)_{cell} = \mathbf{R}_z(\phi)\mathbf{R}_y(\Theta)(0,0,1)^t \tag{51}$$

Next, the new velocity vector should be transformed back to the laboratory coordinates, which means rotation by angle β around $\mathbf{Y}$ axis and then by α around $\mathbf{Z}$ (the order is important).

$$\mathbf{v}(t+\Delta t) = \mathbf{R}_z(\alpha)\mathbf{R}_y(\beta)\mathbf{v}(t+\Delta t)_{cell} \tag{52}$$

Taken together, the new velocity vector, after tumble, is calculated from formula

$$\mathbf{v}(t+\Delta t) = \mathbf{R}_z(\alpha)\mathbf{R}_y(\beta)\mathbf{R}_z(\phi)\mathbf{R}_y(\Theta)(0,0,1)^t \tag{53}$$

where α and β are the orientation angles of the old velocity vector $\mathbf{v}(t)$, Θ is the tumbling angle, and ϕ is randomly chosen within $[0, 2\pi)$. The reorientation is assumed to be instant, within one time step. The exact expression of these matrices are shown below.

$$\mathbf{R}_y(\Theta) = \begin{bmatrix} \cos(\Theta) & 0 & \sin(\Theta) \\ 0 & 1 & 0 \\ -\sin(\Theta) & 0 & \cos(\Theta) \end{bmatrix} \tag{54}$$

$$\mathbf{R}_z(\phi) = \begin{bmatrix} \cos(\phi) & -\sin(\phi) & 0 \\ \sin(\phi) & \cos(\phi) & 0 \\ 0 & 0 & 1 \end{bmatrix} \tag{55}$$

$$\mathbf{R}_y(\beta) = \begin{bmatrix} \cos(\beta) & 0 & \sin(\beta) \\ 0 & 1 & 0 \\ -\sin(\beta) & 0 & \cos(\beta) \end{bmatrix} \tag{56}$$

$$\mathbf{R}_z(\alpha) = \begin{bmatrix} \cos(\alpha) & \sin(\alpha) & 0 \\ \sin(\alpha) & -\cos(\alpha) & 0 \\ 0 & 0 & 1 \end{bmatrix} \tag{57}$$

However, for simulations it would be more convenient to use final bulk formula than multiply four matrices at every step. The final formula for after-tumble velocity vector is

$$\mathbf{v}(t+\Delta t) = \begin{bmatrix} \cos(\alpha)\cos(\beta)\cos(\phi)\sin(\Theta) + \sin(\alpha)\sin(\phi)\sin(\Theta) + \cos(\alpha)\sin(\beta)\cos(\Theta) \\ \sin(\alpha)\cos(\beta)\cos(\phi)\sin(\Theta) - \cos(\alpha)\sin(\phi)\sin(\Theta) + \sin(\alpha)\sin(\beta)\cos(\Theta) \\ -\sin(\beta)\cos(\phi)\sin(\Theta) + \cos(\beta)\cos(\Theta) \end{bmatrix} \tag{58}$$

Analytical expressions were obtained and verified using Maple 9.5 (Waterloo Maple Inc.).

Appendix E

Publications in peer-reviewed journals

1. Vladimirov, N., Lebiedz, D., Sourjik, V. Auxiliary navigation mechanism of peritrichous chemotactic bacteria. (submitted).

2. Vladimirov N., Sourjik V. (2009) Chemotaxis: how bacterium uses memory. Biological Chemistry (*in press*).

3. Løvdok* L., Bentele* K., Vladimirov* N., Müller* A., Pop F., Lebiedz D., Kollmann M., Sourjik V. (2009) Role of translational coupling in robustness of bacterial chemotaxis pathway. PLoS Biology 7(8): e1000171.
   * *these authors equally contributed to this paper*

4. Vladimirov N., Løvdok L., Lebiedz D., Sourjik V. (2008) Dependence of chemotaxis on gradient shape and adaptation rate. PLoS Computational Biology 4(12): e1000242.

Appendix F

Texts of the publications and manuscripts

OPEN ACCESS Freely available online

PLoS COMPUTATIONAL BIOLOGY

Dependence of Bacterial Chemotaxis on Gradient Shape and Adaptation Rate

Nikita Vladimirov[1]*, Linda Løvdok[2], Dirk Lebiedz[3], Victor Sourjik[2]

1 Interdisziplinäres Zentrum für Wissenschaftliches Rechnen (IWR), University of Heidelberg, Heidelberg, Germany, **2** Zentrum für Molekulare Biologie (ZMBH), University of Heidelberg, Heidelberg, Germany, **3** Zentrum für Biosystemanalyse (ZBSA), University of Freiburg, Freiburg, Germany

Abstract

Simulation of cellular behavior on multiple scales requires models that are sufficiently detailed to capture central intracellular processes but at the same time enable the simulation of entire cell populations in a computationally cheap way. In this paper we present RapidCell, a hybrid model of chemotactic *Escherichia coli* that combines the Monod-Wyman-Changeux signal processing by mixed chemoreceptor clusters, the adaptation dynamics described by ordinary differential equations, and a detailed model of cell tumbling. Our model dramatically reduces computational costs and allows the highly efficient simulation of *E. coli* chemotaxis. We use the model to investigate chemotaxis in different gradients, and suggest a new, constant-activity type of gradient to systematically study chemotactic behavior of virtual bacteria. Using the unique properties of this gradient, we show that optimal chemotaxis is observed in a narrow range of CheA kinase activity, where concentration of the response regulator CheY-P falls into the operating range of flagellar motors. Our simulations also confirm that the CheB phosphorylation feedback improves chemotactic efficiency by shifting the average CheY-P concentration to fit the motor operating range. Our results suggest that in liquid media the variability in adaptation times among cells may be evolutionary favorable to ensure coexistence of subpopulations that will be optimally tactic in different gradients. However, in a porous medium (agar) such variability appears to be less important, because agar structure poses mainly negative selection against subpopulations with low levels of adaptation enzymes. RapidCell is available from the authors upon request.

Citation: Vladimirov N, Løvdok L, Lebiedz D, Sourjik V (2008) Dependence of Bacterial Chemotaxis on Gradient Shape and Adaptation Rate. PLoS Comput Biol 4(12): e1000242. doi:10.1371/journal.pcbi.1000242

Editor: Christopher Rao, University of Illinois at Urbana-Champaign, United States of America

Received July 9, 2008; **Accepted** November 5, 2008; **Published** December 19, 2008

Funding: This work is supported by the Bioquant Graduate Program of Land Baden-Württemberg ''Molecular machines: mechanisms and functional interconnections''.

Competing Interests: The authors have declared that no competing interests exist.

* E-mail: nikita.vladimirov@gmail.com

Introduction

One of the central questions of modern systems biology is the influence of microscopic parameters of a single cell on the behavior of a cell population, a common problem in multi-scale modeling. In terms of bacterial chemotaxis, this issue can be formulated as the influence of signaling network parameters on the spatiotemporal dynamics of a population in various gradients of chemoattractants. The problem of efficient multi-scale simulation imposes strict requirements on the model: it should be maximally detailed to grasp the main features of the signaling network yet computationally cheap to simulate large numbers of bacteria.

Chemotaxis plays an important role in microbial population dynamics. Chemotactic bacteria in a nonmixed environment—that is in presence of nutrient gradients—have significant growth advantages, as shown experimentally for different bacterial species [1–4]. Modeling of microbial population dynamics indicates that motility and chemotactic ability can be as important for evolutionary competition as cell growth rate [5,6].

Escherichia coli is an ideal organism for chemotaxis modeling, because of the rich experimental information collected over years of extensive research. In common with many other bacteria, *E. coli* can migrate towards high concentrations of attractants and away from repellents. In the adapted state, cells perform a random walk, which becomes biased in the presence of a spatial gradient. This swimming bias is based on temporal comparisons of attractant concentrations during cell runs. If the direction of a run is favorable, i.e. up the attractant gradient or down the repellent gradient, the run become longer. Between runs, the cell tumbles and reorients for the next run [7].

Chemotaxis in *E. coli* is mediated by an atypical two-component signal transduction pathway (for recent reviews see [8,9]). Ligand molecules bind to clusters of transmembrane receptors, which are in complex with the histidine kinase CheA and the adaptor CheW. Each receptor can be either active or inactive, depending on ligand binding and the methylation level. The active receptor activates CheA, eliciting downstream phosphorylation of the response regulator CheY. Phosphorylated CheY (CheY-P) is dephosphorylated by CheZ. Receptors can be methylated by the methyltransferase CheR and demethylated by the methylesterase CheB, and methylation regulates the receptor activity. The methylation of receptors provides a sort of chemical 'memory', which allows the cell to compare the current ligand concentration with the past. Phosphorylation of CheB by CheA provides a negative feedback to the system, although it appears nonessential for exact adaptation [10,11]. Phosphorylated molecules of CheY-P freely diffuse through the cytoplasm and bind to the flagellar motor protein FliM, causing motors to switch from CCW to CW

Author Summary

Chemotaxis plays an important role in bacterial lifestyle, providing bacteria with the ability to actively search for an optimal growth environment. The chemotaxis system is likely to be highly optimized, because on the evolutionary time scale even a modest enhancement of its efficiency can give cells a large competitive advantage. In this study, we use up-to-date experimental and modeling information to construct a new computational model of chemotactic *E. coli* and implement it in a computationally efficient way to simulate large bacterial populations. Our simulations are performed in a new type of attractant gradient that ensures a constant level of chemotactic excitation at any position. We show that optimal chemotactic movement in a gradient results from a fine balance between excitation and adaptation. As a consequence, steeper gradients require higher optimal rates of adaptation. Simulations demonstrate that the observed intercellular variability of adaptation times, which is caused by gene expression noise, may play a positive role for the bacterial population as a whole, by allowing its subpopulations to be optimally tactic in gradients of different strengths. We further show that optimal chemotactic properties in a porous medium (agar) are different from those in a liquid.

rotation. Switching of the motors to the CW state results in a tumble and reorientation, whereas the CCW rotation corresponds to straight runs.

A number of mathematical models of chemotaxis have been proposed [10,12–18], including two recent programs that simulate cell motion along with the intracellular pathway dynamics: AgentCell [19], which is based on the StochSim pathway simulator [20–22], and *E. solo* [23], which is based on the BCT simulator [24–26]. The current version of AgentCell (2.0) simulates the whole pathway stochastically, making it thus computationally very expensive. The *E. solo* program simulates the pathway using about 90 ordinary differential equations (ODEs). However, simulation of large bacterial populations on long time scales requires computationally cheaper models.

It was recently shown using fluorescence resonance energy transfer (FRET) that the amplitude of the initial CheY-P response can be described by a Hill function of a relative change in receptor occupancy during stepwise ligand stimulation [27]. Recent modeling efforts [12,28,29] show that a mixed-cluster Monod-Wyman-Changeux (MWC) model of strongly coupled receptors is consistent with the FRET data, and can account for the observed sensitivity and precise adaptation over a wide range of ligand concentrations. The amplitude of pathway excitation can therefore be determined using several algebraic equations describing the free energy of the cluster.

In our model (Figure 1A), we employed the MWC model for a mixed receptor cluster [12] with a mean-field approximation for adaptation kinetics [30]. Due to its hybrid approach, the model allowed us to reduce the computational costs dramatically, while keeping the main quantitative characteristics of the cell response (methylation level, relative CheY-P concentration, motor bias) consistent with experimental data. To couple the bias of individual motors to the probability of tumbling, we applied a voting model for several independent motors, based on detailed experimental investigation of tumbling mechanics [31].

These components were combined into a new simulator for *E. coli* chemotaxis—RapidCell, which uses a hybrid pathway simulation instead of a fully stochastic or ODE approach, and is therefore computationally cheap. This allows the simulation of populations of 10^4–10^5 cells on a time scale of hours using a desktop computer.

To study the dependence of chemotaxis on gradient strength in a systematic way, we propose a new—constant-activity—gradient which ensures a constant average CheY-P level and cellular drift velocity along the gradient, in contrast to commonly used Gaussian and linear gradients. We show that the MWC model gives an approximately constant response over a wide range of ligand concentrations. Though purely theoretical, such a gradient serves as a perfect *in silico* assay to study the chemotactic properties of cells.

The chemotaxis pathway is robust to changes in network parameters and intracellular protein concentrations [10,15,32]. This enables efficient chemotaxis with varying levels of intracellular components and under perturbations from extracellular environment. However, adaptation time is not robust [10,11,33,34] and varies even among genetically identical cells in a population because of stochastic variations in gene expression and low copy numbers of the adaptation enzymes.

Our simulations predict that in liquid media for any given gradient steepness, there is an optimal adaptation rate that provides the highest cellular drift velocity. We suggest a simple mechanism for this phenomenon: the optimal rate of adaptation is observed in a narrow range of kinase activity, where the average CheY-P level fits the operating range of the flagellar motor. In this range, the relation between CheY-P and motor bias is approximately linear, and cells perform chemotaxis with the highest efficiency.

The situation is different for cells swimming in agar. Here, the optimal range of motor bias appears to be very narrow and just slightly higher than in the non-stimulated state. Due to the porous structure of agar, cells with a higher CCW motor bias stay trapped for a longer time, thus negating advantage in chemotactic efficiency. This leads to a strong selection against cells which adapt slowly and therefore tend to overreact to chemotactic stimulation. On the other hand, chemotaxis in agar poses only a weak selection against cells with a high adaptation rate.

Our simulations suggest that in liquid media the variability in protein levels among cells may be advantageous for bacterial populations on a long time scales. In a nonmixed environment with different food sources and gradient intensities, such variability can help the whole population to respond to different gradients more readily, due to positive selection of subpopulations with optimal levels of adaptation enzymes in a given gradient.

Methods

Model of *E. coli* Signaling Network

MWC model. We applied the recently proposed MWC model for a mixed receptor cluster [12,28,29], which accounts for the observed experimental dose-response curves of adapted cells measured by *in vivo* FRET [27]. An individual receptor homodimer of type r ($r = a$ and s for Tar and Tsr, respectively) is described as a two-state receptor, being either 'on' or 'off'. Receptors form clusters with all receptors in a cluster either 'on' or 'off' together. The clusters are composed of mixtures of Tar and Tsr receptors. At equilibrium, the probability that a cluster will be active is [12]:

$$A = \frac{1}{1+e^{F}} \tag{1}$$

where $F = F^{on} - F^{off}$, and $F^{on/off}$ is the free energy of the cluster to be on/off as a whole. For a cluster composed of n_a Tar and n_s Tsr

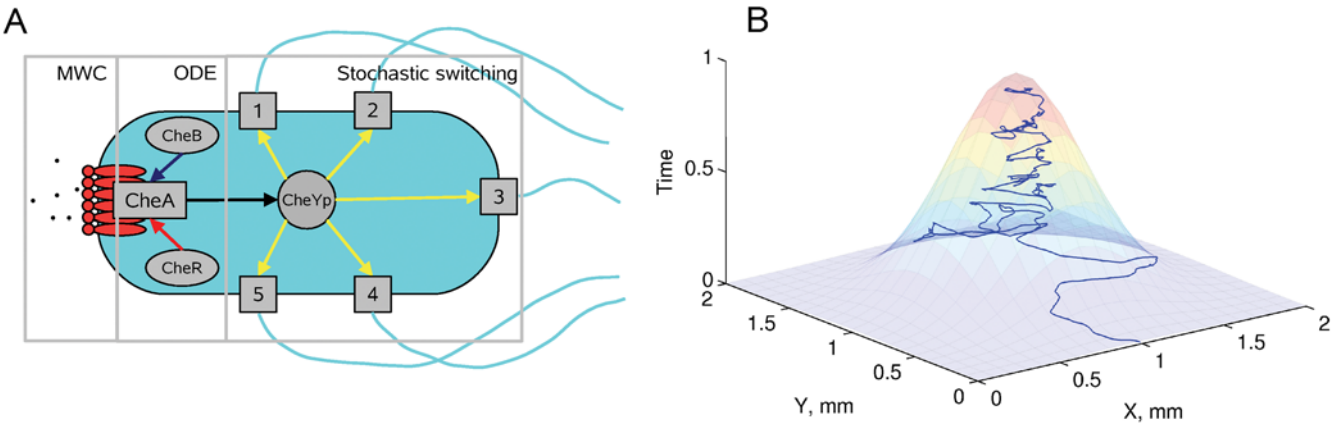

Figure 1. Model of chemotactic *E. coli*. (A) Scheme of the hybrid model. The activity of the receptor cluster depends on the local ligand concentration and the methylation level according to the MWC model. Methylation (red arrow) and demethylation (blue arrow) are performed by CheR and CheB. The phosphate group is transferred from active CheA to the response regulator CheY (black arrow). The concentration of CheY-P modulates the motor bias of 5 independent motors (yellow arrows), and their collective behavior makes the cell run or tumble. Ligand binding, receptors cluster switching, CheY phosphorylation and motor switching are considered to be in rapid equilibrium and are described by algebraic equations, while the methylation and demethylation kinetics are relatively slow and simulated using an ODE. Motor switching is simulated stochastically. (B) The model reproduces the swimming of *E. coli* cells up gradients of attractants, taking into account the effect of rotational diffusion. A typical path of a swimming virtual cell is shown in 2D space, with the relative time course shown along the Z axis, demonstrating how the cell finds the maximum attractant concentration and stays in its vicinity. The attractant concentration profile is overlayed.
doi:10.1371/journal.pcbi.1000242.g001

receptors, the total free-energy difference is, in the mean-field approximation, $F = n_a f_a(m) + n_s f_s(m)$, which is the sum of the individual free-energy differences between the two receptor states

$$f_r(m) = f_r^{on}(m) - f_r^{off} = \varepsilon_r(m) + \log\left(\frac{1+[S]/K_r^{off}}{1+[S]/K_r^{on}}\right) \quad (2)$$

where $[S]$ is the ligand concentration, $K_r^{on/off}$ is the dissociation constant for the ligand in the on and off state, respectively. The methylation state of the receptor enters via the 'offset energy' $\varepsilon_r(m)$.

The model can also be generalized for binding multiple types of ligand [12,28].

Adaptation model. Adaptation is modeled according to the mean-field approximation of the assistance-neighborhood (AN) model [12,30]. Both CheR and CheB are assumed to bind receptors independent of their activity. A bound CheR (CheB) can (de-)methylate any inactive (active) receptor within the AN. Each bound CheR adds methyl groups at a rate $a(1-A)$, and each bound CheB removes methyl groups at a rate bA. Under these assumptions, the kinetics in the AN model are given by

$$\frac{dm}{dt} = a(1-A)[CheR]\frac{[MCP]}{K_R+[MCP]} - bA[CheB]\frac{[MCP]}{K_B+[MCP]} \quad (3)$$

We further assume that both enzymes work at saturation:

$$\frac{dm}{dt} \approx a(1-A)[CheR] - bA[CheB] \quad (4)$$

Note that this equation does not imply a first-order reaction mechanism between the adaptation enzymes and receptors—the enzymes work in the zero-order regime. The linear products $a(1-A)[CheR]$ ($bA[CheB]$) mean that a bound CheR (CheB) can only act if the receptor cluster is inactive (active), with probability $(1-A)$ and A, respectively.

We further define the *relative adaptation rate k*:

$$\frac{dm}{dt} = k(a[CheR](1-A) - b[CheB]A) \equiv kV \quad (5)$$

The parameter k indicates the adaptation rate relative to the wild-type adaptation rate V. In the cells with normal steady-state activity ($A^* = 1/3$), the rates and concentrations of the adaptation enzymes are related through $b[CheB] = 2a[CheR]$. In this work we assume that reaction rates a and b remain unchanged, and the variability in adaptation rate k is caused by variability in [CheR,CheB], provided that they change in a coordinated manner with the fixed ratio: [CheR]/[CheB] = 0.16/0.28 [35]. The latter ODE for methylation is integrated using the Euler method, so that the average methylation level evolves in time as

$$m(t+\Delta t) = m(t) + kV\Delta t \quad (6)$$

To achieve high computational efficiency in the model, we assumed that the average methylation level m is a continuously changing variable within the interval [0,8], with linear interpolation between the key offset energies: $\varepsilon_r(0)$, 1.0; $\varepsilon_r(1)$, 0.5; $\varepsilon_r(2)$, 0.0; $\varepsilon_r(3)$, −0.3; $\varepsilon_r(4)$, −0.6; $\varepsilon_r(5)$, −0.85; $\varepsilon_r(6)$, −1.1; $\varepsilon_r(7)$, −2.0; $\varepsilon_r(8)$, −3.0, according to [12,30].

Kinase activity. CheA kinase activity is assumed to be equal to the activity of the receptor complex (A). The differential equation for CheY-P is [32]

$$\frac{dYp}{dt} = k_Y Ap\left(Y^T - Yp\right) - k_Z YpZ - \gamma_Y Yp \quad (7)$$

Here Yp is [CheY-P], Y^T — total [CheY], Z^T — total [CheZ], Ap — active CheA, and $k_y = 100\ \mu M^{-1}\ s^{-1}$, $k_Z = 30/[CheZ]\ s^{-1}$, $\gamma_Y = 0.1$ are the rate constants according to [32,36,37]. The rate of phosphotransfer from active CheA to CheY is much faster than the rate of CheA autophosphorylation (Table S1). Therefore, the

concentration of CheY-P is obtained as a function of active CheA from the steady-state equation:

$$Yp = \frac{k_Y A p Y^T}{k_Y A p + k_Z Z + \gamma_Y} \quad (8)$$

In relative units, $[\text{CheY-P}] = 3\frac{k_Y k_s A}{k_Y k_s A + k_Z Z + \gamma_Y}$, where $k_s = 0.45$ is a scaling coefficient. The relative [CheY-P] = 0,1,3 correspond to fully inactive, adapted and fully active cluster, respectively. The absolute concentration relates to the relative as $[\text{CheY-P}]_{abs} = 3.1[\text{CheY-P}]$ (μM), following [38].

CheB phosphorylation. To study the effect of kinase-dependent CheB phosphorylation, we assumed that the concentration of phosphorylated (active) CheB follows the steady-state equation [15,32]:

$$[CheB] = [CheB]_{tot}\frac{A}{A + k_{0.5}} \quad (9)$$

where $[CheB]_{tot}$ is the total concentration of CheB (relative), and A is the kinase activity. In the steady state $A^* = \frac{1}{3}$ we assumed that 100%, 50%, or 25% of CheB can be phosphorylated, corresponding to $[CheB]_{tot} = 1,2,4$ and $k_{0.5} = 0, \frac{1}{3}, 1$, respectively. Note that at maximum kinase activity $A = 1$, the active [CheB] increases 1, 1.5 and 2 times compared to [CheR]; at steady state $A = \frac{1}{3}$ both enzymes have equal levels, whereas at positive chemotactic signal $A < \frac{1}{3}$ [CheB] is equal to [CheR] ($k_{0.5} = 0$) or lower than [CheR] ($k_{0.5} = \frac{1}{3}, 1$).

Time-scale separation. We assume that the rates of ligand binding t_l, rates of receptor-cluster conformational changes t_k and receptor covalent modification t_m are well separated in scales: $t_l \ll t_k \ll t_m$. On our scale ($\sim$1 s) the reactions of CheA autophosphorylation, phosphotransfer from CheA to CheY and CheB can be described as a rapid equilibrium state through algebraic equations. The slowest reactions—methylation by CheR and demethylation by CheB—are described through an ODE to reproduce the time scales of seconds and minutes required for adaptation. Table S1 shows the comparative rates of the main reactions.

Model verification. A summary of the parameters used in the model is given in Table 1, and a summary of models and assumptions is shown in Table 2. Along the lines of the MWC model for a mixed receptor cluster [12], we model a cluster of 18 receptors, composed of 6 Tar and 12 Tsr receptors. The catalytic rates a and b were chosen to achieve the proper time scale of adaptation according to *in vivo* FRET dose-response curves.

As shown previously in [12,29,39], the MWC model for a mixed receptor cluster correctly reproduces the *in vivo* FRET response amplitudes to step-wise addition and removal of MeAsp [27,40]. We also compare our model output with the published FRET response (Figure S1A), and show that the simulation is in good agreement with experiment, both for the amplitude and the duration of the chemotactic response. However, the steepness of the adaptation curve after attractant removal can only be roughly described by the existing model of CheB activity, a deficiency which needs to be addressed for more precise modeling in future.

The spatially extended StochSim model gives lower response amplitudes compared to FRET experiments [14]. Comparison of RapidCell and StochSim responses to addition and removal of Asp is shown in Figure S1B. The adaptation rate of StochSim seems very high compared to FRET experiments and RapidCell simulations ($k = 8$ times higher than the wild-type rate), which suggests that RapidCell will be much more sensitive to gradients than AgentCell [19].

RapidCell also reproduces experimental data on tethered cell stimulation with pulse and step changes of Asp concentration [41] (Figure S2A and S2B). The adaptation times after a step increase of α-methylaspartate (MeAsp) concentration over three orders of magnitude agree with experimental data reported in [33] (Figure S2C).

Table 1. Parameters used in RapidCell.

Parameter	Value	Reference
K_a^{on}	12 μM	Tar to Asp [21]
K_a^{off}	1.7 μM	Tar to Asp [21]
$K^*(K_D)$	4.52 μM	Tar to Asp [14], this work
K_s^{on}	10^6 μM	Tsr to (Me-)Asp [12,29,30]
K_s^{off}	100 μM	Tsr to (Me-)Asp [12,29,30]
n_a	6	[12]
n_s	12	[12]
[*CheR*]	0.16 μM	wild-type level [35]
[*CheB*]	0.28 μM	wild-type level [35]
a	0.0625	this work
b	0.0714	this work
$[CheY]_{tot}$	9.7 μM	[35]
A^*	1/3	[12,30]
CCW mb_0	0.65	[38,41]
H	10.3	[38]
v	20 $\mu m\ s^{-1}$	[38]
D_r	0.062 $rad^2\ s^{-1}$	[7,42]
Δt	0.01 s	this work

doi:10.1371/journal.pcbi.1000242.t001

Model of *E. coli* Motion

During a run, the cell is assumed to move with a constant speed $v = 20\ \mu m/s$, while the direction of motion is affected by rotational diffusion [7,42]. After each time step, the running direction is

Table 2. Models used in RapidCell.

Model	Reference
Receptor free energy: $f_r(m) = f_r^{on}(m) - f_r^{off}$ $f_r^{on}(m) = \varepsilon_r(m)$ $f_r^{off} = \log\left(\frac{1+[S]/K_r^{off}}{1+[S]/K_r^{on}}\right)$	[12,28–30]
Cluster free energy, in the mean-field approximation: $F = n_a f_a(m) + n_s f_s(m)$	[12,29]
Cluster activity: $A = \frac{1}{1+e^F}$	[12,28–30]
Rate of receptor methylation, AN-model at saturation: $\frac{dm}{dt} = a(1-A)[CheR] - bA[CheB]$	[12,30]
Steady-state CheY-P concentration: $[\text{CheY-P}] = 3\frac{k_Y k_s A}{k_Y k_s A + k_Z Z + \gamma_Y}$	[32]
CCW motor bias: $mb = (1+(1/mb_0 - 1)(CheYp)^H)^{-1}$	[38,41]

doi:10.1371/journal.pcbi.1000242.t002

changed by adding a stochastic component with normal distribution $N(m,\sigma)=N\left(0,\sqrt{2D_r\Delta t}\right)$ and diffusion coefficient $D_r=0.062\ rad^2\ s^{-1}$ [42].

Motor switching. The relative concentration of the response regulator [CheY-P] is converted into motor bias using a Hill function [38] (Table 2). Motor bias is the mean fraction of CCW rotation time for a motor: $mb=T_{ccw}/(T_{ccw}+T_{cw})$, where T_{ccw} and T_{cw} are the means of exponentially distributed CCW and CW intervals, respectively. The equation

$$\lambda_{forw}=1/T_{ccw}=T_{cw}^{-1}(mb(CheYp))^{-1}-1 \qquad (10)$$

gives the frequency of the Poisson process of CCW→CW motor switching. The frequency of reverse switching CW→CCW is $\lambda_{rev}=1/T_{cw}$. After each time step Δt, the motor can switch its direction from the present state, according to the current switching frequency $\lambda_{forw(rev)}$, with probability $P_{forw(rev)}=\lambda_{forw(rev)}\Delta t$.

Runs and tumbles. Run and tumble events include the complex interplay of filaments in a bundle, the details of which have been investigated experimentally [31,43]. To simulate the run and tumble behavior of a cell with several motors ($N=3$–7) we consider the voting model, where the majority of the motors determines the cellular behavior.

Model of voting motors. The cell has $N=5$ motors switching independently, and the state of the cell is determined according to a voting model [13,31,44]. The cell switches from 'Run' to 'Tumble', if at least 3 of its 5 motors rotate CW, and from 'Tumble' to 'Run', if at least 3 of the 5 rotate CCW. The choice of $N=5$ is arbitrary, and similar results are obtained for $N=3,7$ under the condition of majority voting.

For model validation, simulations of cells with $N=3,5,7$ motors were carried out (Table 3). The simulated run times (1.04–1.11 s) agree with the experimental value of 1.24 ± 1.16 s [45]. The simulated tumble times (0.26–0.44 s) appear higher than the measured 0.14 ± 0.08 s [7,31]. However, the latter study [31] shows that the full tumble time, from bundle breaking in the old run to bundle consolidation in the new is 0.43 ± 0.27 s. This estimate of tumble time reflects not only cell reorientation, but also the interplay of flagella and the resulting drop in cell speed, and the voting model reflects specifically this kind of tumble time estimate. The model with 5 motors is used in the following as default.

Tumbling angle. The tumbling angle is distributed according to the probability density function $f(\Theta)=0.5(1+cos\Theta)sin\Theta$, $0<\Theta<\pi$ [46,47], with $M(\Theta)=67.5^\circ$ which is close to the experimental measurement of 68° [7], and the corresponding shape of the function (Figure S3).

Model of the Environment

The virtual cells are swimming in a 2D environment with a predefined attractant concentration field $S(x, y, t)$. The domain geometry is either rectangular or circular, with reflecting walls. The simulation time was chosen to be short enough to avoid boundary effects. The rectangular domain is within $(0, x_{max})\times(0, y_{max})$, and the circular domain within $(0, r_{max})$, with $x_{max}=y_{max}=2r_{max}=20\ mm$.

Table 3. Simulated run and tumble times for cells with different number of motors. Parameters: $T_{ccw}=1.33$ s, $T_{cw}=0.72$ s, $mb=0.65$, $n=10000$.

N Motors	Voting Threshold	T_{run}	T_{tumble}
3	2	1.11	0.44
5	3	1.09	0.33
7	4	1.04	0.26

doi:10.1371/journal.pcbi.1000242.t003

The constant-activity gradient. The gradients used in chemotaxis modeling are usually linear, Gaussian or exponential [19,23]. However, in these gradients the signal is non-constant, which means it is strong at low attractant concentrations, and weak at high concentrations due to receptors saturation. Such a non-uniform distribution of the signal makes it difficult to estimate chemotactic efficiency over long time intervals—cells soon become 'blind' because receptors are saturated, and chemotactic drift decreases.

According to the MWC model, an increase in ligand concentration ΔS causes an initial rise in receptor free-energy difference

$$\Delta f=log\left(1+\frac{\Delta S}{S+K^{off}}\right)-log\left(1+\frac{\Delta S}{S+K^{on}}\right) \qquad (11)$$

Using the Taylor-series approximation,

$$\Delta f\approx\frac{\Delta S}{S+K^{off}}-\frac{\Delta S}{S+K^{on}} \qquad (12)$$

leads us to the following approximation for free energy per concentration change:

$$\Delta f=\Delta S\frac{K^{on}-K^{off}}{(S+K^{on})(S+K^{off})} \qquad (13)$$

Simplified solution. The denominator in Eqn. 13 can be simplified by assuming

$$(S+K^{on})(S+K^{off})\approx(S+K^*)^2 \qquad (14)$$

and the unknown K^* can be found from equation

$$(S+K^{on})(S+K^{off})=(S+K^*)^2 \qquad (15)$$

$$S^2+SK^{on}+SK^{off}+K^{on}K^{off}=S^2+2SK^*+(K^*)^2 \qquad (16)$$

$$S(K^{on}+K^{off})+K^{on}K^{off}=2SK^*+(K^*)^2. \qquad (17)$$

which gives two alternative estimates for K^*: $K^*=\frac{K^{on}+K^{off}}{2}$ and $K^*=\sqrt{K^{on}K^{off}}$, i.e. the arithmetic and geometric means of K^{on} and K^{off}.

At zero or relatively low ligand concentrations, the geometric mean has a high impact in Eqn. 17, and is preferable as an estimate. Indeed, in earlier work it was earlier referred to as the apparent dissociation constant K_D of ligand binding [14]. However, at high concentrations, the arithmetic mean will have a higher impact in Eqn. 17, so it can be used as an alternative estimate. Our simulations indicate that within four orders of aspartate concentration the geometric mean serves as the best estimate of K^* (Figure S4).

Taken together, the energy difference is approximated by $\Delta S\frac{K^{on}-K^{off}}{(S+K^*)^2}$. The differential equation

$$\frac{S'\left(K^{on}-K^{off}\right)}{(K_D+S)^2}=C \tag{18}$$

describes the unknown function $S(x)$, which will give the 'constant-activity' gradient shape. The function $S(x)$ will give a constant change of energy difference C per length unit dx of cellular path along the gradient. In other words, such a shape of gradient will give a constant cluster activity at any ligand concentration.

Within the accuracy of a constant term, the latter differential equation was previously used by Block and Berg in [48], who derived it assuming that receptor occupancy is proportional to $S/(S+K_D)$, with a single K_D for active and inactive receptors. The authors assumed that the chemotactic response is proportional to the change in receptor occupancy [27,48]. They simplified this equation to reduce the variability of the $\frac{1}{(K_D+S)^2}$ term, leading to the exponential form of the solution.

However, we can solve Eqn. 18 analytically:

$$S(x)=\left(K^{on}-K^{off}\right)\left(\frac{1}{C(C_1-x)}\right)-K^* \tag{19}$$

where $C_1=\frac{\left(K^{on}-K^{off}\right)}{C(S(0)-K^*)}$ is the constant of integration, determined by the initial condition $S(0)$. The condition $S(0)=0$ gives the following chemoattractant function:

$$S(x)=K^*\frac{Cx}{\frac{K^{on}-K^{off}}{K^*}-Cx} \tag{20}$$

Constant-activity gradient of Asp. In the case of aspartate ($K^{on}=12$, $K^{off}=1.7$, $K^*=4.52\ \mu M$), the $S(x)$ function reads:

$$S(x)=K^*\frac{Cx}{2.28-Cx} \tag{21}$$

Our simulations demonstrate that this form of constant-activity Asp gradient gives a constant cluster-activity response with reasonably good precision (see Results).

Gradient steepness. A cell swimming with speed v along the axis X from the point ($x=0$) senses the monotonically increasing function $S(x)$ and a constant change in receptor free energy

$$dE/dt=Cdx/dt=Cv \tag{22}$$

per second, which is defined as the *steepness* of the constant-activity gradient.

Limiting condition. Note the necessary condition ($\frac{K^{on}-K^{off}}{K^*}-Cx>0$) for Eqn. 20 to avoid singularity and negative concentrations. It sets the upper limit $C<C_{max}=\frac{K^{on}-K^{off}}{K^*}\frac{1}{x_{max}}$ for the gradient steepness C within the domain $(0,\ x_{max})$. For example, within a domain of size $x_{max}=10\ mm$, the maximum steepness of a gradient of aspartate is $Cv=2.28/x_{max}v=4.56\times10^{-3}$.

Constant-activity and exponential ramps. In contrast to spatial gradients, which direct the cellular motility in a certain direction, time ramps are used to study the chemotactic response of tethered cells [41,48].

The constant-activity ramp of Asp was simulated according to Eqn. 20:

$$S(t)=K^*\frac{Ct}{\frac{K^{on}-K^{off}}{K^*}-Ct},\ C=\frac{K^{on}-K^{off}}{K^*}\cdot0.9999/T_{max} \tag{23}$$

with simulation time $T_{max}=1000$ seconds. The resulting value of C gives the maximum ligand concentration $S(T_{max})=9999K^*$.

The exponential ramp was simulated as:

$$S_e(t)=0.31K_D\exp(0.005(t-200)),(t\geq200) \tag{24}$$

after 200 s of adaptation to the initial stimulus $0.31K_D$, following the model and experiments of [48]. The concentration profiles are shown in Figure 2A.

Constant-activity gradient simulations. The constant-activity gradient (Eqn. 20) has an intensity $C=\frac{K^{on}-K^{off}}{K^*}\frac{0.999}{x_{max}}$, and the domain has a rectangular $(0,\ x_{max})\times(0,\ y_{max})$ or circular $(0,\ r_{max})$ shape. The gradient has its minimum $S=0$ at $x=0$ (or $r=0$) and reaches its maximum $S=999K^*$ at $x=x_{max}$ (or $r=r_{max}$) (Figure 3A). In most simulations we used the circular gradient $S(r)$, and the cells start swimming in random directions from the center $r=0$.

Comparative set of constant-activity gradients (N1, N2, N3). The circular constant-activity gradient ($r_{max}=10\ mm$) has steepness $dE/dt=Cv=4.56\times10^{-3}$. A set of other constant-activity gradients was obtained by changing the steepness by a factor of two: $(1.14,\ 2.28,\ 4.56,\ 9.11,\ 18.22,\ 36.44,\ 72.88)\times10^{-3}$. We further compare the chemotactic efficiency in three of them with moderate steepness $(2.28,\ 4.56,\ 9.11)\times10^{-3}$, and designate them as constant-activity gradients N1, N2 and N3. In other words, they are radially symmetric and have the form

$$S(r)=K^*\frac{Cr}{\frac{K^{on}-K^{off}}{K^*}-Cr},\ C=\frac{K^{on}-K^{off}}{K^*}\cdot\frac{0.999}{r_{max}} \tag{25}$$

with $r_{max}=20,10,5$ mm for N1, N2 and N3, respectively.

Linear gradient. We use a linear gradient $S(x)=Kx$, $x\in(0,10\ \text{mm})$ with coefficient $K=10^{-8}\ M\ \mu m^{-1}=10^{-2}\ mM\ mm^{-1}$ (Figure 3A).

Gaussian gradient. Another form of gradient we used is Gaussian $S(x)=10K\exp(-(x-10)^2/(2\sigma^2))$, with shape parameter $\sigma=3.33$ and the same coefficient $K=10^{-2}\ mM\ mm^{-1}$ (Figure 3A).

Chemotactic efficiency. Chemotactic efficiency was estimated as the average drift velocity of a cell population, measured between 200 and 500 s of simulation time, in the three basic constant-activity gradients N1, N2, N3. As shown in Figure 4, within this interval the average CheY-P level of cells is constant, and the drift velocity can be accurately measured by a linear fit.

Population behavior. The population behavior in the absence of attractant fits the diffusion equation $\langle r^2\rangle=4Dt$. Simulations give a diffusion coefficient $D=2.56\times10^{-6}\ cm^2\ s^{-1}$, in agreement with the experimental $D=2.5\text{–}3.8\times10^{-6}\ cm^2\ s^{-1}$ (see [45] and the review of other published values therein).

Program RapidCell

The output file of the RapidCell program contains the key characteristics of the intracellular state (CheY-P level, methylation state, motor bias) and the geometric characteristics of cell motion (position and orientation). The model was implemented using Java classes similar to AgentCell [19], but with simplified architecture. The algorithm is implemented as a discrete-time Monte Carlo scheme with time step $\Delta t=0.01\ s$. For random-number generation, we used external Java libraries [49,50]. The code was written

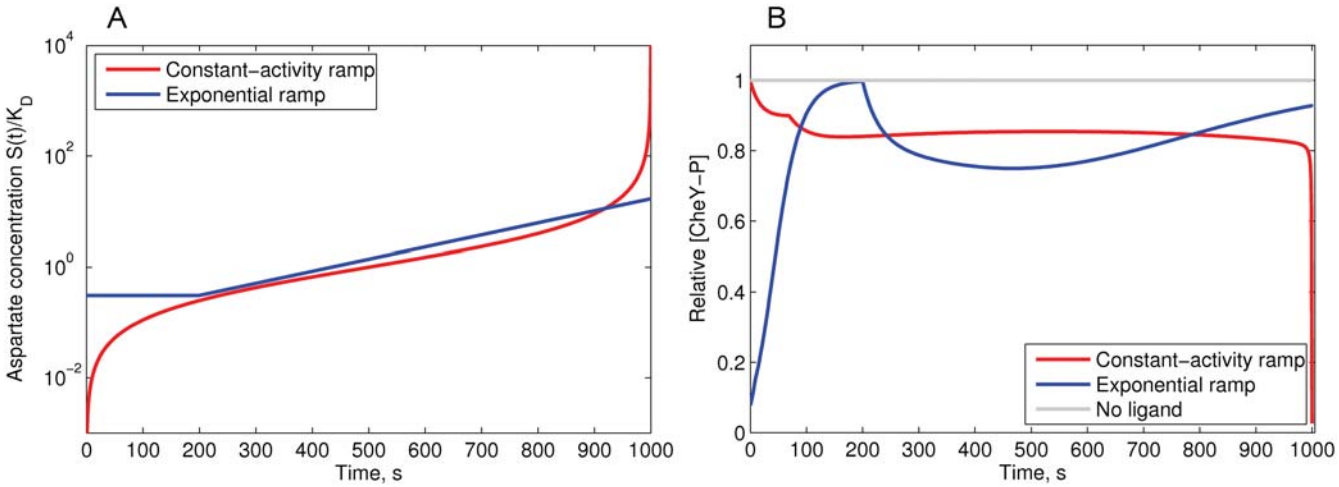

Figure 2. Simulation of the MWC model response to the constant-activity and exponential ramps of aspartate. (A) The concentration profiles of constant-activity and exponential ramps of aspartate, relative to $K_D = 4.52\ \mu M$ (logarithmic scale). (B) The response of the MWC model to the applied constant-activity and exponential ramps. Upon stimulation with the constant-activity ramp, the [CheY-P] rapidly goes down during initial excitation—the single non-smooth point on the slope is the result of the piece-wise linearity of the methylation energy function. The constant-activity ramp produces a long flat response up to a concentration of $100K_D$, above which Tsr receptors become sensitive to the ligand and the cluster activity falls. Upon stimulation with the exponential ramp, the cell initially adapts to the minimum concentration $C_{min} = 0.31K_D$, and after 200 s the exponential ramp begins. After 700 s, adaptation overcomes excitation and [CheY-P] slowly returns to the steady state. Relative adaptation rate $k = 1$.
doi:10.1371/journal.pcbi.1000242.g002

using Eclipse SDK (www.eclipse.org). The output data were analyzed with MATLAB (The MathWorks, MA).

Computational costs. Extensive computations of the chemotaxis signaling pathway are avoided in RapidCell due to the hybrid description of the signaling network. This leads to a dramatic drop in computational costs. For example, simulation of 1000 s long walk of a single cell in a ligand gradient takes only 1 s to run in RapidCell, compared to 133 minutes for AgentCell (based on StochSim without receptor coupling), while the spatially extended version of StochSim requires several days on the same hardware (Intel Pentium 4 CPU 2.40 GHz, RAM 1 GB, OS Linux Suse 10.2). Simulation of 1000 s long series of step responses with the BCT program—the core simulator of *E. solo*—takes 100 s under similar conditions (PowerPC G5, 1.8 GHz, RAM 1 GB, MacOS X).

RapidCell is platform-independent and runs as a console application. Its implementation provides a computational speedup of 8000 times compared to AgentCell (based on StochSim without receptor coupling), and approximately 100 times compared to BCT. It enables simulations of up to 100,000 cells to be completed within a time frame of hours using a desktop computer with comparable CPU power and RAM to those mentioned above.

Experimental Methods

Strains and plasmids. *E.coli* strain RP2867 (*tap cheR cheB*) is a derivative of RP437 [51]. Plasmid pVS571 encodes *cheR* and *cheB-eyfp* as parts of one operon under control of a *pBAD* promoter and native ribosome binding sites. The insert *cheR cheB-eyfp* was recloned with *Sac*I and *Xba*I from the plasmid pVS145 which was constructed by cloning a PCR-amplified fragment containing *cheR* upstream of *cheB-eyfp* in the pVS138 plasmid [52] using a *Sac*I site introduced by the upstream PCR primer and a *Hin*dIII site in *cheB*.

Swarm experiments in soft agar plates. Tryptone-broth (TB; 1% tryptone, 0.5% NaCl) soft agar plates were prepared by supplementing TB with 0.27% agar (Applichem), 34 $\mu g\ ml^{-1}$ chloramphenicol, and indicated concentrations of arabinose. Cells

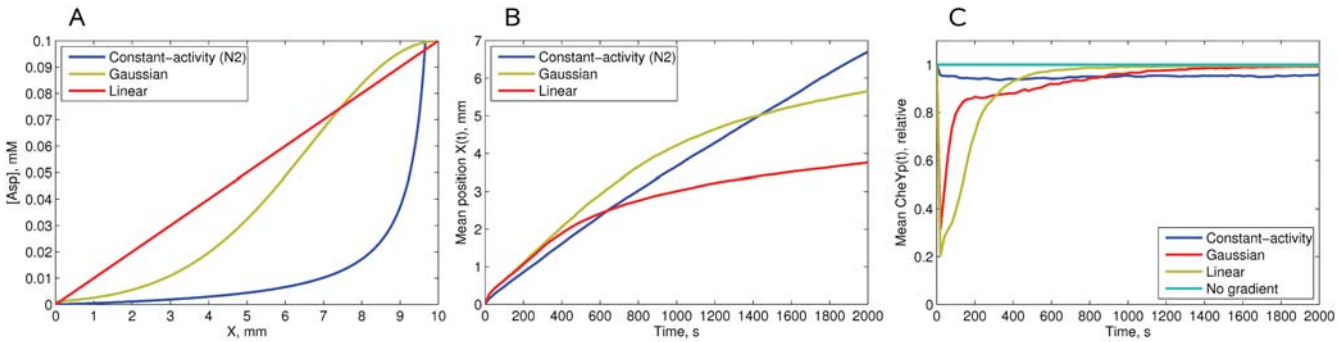

Figure 3. Simulations of chemotaxis in different gradients. (A) Concentration profiles of the gradients used in the simulations. (B) Chemotactic drift of cells in these gradients. The average position $\langle X \rangle$ of the cells is shown as a function of time. A population of 2000 cells starts moving from the left wall ($x_0 = 10\ \mu m$, y_0 randomly distributed in $(0, y_{max})$), and swims for 2000 s. (C) Relative CheY-P concentration as a function of time, averaged over 2000 cells in the same gradients. The gray line indicates the fully adapted state [CheY-P] = 1.0 in a medium without attractant. Relative adaptation rate $k = 1$. All cellular parameters are as described in Table 1.
doi:10.1371/journal.pcbi.1000242.g003

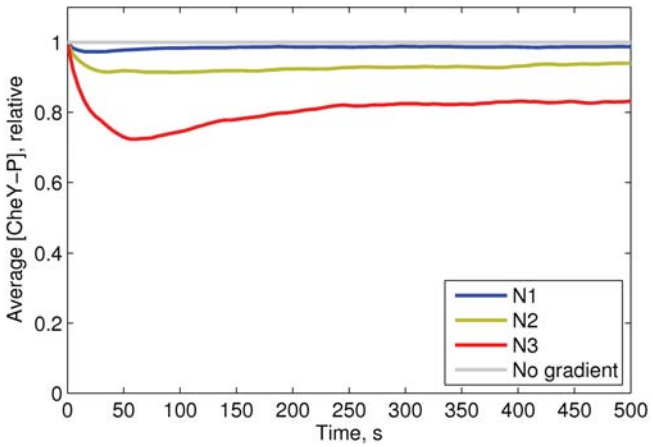

Figure 4. Average CheY-P levels of 5000 cells swimming in the constant-activity gradients N1 (blue), N2 (green) and N3 (red). Relative adaptation rate $k = 1$. The cell parameters are as described in Table 1.
doi:10.1371/journal.pcbi.1000242.g004

were inoculated from fresh colonies grown on LB agar plates. Swarm assays were performed at 34°C for 10 hours or at 30°C for 17 hours. Following incubation, photographs of plates were taken using a Canon EOS 300 D camera, and subsequently analyzed with ImageJ (Wayne Rasband, NIH) to determine the diameter of the swarm rings.

Quantification of gene expression. For quantification of mean expression levels of the fluorescent reporter protein CheB-YFP, cells were grown in liquid TB medium supplemented with 34 $\mu g\ ml^{-1}$ chloramphenicol, and indicated concentrations of arabinose. Fluorescence was determined in a population of cells using flow cytometry on a FACScan (BD Biosciences) equipped with a 488 nm argon laser [32,52]. The autofluorescence background was measured for control cells and subtracted from all values. Single-cell levels of fluorescent reporter proteins in swarm assays were measured by fluorescence imaging on a Zeiss AxioImager microscope and quantified with an automated custom-written ImageJ plugin [52].

To calibrate the fluorescence intensity in FACS and imaging data, a PerkinElmer LS55 luminescence spectrometer was used to determine the absolute number of reporter proteins in control cells. The cells were sonicated with a Branson Sonifier 450 until complete lysis was achieved and YFP fluorescence was measured at 510 nm excitation and 560 nm emission. Sonicated cells without a fluorescence reporter were used as a negative control, and their autofluorescence was subtracted from all values as background. A solution of purified YFP of known concentration, determined by Bradford assay and absorbance measurement by a Specord205 spectrophotometer (Analytik Jena), was used to produce a calibration curve, relating fluorescence to molecule number. Cell number in 1 ml culture was counted using a Neubauer counting chamber, and cell volume was determined by measuring cell width and length by imaging. These values from one culture were used to provide a conversion factor from FACS or imaging values to single-cell protein levels.

Results

Chemotaxis in Different Gradients

To test our model (Figure 1A), we compared cellular behavior in the proposed universal constant-activity gradient with other gradients, observing the single cell swimming (Figure 1B) and the behavior of large populations. The key characteristics we consider are the CheY-P concentration and the drift velocity along the gradient.

Response of the MWC model to ramps. It was previously shown that tethered cells respond with constant strength to an exponentially rising gradient of MeAsp, in the range between 0.31 and $3.2K_D$ [48]. We simulated the response of the MWC model to increasing ramps of Asp in the exponential and constant-activity form (Figure 2A). Indeed, the exponential ramp gives nearly constant response between 0.5 and $3.0K^*$, consistent with the model of [48].

However, the constant-activity ramp results in a chemotactic response that remains approximately constant over three orders of ligand concentration—between 0.1 and $100K_D$ (Figure 2B). If Tsr is non-sensitive to the ligand, constant activity remains up to $1000K_D$. However, since Tsr receptors are able to respond to aspartate non-specifically, the activity drops to zero, as previously shown for a mixed-receptor cluster [12,27].

Chemotactic efficiency of cell populations in different gradients. To study chemotactic efficiency in common gradients that arise from general diffusion models, we simulated chemotactic motility in linear and Gaussian gradients (Figure 3A), and compared them with the constant-activity gradient. The chemotactic efficiency was estimated by the average drift velocities of populations consisting of 1000 identical cells. In Figure 3B, one can see that in the linear and Gaussian gradients the drift velocity decays after about 400 and 800 s, respectively, indicating that cells loose sensitivity due to receptor saturation. In contrast, the constant-activity gradient keeps the drift velocity constant at any point (Figure 3B), as expected.

This population behavior can be explained by the intracellular CheY-P levels of the cells in these gradients. Gaussian and linear gradients result in a strong excitation at low attractant concentrations, and poor excitation at high concentrations (Figure 3B). In contrast, the constant-activity gradient produces an approximately constant level of CheY phosphorylation across the cell population (Figure 3C). These two unique properties of the constant-activity gradient—constant drift velocity and constant average CheY-P—favor this gradient as a reliable *in silico* assay to study the chemotactic motility of cells.

Average CheY-P level in the constant-activity gradients. Simulation of cell populations in the constant-activity gradients N1, N2 and N3 demonstrate that the average CheY-P level depends on gradient steepness and remains stable

over long time intervals (Figure 4). These three gradients were used further, as default, to measure chemotactic efficiency under different test conditions.

Optimal Adaptation Rates in a Liquid Medium

We used the constant-activity gradient to study the effect of adaptation rate on chemotactic efficiency. For this purpose, we simulated homogeneous populations consisting of cells with the same adaptation rate. In a fixed constant-activity gradient, the population drift velocity depends on adaptation rate in a unimodal manner (Figure 5A). A zero level of adaptation enzymes (non-adapting cells) results in a low drift velocity, though it is clearly distinguishable from non-chemotactic behavior. A proportional increase of adaptation rate improves cellular drift velocity up to a certain maximum, after which it slowly declines again. Extremely high adaptation rates, more than 100 times higher than wild-type, make the cells non-chemotactic (Figure 5A).

To study chemotactic efficiency as a function of gradient steepness, cells were simulated in six constant-activity gradients with the steepness changing 64-fold, from 1.14 to 72.88×10^{-3}, (Figure 5B). In each gradient, we determined the optimal adaptation rate, at which cellular drift velocity reaches its maximum. The simulated drift velocities are in the same range as those measured experimentally for *E. coli* in steep gradients ($7\ \mu m\ s^{-1}$) [53]. Our simulations indicate that experimental cell-drift velocities are inlikely to exceed $15\ \mu m\ s^{-1}$, corresponding to an extremely steep and short-scale gradient. In very weak gradients, the drift velocity can be as low as $2.5\ \mu m\ s^{-1}$, still distinguishable from the non-chemotactic cellular drift ($0.8\ \mu m\ s^{-1}$). Interestingly, we observed that the optimal adaptation rate rises in proportion with the gradient steepness (Figure 5B).

To investigate the latter effect in more detail, we varied the adaptation rate from 0 to 10-fold relative to the wild-type. In steeper gradients, the optimal adaptation rate is indeed higher (Figure 6A), and the peak of the drift velocity becomes less sharp. To find the reason for the observed dependence between the gradient steepness and optimal adaptation rate, we tracked the average CheY phosphorylation levels of the virtual cells. As one can see in Figure 6A and 6B, in all gradients the 90%-intervals around the velocity peaks correspond to adaptation rate intervals [0.1,0.5], [0.4,1.5], [1,3], respectively. These three intervals fall into to the same interval [0.80≤CheY-P≤0.97], within the error of estimation. The optimal adaptation rates which give maximal drift velocities correspond to an average [CheY-P]~0.9. In steep gradients, the profile of average CheY-P flattens, and the optimal adaptation rate becomes higher (Figure 6B).

The reason why the interval [0.80≤CheY-P≤0.97] corresponds to optimal chemotaxis is evident from the profile of motor bias as a function of CheY-P (Figure 6C). The interval [0.80≤CheY-P≤0.97] corresponds to the operating range of the motor [$0.95\geq mb\geq0.72$], where the dependence between *mb* and CheY-P is approximately linear. In this interval, chemotactic behavior is most efficient in liquid media. The optimal adaptation rate therefore sets the CheY-P level to fit the motor operating range. In steep gradients, the adaptation rate must be high enough to balance the strong excitation and set CheY-P within this optimal interval. In shallow gradients, adaptation must be slow enough to allow excitation, otherwise the cells become adapted before they are able to respond.

Effect of [CheR] to [CheB] Ratio on Chemotactic Efficiency

The effect of varying the [CheR] to [CheB] ratio was studied at fixed [CheB] in three constant-activity gradients N1, N2, and N3 in a liquid medium. The chemotactic efficiency dramatically decreases above [*CheR*] = 1 (Figure 7), because the resulting higher steady-state CheY-P level produces tumbling behavior. Below [*CheR*] = 1, chemotactic efficiency decreases slowly for N3, or goes up for the N1 and N2 gradients. The latter effect is caused by a shift of average CheY-P level to the optimal interval, where the chemotactic sensitivity is the highest due to a more optimal fit to the motor operating range.

Effect of CheB Phosphorylation on Chemotactic Efficiency

We have further studied the effect of CheB phosphorylation feedback on chemotactic efficiency in a liquid medium. Under the

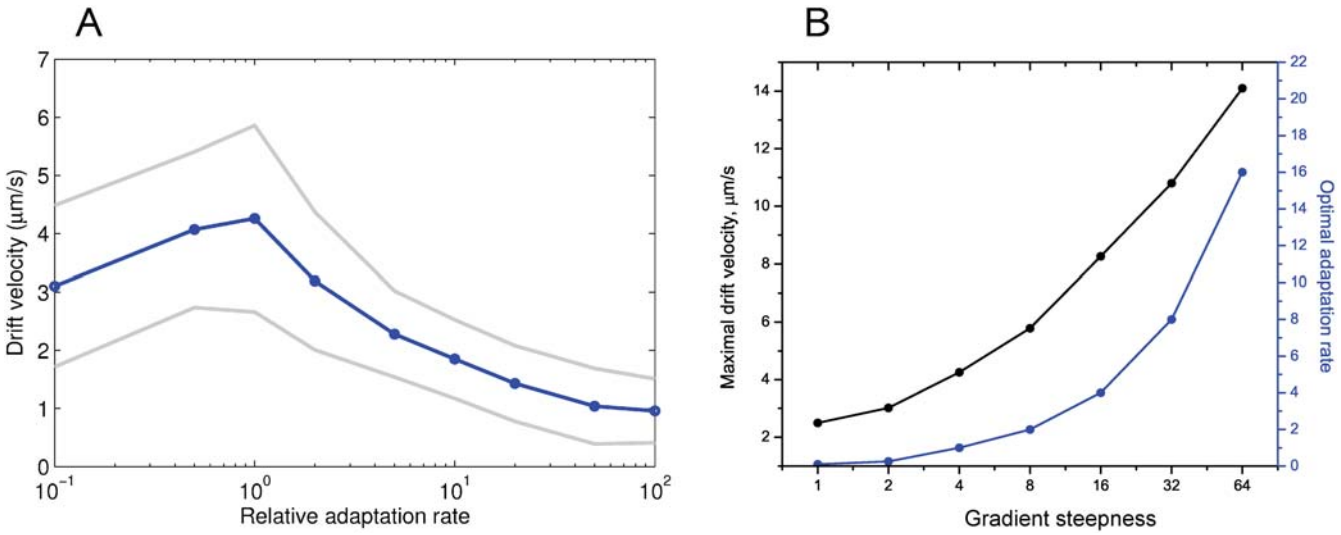

Figure 5. Chemotactic properties of cells at different adaptation rates in constant-activity gradients. (A) Drift velocity of cells in the constant-activity gradient N2 as a function of adaptation rate. The horizontal axis shows the adaptation rate *k* relative to the wild type (logarithmic scale). Gray lines show standard deviations. (B) Maximal drift velocities (black) and the corresponding optimal adaptation rates (blue) as a function of gradient steepness. The steepness of the constant-activity gradients was changed over a 64-fold range, as described in the section 'Model of the environment'.

doi:10.1371/journal.pcbi.1000242.g005

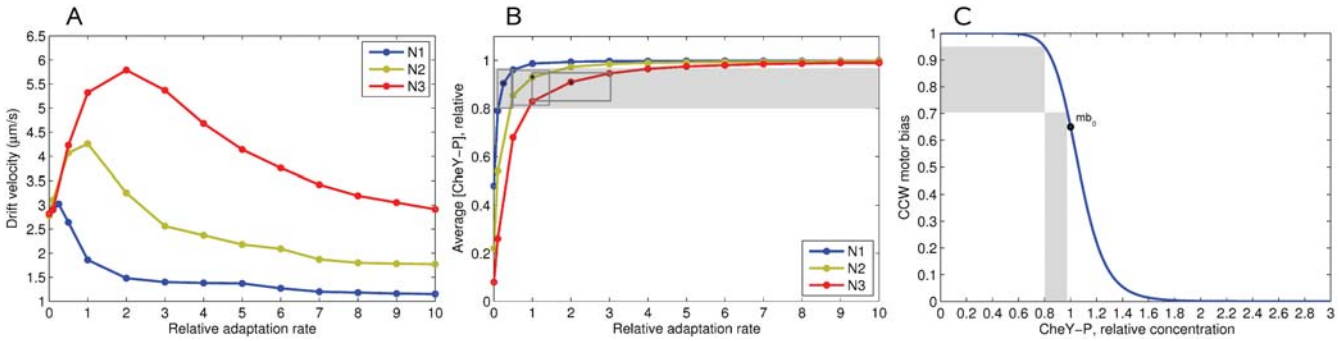

Figure 6. Optimal chemotactic behavior at different adaptation rates. (A) Drift velocities of cells as a function of adaptation rate, in the constant-activity gradients N1 (blue), N2 (green), N3 (red). For each adaptation rate, the drift velocity was estimated from the simulation of 1000 cells, with standard error of mean 0.05. (B) Average CheY-P levels of cells in the same simulations. Black dots indicate the adaptation rate at which drift velocity is maximal. Gray rectangles show the intervals of optimal adaptation rates, defined by taking the 90%-interval from the drift velocity maximum. The width of each rectangle indicates the optimal adaptation-rate interval, and height shows the corresponding CheY-P interval. All three intervals of adaptation rates fall into the same CheY-P interval: [0.80,0.97], shown by the gray band. (C) The CCW motor bias as a function of CheY-P. Gray bands indicate the optimal CheY-P interval and the corresponding operating range of the motor. The cell parameters are as described in Table 1.
doi:10.1371/journal.pcbi.1000242.g006

assumption that [CheR] and [CheB] perfectly match each other ($A^* = 1/3$), the CheBp-effect is positive when the adaptation rate is lower than the optimum, and negative when the adaptation rate is higher, in the given gradient (Figure 8A). This effect is caused by the reduction of CheB activity relative to CheR, when the kinase activity A is below the steady-state level ($A^* = 1/3$), as described in the section 'Model of *E. coli* Signaling Network'. The average CheY-P level is thus shifted up, which results in a positive or negative effect of CheB phosphorylation, depending on the rate of adaptation (Figure 8B).

The positive role of phosphorylation can be significantly increased when the ratio of [CheR] to [CheB] is non-perfect (Figure 8C). For example, 25%-active CheB can significantly counteract the strong negative effect of [CheR] = 1.25 in the N3 gradient—the drift velocity rises from 1.8 to 2.8 $\mu m\ s^{-1}$ (55%). At [CheR] = 0.75 the effect is not so dramatic, but remains significant—the average drift velocities increase by about 10–15% in all three gradients. This suggests that CheB phosphorylation helps to maintain chemotaxis at fluctuating concentrations of CheR and CheB, when their ratio is not perfect due to gene-expression noise.

Swarm Plate Simulations

In the swarm assay in soft agar, bacteria consume an attractant, thereby creating a local gradient, and follow it in the form of a growing ring [54,55]. We assume that the intensity of the moving gradient remains constant, and use the constant-activity gradient as a simple model for the swarm assay simulation. The constant-activity gradient provides a constant cellular-drift velocity at any distance from the center of the plate. This property allows us to use it as a stationary model of the real moving gradient of attractant.

In swarm assays, bacteria move in a labyrinth of agar filaments, with obstacles and traps along the cell's path. The cell can encounter traps during its run, and stays trapped until it makes the next tumble, as observed by Wolfe and Berg [55]. Therefore, non-adapting cells and non-tumbling mutants form the smallest rings. To simulate motility in such a porous medium as agar, we have introduced a new state of the cell, corresponding to a stop in a trap

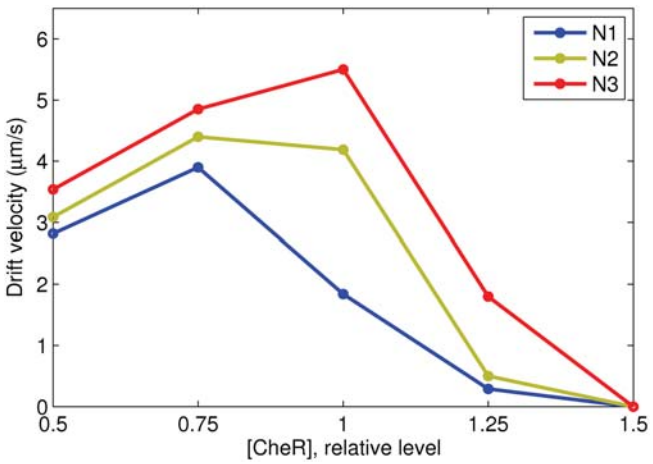

Figure 7. Effect of variable [CheR] on chemotactic efficiency. The vertical axis shows drift velocities. The level of [CheB] is fixed at the wild-type value (0.28 μM), while [CheR] is varied relative to wild type (0.16 μM). Note the steep fall in the drift velocities for [*CheR*]>1, where the steady-state CheY-P produces tumbling behavior.
doi:10.1371/journal.pcbi.1000242.g007

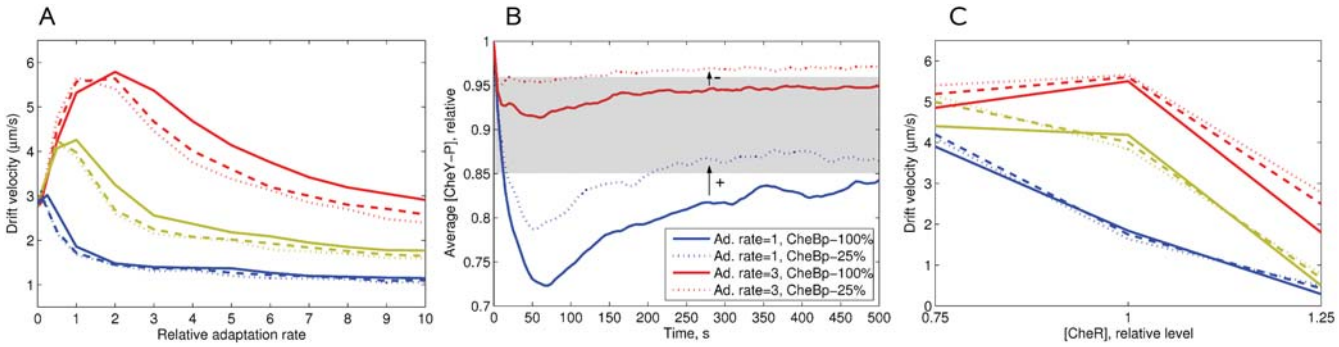

Figure 8. Effect of CheB phosphorylation on chemotactic efficiency in a liquid medium. (A) Drift velocity as a function of adaptation rate in the constant-activity gradients N1 (blue), N2 (green), N3 (red). The ratio of [CheR] to [CheB] at steady state is left as in the wild type (0.16/0.28), ensuring the steady-state activity $A^* = 1/3$ in all cases. Solid lines correspond to cells with 100%-active CheB at steady state, dashed lines - 50%-active, finely dashed - 25%-active CheB. (B) The average [CheY-P] resulting from the balance between CheR and CheB activity determines the positive or negative role of CheB phosphorylation. Cells are simulated in the gradient N3, at adaptation rates of 1.0 and 3.0. Kinase-dependent CheB activity means that CheB works more weakly at $A<1/3$, and thus the average [CheY-P] is higher than the level obtained for constantly active CheB. Such a shift improves chemotaxis at low adaptation rates, but reduces it at high rates. The optimal range of CheY-P is shown by the gray band. (C) Drift velocities at variable [CheR] and variable CheB activity and fixed [CheB] (0.28 μM, wild type). Solid, dashed and finely dashed lines indicate 100%, 50% and 25% active CheB, respectively. Adaptation rate $k = 1$, other cell parameters as described in Table 1.
doi:10.1371/journal.pcbi.1000242.g008

during a run (Figure 9). The positions of traps are not fixed in space. Instead, it is assumed that each cell encounters traps in an exponentially distributed time series, which mimics the random collisions of the cell with agar filaments. The mean free time between traps is set to 2.0 s to achieve biologically realistic drift velocities (about 1 $\mu m\ s^{-1}$). While it is trapped, the cell remains stationary until it makes a tumble, whereupon normal run and tumble behavior resumes until the next stop occures [55].

Optimal [CheR,CheB] in Agar—Experiments and Simulations

In our model, we assumed that the levels of the adaptation enzymes CheR and CheB vary in a coordinated manner, leaving the [CheR]/[CheB] ratio the same as in the wild type. The ratio of CheR to CheB can be assumed to remain largely fixed because their genes are adjacent and transcriptionally coupled in the *meche* operon. The adaptation rate in our model is thus proportional to the level of co-expression of CheR and CheB, which will be further denoted as [CheR,CheB].

In order to study chemotactic efficiency at different adaptation rates in agar, we have experimentally measured chemotactic efficiency on swarm plates. In these experiments, CheR and CheB-YFP were co-expressed from one operon under control of a pBAD promoter and native ribosome-binding sites. The pBAD promoter gives expression levels lower or higher than the wild-type value, depending on the strength of arabinose induction. Mean protein levels in the population at a given induction were determined as described in Experimental Methods.

Experiment and simulations show that cells with [CheR,CheB] above a certain threshold perform chemotaxis equally efficiently (Figure 10A and 10B). However, the cells with [CheR,CheB] below the threshold have severely impaired chemotactic behavior. According to the simulations, cells with low [CheR,CheB] tend to run without tumbling and stay trapped most of the time. On the other hand, cells with extremely high [CheR,CheB] loose their sensitivity to the gradient and also have poor chemotactic efficiency (Figure S5).

This suggests a positive selection for cells with optimal [CheR,CheB] in liquid media—such cells can reach the nutrient source faster and have more available substrates for growth. In contrast, swimming in agar poses mainly negative selection—cells with low [CheR,CheB] are filtered out from the chemotactic population. The limits of motor bias for optimal chemotaxis in agar are also different from those in liquid media. As one can see in Figure 10C, the average CCW motor bias of successful cells is just slightly higher than the steady-state mb_0. Cells with higher motor bias would drift faster in liquid media, but not in agar, because the period of time they remain trapped also increases with CCW motor bias.

Swimming in a Liquid Medium and Agar with a Log-Normal Distribution of [CheR,CheB]

To model swarm assays more realistically, we simulated cell populations with a log-normal distribution of [CheR,CheB] values. The mean (1.6) and standard deviation (0.48) are fitted to reproduce the variability of adaptation times observed for wild-type cells [33]: $T_{ad} = 311 \pm 150$ s in response to a $0–10^{-3}$ M MeAsp step.

The scatter plot of distances travelled by cells along the gradient N2 in a liquid medium shows that a subpopulation with optimal [CheR,CheB] levels drifts more rapidly than other cells (Figure 11A). Simulations in the N3 gradient in agar show that cells with low [CheR,CheB] levels are hindered by agar traps, while other cells drift successfully (Figure 11B). In Figure 11C and 11D the same cells are colored from deep blue to red, according to their [CheR,CheB]. The outer edge of the bacterial ring in a liquid medium contains many blue cells with [CheR,CheB] between 0.5 and 2. In contrast, the outer edge in the agar contains a uniform mixture of cells with different [CheR,CheB] levels, while deep blue cells with low [CheR,CheB] tend to be left behind.

Measurement of [CheR,CheB] in Individual Cells in Different Parts of Swarm Rings

To confirm that chemotactic cells are selected for their [CheR,CheB] levels in swarm plates, cells expressing CheR and CheB-YFP from one operon were taken from two positions in the swarm ring—at the center and at the outer edge—and protein levels in individual cells were determined using fluorescence imaging. The cells collected near the center at a standard agar concentration (0.27%) have on average lower copy numbers of adaptation enzymes than cells at the outer edge, confirming the

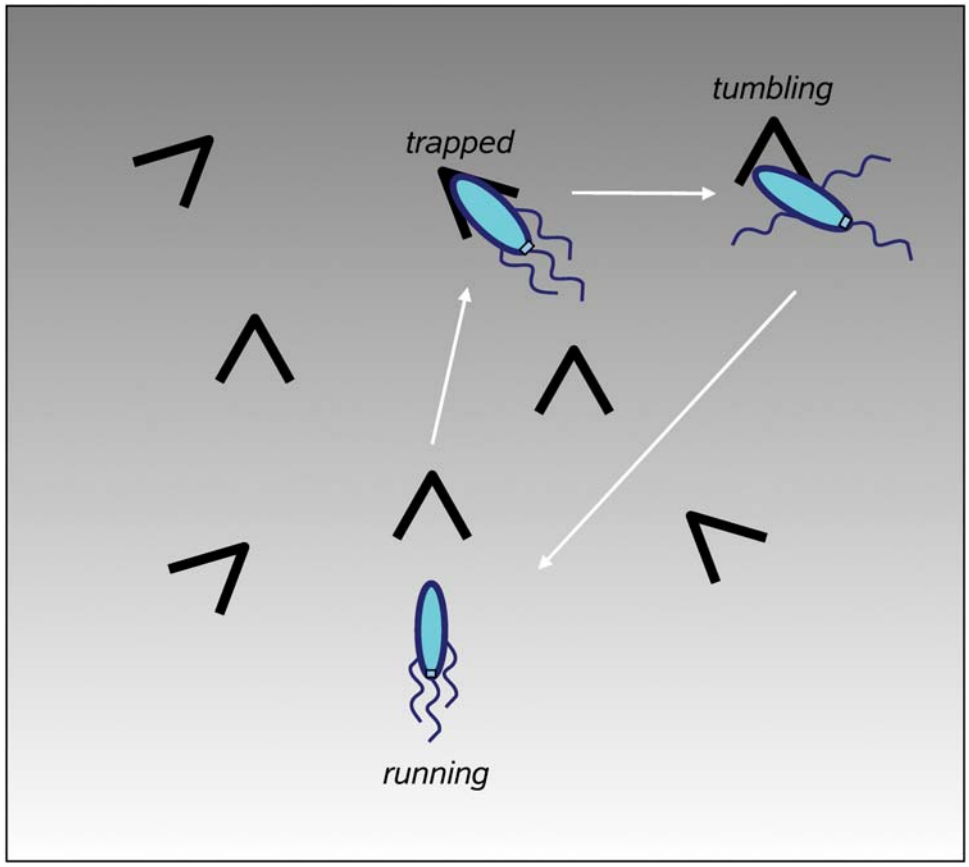

Figure 9. Model of motility in a porous medium (agar). A cell encounters traps along its run, and stops in the traps. It stays in the trapped state until the first tumble occurs, then normal run and tumble behavior resumes. The trap positions are not fixed in the 2D space - instead, it is assumed that each cell encounters traps in a series of randomly distributed time intervals.
doi:10.1371/journal.pcbi.1000242.g009

predicted selection against low copy numbers (Figure 12A). As expected, in the swarm plates with a reduced agar concentration (0.20%), the difference between center and outer edge is much smaller (Figure 12B), suggesting that there is no strong selection against low copy numbers in liquid media. It should be noted that agar concentrations below 0.20% do not produce a stable gel structure, and therefore that is probably the most liquid agar that can be used for swarm plate experiments.

Our simulations and additional experiments with a pTrc promoter, which gives much higher basal expression level of

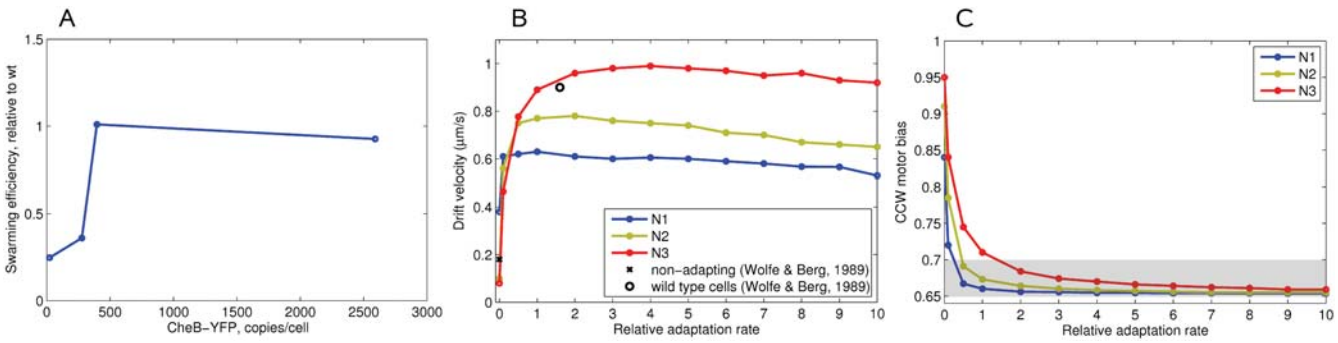

Figure 10. Swarm-plate assay at different [CheR,CheB]. (A) Experimentally measured chemotactic efficiency at different expression levels of the *cheR cheB-eyfp* operon under the control of a pBAD promoter. The applied arabinose concentrations were 0.0, 0.0005, 0.001, 0.01%, respectively. The CheB-YFP level reflects the concerted [CheR,CheB-YFP] due to strong translational coupling. For scale conversion, the wild-type level of CheB can be taken as 240 copies/cell [35]. (B) Simulated chemotactic efficiency as a function of [CheR,CheB]. Cells are simulated in the constant-activity gradients N1 (blue), N2 (green), N3 (red). The black open circle shows the experimentally observed drift velocity of wild-type cells, estimated from Figure 4 of [55]. The cross shows the drift velocity of non-adapting cells, from Figure 6 of [55]. The cell parameters are as described in Table 1. (C) Average motor bias of cells as a function of [CheR,CheB]. The steady-state motor bias is 0.65, with the gray band indicating the region of optimal motor bias for chemotaxis in agar.
doi:10.1371/journal.pcbi.1000242.g010

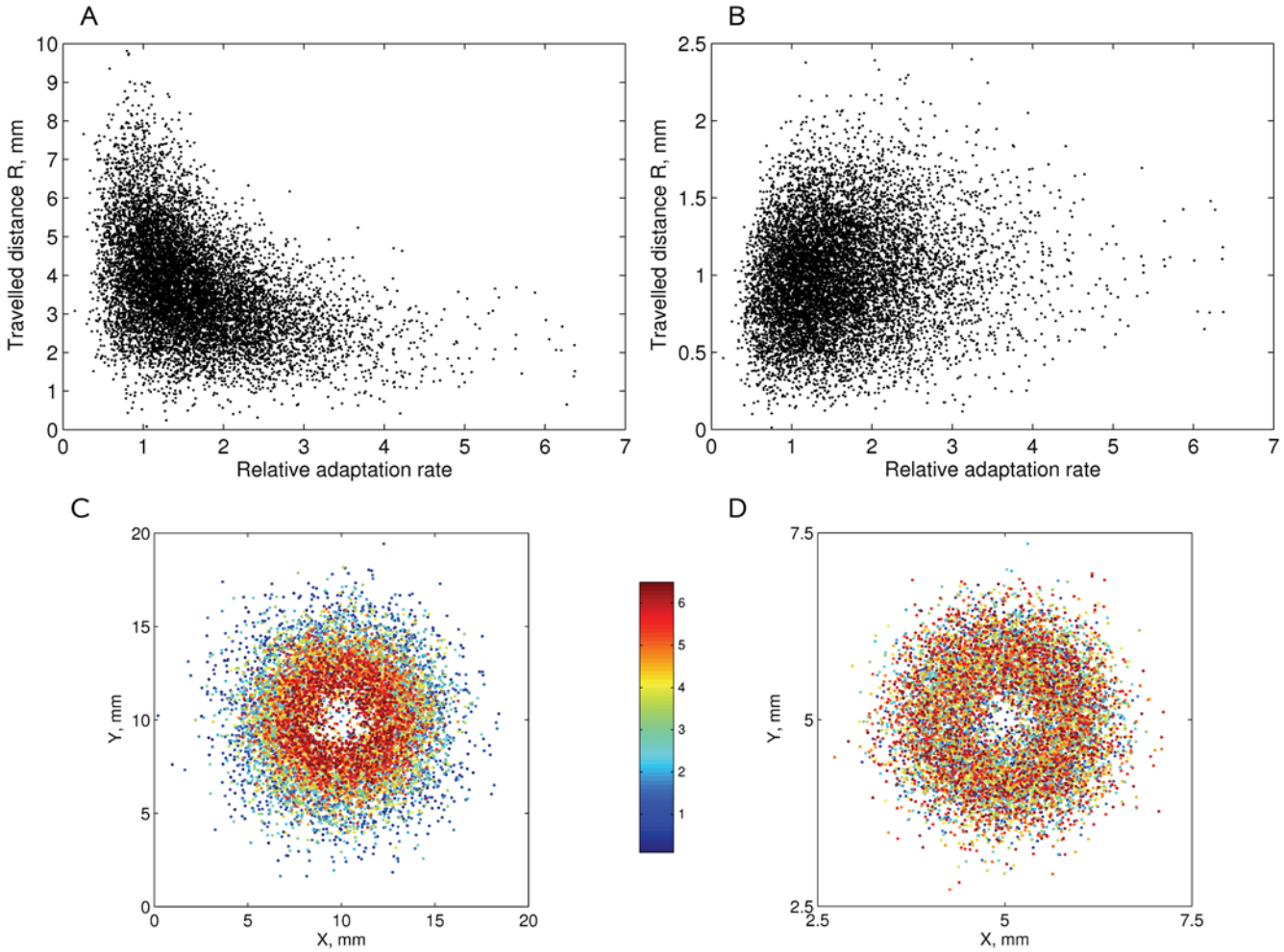

Figure 11. Simulation of motility in a liquid medium and agar with a physiological [CheR,CheB] distribution. The distances *R* travelled by 10^4 cells after 1000 s of simulation time in (A) the liquid medium, N2 gradient; (B) agar, N3 gradient. The (x,y)-positions of cells colored from deep blue to red, according to their [CheR,CheB], are shown in (C) for the liquid medium, (D) for agar. The smallest [CheR,CheB] values correspond to deep blue, the highest values correspond to red. Note the different scales of the figures. The cell parameters are as described in Table 1.
doi:10.1371/journal.pcbi.1000242.g011

[CheR,CheB], show that very high levels of the adaptation enzymes, over 20-fold, can again decrease chemotactic efficiency in agar (Figures S5 and S6).

Discussion

In this paper, we present RapidCell—a model of chemotactic *E. coli*, which allows us to study the effect of chemotaxis network properties on the behavior of large bacterial populations. RapidCell uses a hybrid model for pathway simulation, with mixed algebraic and ODE description instead of a fully stochastic model, AgentCell [19], or a complete system of ordinary differential equations, *E. solo* [23]. Our model allowed us to dramatically decrease in computational costs. Though many molecular details are skipped or modeled in a rapid-equilibrium (algebraic) approximation, the key steps of the network are reproduced in agreement with up-to-date experimental data. In contrast to detailed single-cell simulation programs which reproduce the noisy behavior of individual cells [19,56], RapidCell is aimed at predicting the averaged behavior of bacterial populations, and to investigate how it is affected by the signaling network parameters, neglecting the intrinsic noise coming from molecular reactions. However, artificial sources of noise can be further added in the deterministic model of the signaling pathway. In the present version of RapidCell, the noise arises only from rotational diffusion and stochastic switching of the motors.

For the receptor cluster simulation, we used the mixed-receptor cluster MWC model [12,28,30], which accounts for the observed broad range of sensitivity and reproduces the recent *in vivo* FRET data [27]. Adaptation is modeled according to the mean-field approximation of the assistance-neighborhood model, with the assumption that the average methylation level of multiple receptors can be represented as a continuous rather than a discrete variable [30]. In contrast to the other reactions, methylation and demethylation are relatively slow and therefore described by an ODE. The ODE is integrated by the first-order Euler scheme to ensure high computational speed of the program, while the time step is chosen as 0.01 s to keep the simulation error low.

Taking into account the available experimental studies on tumble mechanics [31,57], we use a voting model of run-tumble switching [13,31,44]. The model is in a good agreement with experimentally measured run and tumble times. However, more high-resolution experimental data on the interplay among multiple

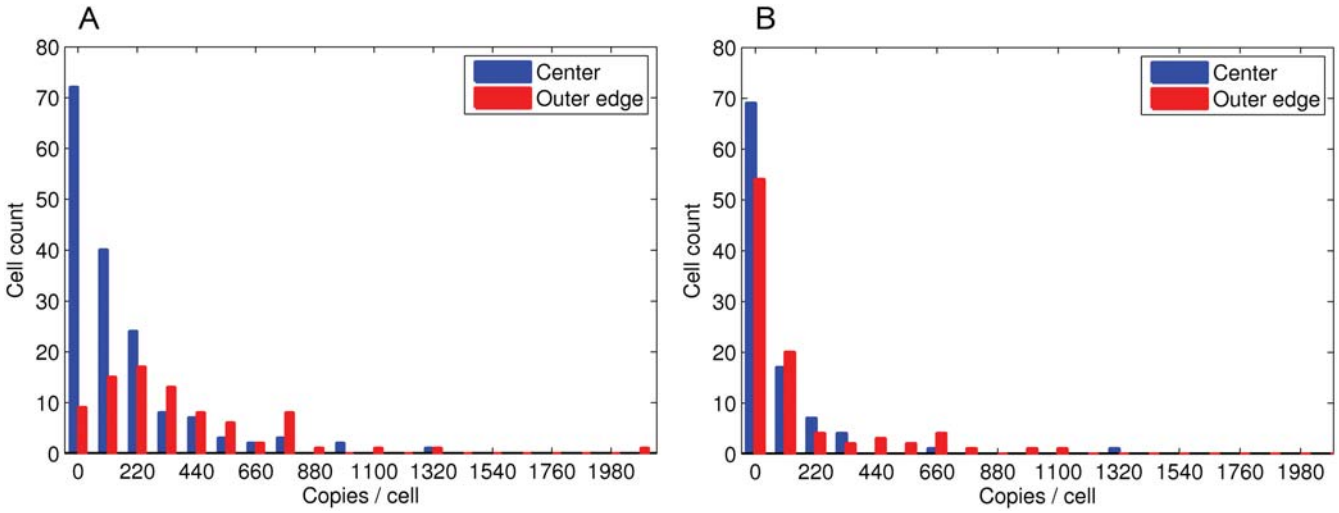

Figure 12. Experimental measurement of [CheR,CheB-YFP] in individual cells at different points in the swarm ring, for plates with (A) normal agar (0.27%); (B) liquid agar (0.20%). Blue columns show the least swarming cells in the center of the swarm plate, and the red ones—the best swarming cells from the outer edge. The expression of *cheR cheB-yfp* was under the control of a pBAD promoter, which gives a basal expression level close to wild-type. The bin size is 110 copies/cell.
doi:10.1371/journal.pcbi.1000242.g012

flagella during the run and the tumble would be necessary for a detailed model of run-tumble cellular behavior.

There are several types of gradients usually applied in computer models of chemotaxis. The linear gradient arises between stationary source and adsorber, and can often be observed under natural conditions. The Gaussian, another commonly used gradient, appears when a limited amount of molecules is injected into the medium from a micropipette or a similar source [42]. Other gradients that arise from general models of diffusion have hyperbolic or exponential shapes. However, all commonly used gradients have a 'blind' zone where receptors are saturated and cells do not respond. When cells drift along these gradients, the average profile of CheY-P changes dramatically, from a steep fall at low concentrations to a weakly stimulated state at high concentrations (Figure 3C). This makes it difficult to compare long-term chemotactic efficiency, because the average CheY-P and drift velocity are non-stable along the gradient.

To study chemotaxis systematically, we propose a new—constant-activity—type of gradient. This gradient has the unique property of providing the same CheY-P level and cellular-drift velocity over a wide range of ligand concentrations. The stability of the CheY-P level allows us to study properties of virtual chemotactic cells systematically, and to compare chemotactic behavior over long time periods and concentration ranges.

The form of the constant-activity gradient is derived from the MWC model, by formulating the differential equation for the gradient shape which will give a constant rate of receptor free energy change due to ligand binding. In earlier work, the condition of constant chemotactic response was studied using a phenomenological model of ligand binding, with a single dissociation constant K_D [48]. The study of Block and co-authors showed that such a model can be simplified, and as a result an exponential ramp of ligand should give a constant response in the range between $C_{min} = 0.31K_D$ and $C_{max} = 3.2K_D$, a prediction that was supported by their experiments [48].

In our study, we show that the differential equation for the constant-response gradient proposed in [48] is the result of the MWC model. We further solve this differential equation analytically, and find the exact form of the constant-activity gradient. This gradient grows similarly to the exponential function at moderate ligand concentrations, and increases faster than exponential at low and high concentrations (Figure 2A).

Our simulations show that the chemotactic response of the MWC model in the constant-activity gradient remains stable over four orders of ligand concentration—between 0.1 and $1000K_D$, in the case when Tsr receptors are fully insensitive to the ligand. However, in the case of (Me)-Asp, the Tsr receptors are able to respond non-specifically to high ligand concentrations, therefore above $100K_D$ the cluster activity drops to zero in a mixed-receptor cluster [12,27]. However, our simulations of population behavior consider only moderate Asp concentrations, so the cluster activity remains nearly constant in all observed cases.

The exponential ramp also gives nearly constant response in the MWC model, but over a much smaller range—between 0.5 and $3.0K_D$, in agreement with [48] and the recent study of Tu et al. [58].

We also show that the apparent dissociation constant K_D can be estimated by either the arithmetic or geometric mean of K^{off} and K^{on}, but the geometric mean gives a better approximation over a wide range of ligand concentrations.

The shape of the constant-activity gradient is also close to a hyperbolic gradient, with the change of variables, $K_DCx/(1-Cx) = K_D(1/y-1) \sim K_D/y$, $(y = 1-Cx,\ K_D \ll 1)$. The hyperbolic gradient arises from simple models of diffusion, when ligand molecules are emitted from a spherical source into the surrounding medium. In nature, such conditions can be observed, for example, in aquatic ecosystems where microalgae leak organic matter attractive for bacteria [59]. This suggests that hyperbolic and exponential gradients with appropriate parameters can be good approximations for the constant-activity gradient.

In our model, the adaptation rate is assumed to be proportional to the co-varied concentration of the adaptation enzymes [CheR,CheB], and we use both terms to denote the rate of adaptation. However, increasing expression of the adaptation enzymes may lead to saturation of the adaptation rate at some point, because the enzymes will start working out of saturation kinetics. For these reasons, it is more correct to consider our results in terms of adaptation-rate effects on chemotaxis, whatever the origins of adaptation-rate variability may be.

The effect of adaptation rate on chemotaxis agrees in many respects with the results reported in [13] for optimal noise filtering of the chemotaxis signaling system. In their work, the authors demonstrated the existence of an optimal cutoff frequency, an analog of the adaptation rate in our study, for efficient chemotaxis. For a fixed linear gradient, they show the same shape of chemotactic efficiency as a function of cutoff frequency (Figure 3B in [13]) as we found in our simulations (Figure 5A). The authors also show that the optimal cutoff frequency depends on gradient steepness in a linear manner (Figure 5A in [13]), consistent with our results (Figure 5B) for steep gradients.

Our simulations in the constant-activity gradient suggest a simple biological mechanism that determines the optimal adaptation rate for a given gradient steepness. Different optimal adaptation rates correspond to a single CheY-P interval, which fits the linear range of the motor-response function. This means that the highest drift velocity in liquid media is observed when the CheY-P level is in the narrow interval fitting the operating range of the motor. In this range, the dependence between CheY-P and *mb* is approximately linear (Figure 6C).

We found that the CheB phosphorylation feedback can have either a positive or negative effect on chemotactic efficiency, depending on how it shifts the average CheY-P level relative to the region of linear motor response. In the case of non-perfect ratio of CheR to CheB, the CheB phosphorylation mechanism can partially counteract the negative effect of unbalanced [CheR]/[CheB], by shifting the average CheY-P towards the optimal region. This confirms that CheB phosphorylation can improve the chemotactic properties of cells with deviations in the ratio of [CheR]/[CheB], as well as in the ratios of other proteins, from the optimum [32].

Chemotactic behavior in liquid media differs from that in agar. We simulated agar effects using traps randomly distributed over time - a cell can encounter traps during its run, and stays trapped until it makes the next tumble, as observed by Wolfe and Berg [55]. This restricts cellular motility—cells that are highly biased towards running remain in traps longer. In agar, the region of optimal motor bias is very narrow and is just above the unstimulated state mb_0, because higher bias increases the period of time cells remain in traps.

In our model, we did not take into account the growth of a bacterial populations. The typical swarm plate experiments last several hours, and cells grow and divide during the experiment, leading to variations in protein levels and to redistribution of proteins from generation to generation. However, the effect of different adaptation rates in our simulations is clearly visible already within one cell generation over 1000 s of model time (Figure 11B). The selection thus works on a time scale that is shorter than the generation time, which, in our opinion, justifies using a fixed protein distribution. Therefore, the addition of cell growth should not change our results qualitatively. In experiments, daughter cells with sub-optimal levels of CheR and CheB will rapidly fall behind the spreading swarm ring in the vicinity of the division site, while the subpopulation with optimal adaptation rates will be always at the front edge of the ring.

In most of our simulations, we assume that the CheR and CheB ratio is constant due to the genetic coupling between the two respective genes, and that cell-to-cell variation in adaptation rates arises from concerted variation in the levels of both enzymes [32]. We also investigated the effects of variation in the [CheR]/[CheB] ratio, which results from translational noise, and affect both the adaptation rate and the steady-state motor bias. In addition to these investigated sources of noise, there is intrinsic noise in the pathway activity which arises from the stochastic nature of (de-)methylation events. The latter sort of noise can also have positive effects on the spreading of cells in a ligand-free medium [56], and even on chemotactic drift in weak gradients [60]. Superposition of variable noise effects on chemotactic efficiency in variable gradients would be an interesting issue for further study.

In this work, we have estimated the variability in concerted CheR and CheB concentrations using available experimental data on cell-to-cell variability in adaptation times [33]. We assumed a log-normal distribution for protein concentrations, which also gives a log-normal distribution of adaptation times to a step-wise stimulus from 0 to 10^{-3} *M* MeAsp [33]. There are also other experimental estimates of cell-to-cell variation in adaptation times [34] and related simulations [61], but the adaptation rates observed in those experiments were several times higher, presumably due to different culture growth conditions.

Our simulations suggest some evolutionary implications. In liquid media with variable food sources and gradient intensities, variability in adaptation times (protein levels) among cells can help the whole population to respond to different gradients more readily, due to positive selection of cells with optimal [CheR,CheB]. In other words, for any given gradient steepness, there will be a subpopulation which has the best [CheR,CheB] to follow this gradient. In contrast, agar poses mainly negative selection on cell populations - cells with low [CheR,CheB] are filtered out from competition, while all other cells travel with approximately equal efficiency.

Inspired by the implementation of AgentCell, RapidCell focuses on highly efficient computation of large populations over long periods, keeping cell-response properties consistent with experimental data. The first version of RapidCell allows us to simulate *E. coli* populations of size 10^4–10^5 cells over a time scale of hours, while tracking the signal network dynamics of individual cells. These capabilities permit the modeling of cellular behavior on a macroscopic scale, as in swarm-plate experiments, and the prediction of properties of heterogeneous populations with noisy components of the signaling network.

Supporting Information

Figure S1 Comparison of the RapidCell network response with experimental and simulated data. (A) FRET experiment and RapidCell simulation of cell response to a step-wise stimulus of MeAsp. The initial ambient concentration is zero; at t = 80 s 30 μM MeAsp is added and removed at 480 s. The best fit by RapidCell is obtained with an adaptation rate of k = 0.5, corresponding to the temperature T = 20°C at which the FRET experiments were carried out. At T = 30°C, the fitted adaptation rate will be k = 1.0 (V.Sourjik, unpublished data). (B) StochSim and RapidCell simulations of cell response to a step-wise stimulus of Asp. The initial ambient concentration is zero; at t = 20 s 3.5 μM Asp is added and removed at 70 s. The best fit by RapidCell is obtained with an adaptation rate of k = 8 - a very rapid rate of adaptation. The StochSim simulations were carried out with a coupled model (Shimizu et. al, 2003), consisting of 65×65 square receptor lattice with coupling energy $E_J = -3.1$ kT. Found at: doi:10.1371/journal.pcbi.1000242.s001 (0.30 MB TIF)

Figure S2 Comparison of the RapidCell network response with experimental data on tethered cells. (A) Simulation of CCW motor bias response to a short pulse of attractant. The initial ambient concentration is zero; at t = 5 s 1.0 mM Asp is added for a 0.35 s interval; solid line - simulations (the best fit is obtained with an adaptation rate of 2.0), circles - experimental data (Segall et. al., 1986). (B) Simulation of CCW motor bias response to a step-wise stimulus. The initial ambient concentration is zero; at t = 1 s

0.075 μM Asp is added; solid line - simulations, circles - experimental data (Segall et. al., 1986). The best fit is obtained with an adaptation rate of 5.0. (C) Adaptation times to a step increase of MeAsp from zero ambient level, obtained in simulations (solid line) and in experiments (Berg and Tedesco, 1975) (circles). In the simulations, the dissociation constants used were $K_a^{off} = 0.02$ mM and $K_a^{on} = 0.5$ mM (Keymer et. al., 2006). The best fit is obtained with an adaptation rate of 1.3.
Found at: doi:10.1371/journal.pcbi.1000242.s002 (0.06 MB TIF)

Figure S3 Probability density function of tumbling angles $f(\Theta) = 0.5(1+\mathrm{Cos}\Theta)\mathrm{Sin}\Theta$ used in the model (solid line), and experimental measurements (cross markers) (Berg and Brown, 1972).
Found at: doi:10.1371/journal.pcbi.1000242.s003 (0.04 MB TIF)

Figure S4 The CheY-P response of the MWC model to the constant-activity ramp of aspartate from 0.1 to $10000K_D$. The ramp is simulated according to Eqn. 22 in two forms, with $K^* = 0.5(K^{on}+K^{off})$ (arithmetic mean), or $K^* = (K^{on}K^{off})^{0.5}$(geometric mean). The MWC model shows an approximately constant response for both approximations, but the geometric mean gives the more stable response over a wider range of concentrations.
Found at: doi:10.1371/journal.pcbi.1000242.s004 (0.12 MB TIF)

Figure S5 Chemotactic efficiency in agar as a function of highly over-expressed [CheR,CheB], observed in experiments and simulations: (black line) swarm-plate efficiency of cells with CheR and CheB-YFP expression under the control of a pTrc promoter. The chemotactic efficiency was estimated relative to the diameters of wild-type swarm rings. Color lines denote simulated chemotactic efficiency in three constant-activity gradients N1 (blue), N2 (green), N3 (red). The chemotactic efficiency in the simulations was estimated as the average distance travelled by cells, divided by the distance with the optimal [CheR,CheB]. Error bars indicate standard deviations.
Found at: doi:10.1371/journal.pcbi.1000242.s005 (0.06 MB TIF)

Figure S6 Measurement of [CheR,CheB] in individual cells in different points of the swarm ring, for cells with (A) the least, and (B) the best swarming efficiency. CheR and CheB-YFP were expressed from one operon under the control of a pTrc promoter and native ribosome-binding sites. The pTrc promoter gives high basal expression relative to the wild-type level. The least swarming cells were taken from the center of the swarm plate, and the best swarming - from the outer edge of the swarm ring. The mean protein levels were determined as described in Experimental Methods.
Found at: doi:10.1371/journal.pcbi.1000242.s006 (0.06 MB TIF)

Table S1 Rates of reactions
Found at: doi:10.1371/journal.pcbi.1000242.s007 (0.02 MB PDF)

Acknowledgments

We thank Thomas Shimizu, Ned Wingreen, and Matthew Levin for their valuable suggestions for improvement of the manuscript.

Author Contributions

Conceived and designed the experiments: NV LL DL VS. Performed the experiments: NV LL. Analyzed the data: NV LL DL VS. Contributed reagents/materials/analysis tools: NV DL VS. Wrote the paper: NV VS.

References

1. Kennedy MJ (1987) Role of motility, chemotaxis, and adhesion in microbial ecology. Ann N Y Acad Sci 506: 260–273.
2. Kennedy MJJ, Lawless JGG (1985) Role of chemotaxis in the ecology of denitrifiers. Appl Environ Microbiol 49: 109–114.
3. Pilgram WK, Williams FD (1976) Survival value of chemotaxis in mixed cultures. Can J Microbiol 22: 1771–1773.
4. Freter R, O'Brien PC, Halstead SA (1978) Adhesion and chemotaxis as determinants of bacterial association with mucosal surfaces. Adv Exp Med Biol 107: 429–437.
5. Lauffenburger D (1991) Quantitative studies of bacterial chemotaxis and microbial population dynamics. Microb Ecol 22: 175–185.
6. Kelly FX, Dapsis KJ, Lauffenburger DA (1988) Effect of bacterial chemotaxis on dynamics of microbial competition. Microb Ecol 16: 115–131.
7. Berg HC, Brown DA (1972) Chemotaxis in Escherichia coli analysed by three-dimensional tracking. Nature 239: 500–504.
8. Bren A, Eisenbach M (2000) How signals are heard during bacterial chemotaxis: protein-protein interactions in sensory signal propagation. J Bacteriol 182: 6865–6873.
9. Falke JJ, Bass RB, Butler SL, Chervitz SA, Danielson MA (1997) The two-component signaling pathway of bacterial chemotaxis: a molecular view of signal transduction by receptors, kinases, and adaptation enzymes. Annu Rev Cell Dev Biol 13: 457–512.
10. Barkai N, Leibler S (1997) Robustness in simple biochemical networks. Nature 387: 913–917.
11. Alon U, Surette MG, Barkai N, Leibler S (1999) Robustness in bacterial chemotaxis. Nature 397: 168–171.
12. Endres RG, Wingreen NS (2006) Precise adaptation in bacterial chemotaxis through "assistance neighborhoods". Proc Natl Acad Sci U S A 103: 13040–13044.
13. Andrews BW, Yi TM, Iglesias PA (2006) Optimal noise filtering in the chemotactic response of Escherichia coli. PLoS Comput Biol 2: e154. doi:10.1371/journal.pcbi.0020154.
14. Shimizu TS, Aksenov SV, Bray D (2003) A spatially extended stochastic model of the bacterial chemotaxis signalling pathway. J Mol Biol 329: 291–309.
15. Mello BA, Tu Y (2003) Quantitative modeling of sensitivity in bacterial chemotaxis: the role of coupling among different chemoreceptor species. Proc Natl Acad Sci U S A 100: 8223–8228.
16. Hauri DC, Ross J (1995) A model of excitation and adaptation in bacterial chemotaxis. Biophys J 68: 708–722.
17. Lipkow K, Andrews SS, Bray D (2005) Simulated diffusion of phosphorylated CheY through the cytoplasm of Escherichia coli. J Bacteriol 187: 45–53.
18. Spiro PA, Parkinson JS, Othmer HG (1997) A model of excitation and adaptation in bacterial chemotaxis. Proc Natl Acad Sci U S A 94: 7263–7268.
19. Emonet T, Macal CM, North MJ, Wickersham CE, Cluzel P (2005) AgentCell: a digital single-cell assay for bacterial chemotaxis. Bioinformatics 21: 2714–2721.
20. Morton-Firth CJ, Bray D (1998) Predicting temporal fluctuations in an intracellular signalling pathway. J Theor Biol 192: 117–128.
21. Morton-Firth CJ, Shimizu TS, Bray D (1999) A free-energy-based stochastic simulation of the tar receptor complex. J Mol Biol 286: 1059–1074.
22. Le Novere N, Shimizu TS (2001) STOCHSIM: modelling of stochastic biomolecular processes. Bioinformatics 17: 575–576.
23. Bray D, Levin MD, Lipkow K (2007) The chemotactic behavior of computer-based surrogate bacteria. Curr Biol 17: 12–19.
24. Bray D, Bourret RB, Simon MI (1993) Computer simulation of the phosphorylation cascade controlling bacterial chemotaxis. Mol Biol Cell 4: 469–482.
25. Bray D, Bourret RB (1995) Computer analysis of the binding reactions leading to a transmembrane receptor-linked multiprotein complex involved in bacterial chemotaxis. Mol Biol Cell 6: 1367–1380.
26. Levin MD, Morton-Firth CJ, Abouhamad WN, Bourret RB, Bray D (1998) Origins of individual swimming behavior in bacteria. Biophys J 74: 175–181.
27. Sourjik V, Berg H (2002) Receptor sensitivity in bacterial chemotaxis. Proc Natl Acad Sci U S A 99: 123–127.
28. Mello BA, Tu Y (2005) An allosteric model for heterogeneous receptor complexes: understanding bacterial chemotaxis responses to multiple stimuli. Proc Natl Acad Sci U S A 102: 17354–17359.
29. Keymer JE, Endres RG, Skoge M, Meir Y, Wingreen NS (2006) Chemosensing in Escherichia coli: Two regimes of two-state receptors. Proc Natl Acad Sci U S A 103: 1786–1791.
30. Hansen CH, Endres RG, Wingreen NS (2008) Chemotaxis in Escherichia coli: a molecular model for robust precise adaptation. PLoS Comput Biol 4: e1. doi:10.1371/journal.pcbi.0040001.
31. Turner L, Ryu WS, Berg HC (2000) Real-time imaging of fluorescent flagellar filaments. J Bacteriol 182: 2793–2801.
32. Kollmann M, Lovdok L, Bartholomé K, Timmer J, Sourjik V (2005) Design principles of a bacterial signalling network. Nature 438: 504–507.
33. Berg HC, Tedesco PM (1975) Transient response to chemotactic stimuli in Escherichia coli. Proc Natl Acad Sci U S A 72: 3235–3239.
34. Spudich JL, Koshland DE (1976) Non-genetic individuality: chance in the single cell. Nature 262: 467–471.
35. Li M, Hazelbauer GL (2004) Cellular stoichiometry of the components of the chemotaxis signaling complex. J Bacteriol 186: 3687–3694.

36. Stewart RC, Jahreis K, Parkinson JS (2000) Rapid phosphotransfer to CheY from a CheA protein lacking the CheY-binding domain. Biochemistry 39: 13157–13165.
37. Sourjik V, Berg HC (2002) Binding of the escherichia coli response regulator CheY to its target measured in vivo by fluorescence resonance energy transfer. Proc Natl Acad Sci U S A 99: 12669–12674.
38. Cluzel P, Surette M, Leibler S (2000) An ultrasensitive bacterial motor revealed by monitoring signaling proteins in single cells. Science 287: 1652–1655.
39. Skoge ML, Endres RG, Wingreen NS (2006) Receptor-receptor coupling in bacterial chemotaxis: evidence for strongly coupled clusters. Biophys J 90: 4317–4326.
40. Sourjik V (2004) Receptor clustering and signal processing in E. coli chemotaxis. Trends Microbiol 12: 569–576.
41. Segall JE, Block SM, Berg HC (1986) Temporal comparisons in bacterial chemotaxis. Proc Natl Acad Sci U S A 83: 8987–8991.
42. Berg HC (1993) Random Walks in Biology. Princeton, New Jersey: Princeton University Press.
43. Darnton NC, Turner L, Rojevsky S, Berg HC (2007) On torque and tumbling in swimming Escherichia coli. J Bacteriol 189: 1756–1764.
44. Ishihara A, Segall JE, Block SM, Berg HC (1983) Coordination of flagella on filamentous cells of Escherichia coli. J Bacteriol 155: 228–237.
45. Lewus P, Ford RM (2001) Quantification of random motility and chemotaxis bacterial transport coeffcients using individual-cell and populationscale assays. Biotechnol Bioeng 75: 292–304.
46. Chen KC, Ford RM, Cummings PT (2003) Cell balance equation for chemotactic bacteria with a biphasic tumbling frequency. J Math Biol 47: 518–546.
47. Chen KC, Ford RM, Cummings PT (1998) The global turning probability density function for motile bacteria and its applications. J Theor Biol 195: 139–155.
48. Block SM, Segall JE, Berg HC (1983) Adaptation kinetics in bacterial chemotaxis. J Bacteriol 154: 312–323.
49. Flanagan M (2007) Java scientific library. http://www.ee.ucl.ac.uk/~mflanaga/java/index.html.
50. Matsumoto M, Nishimura T (1998) Mersenne twister: a 623-dimensionally equidistributed uniform pseudo-random number generator. ACM Trans Model Comput Simul 8: 3–30. URL http://cs.gmu.edu/~sean/research/.
51. Parkinson JS, Houts SE (1982) Isolation and behavior of escherichia coli deletion mutants lacking chemotaxis functions. J Bacteriol 151: 106–113.
52. Løvdok L, Kollmann M, Sourjik V (2007) Co-expression of signaling proteins improves robustness of the bacterial chemotaxis pathway. J Biotechnol 129: 173–180.
53. Berg HC, Turner L (1990) Chemotaxis of bacteria in glass capillary arrays. escherichia coli, motility, microchannel plate, and light scattering. Biophys J 58: 919–930.
54. Adler J (1966) Chemotaxis in bacteria. Science 153: 708–716.
55. Wolfe AJ, Berg HC (1989) Migration of bacteria in semisolid agar. Proc Natl Acad Sci U S A 86: 6973–6977.
56. Korobkova E, Emonet T, Vilar JM, Shimizu TS, Cluzel P (2004) From molecular noise to behavioural variability in a single bacterium. Nature 428: 574–578.
57. Darnton NC, Turner L, Rojevsky S, Berg HC (2007) On torque and tumbling in swimming Escherichia coli. J Bacteriol 189: 1756–1764.
58. Tu Y, Shimizu TS, Berg HC (2008) Modeling the chemotactic response of Escherichia coli to time-varying stimuli. Proc Natl Acad Sci U S A 105: 14855–14860.
59. Jackson GA (1987) Simulating chemosensory responses of marine microorganisms. Limnol Oceanogr 32: 1253–1266.
60. Emonet T, Cluzel P (2008) Relationship between cellular response and behavioral variability in bacterial chemotaxis. Proc Natl Acad Sci U S A 105: 3304–3309.
61. Levin MD (2003) Noise in gene expression as the source of non-genetic individuality in the chemotactic response of Escherichia coli. FEBS Lett 550: 135–138.

Role of Translational Coupling in Robustness of Bacterial Chemotaxis Pathway

Linda Løvdok[1☯], Kajetan Bentele[2☯], Nikita Vladimirov[3☯], Anette Müller[1☯], Ferencz S. Pop[1], Dirk Lebiedz[4], Markus Kollmann[2]*, Victor Sourjik[1]*

1 Zentrum für Molekulare Biologie der Universität Heidelberg, DKFZ-ZMBH Alliance, Heidelberg, Germany, **2** Institut für Theoretische Biologie, Humboldt Universität, Berlin, Germany, **3** Interdisziplinäres Zentrum für Wissenschaftliches Rechnen der Universität Heidelberg, Heidelberg, Germany, **4** Zentrum für Biosystemanalyze, Universität Freiburg, Freiburg, Germany

Abstract

Chemotaxis allows bacteria to colonize their environment more efficiently and to find optimal growth conditions, and is consequently under strong evolutionary selection. Theoretical and experimental analyses of bacterial chemotaxis suggested that the pathway has been evolutionarily optimized to produce robust output under conditions of such physiological perturbations as stochastic intercellular variations in protein levels while at the same time minimizing complexity and cost of protein expression. Pathway topology in *Escherichia coli* apparently evolved to produce an invariant output under concerted variations in protein levels, consistent with experimentally observed transcriptional coupling of chemotaxis genes. Here, we show that the pathway robustness is further enhanced through the pairwise translational coupling of adjacent genes. Computer simulations predicted that the robustness of the pathway against the uncorrelated variations in protein levels can be enhanced by a selective pairwise coupling of individual chemotaxis genes on one mRNA, with the order of genes in *E. coli* ranking among the best in terms of noise compensation. Translational coupling between chemotaxis genes was experimentally confirmed, and coupled expression of these genes was shown to improve chemotaxis. Bioinformatics analysis further revealed that *E. coli* gene order corresponds to consensus in sequenced bacterial genomes, confirming evolutionary selection for noise reduction. Since polycistronic gene organization is common in bacteria, translational coupling between adjacent genes may provide a general mechanism to enhance robustness of their signaling and metabolic networks. Moreover, coupling between expression of neighboring genes is also present in eukaryotes, and similar principles of noise reduction might thus apply to all cellular networks.

Citation: Løvdok L, Bentele K, Vladimirov N, Müller A, Pop FS, et al. (2009) Role of Translational Coupling in Robustness of Bacterial Chemotaxis Pathway. PLoS Biol 7(8): e1000171. doi:10.1371/journal.pbio.1000171

Academic Editor: Andre Levchenko, Johns Hopkins, United States of America

Received November 17, 2008; **Accepted** July 7, 2009; **Published** August 18, 2009

Funding: This work is supported by Deutsche Forschungsgemeinschaft grants SO 421/3-2 and SO 421/3-3 and Emmy Noether Research Programme (http://www.dfg.de/en/index.html), EMBO Young Investigator Programme (http://www.embo.org/programmes/yip.html), and Promotionskolleg Bioquant of the Land Baden-Württemberg (http://www.zmbh.uni-heidelberg.de/public_html/promotionskolleg/). The funders had no role in study design, data collection and analysis, decision to publish, or preparation of the manuscript.

Competing Interests: The authors have declared that no competing interests exist.

Abbreviations: CW, clockwise; RBS, ribosome-binding site; SD, Shine-Dalgarno.

* E-mail: m.kollmann@biologie.hu-berlin.de (MK); v.sourjik@zmbh.uni-heidelberg.de (VS)

☯ These authors contributed equally to this work.

Introduction

Any intracellular network is permanently exposed to a wide range of intra- and extracellular perturbations that affect levels of components and reaction rates. Both eukaryotic and prokaryotic systems have therefore evolved mechanisms that allow them to produce a robust output under varying conditions. In prokaryotes, the best-studied model system for signaling and robustness is the chemotaxis pathway of *E. coli* [1,2]. The pathway includes transmembrane receptors (also called methyl-accepting chemotaxis proteins, or MCPs) of five types, the receptor-coupled kinase CheA, the adaptor CheW, the response regulator CheY, and the phosphatase CheZ, as well as the adaptation system that consists of two opposing receptor modification enzymes, the methyltransferase CheR and the methylesterase CheB. CheA autophosphorylation activity is controlled by ligand binding to receptors, with CheW needed to couple CheA to receptors. Phosphorylated CheA rapidly transfers the phosphate group to CheY, which controls direction of flagellar motor rotation and thereby bacterial swimming behavior. Phospho-CheY (CheY-P) dephosphorylation is accelerated by CheZ. Cells adapt to a constant stimulation by adjusting levels of receptor methylation, with higher methylated receptors being more efficient in kinase activation.

Robustness of the pathway output—the concentration of CheY-P—against varying levels of ambient stimulation and against intercellular variation in gene expression, or gene expression noise, is ensured by specific features of the pathway topology. Robust adaptation to a wide range of stimulus strength is achieved by an integral feedback from an activity state of receptors (kinase-activating vs. kinase-inactivating) to the methylation system, whereby CheR preferentially methylates inactive receptors and CheB demethylates active receptors [3–6]. On the other hand, robustness against natural intercellular variation in protein levels, or gene expression noise, primarily relies on the balance of

Author Summary

All cellular networks are subject to fluctuations in the levels of their components. Robustness of the network output in the face of stochastic gene expression, or gene expression noise, is therefore essential to ensure proper function. Selection for robustness might thus have shaped much of the cellular evolution. We have used *Escherichia coli* chemotaxis, one of the most thoroughly studied model systems for signal transduction, to analyze the role of gene organization in robustness. Our mathematical modeling predicted that coupling the expression of chemotaxis proteins with opposing functions should buffer the output of the signaling pathway against stochastic variations in protein production. Consistent with this model, protein coexpression was indeed observed to improve chemotaxis and to be under selection during chemotaxis-driven spreading of a cell population. We show that tight coexpression is ensured by both transcriptional and translational gene coupling. We conclude that evolutionary selection for pathway robustness in the presence of gene expression noise can explain, not only the polycistronic organization of chemotaxis genes, but also the gene order within chemotaxis operons. Selection on the gene order was further confirmed by the observation of a strong bias towards specific pairwise occurrences of chemotaxis genes in sequenced prokaryotic genomes.

opposing enzymatic activities, CheR/CheB and CheA/CheZ [7]. Such balance can perfectly compensate for the concerted expression noise, and it has been shown that the topology and reaction rates of the pathway are such that its output remains invariant under perfectly coupled overexpression of all chemotaxis proteins [7]. Robustness against expression noise is further improved by a negative phosphorylation feedback from the active CheA to CheB, which greatly enhances enzymatic activity of the latter, and partly compensates for both concerted and uncorrelated variations in protein expression.

These model predictions are consistent with the experimentally observed high correlation in the levels of individual chemotaxis proteins [7], which can be partly attributed to the gene organization in polycistronic transcriptional units, or operons, in which multiple genes are transcribed as one mRNA. Chemotaxis genes are organized into two operons: *mocha*, which encodes CheA and CheW along with flagellar motor proteins, and *meche*, which encodes two receptors—Tar and Tap—as well as CheR, CheB, CheY, and CheZ, whereas three other receptors are encoded elsewhere in the genome. However, even *cheA* and *cheY* genes that do not belong to the same operon show strong correlation in their single-cell expression levels, suggesting that a large part of gene expression noise originates at the upper level of transcriptional hierarchy that controls expression of all chemotaxis and flagellar genes [7].

Despite its success in accounting for robustness against concerted overexpression of all proteins, our previous computer model could not explain robustness against the experimentally observed degree of uncorrelated variation in protein levels in the population and predicted larger variation of the motor bias in the population than observed when identical levels of intercellular variation were assumed for all chemotaxis proteins [7]. This discrepancy indicated presence of additional robustness mechanisms, and in this work, we propose that translational coupling between adjacent genes on the *meche* and *mocha* operons represent such a mechanism. Translational coupling—defined as the interdependence of translation efficiency of neighboring genes encoded by the same polycistronic mRNA—has been previously described in *E. coli* [8–11], and can help to maintain a constant ratio between proteins expressed from the same operon. We experimentally demonstrated coupling for most pairs of chemotaxis genes in *E. coli* and confirmed that coexpression of these genes improves chemotactic performance. Computer simulations confirmed that negative effects of the uncorrelated expression noise can be reduced by genomic order of chemotaxis genes, in agreement with the gene arrangement in *E. coli*. Evolutionary importance of noise reduction mediated by translational coupling was further confirmed by strong bias towards particular pairwise coupling order of chemotaxis genes in bacterial genomes.

Results

Translational Coupling between Chemotaxis Genes

To test whether expression of neighboring chemotaxis genes might be coupled on a translational level, we analyzed three pairs of genes, *cheR_cheB*, *cheB_cheY*, and *cheY_cheZ*, from the *meche* operon, and one pair, *cheA_cheW*, from the *mocha* operon. Gene pairs were cloned as they appear in the genome, and the second gene was fused to a *eyfp* reporter (encoding yellow fluorescent protein, or YFP). The level of translation of the first gene was then selectively varied by placing ribosome-binding sites (RBSs) of different strength in front of it. As a control of the RBS strength, *eyfp* fusion to the first gene in the pair was placed under the same RBSs (Figure 1A). Thus determined differences in the RBS strengths varied from five to nine (Figure 1B) and were independent of the levels of IPTG-induced transcription (unpublished data). For the *cheA_cheW* pair, this strategy was complicated by the fact that CheA is expressed from two alternative translation initiation codons, yielding a long and a short version, $CheA_L$ and $CheA_S$, respectively [12]. Consequently, changing the strength of the first RBS had only a moderate effect on the total expression level of CheA. Instead, we compared constructs expressing $CheA_L$ under the external RBS and $CheA_S$ under the endogenous RBS with those expressing only $CheA_S$ under the external RBS. The resulting net level of translation of $CheA_L$-YFP and $CheA_S$-YFP in the first construct was about four times higher than that of $CheA_S$-YFP in the second construct.

For all pairs, stronger translation of the upstream gene resulted in an elevated expression of the downstream gene, implying the existence of a translational coupling (Figure 1B). The coupling was quantified as a ratio of the indirect up-regulation seen in constructs that carry gene pairs to the direct up-regulation of the first gene. The strength of translational coupling varied among gene pairs from approximately 0.2 to 0.6 (Figure 1C), apparently inversely correlating with the level of translational enhancement. Indeed, when an even stronger *cheR* RBS was used for the *cheR_cheB* pair to enhance translation approximately 30-fold, the observed coupling ($\sim$0.2) was significantly weaker than the coupling at approximately 5-fold enhancement shown in Figure 1C. Such dependence may indicate saturation of coupling at high translational levels of the upstream gene, as expected if coupling results from the mRNA unfolding (see Discussion).

Pairwise Coexpression of Genes Improves Chemotaxis

Maintaining a constant ratio between signaling proteins may be important for a proper functioning of the chemotaxis pathway under varying protein levels, and we have recently shown that the chemotaxis system is much less sensitive to a concerted overexpression of CheY and CheZ than to the overexpression of each of these proteins individually [13]. We thus tested whether a coexpression of

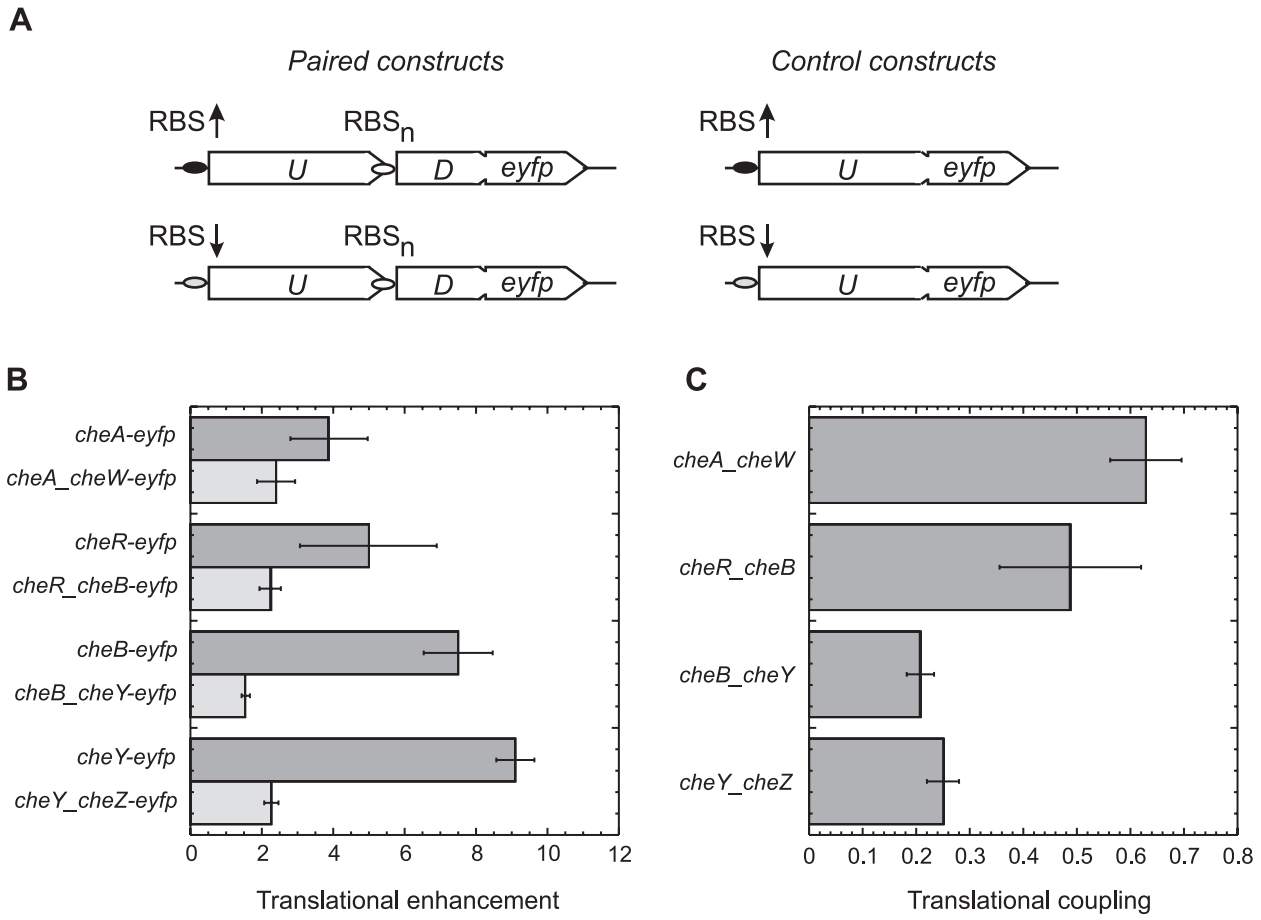

Figure 1. Translational coupling between neighboring genes. (A) Experimental strategy. Bicistronic constructs that contained pairs of neighboring chemotaxis genes in their chromosomal arrangement (*U*, upstream gene; *D*, downstream gene) were cloned under RBSs of different strength as indicated to create a C-terminal YFP fusion (*eyfp*, enhanced YFP gene) to a downstream gene. Strong RBS is indicated by a black oval and an up arrow, weak RBS by a grey oval and a down arrow. As a control of the RBS strength, the same sequence was placed in front of the monocistronic YFP fusion to the upstream gene. Downstream gene is under control of its native RBS (RBS_n, open oval). Expression of the constructs was analyzed using FACS as described in Materials and Methods. (B) Direct (dark-grey) and indirect (light-grey) up-regulation of expression level of the fusion reporter by the stronger RBS, defined as the ratio of expression of constructs with the strong RBS to expression of corresponding constructs with the weak RBS. For the *cheA/cheW* pair, translation was regulated by using constructs that express either only short version of CheA or both long and short versions (see text for details). The values of up-regulation at varying (0 to 50 μM) levels of IPTG induction did not differ significantly and were averaged. (C) Translational coupling, defined as the ratio of indirect to direct up-regulation of expression levels by the stronger RBS. Error bars in (B and C) indicate standard deviations.
doi:10.1371/journal.pbio.1000171.g001

the proteins from bicistronic constructs will improve performance of the pathway in a chemotaxis-driven spreading of bacteria in soft agar (Figure 2). Indeed, cells that express a YFP fusion to a particular gene as a monocistronic construct in the respective knock-out strain spread less efficiently than the cells that express this fusion as a downstream gene in bicistronic constructs at the same level (Figure 2A), with a clear enhancement of chemotaxis that resulted from gene coexpression (Figure 2B).

Such enhancement suggests that the coexpression of particular chemotaxis genes should be evolutionary selected, although it does not specifically distinguish between translational and transcriptional coupling. To directly test whether there is a chemotaxis-driven selection for the expression coupling beyond cotranscription, we compared single-cell levels of CheY-YFP and CheZ fused to cyan fluorescent protein, CheZ-CFP, that were expressed from one bicistronic construct in *E. coli* population spreading in soft agar (Figure 3 and Figure S3). Best-chemotactic cells at the front edge of the spreading ring (Figure 3A and Figure S3A) showed very strong correlation between the levels of both proteins (Figure 3B and Figure S3B). In contrast, the correlation in cells that remained behind and were not selected for chemotaxis was significantly weaker (Figure 3C and Figure S3C), despite the fact that both subpopulations express CheY-YFP and CheZ-CFP from the same bicistronic mRNA. This demonstrates chemotactic selection for the posttranscriptional coupling between protein levels and supports our assumption that translational coupling should be evolutionary beneficial.

Translational Coupling between Selected Genes Is Predicted to Enhance Robustness of the Pathway

Why are some proteins and not the others coupled through sequential gene arrangement in one operon? As mentioned above, enhanced robustness against uncorrelated gene expression noise—resulting from stochasticity of translation—is the most likely mechanism by which translational coupling could benefit chemotaxis. We thus used computer simulations to test whether

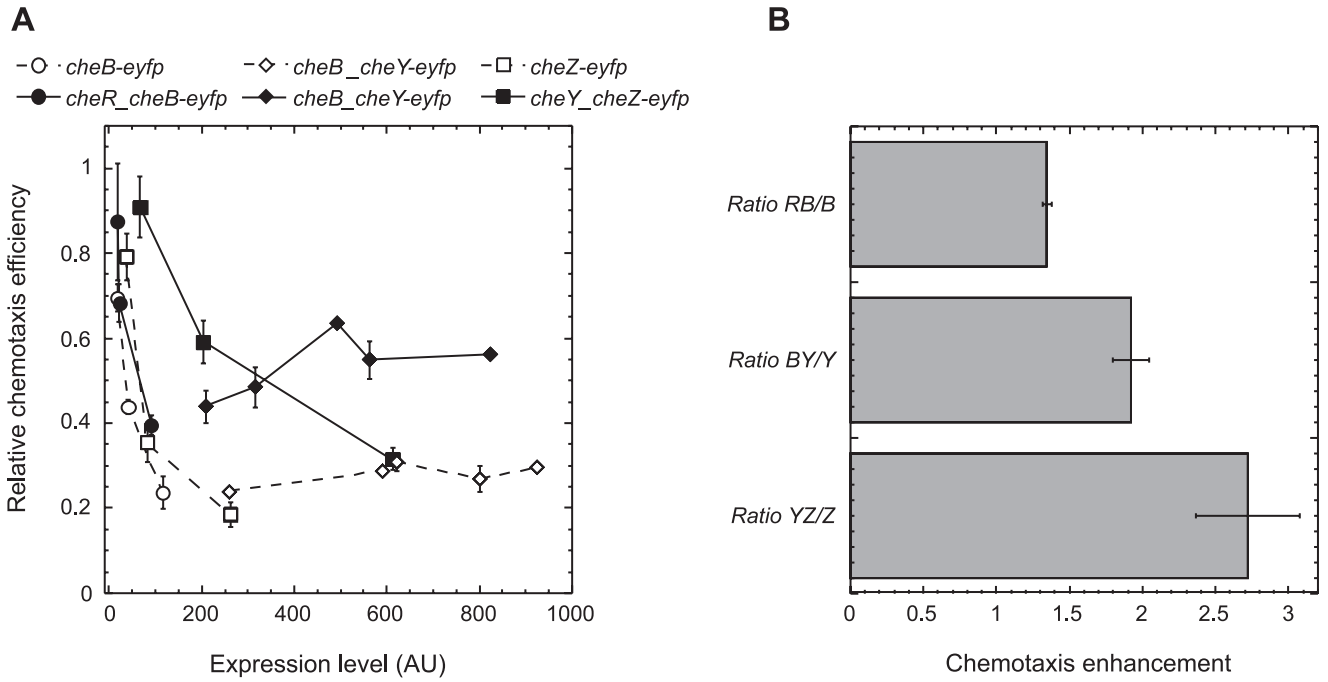

Figure 2. Improvement of chemotaxis by coexpression of signaling proteins. (A) Dependence of the chemotaxis-driven spreading of bacteria on soft agar (swarm) plates on the protein expression level for monocistronic (open symbols, dashed lines) or bicistronic (filled symbols, solid lines) constructs. Protein expression from pTrc99A-based plasmids pVS138 (*cheB-eyfp*) and pVS145 (*cheR_cheB-eyfp*) in strain RP4972 (*ΔcheB*) and pVS64 (*cheZ-eyfp*) and pVS305 (*cheY_cheZ-eyfp*) in strain VS161 (*ΔcheZ*) was induced by 10, 25, or 100 μM IPTG. A nontranslated 316-nucleotide fragment of *cheB* was included upstream of the *cheY* start codon in pLL33 (−316_*cheY-eyfp*) plasmid to achieve expression comparable to pLL36 (*cheB_cheY-eyfp*) construct (see Materials and Methods for details), and both constructs were expressed in strain VS100 (*ΔcheY*) under weaker pBAD promoter induced by 0%, 0.0005%, 0.001%, 0.003%, 0.005%, or 0.01% arabinose. Expression levels were measured in liquid cultures grown under the same induction as described in Materials and Methods. Chemotaxis efficiency was determined as the size of a swarm rings and normalized to that of wild-type strain RP437 transformed with either a pTrc99A (for pVS138, pVS145, pVS64, and pVS305) or a pBAD33 (for pLL33 and pLL36) vector. (B) Enhancement of chemotactic efficiency by expression coupling. Enhancement was calculated as a ratio of chemotaxis efficiency at a given expression level of the monocistronic construct to the interpolated efficiency at the same expression level of the YFP fusion in the respective bicistronic construct in (A), and values at different expression levels were averaged. Error bars indicate standard deviations.
doi:10.1371/journal.pbio.1000171.g002

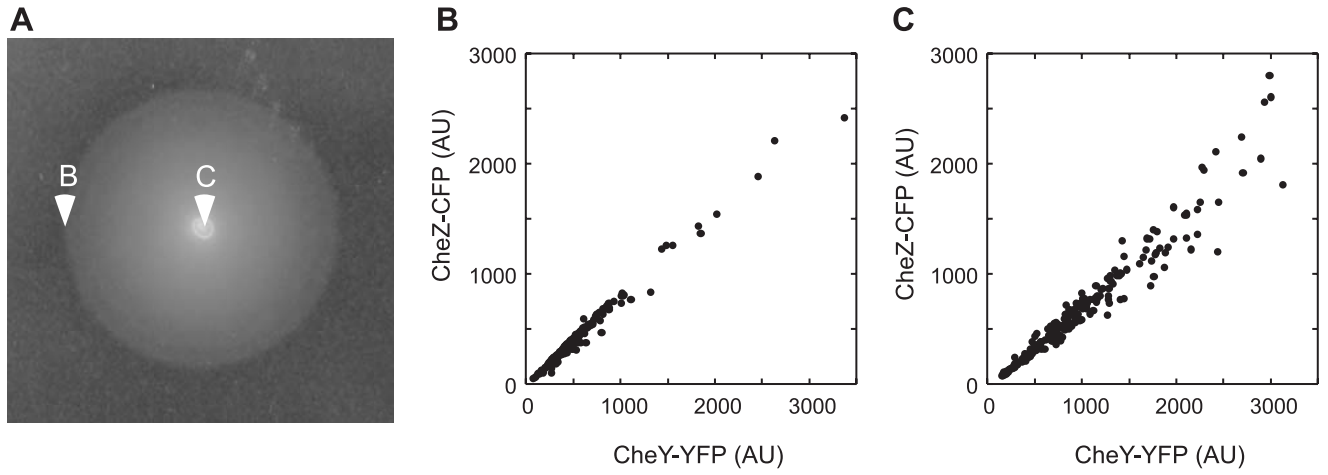

Figure 3. Chemotactic selection for posttranscriptional coupling. (A) Chemotaxis-driven spreading of VS104 [*Δ(cheYcheZ)*] cells expressing CheY-YFP and CheZ-CFP from a bicistronic construct pVS88 on soft agar (swarm) plates. (B and C) Scatter plots of single-cell levels of CheY-YFP and CheZ-CFP in cells taken from the edge (B) and from the middle (C) of the spreading colony. Relative concentrations of fluorescent proteins in individual cells were determined using fluorescence microscopy as described in Materials and Methods. Protein expression was induced with 17 μM IPTG; data for 10 μM IPTG induction are shown as supporting Figure S3. AU, arbitrary units.
doi:10.1371/journal.pbio.1000171.g003

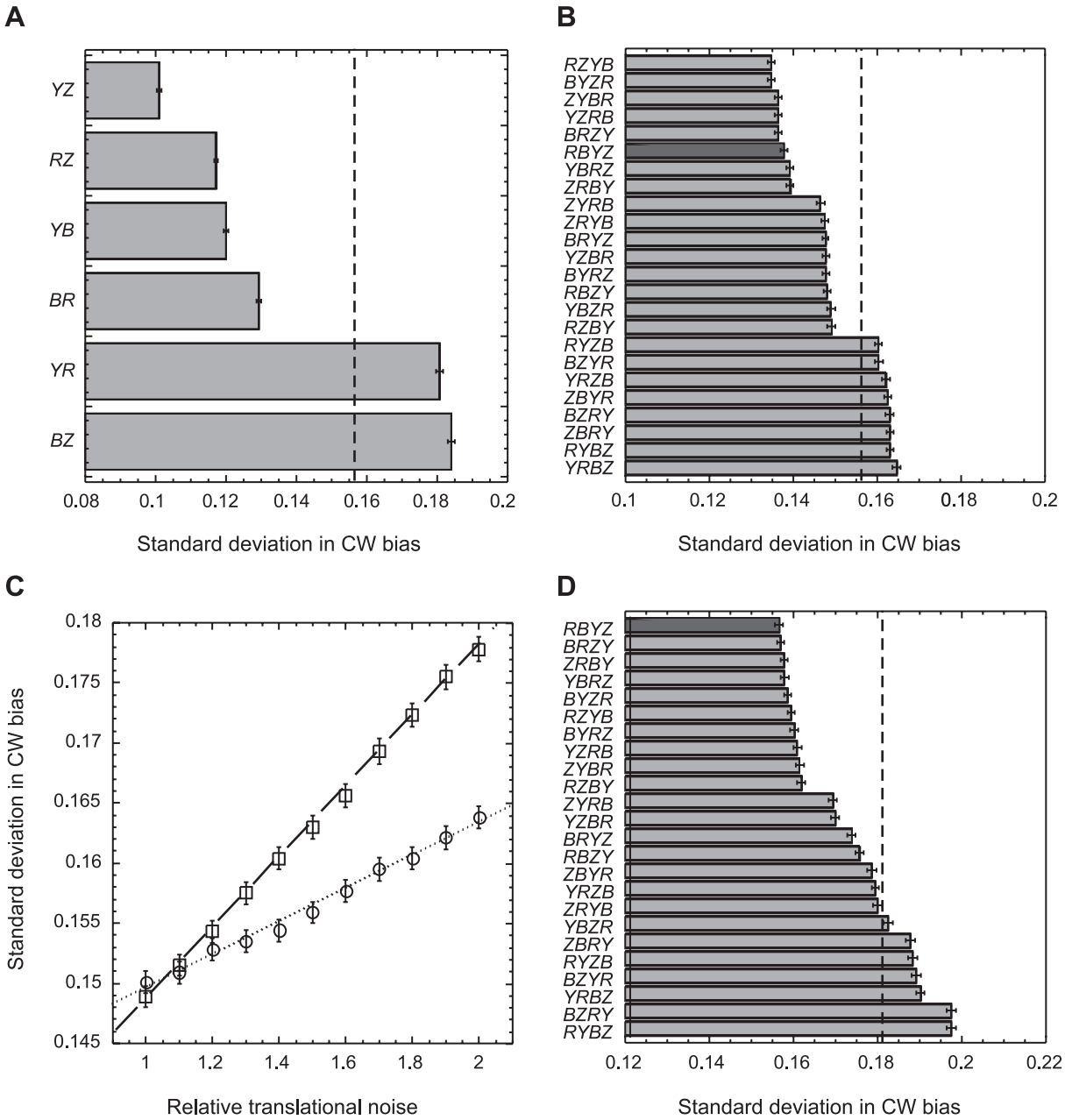

Figure 4. Simulated effects of translational coupling on robustness of the signaling output. Standard deviation of the CW motor bias in a population of 10^5 cells was simulated in presence of gene expression noise as described in Materials and Methods and in supporting information (Text S1). (A) Simulations for 100% pairwise coupling of indicated chemotaxis genes, with remaining genes being uncoupled. (B) Simulations for different arrangements of translationally coupled chemotaxis genes, performed at equal noise levels for all genes and 25% coupling. (C) Asymmetric effects of translational noise for 25% coupling between *cheR_cheZ* (circles, dotted line) and *cheZ_cheR* (squares, dashed line). Linear fits to the data are guide to the eye. (D) Simulations for different gene orders as in (B), at 1.5-fold higher noise for the weakly expressed *cheR* and *cheB* genes. Dark-grey bars indicate gene order in *E. coli*. Standard deviation of CW bias in absence of coupling is indicated by vertical dashed lines. Genes are indicated by single letters, i.e., Y = CheY, and so forth. Error bars indicate confidence intervals.
doi:10.1371/journal.pbio.1000171.g004

preferential pairing of particular chemotaxis genes and the resulting gene order on the chromosome can improve robustness of the pathway output—adapted clockwise (CW) rotation bias of flagellar motor—against translational noise when translational coupling is taken into account. Considering four genes *cheR*, *cheB*, *cheY*, and *cheZ*, our in silico chemotaxis network model indeed confirmed that positive correlations between expression of adjacent genes via translational coupling affect deviations from the optimal adapted CW bias within a population (Figure 4). Simulating a 100% pairwise translational coupling between particular genes in the background of uncorrelated fluctuations of all other genes (Figure 4A) showed favorable reduction in the standard deviation of CW bias for four adjacent gene pairs—*cheY_cheZ*, *cheR_cheZ*, *cheY_cheB*, and *cheR_cheB*. Note that because of the perfect coupling, the gene order in these simulations is not important, so that *cheY_cheZ* and *cheZ_cheY* pairs are equivalent. In

Table 1. Absolute frequencies[a] of a pairwise occurrence of chemotaxis genes in 527 genomes containing at least one chemotaxis gene.

Gene	*cheA* (771)		*cheW* (1,232)		*cheR* (802)		*cheB* (656)		*cheY* (1,376)		*cheZ* (209)		*mcp*[b] (6,521)	
	left	**right**	**left**	**right**	**left**	**right**	**left**	**right**	**left**	**right**	**left**	**right**	**left**	**right**
cheA	1.0	<1	**19.6**	3.2	2.7	2.2	14.8	8.6	<1	7.7	<1	**32.5**	<1	<1
cheW	7.4	**37.8**	5.9	5.6	**20.8**	7.2	5.2	1.4	2.3	2.8	0.0	0.0	4.0	3.0
cheR	2.3	3.9	4.6	13.7	<1	<1	**28.6**	10.7	1.9	<1	0.0	0.0	<1	2.0
cheB	5.2	15.1	<1	2.7	8.6	**26.1**	<1	<1	**7.2**	2.3	<1	0.0	<1	<1
cheY	**15.7**	<1	3.4	2.3	1.4	3.1	4.9	**15.0**	1.9	1.7	**90.0**	0.0	<1	<1
cheZ	8.1	<1	0.0	0.0	0.0	0.0	0.0	0.0	<1	**9.6**	0.0	0.0	<1	0.0
mcp	10.5	6.4	13.0	**16.5**	16.8	2.1	1.1	2.3	1.9	1.2	0.0	<1	**5.3**	**5.1**

[a]Absolute frequencies were calculated as the number of gene occurrences in −1 (left neighbor) or +1 (right neighbor) positions relative to a reference gene, normalized by the total number of reference gene counts (shown in parentheses). Strongest genomic coupling on each side (highest co-occurrence frequency) is marked in bold.
[b]Genes encoding chemoreceptors (methyl-accepting chemotaxis proteins).
doi:10.1371/journal.pbio.1000171.t001

all these cases, a positive effect is observed whenever a gene that enhances CheY-P level upon overexpression is coupled to a gene that reduces CheY-P level upon overexpression or vice versa (see Discussion). A negative effect—the increased variation in CW bias—was observed by coupling *cheY_cheR* and *cheB_cheZ* genes that have similar effects on the CheY-P level.

We next investigated which overall order of chemotaxis genes would yield the optimal noise reduction based on the observed preferences in pairwise gene coupling. When levels of translational noise and coupling efficiency were assumed to be equal for all four genes, 16 gene orders out of possible 24 permutations were predicted to reduce variation of the bias in the population compared to the simulation in absence of coupling, whereas eight gene orders increased that variation (Figure 4B). The degree of noise reduction or enhancement in this case was largely the consequence of maximizing favorable pairings and minimizing unfavorable pairings. Eight gene orders with three positive couplings—including the native gene order in *E. coli*—showed the most pronounced noise reduction. Additional weak gradation in the ranking resulted from the pair-specific differences in the extent of noise reduction or enhancement (Figure 4A), with the *cheY_cheZ* (or *cheZ_cheY*) pair being present in all of the highest ranked orders. The detailed ranking among arrangements with the same number of positive couplings depended only weakly on the reaction rates in the pathway but strongly on the strength of translational noise. For different gene-specific levels of translational noise, the optimal gene order becomes dependent not only on the number of positive pairs but also on their sequence, due to asymmetric effects of coupling on the output noise (Figure 4C; see Text S1 for details). As a result, in a more physiological case of 1.5-fold higher noise in expression of the weakly translated genes CheR and CheB (Figure 4D) the ranking of gene orders becomes more differentiated, with the native order of chemotaxis genes in *E. coli* providing the largest noise reduction.

Consensus Order of Chemotaxis Genes in Bacteria

Our analyses imply that the order of chemotaxis genes coupling on the chromosome should be subject to evolutionary selection and therefore conserved among bacteria. A comprehensive analysis of 824 sequenced bacterial genomes, 527 of which contain annotated chemotaxis genes (Table S1, Text S2), confirmed existence of a strong bias in the pairwise co-occurrence of these genes in the genome and in their order (Table 1). The resulting consensus order (Figure 5A) was consistent with the modeling predictions and showed a nearly perfect match to the chemotaxis gene arrangement in *E. coli*. Because our mathematical model explicitly includes the phosphatase CheZ, which is only found in a subset of 200 bacterial species, gene coupling in genomes with and without *cheZ* was also analyzed separately (Tables S2 and S3, respectively). Both yielded essentially the same consensus gene order, except for weaker coupling between *cheB* and *cheY* in absence of *cheZ*. This confirms that selection for other pairs does not depend on specific mechanism of CheY dephosphorylation. Notably, the overall gene order in individual prokaryotes, including those with most studied chemotaxis systems [14], is only conserved among closely related species (Figure S1). This suggests—in agreement with the results of our modeling analysis—that it is primarily the pairwise gene coupling rather than the consensus as a whole that is under selection.

Additional statistical analysis of distances between neighboring chemotaxis genes (Figure S2) confirmed that most frequently coupled genes are typically close enough to each other, less than 30 nucleotides, to allow a simultaneous ribosome interaction with the stop codon of upstream gene and the RBS of the downstream gene, and are thus likely to be translationally coupled. The only exceptions are *mcp_mcp* and *cheW_mcp* pairs that are frequently separated by a larger intergenic distance. Such separation is consistent with genetic organization in *E. coli*, where *cheW* and the downstream *mcp* (*tar*) belong to different operons, and three receptor genes are uncoupled from the chemotaxis operons.

Discussion

Translational Coupling as a Mechanism of Noise Reduction

Intercellular variation in protein levels in a genetically homogeneous cell population, or gene expression noise, is the major source of perturbations that affect performance of all cellular pathways. In prokaryotes, as in eukaryotes, the largest part of this noise appears to originate from fluctuations of global factors that affect expression of all genes in a cell, and from stochastic variations in promoter activity [15–18]. Since bacterial genes of related function are typically transcriptionally coupled through the polycistronic gene organization and common regulation, concerted variations in the levels of related genes are therefore expected to be the dominant type of the expression noise. Strong correlation in the single-cell levels of individual chemotaxis proteins has been indeed observed in *E. coli*, and the chemotaxis pathway was shown to be primarily robust against such concerted variation [7].

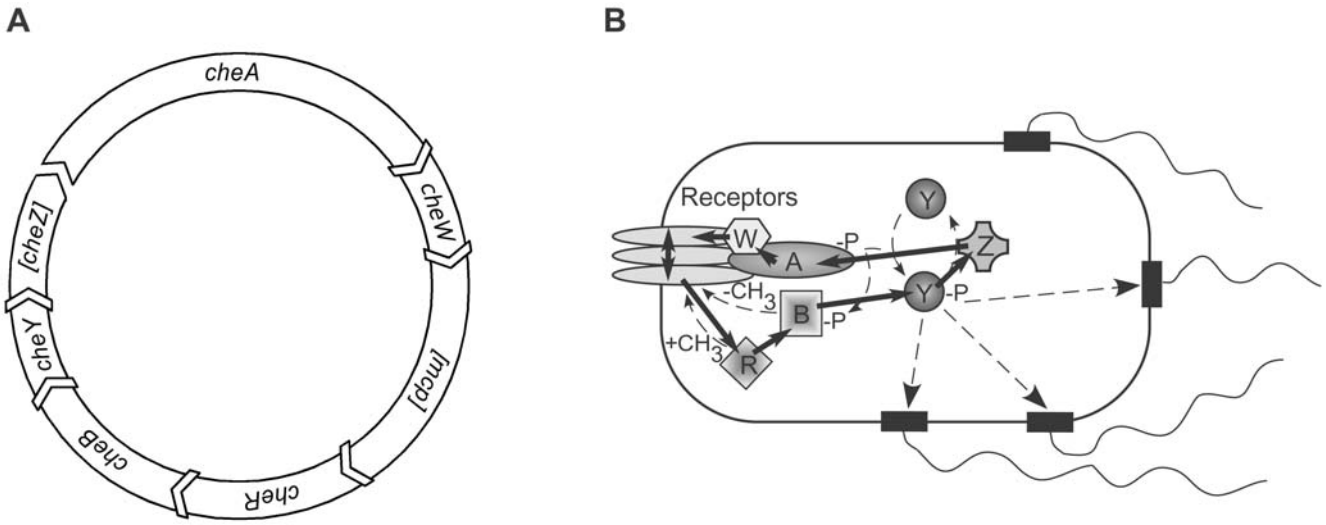

Figure 5. Genetic coupling of chemotaxis genes in bacteria. (A) Preferential order of pairwise chemotaxis gene coupling among analyzed bacteria. Receptor (*mcp*) gene is shown in brackets because the number of receptor genes between *cheW* and *cheR* is variable; *cheZ* is shown in brackets because it is only present in a subset of bacteria. See Table 1 and Tables S2 and S3 for the frequencies of relative occurrence. (B) Genetic coupling (solid arrows) among chemotaxis proteins shown for *E. coli* pathway. Thin dashed arrows denote pathway reactions and CheY-P binding to flagellar motor.
doi:10.1371/journal.pbio.1000171.g005

However, stochasticity of translation results in significant uncorrelated variation in the levels of two proteins produced from one polycistronic mRNA [7], and it is thus not surprising that bacteria evolved mechanisms to reduce effects of such translational noise. Translational coupling between bacterial genes in operons has been described before, primarily in metabolic operons [10,11,19–21], but also between genes encoding ribosomal proteins [8] and a two-component sensor [9]. Such coupling mostly happens when the stop codon of the upstream gene is close to or overlaps with the start codon or with the Shine-Dalgarno (SD) sequence of the downstream gene. Translational coupling may result from a combination of several factors. First, translation of the upstream gene will locally increase the number of ribosomes close to the initiation codon of the downstream gene, which could then efficiently reinitiate translation of the downstream gene even in absence of a strong SD sequence [20]. Second, ribosomes translating the upstream gene will also unwind any secondary structure of the mRNA that might form around the SD sequence of the downstream gene, as long as this sequence belongs to the translated region of the upstream gene. Such opening of the SD sequence will facilitate both reinitiation of translation by already bound ribosomes and entry of new ribosomes [19]. The latter mechanism is supported by the observed inverse correlation of coupling with the translation strength, since in this case, coupling is expected to saturate as soon as the mRNA is completely unfolded. Whatever the mechanism of coupling is, it has been proposed to enable a tighter control of the stoichiometry of protein complexes [10].

Selection for Robustness Can Explain Order of Chemotaxis Genes

Our experimental results and computational analyses suggest that—along with the robust pathway topology and transcriptional coupling between chemotaxis genes—translational coupling is yet another factor that contributes to the robustness of signaling in chemotaxis. Functional importance of the tight pairwise coupling between protein levels was demonstrated by the improvement of chemotaxis when any of tested endogenous pairs was expressed from one bicistronic construct. Furthermore, selection for the enhanced posttranscriptional coupling between protein levels was observed in cells that were spreading most efficiently in a chemotaxis assay. Translational coupling appears to specifically compensate the output level of CheY-P and thereby CW motor bias against stochastic variations in translation of individual genes. In silico analysis demonstrated higher robustness of particular arrangements of chemotaxis genes against translational noise, namely those that maximize the number of gene couples with opposing effects on the CheY-P level. Although better knowledge of modeling parameters would be required to definitively resolve relative positions of the gene orders with highest ranking within our model, *E. coli* gene order ranked best for output robustness when we assumed that the weakly translated genes *cheR* and *cheB* have slightly higher (1.5-fold) noise levels than the more efficiently translated genes *cheY* and *cheZ*. Thus, both modeling and experiments suggest that *E. coli* gene order is likely to have evolved under pressure to maximize coupling between expression of antagonistic proteins, and thereby robustness of the pathway output. This idea is further supported by the observation that the order of chemotaxis genes in bacterial genomes is not random, with a strong bias towards the same gene coupling as in *E. coli*.

Selection for coupling in all studied *E. coli* gene pairs can be explained based on the known properties of the chemotaxis pathway (Figure 5B). CheA and CheW form a stable complex with chemotaxis receptors [22,23]. The stoichiometry and functional properties of this complex are affected by the relative levels of individual proteins [24,25], and relative translation of CheA and CheW is thus expected to be under a tight control. Coupling between expression of CheY and CheZ serves to reduce the level of CheY-P when CheY is up-regulated, by increasing the level of phosphatase and thereby returning the pathway to homeostasis. Inversely, coupling could increase the rate of CheY phosphorylation when CheZ is up-regulated. Coupling between the levels of CheR and CheB is also expected to increase robustness of the CheY-P output, since these proteins form a pair of counteracting enzymes that control the steady-state level of receptor methylation and, as a consequence, that of kinase activity. From the point of robustness, coupling between CheB and CheY is not surprising

either. On one hand, these two proteins compete for CheA-dependent phosphorylation, including stimulation-dependent competitive binding at the P2 domain of CheA [26,27]. On the other hand, higher CheB activity reduces the level of receptor methylation and thereby the rate of CheY phosphorylation. A coelevated level of CheY would thus counteract an increase in the level of CheB both directly, by reducing CheB phosphorylation, and indirectly, by increasing the level of phospho-CheY. Similarly, the up-regulation of CheB should counterbalance an increased level of CheY.

In addition to these pairs, our bioinformatics analysis revealed a strong coupling between receptor (*mcp*) genes and *cheW*, in agreement with these gene products being parts of the same stable signaling complex. This coupling is stronger than that between receptors and *cheA*, apparently consistent with a role of CheW as an adapter between receptors and CheA [22]. Coupling between *cheZ* and *cheA*, which is also statistically significant in *cheZ*-containing genomes, could serve a similar function as the coupling between *cheY* and *cheZ*, and compensate for an increase in the level of phosphatase by an increase in the kinase activity. A compensatory effect on noise is also expected for the coupling between *cheA* and *cheB*, since CheB provides a negative feedback to the kinase activity. The reason for coupling between receptor genes (or *cheW*) and *cheR* is less obvious, but keeping a proper ratio between receptors and methyltransferase activity might be important for maintaining a constant steady-state level of receptor methylation. Significant coupling between *cheY* and *cheA* resembles translation coupling observed in other two-component systems, although theoretical analysis suggests that such coupling should only take place when—like in these other systems—the kinase is bifunctional, i.e., has a phosphatase activity [28]. This prediction remains to be experimentally tested for bacterial chemotaxis systems.

Evolution of Gene Order in Chemotaxis Operons

In agreement with our mathematical model, pairwise coupling between particular chemotaxis genes rather than the gene order as a whole appears to be primarily under evolutionary selection, with the overall gene order being conserved only among closely related species. It is thus unlikely that the observed consensus is a consequence of the conservation—or lateral transfer—of the same chemotaxis operon across prokaryotes. Individual genes appear to have been rearranged multiple times throughout the evolution, with differences in gene order between groups of closely related species possibly reflecting variations in the pathway topology and gene regulation.

Proposed robustness-driven mechanism of gene ordering in operons can be seen as a refinement of the models that explain operon formation by positive selection for the coregulation of genes encoding components of the same pathway or of one multicomplex [29]. Particularly, it is closely related to the previously discussed balance hypothesis [30,31], which postulates that an imbalance in the concentrations of two subcomponents of a multiprotein complex can result in the formation of nonfunctional complexes with wrong stoichiometry and will be therefore under negative evolutionary selection. The balance hypothesis can be well used, for example, to explain the polycistronic organization of metabolic genes, which indeed frequently encode components of multisubunit enzymes. In case of chemotaxis, strong coupling between *cheA* and *cheW* presumably results from similar constrains. However, our model does not require that proteins form stable complexes, or even directly interact with each other, to have mutually compensatory effects on the output and thus to benefit from coupling. At the same time, we predict that coupling of other proteins in the pathway can be detrimental and thus under negative selection. Our analysis thus extends the regulation-based model of operon formation to explain the internal operon structure.

Although our model does not describe the process of chemotaxis operon formation itself, evolutionary selection for the gradual increase in proximity of chemotaxis genes through genome rearrangements seems to be the most likely mechanism. Due to the correlation in expression of bacterial genes that are close on the chromosome [32,33], such increase in proximity would lead to the gradual increase in gene coupling and thereby in robustness of the pathway output. Additional selection for the lateral gene cotransfer, as proposed by the selfish operon model [34], might be also involved in the initial grouping of chemotaxis genes. However, because in this case transferred genes as a group must provide an immediate benefit to the host, selfish operon model would require grouping and cotransfer of multiple genes involved in flagellar assembly and would therefore not explain emergence of selective pairing between chemotaxis genes.

Conclusions

Taken together, our results emphasize the importance of translational coupling and gene order in the overall organization of the chemotaxis pathway in *E. coli* and other bacteria. Strong bias towards a particular order of genes on the chromosome was predicted by our computer simulations assuming selection for robustness of the pathway output against gene expression noise, and confirmed by the bioinformatics' analysis of sequenced bacterial genomes. Such organization is evolutionary beneficial because it improves robustness of the signaling output without adding a cost of the increased complexity and is thus expected to be ubiquitous in bacterial networks. Although translational coupling is absent in eukaryotes, expression levels of neighboring genes are frequently coupled on the level of chromatin remodeling [35,36]. Moreover, it has been recently proposed that segregation of eukaryotic genes into particular chromosomal regions is driven by the reduction in gene expression noise [37]. The gene order on the chromosome may thereby contribute to network robustness in all organisms.

Materials and Methods

Strains and Plasmids

E. coli K-12 strains used in this study were derived from RP437 [38]. All strains and plasmids are summarized in Tables 2 and 3. Monocistronic constructs expressing YFP fusions to CheR, CheB, CheY, CheZ, and CheA under moderately strong RBSs and pTrc promoter inducible by isopropyl β-D-thiogalactoside (IPTG) have been described before [13,26,39–41]. They were used to obtain constructs with strong RBSs (summarized in Table 4) and bicistronic constructs by using PCR and cloning to modify the upstream sequence. Because expression of *cheY* is strongly up-regulated by a sequence inside *cheB* gene (A. Müller and V. Sourjik, unpublished data), a nontranslated 316-nucleotide fragment of *cheB* was included upstream of the *cheY* start codon in pVS319 (−316_*cheY-eyfp*) plasmid to achieve expression comparable to pVS142 (*cheB_cheY-eyfp*) construct. To reduce levels of expression for the *cheB_cheY-eyfp* and −316_*cheY-eyfp* constructs, both fragments were cloned under weaker pBAD promoter inducible by L-arabinose, to obtain pLL33 and pLL36, respectively.

Growth Conditions

Overnight cultures were grown in tryptone broth (TB; 1% tryptone, 0.5% NaCl) containing ampicillin (100 μg/ml) or

Table 2. Strains used in this study.

Strain	Description/Relevant Genotype	Reference
RP437	Wild type for chemotaxis	[38]
VS100	*ΔcheY*	[40]
VS104	*Δ(cheYcheZ)*	[41]
VS161	*ΔcheZ*	[13]
RP4972	*ΔcheB*	J. S. Parkinson, personal gift

doi:10.1371/journal.pbio.1000171.t002

chloramphenicol (100 μg/ml) at 30°C for 16 h. For measurements of the YFP expression in liquid cultures, overnight cultures were diluted 1:100 in fresh TB containing ampicillin and indicated concentrations of IPTG or L-arabinose. Cell cultures were allowed to grow 3.5–4 hours at 34°C in a rotary shaker until an optical density at 600 nm (OD_{600}) of 0.45, then harvested by centrifugation (8,000 rpm, 1 min), washed, and then resuspended in tethering buffer (10 mM potassium phosphate, 0.1 mM EDTA, 1 μM L-methionine, 10 mM sodium lactate [pH 7]).

TB soft agar (swarm) plates were prepared by supplementing TB with 0.3% agar (Applichem), required antibiotics (100 μg/ml ampicillin; 34 μg/ml chloramphenicol), and indicated concentrations of IPTG and L-arabinose. Plates were inoculated using fresh cells from LB agar plates, and swarm assays were performed for 6–

Table 4. Upstream ribosome binding sequences of the fusion constructs.

Construct	Upstream Sequence[a]
RBS^{CheR}	*GAGCTC*TTGAGAAGGCGCT**ATG**
RBS^{CheB}	*GAGCTC*AGTAAGGATTAACG**ATG**
RBS^{CheY}	*GAGCTC*CGTATTTAAATCAGGAGTGTGAA**ATG**
RBS^{CheZ}	*GAGCTC*CAGGGCATGTGAGGATGCGACT**ATG**
RBS^{CheYS}	*ACTAGT*GAAGGAGTGTGCC**ATG**
$RBS^{CheR\uparrow}$	*GAGCTC*GATAGGGTGGGCGCT**ATG**
$RBS^{CheR\uparrow\uparrow}$	*GAGCTC*GATAGGAAAGGCGCT**ATG**
$RBS^{CheB\uparrow}$	*GAGCTC*AAGAGGAAATTAACG**ATG**
$RBS^{CheY\uparrow}$	*GAGCTC*AATAGAGGAAATGTGAA**ATG**

A single upward arrow (↑) indicates an enhanced RBS; double arrows (↑ ↑) indicate a strongly enhanced RBS.

[a]Italic type indicates recognition site of restriction enzymes, SacI or SpeI, used for cloning the constructs; boldface font indicates the start codon.

doi:10.1371/journal.pbio.1000171.t004

Table 3. Plasmids used in this study.

Plasmid	Description[a]	Reference
pTrc99A	Expression vector; pBR ori, pTrc promotor, Amp^R	[45]
pBAD33	Expression vector; pACYC ori, pBAD promotor, Cm^R	[46]
pDK57	RBS^{CheYS2}_$CheA_S$-YFP expression plasmid; pTrc99a derivate	[26]
pDK66	Expression vector for cloning of C-terminal YFP fusions; RBS^{CheYS} pTrc99a derivative	[47]
pVS18	RBS^{CheY}_CheY-YFP expression plasmid; pTrc99a derivate	[41]
pVS64	RBS^{CheZ}_CheZ-YFP expression plasmid; pTrc99a derivate	[39]
pVS88	RBS^{CheY}_CheY-YFP_ RBS^{CheZ}_CheZ-YFP bicistronic construct; pTrc99a derivate	[25]
pVS137	RBS^{CheR}_CheR-YFP expression plasmid; pTrc99a derivate	[13]
pVS138	RBS^{CheB}_CheB-YFP expression plasmid; pTrc99a derivate	[13]
pVS142	RBS^{CheB}_CheB_CheY-YFP expression plasmid; pTrc99a derivate	This work
pVS145	RBS^{CheR}_CheR_CheB-YFP expression plasmid; pTrc99a derivate	This work
pVS261	RBS^{CheYS}_CheA-YFP expression plasmid; pTrc99a derivate	This work
pVS305	RBS^{CheY}_CheY_CheZ-YFP expression plasmid; pTrc99a derivate	This work
pVS319	−316_CheY-YFP expression plasmid; pTrc99a derivate	This work
pVS321	$RBS^{CheY\uparrow}$_CheY_CheZ-YFP expression plasmid; pTrc99a derivate	This work
pVS450	$RBS^{CheB\uparrow}$_CheB_CheY-YFP expression plasmid; pTrc99a derivate	This work
pVS451	$RBS^{CheR\uparrow\uparrow}$_CheR_CheB-YFP expression plasmid; pTrc99a derivate	This work
pVS452	$RBS^{CheR\uparrow\uparrow}$_CheR-YFP expression plasmid; pTrc99a derivate	This work
pVS487	$RBS^{CheB\uparrow}$_CheB-YFP expression plasmid; pTrc99a derivate	This work
pVS490	RBS^{CheYS2}_CheA_CheW-YFP expression plasmid; pTrc99a derivate	This work
pVS495	$RBS^{CheY\uparrow}$_CheY-YFP expression plasmid; pTrc99a derivate	This work
pVS520	RBS^{CheYS}_$CheA_S$_CheW-YFP expression plasmid; pTrc99a derivate	This work
pAM80	$RBS^{CheR\uparrow}$_CheR-YFP expression plasmid; pTrc99a derivate	This work
pAM81	$RBS^{CheR\uparrow}$_CheR_CheB-YFP expression plasmid; pTrc99a derivate	This work
pLL33	−316_CheY-YFP expression plasmid; pBAD33 derivate	This work
pLL36	RBS^{CheB}_CheB_CheY-YFP expression plasmid; pBAD33 derivate	This work

[a]See Table 4 for description and exact sequence of RBS.

doi:10.1371/journal.pbio.1000171.t003

8 h at 34°C. Images of swarm plates were taken using a Canon EOS 300 D (DS6041) camera, and analyzed with ImageJ (Wayne Rasband, NIH) to determine the diameter of the swarm rings.

Quantification of Gene Expression

Mean expression levels of fluorescent proteins were quantified in a population of approximately 10^4 cells as described before [7] using flow cytometry on a FACScan (BD Biosciences) equipped with an argon 488-nm laser. FACScan data were analyzed using CellQuestTM Pro 4.0.1 software. Mean value of the autofluorescence background, measured for control cells, was subtracted from all values. Single-cell protein levels were measured using fluorescence microscopy on a Zeiss AxioImager Z1 microscope equipped with an ORCA AG CCD Camera (Hamamatsu) and HE YFP (Excitation BP 500/25; Dichroic LP 515; Emission BP 535/30) and HE CFP (Excitation BP 436/25; Dichroic LP 455; Emission BP 480/40) filter sets. Integral levels of fluorescence in individual cells were quantified using an automated custom-written ImageJ plug-in [13] and normalized to cell length to obtain relative concentrations of fluorescent proteins [42].

Analysis of Gene Order

Analysis of the order of chemotaxis genes was performed using a custom-written Perl program. The program scanned text files of 824 microbial genomes from the GenBank database using variable regular expressions to identify chemotaxis genes in the annotation. Features which may contain information about the gene function (\gene, \function, \product, \note) were successively retrieved for every coding sequence (CDS) in a genome, recorded, and then analyzed for occurrence of chemotaxis terms. Because the description of chemotaxis genes was often periphrastic, we performed a preliminary manual analysis of selected genomes to determine the most frequently used and misused synonyms, which were further used to define positive and negative terms for automatic chemotaxis genes recognition. A chemotaxis gene was recognized if its annotation contained one of the positive terms that point to its specific function and did not contain negative terms which indicate that the gene function is ambiguous or related to another chemotaxis gene (Table S1). Identified genes were then verified manually by looking through their extracted annotations, to remove possible false-positive entries; this verification confirmed high efficiency of the annotation-based gene recognition. Only genes with clearly defined chemotaxis-related annotations were included in the final analysis. Additionally, we restricted our analysis to chemotaxis genes that are present in *E. coli*, which are well annotated and —with the sole exception of *cheZ*—conserved in most prokaryotes. Homologs of these genes were found in 527 genomes. Starting and ending nucleotide positions of each recognized chemotaxis gene as well as the upstream and downstream neighboring genes were recorded. Names and genomic positions of all recognized chemotaxis genes are provided as supporting information (Text S2). The resulting gene duplets were analyzed to calculate co-occurrences of neighbors (Table 1 and Tables S2 and S3) and to determine intergenic distances (Figure S2).

Phylogenetic analysis of chemotaxis gene order in selected genomes (Figure S1) was performed using the Web-based program Composition Vector Tree (CVTree, http://cvtree.cbi.pku.edu.cn/), which constructs *phylogenetic trees* based on the organism's complete genomic sequence [43]. The resulting phylogenetic trees were plotted using a Java-based program Archaeopteryx (http://www.phylosoft.org/archaeopteryx/).

Computer Simulations

To calculate the adapted level of free phosphorylated CheY, we simulated the pathway using differential equations based on mass action kinetics. Rates and binding constants are taken from in vitro and in vivo experiments (http://www.pdn.cam.ac.uk/comp-cell). The mathematical model includes all known protein interactions among CheR, CheB, CheY, and CheZ. The adapted receptor activity is determined by the methylation level and consequently by the ratio between receptor-bound CheR and CheB, allowing us to omit all details of transient adaptation kinetics. The relation of phosphorylated CheY to the flagellar motor rotation bias follows from the experimentally determined motor response curve [44]. Our mathematical model reflects the experimentally observed robustness of the pathway output against concerted overexpression of all chemotaxis proteins but shows the expected sensitivity to independent variations in protein levels. Effects of translational noise on protein concentration has been simulated by Gaussian random variables with means given by the measured wild-type concentrations and a common standard deviation over mean of 0.05 to arrive at the experimentally observed cell-to-cell variations of the CW bias [7]. The strength of translational coupling constant was set to 25% of the mean translational efficiency to generate the rank list (Figure 4). The error bars in Figure 4 indicate the 95% confidence intervals for the standard deviation of the CW bias for a cell population of 10^5 individuals, resulting from data resampling using bootstrap. The influence of transcriptional noise or extrinsic noise on the gene order was not significant as both CheY-P level of our chemotaxis pathway model and experimentally measured CW rotation bias [7] are almost insensitive to increased transcriptional activity. The details of mathematical model are provided as supporting information (Text S1)

Supporting Information

Figure S1 Phylogenetic map of chemotaxis gene order in selected prokaryotes. Order of chemotaxis genes in selected prokaryotes was mapped on the phylogenetic tree, constructed as described in Materials and Methods. Receptor genes or *mcp* are indicated by m, *cheA* by A, *cheB* by B, and so on. A minus sign (−) indicates hypothetical protein of unknown function or protein unrelated to chemotaxis. Independent gene groups are separated by dots.
Found at: doi:10.1371/journal.pbio.1000171.s001 (0.44 MB PDF)

Figure S2 Pairwise distances between the most frequently neighboring chemotaxis genes over 527 genomes. Distance between neighboring chemotaxis genes was defined as the number of nucleotides between the last nucleotide of the stop codon of the upstream gene and the first nucleotide of start codon of the downstream gene. Intergenic distances were determined as described in Materials and Methods, and plotted as histograms.
Found at: doi:10.1371/journal.pbio.1000171.s002 (0.47 MB PDF)

Figure S3 Chemotactic selection for posttranscriptional coupling of CheY-YFP and CheZ-CFP at 10 μM IPTG induction. (A) Chemotaxis-driven spreading of VS104 [*Δ(cheY-cheZ)*]/pVS88 cells on soft agar (swarm) plates. (B and C) Scatter plots of single-cell levels of CheY-YFP and CheZ-CFP in cells taken from the edge (B) and from the middle (C) of the spreading colony. Relative concentrations of fluorescent proteins in individual cells were determined using fluorescence microscopy as described in Materials and Methods. See description of Figure 3 in the main text for more details.
Found at: doi:10.1371/journal.pbio.1000171.s003 (0.62 MB PDF)

Table S1 Terms used for identification of chemotaxis genes.
Found at: doi:10.1371/journal.pbio.1000171.s004 (0.07 MB DOC)

Table S2 Pairwise occurrence of chemotaxis genes in 200 genomes containing *cheZ*.
Found at: doi:10.1371/journal.pbio.1000171.s005 (0.05 MB DOC)

Table S3 Pairwise occurrence of chemotaxis genes in 327 genomes without *cheZ*.
Found at: doi:10.1371/journal.pbio.1000171.s006 (0.05 MB DOC)

Text S1 Mathematical model.
Found at: doi:10.1371/journal.pbio.1000171.s007 (0.15 MB PDF)

Text S2 List of identified chemotaxis genes.
Found at: doi:10.1371/journal.pbio.1000171.s008 (1.22 MB TXT)

Acknowledgments

We thank David Kentner for sharing constructs and assistance with cloning, and Simone Pröbstle for assistance with swarming experiments.

Author Contributions

The author(s) have made the following declarations about their contributions: Conceived and designed the experiments: VS. Performed the experiments: LL AM FSP. Analyzed the data: KB MK VS. Contributed reagents/materials/analysis tools: LL KB NV MK VS. Wrote the paper: MK VS. Designed the computational simulations: MK. Performed the computational simulations: KB MK. Designed the bioinformatics analysis: NV. Performed the bioinformatics analysis: NV DL.

References

1. Wadhams GH, Armitage JP (2004) Making sense of it all: bacterial chemotaxis. Nat Rev Mol Cell Biol 5: 1024–1037.
2. Sourjik V (2004) Receptor clustering and signal processing in *E. coli* chemotaxis. Trends Microbiol 12: 569–576.
3. Alon U, Surette MG, Barkai N, Leibler S (1999) Robustness in bacterial chemotaxis. Nature 397: 168–171.
4. Barkai N, Leibler S (1997) Robustness in simple biochemical networks. Nature 387: 913–917.
5. Mello BA, Tu Y (2003) Perfect and near-perfect adaptation in a model of bacterial chemotaxis. Biophys J 84: 2943–2956.
6. Yi TM, Huang Y, Simon MI, Doyle J (2000) Robust perfect adaptation in bacterial chemotaxis through integral feedback control. Proc Natl Acad Sci U S A 97: 4649–4653.
7. Kollmann M, Løvdok L, Bartholome K, Timmer J, Sourjik V (2005) Design principles of a bacterial signalling network. Nature 438: 504–507.
8. Baughman G, Nomura M (1983) Localization of the target site for translational regulation of the L11 operon and direct evidence for translational coupling in *Escherichia coli*. Cell 34: 979–988.
9. Liljestrom P, Laamanen I, Palva ET (1988) Structure and expression of the ompB operon, the regulatory locus for the outer membrane porin regulon in *Salmonella typhimurium* LT-2. J Mol Biol 201: 663–673.
10. Oppenheim DS, Yanofsky C (1980) Translational coupling during expression of the tryptophan operon of *Escherichia coli*. Genetics 95: 785–795.
11. Schumperli D, McKenney K, Sobieski DA, Rosenberg M (1982) Translational coupling at an intercistronic boundary of the *Escherichia coli* galactose operon. Cell 30: 865–871.
12. Smith RA, Parkinson JS (1980) Overlapping genes at the cheA locus of *Escherichia coli*. Proc Natl Acad Sci U S A 77: 5370–5374.
13. Lovdok L, Kollmann M, Sourjik V (2007) Co-expression of signaling proteins improves robustness of the bacterial chemotaxis pathway. J Biotechnol 129: 173–180.
14. Szurmant H, Ordal GW (2004) Diversity in chemotaxis mechanisms among the bacteria and archaea. Microbiol Mol Biol Rev 68: 301–319.
15. Ozbudak EM, Thattai M, Kurtser I, Grossman AD, van Oudenaarden A (2002) Regulation of noise in the expression of a single gene. Nat Genet 31: 69–73.
16. Raser JM, O'Shea EK (2004) Control of stochasticity in eukaryotic gene expression. Science 304: 1811–1814.
17. Raser JM, O'Shea EK (2005) Noise in gene expression: origins, consequences, and control. Science 309: 2010–2013.
18. Rosenfeld N, Young JW, Alon U, Swain PS, Elowitz MB (2005) Gene regulation at the single-cell level. Science 307: 1962–1965.
19. Rex G, Surin B, Besse G, Schneppe B, McCarthy JE (1994) The mechanism of translational coupling in *Escherichia coli*. Higher order structure in the atpHA mRNA acts as a conformational switch regulating the access of de novo initiating ribosomes. J Biol Chem 269: 18118–18127.
20. Govantes F, Andujar E, Santero E (1998) Mechanism of translational coupling in the nifLA operon of *Klebsiella pneumoniae*. EMBO J 17: 2368–2377.
21. Little S, Hyde S, Campbell CJ, Lilley RJ, Robinson MK (1989) Translational coupling in the threonine operon of *Escherichia coli* K-12. J Bacteriol 171: 3518–3522.
22. Gegner JA, Graham DR, Roth AF, Dahlquist FW (1992) Assembly of an MCP receptor, CheW, and kinase CheA complex in the bacterial chemotaxis signal transduction pathway. Cell 70: 975–982.
23. Schulmeister S, Ruttorf M, Thiem S, Kentner D, Lebiedz D, et al. (2008) Protein exchange dynamics at chemoreceptor clusters in *Escherichia coli*. Proc Natl Acad Sci USA 105: 6403–6408.
24. Levit MN, Grebe TW, Stock JB (2002) Organization of the receptor-kinase signaling array that regulates *Escherichia coli* chemotaxis. J Biol Chem 277: 36748–36754.
25. Sourjik V, Berg HC (2004) Functional interactions between receptors in bacterial chemotaxis. Nature 428: 437–441.
26. Kentner D, Sourjik V (2009) Dynamic map of protein interactions in the *Escherichia coli* chemotaxis pathway. Mol Syst Biol 5: 238.
27. Li J, Swanson RV, Simon MI, Weis RM (1995) The response regulators CheB and CheY exhibit competitive binding to the kinase CheA. Biochemistry 34: 14626–14636.
28. Shinar G, Milo R, Martinez MR, Alon U (2007) Input output robustness in simple bacterial signaling systems. Proc Natl Acad Sci U S A 104: 19931–19935.
29. Rocha EP (2008) The organization of the bacterial genome. Annu Rev Genet 42: 211–233.
30. Papp B, Pal C, Hurst LD (2003) Dosage sensitivity and the evolution of gene families in yeast. Nature 424: 194–197.
31. Veitia RA (2002) Exploring the etiology of haploinsufficiency. Bioessays 24: 175–184.
32. Carpentier AS, Torresani B, Grossmann A, Henaut A (2005) Decoding the nucleoid organisation of *Bacillus subtilis* and *Escherichia coli* through gene expression data. BMC Genomics 6: 84.
33. Jeong KS, Ahn J, Khodursky AB (2004) Spatial patterns of transcriptional activity in the chromosome of *Escherichia coli*. Genome Biol 5: R86.
34. Lawrence JG (2003) Gene organization: selection, selfishness, and serendipity. Annu Rev Microbiol 57: 419–440.
35. Batada NN, Urrutia AO, Hurst LD (2007) Chromatin remodelling is a major source of coexpression of linked genes in yeast. Trends Genet 23: 480–484.
36. Raj A, Peskin CS, Tranchina D, Vargas DY, Tyagi S (2006) Stochastic mRNA synthesis in mammalian cells. PLoS Biol 4: e309. doi:10.1371/journal.-pbio.0040309.
37. Batada NN, Hurst LD (2007) Evolution of chromosome organization driven by selection for reduced gene expression noise. Nat Genet 39: 945–949.
38. Parkinson JS, Houts SE (1982) Isolation and behavior of *Escherichia coli* deletion mutants lacking chemotaxis functions. J Bacteriol 151: 106–113.
39. Liberman L, Berg HC, Sourjik V (2004) Effect of chemoreceptor modification on assembly and activity of the receptor-kinase complex in *Escherichia coli*. J Bacteriol 186: 6643–6646.
40. Sourjik V, Berg HC (2000) Localization of components of the chemotaxis machinery of *Escherichia coli* using fluorescent protein fusions. Mol Microbiol 37: 740–751.
41. Sourjik V, Berg HC (2002) Receptor sensitivity in bacterial chemotaxis. Proc Natl Acad Sci U S A 99: 123–127.
42. Thiem S, Sourjik V (2008) Stochastic assembly of chemoreceptor clusters in *Escherichia coli*. Mol Microbiol 68: 1228–1236.
43. Qi J, Luo H, Hao B (2004) CVTree: a phylogenetic tree reconstruction tool based on whole genomes. Nucleic Acids Res 32: W45–47.
44. Cluzel P, Surette M, Leibler S (2000) An ultrasensitive bacterial motor revealed by monitoring signaling proteins in single cells. Science 287: 1652–1655.
45. Amann E, Ochs B, Abel KJ (1988) Tightly regulated tac promoter vectors useful for the expression of unfused and fused proteins in *Escherichia coli*. Gene 69: 301–315.
46. Guzman LM, Belin D, Carson MJ, Beckwith J (1995) Tight regulation, modulation, and high-level expression by vectors containing the arabinose pBAD promoter. J Bacteriol 177: 4121–4130.
47. Kentner D, Thiem S, Hildenbeutel M, Sourjik V (2006) Determinants of chemoreceptor cluster formation in *Escherichia coli*. Mol Microbiol 61: 407–417.

Biological Chemistry 'Just Accepted' paper ● ISSN (online) 1437-4315
D O I: 10.1515/BC.2009.130

Review

Chemotaxis: how bacteria use memory

Nikita Vladimirov[1,*] and Victor Sourjik[2]

[1]Interdisziplinäres Zentrum für Wissenschaftliches Rechnen der Universität Heidelberg (IWR), Im Neuenheimer Feld 368, D-69120 Heidelberg, Germany
[2]Zentrum für Molekulare Biologie der Universität Heidelberg, DKFZ-ZMBH Alliance, Im Neuenheimer Feld 282, D-69120 Heidelberg, Germany

*Corresponding author
e-mail: nikita.vladimirov@gmail.com

Abstract

Bacterial chemotaxis represents one of the simplest and best studied examples of unicellular behaviour. Chemotaxis allows swimming bacterial cells to follow chemical gradients in the environment by performing temporal comparisons of ligand concentrations. The process of chemotaxis in the model bacterium *Escherichia coli* has been studied to great molecular detail over the last 40 years, using a large range of experimental tools to investigate physiology, genetics and biochemistry of the system. Abundance of quantitative experimental data enabled detailed computational modelling of the pathway and theoretical analyses of such properties as robustness and signal amplification. Because of the temporal mode of gradient sensing in bacterial chemotaxis, molecular memory is an essential component of the chemotaxis pathway. Recent studies suggest that the memory time scale has been evolutionary optimized to perform optimal comparisons of stimuli while swimming in the gradient. Moreover, noise in the adaptation system, which results from variations of the adaptation rate both over time and among cells, might be beneficial for the overall chemotactic performance of the population.

Keywords: adaptation; *Escherichia coli*; optimal memory.

Introduction

Many motile unicellular organisms are known to direct their movement towards or away from gradients of specific substances – the process called chemotaxis. It plays an important role in the microbial population dynamics. Chemotactic bacteria in a nonmixed environment – that is in presence of nutrient gradients – have significant growth advantage (Pilgram and Williams, 1976; Freter et al., 1978; Kennedy and Lawless, 1985; Kennedy, 1987). Modeling of microbial population dynamics indicates that motility and chemotactic ability can be as important for evolutionary competition as cell growth rate (Kelly et al., 1988; Lauffenburger, 1991).

While eukaryotic cells are able to sense gradients by direct comparison of concentrations across the cell body (Chung et al., 2001), the bacteria employ temporal comparisons along swimming trajectories (Berg and Brown, 1972). Theoretical analysis suggested that such strategy is superior to direct spatial comparisons for objects of bacterial size and swimming speed (Berg and Purcell, 1977). Adapted bacteria have two swimming modes: runs, which are periods of long straight swimming, and tumbles, in which bacterium stops and rapidly changes its orientation (Figure 1A). The runs of a swimming bacterium are interrupted by tumbles, therefore the bacterium moves in a random walk. In response to attractant gradient, this random walk becomes biased: the runs become longer up the gradient, and the cells migrate towards the attractant. On the contrary, in repellent gradient the runs are longer down the gradient (Tsang et al., 1973).

The frequency of tumbles is controlled by the chemotaxis network through switching of individual motors. During a run, flagellar motors rotate counter-clockwise (CCW) and their flagella form a bundle, which works like a screw to propel the cell. Switching of one or several flagellar motors to clockwise (CW) rotation initiates a tumble. During the tumble, the cell stops and changes its orientation because one or more CW-rotating flagella break out of the bundle and rotate as separate rigid screws, deflecting the cell body to a new direction (Turner et al., 2000; Darnton et al., 2007). The CW rotation is induced by the phosphorylated protein CheY (CheYp), which binds to the motor protein FliM and changes the motor bias in a highly sensitive mode (Cluzel et al., 2000). CheYp itself is a small molecule which freely diffuses in the cytoplasm between the receptor clusters and flagellar motors. CheY is phosphorylated by the histidine kinase CheA, which is bound to clusters of transmembrane receptors and the adaptor protein CheW (Figure 1B). Each receptor can be in either active or inactive conformation, depending on ligand binding to its outer (periplasmic) domain and the methylation level of its inner (cytoplasmic) domain. The active receptor promotes CheA autophosphorylation, eliciting downstream phosphorylation of the response regulator CheY. CheYp is dephosphorylated by its phosphatase CheZ, which increases the CheYp turnover. Receptors are methylated by the enzyme CheR and demethylated by its counteracting partner CheB, and methylation regulates the receptor activity (for reviews, see Sourjik, 2004; Wadhams and Armitage, 2004).

The methylation of receptors provides a sort of chemical ’memory’, which allows the cell to compare the current ligand concentration to the past. The idea that bacterial chemotaxis represents probably the simplest behavioral system, and therefore can be related to neuroscience, was discussed in detail by the founders of modern chemotaxis field. For reviews, see (Adler, 1975; Koshland, 1980). Indeed, there are several striking similarities between sensory reception in bacteria and higher organisms, in particular between bacterial cells and neurons (Koshland, 1980): ‘In both cases there is a processing system of moderate complexity within the cell and an output response. In the case of the neuron the output can be the release of a neurotransmitter or an electrical voltage; in the case of the bacterium it is a change in the flagellar rotation. Since the neuron is far larger than the bacterium, it must use additional devices such as an action potential to transmit information over much larger distances. And this of course is one of the distinguishing differences between the two cells. On the other hand the bacterial system shows properties of adaptation, memory, receptor function, focusing of signals, etc, which have high degrees of similarity to the equivalent processes of the neuron.’ There are also striking similarities of stimulus-response behavior between bacteria and higher organisms, which apparently follow the Weber-Fechner law of psychophysics. These and other questions are discussed in our review.

Molecular components of the signaling complex

E. coli can sense a variety of amino acids, sugars and dipeptides, as well as pH, temperature and redox state using five types of receptors. Most abundant and best studied receptors are those for aspartate (Tar) and serine (Tsr). Receptors anchor the complex in the inner membrane and transmit signals from the periplasmic ligand-binding domain to the cytoplasmic part. The cytoplasmic part of the receptor dimer is a four-helix bundle, with highly conserved domain containing four to six specific glutamate residues that are methylated by CheR and demethylated by CheB. The receptor homodimers are organized in trimers by interaction at their helical hairpin tips, and trimers form the minimum functional units. Receptors are predicted to be organised in large allosteric clusters of at least 25 homodimers (Sourjik and Berg, 2004), and these clusters form a high-order structure of thousands of receptors localized at the cell poles. For reviews on function and intracellular organization, see Sourjik, 2004; Kentner and Sourjik, 2006; Hazelbauer et al., 2008.

The signaling clusters contain receptors, histidine kinase CheA and additional protein CheW. The system functioning can be explained quantitatively by the notion that signaling complexes stay in equilibrium between two conformational states, ’on’ and ’off’. In the adapted state, the probabilities of both states are nearly equal. An increase of attractant concentration shifts the equilibrium to ’off’ state, decreasing the CheA activity and hence CheYp level. A removal of attractant shifts the system to the ’on’ state that activates CheA autophosphorylation and hence the downstream CheY phosphorylation. The phosphatase CheZ increases CheY

dephosphorylation rate to ensure prompt change of CheYp in response to changes in CheA activity.

The response clusters with homogeneous (Sourjik and Berg, 2004) and heterogeneous (Mello and Tu, 2005) receptor population is cooperative and can be fitted by the classical Monod-Wyman-Changeux (MWC) model of allosteric proteins (Monod et al., 1965). An alternative, Ising model of receptor cluster comprises an extended two-dimensional lattice of interacting receptors (Shimizu et al., 2003). Both models are discussed and compared in (Skoge et al., 2006).

Methods used to study chemotaxis

During the last forty years of chemotaxis studies, experimental methods became more sophisticated and precise. However, new methods usually do not replace the old ones, but rather extend them and provide insights into particular features of chemotaxis at different scales.

Swarm plate assay

One of the first methods to quantitatively study the chemosensitive behavior of bacteria was the swarm plate assay. A petri dish containing metabolizable attractant, salts needed for growth, and soft agar (a low enough concentration so that the bacteria can swim) is inoculated in the center with the bacteria. As the bacteria grow, they consume the local supply of attractant, thus creating a gradient, which they follow to form a ring surrounding the inoculum (Adler, 1966). Measuring the diameter of the swarm ring after a fixed time gives an estimate of chemotactic efficiency of the bacteria.

Capillary assay

The earliest method to observe chemotaxis was the use of a capillary tube. In the 1880s Pfeffer observed bacterial chemotaxis inserting the capillary containing a solution of test chemical into a bacterial suspension and then looking microscopically for accumulation of bacteria at the mouth of and inside the capillary (positive chemotaxis) or movement of bacteria away from the capillary (negative chemotaxis). This procedure was converted by J. Adler into an objective, quantitative assay by measuring the number of bacteria accumulating inside a capillary containing attractant solution (Adler, 1969). The number of cells inside the capillary is counted by serial dilutions. Unlike in the plate method, where bacteria make the gradient of attractant by metabolizing the chemical, here the experimenter provides the gradient; hence nonmetabolizable chemicals can be also studied. Capillary assays were further improved and parallelized (Berg and Turner, 1990; Bainer et al., 2003), which allows measuring chemotaxis for many strains and/or under many conditions with high accuracy.

Defined gradients

Quantitative analysis of bacterial migration has been achieved by making defined gradients of attractant or repellent (Dahlquist et al., 1972; Tsang et al., 1973; Ford et al., 1991; Lewus and Ford, 2001), and then determining the distribution of bacteria in the gradient by measuring scattering of light by the bacteria. The method allows the experimenter to vary the shape (steepness) of the gradient.

Imaging

The motion of bacteria can be recorded by microcinematography, or followed as tracks that form on photographic film after time exposure (Macnab and Koshland, 1972; Spudich and Koshland, 1975). An improvement of these methods was delivered by fluorescent labelling of cells and filaments, and usage of CCD camera to follow the flagella transformations and cell movement in high contrast and time resolution (Turner et al., 2000; Darnton et al., 2007).

Tracking microscope

Swimming bacteria move rapidly out of focus plane and viewfield, which makes their behavior difficult to track. A breaking progress was made after the invention of an automatic tracking microscope, which allowed objective, quantitative, and much faster observations (Berg, 1971; Berg and Brown, 1972). This method allowed to demonstrate that bacteria migrate in a biased random walk consisting of long runs and short tumbles (originally called ’twiddles’), and that the frequency of tumbles shifts the random walk towards attractants and away from repellents. Despite the long time passed since the construction of tracking microscope in 1971 and its obvious advantages, it did not have successors due to its technical complexity, though the original tracking microscope is still in use (Frymier et al., 1995; Lewus and Ford, 2001).

Tethering experiments

Addition of attractants to *E. coli* cells, tethered to glass by flagella with antibody, results in a counterclockwise rotation of the cell body as viewed from above (Larsen et al., 1974). Addition of repellents causes clockwise rotation of the cells. The response magnitude and adaptation time can be accurately measured in terms of motor bias. The method is widely used for measuring the behavior of individual cells and single motors (Segall et al., 1986; Alon et al., 1998; Khan et al., 2004; Korobkova et al., 2004).

Microchambers

Modern microfabrication techniques open up the possibilities of making spatially complex habitat landscapes and to investigate how bacteria proliferate and communicate through chemotaxis and quorum sensing (Park et al., 2003; Keymer et al., 2006). The microfabricated chemostats contain rectangular volumes, corridors or mazes, with input and output channels that supply bacteria with nutrition medium and oxygen, and remove bacterial wastes and

excessive biomass, therefore supporting stable conditions of the microenvironment. This technique allows novel approach to study bacterial populations in fabricated ecological environments. Microfluidics experiments have further been used to analyse bacterial responses to well-defined gradient on microscopic scale (Mao et al., 2003; Stocker et al., 2008; Kalinin et al., 2009).

FRET experiments

Fluorescence resonance energy transfer (FRET) is a technique that measures the separation of two fluorescently labelled proteins (and hence their interaction) in cells. It relies on the distance-dependent energy transfer from an excited donor fluorophore to an acceptor fluorophore. Because FRET-based measurements are quantitative and non-invasive, FRET is particularly useful for observing transient protein interactions involved in signal transduction. In the chemotaxis pathway, phosphorylation-dependent interactions of the response regulator CheY fused to YFP (CheY-YFP) with its phosphatase CheZ fused to CFP (CheZ-CFP) were used to monitor the activity of the receptor-kinase complexes (Sourjik and Berg, 2002, 2004).

Simulation software

Abundant quantitative data on the pathway (http://www.pdn.cam.ac.uk/groups/comp-cell/Data.html) have inspired a number of mathematical models of chemotaxis (Bray et al., 1993; Barkai and Leibler, 1997; Shimizu et al., 2003; Mello and Tu, 2003; Lipkow et al., 2005). Three recent models reproduce swimming of cells in gradients using pathway simulations of individual cells: AgentCell, which is based on fully stochastic pathway model (Emonet et al., 2005), *E. solo*, which is based on systems of ordinary differential equations (Bray et al., 2007), and RapidCell based on a hybrid approach (Vladimirov et al., 2008). These programs embrace the known experimental data on pathway reactions and physical properties of a swimming cell, thus allowing to study the behavior of bacterial populations *in silico*. For recent reviews of the models, see Tindall et al., 2008a,b.

Signal amplification

The sensory system of *E. coli* demonstrates extreme sensitivity. It is able to respond to the addition of as little as 3 nM aspartate (Mao et al., 2003), which corresponds to only several molecules in a volume of a cell. An increase in attractant concentration that changes the receptor occupancy by 0.2% results in a 23% change in the bias of motor rotation (Segall et al., 1986; Sourjik and Berg, 2002), indicating signal amplification by a factor of approx. 100. This paradox of chemotactic sensitivity was resolved recently by showing that the main signal amplification (ca. 35) arises from the cooperative interactions of neighbouring receptors in clusters (Sourjik and Berg, 2002). Another amplification step is located in the end of pathway, where CheYp binds to FliM molecules in the motor ring in a highly cooperative manner, with a

Hill coefficient of about 10 (Cluzel et al., 2000). When combined, these two amplification steps are sufficient to explain the observed gain.

Methylation

The adaptation enzyme CheR consitutively methylates receptors at four glutamate residues located in the cytoplasmic domain. Methylation increases receptor ability to stimulate CheA activity (Borkovich et al., 1992). As a result, when attractant is added, CheA activity rapidly drops down (Figure 1C), and then slowly recovers back to the steady state by methylation of receptors. Methylation also decreases the affinity of the receptor complex to attractants (Borkovich et al., 1992; Li and Weis, 2000; Levit and Stock, 2002), thereby regulating the ligand binding to receptor complexes.

CheB enzyme works in the way opposite to CheR, removing methyl groups from receptors. The outcome of demethylation is inhibition of CheA autophosphorylation, which allows adaptation to negative stimuli. Therefore, counteraction of CheR and CheB returns CheA activity to its pre-stimulus value after any type of stimulation, positive or negative.

Methylation and demethylation occur at much slower time scales than other reactions involved in the network, thereby providing a memory mechanism which allows a cell to remember its recent past state and compare its present situation to the past.

Adaptation

The chemotaxis network has an amazing property of perfect or nearly perfect adaptation to stimuli, which means that after addition or removal of an attractant the system gradually returns to its prestimulus values in terms of CheA activity, CheYp concentration, and motor bias. The change in ligand binding is compensated by receptor methylation, which provides the mechanism of adaptation.

The role of adaptation is crucial. Bacteria retain high sensitivity for some attractants from nanomolar to millimolar concentrations, spanning five to six orders of magnitude (Berg and Tedesco, 1975; Segall et al., 1986; Kim et al., 2001). To enable high sensitivity over such a wide range, the signal amplification must be coupled with the adaptation. In the absence of adaptation, a 100-fold signal amplification will saturate the system response at 1% receptor occupancy, and the accomplishment of signal amplification with adaptation is a necessary setup of natural signaling systems (Koshland, 1981; Pugh and Lamb, 1990; Kaupp and Koch, 1992; Zufall and Leinders-Zufall, 2000).

Optimal memory length

The way bacteria utilize methylation and demethylation is in ways similar to the use of phosphorylation and dephosphorylation in some mammalian systems. Bacteria follow gradients using temporal sensing in which the ’memory’ of the bacterium plays a key role (Macnab and Koshland, 1972). In terms of chemotaxis, the memory length is the adaptation time required to return the post-stimulus CheA activity to its steady-state level (Figure 1C). The bacterium does not have a fixed memory length. Rather, adaptation time depends on the stimulus strength: under strong stimuli, pathway activity will return to steady state after relatively long time interval, whereas for a weak stimulus it equilibrates very rapidly. Memory is additive: the adaptation time for a step stimulus from to is the sum of the adaptation times for step stimuli from to and from to (Spudich and Koshland, 1975; Berg and Tedesco, 1975).

The memory length of the organism should fit its lifestyle. In the case of *E. coli* and *Salmonella*, which have a typical run time of about a second in adapted state, the optimal memory was shown to be between 1 and 10 seconds (Koshland, 1974, 1981). A longer memory will make the cell to remember the past conditions which are already non-relevant, instead of the prompt response in the present swimming direction. A substantially shorter memory will make the cell ’forget’ the gradient too fast, which means a drop of response accuracy. The cell is faced with the dilemma of the need for a long memory span to improve its analytical accuracy, and a need for a quick response to provide a high correlation with the direction of motion (Macnab and Koshland, 1972). The optimal memory length depends on many factors, and steepness of the gradient is one of the most important.

Computer simulations of bacteria in gradients of defined steepness show that in steeper gradients the maximum of chemotaxis efficiency is observed at higher adaptation rates (Figure 2A) (Andrews et al., 2006; Vladimirov et al., 2008). The optimal adaptation rate is determined by the average CheYp – it should fit the operating range of flagellar motor. Due to high cooperativity of CheYp-motor interaction, its response curve is very steep, so CheYp must fit a very narrow interval (Figure 2B). To set CheYp into this interval, the system excitation must be counterbalanced by adaptation. In steep gradients, the memory length must be therefore short enough to balance the strong excitation by rapid adaptation. In shallow gradients, the memory length must be long enough to allow excitation, otherwise the cells become adapted before they are able to respond. In general, the steeper is the gradient, the shorter must be the adaptation time and hence the chemotactic memory.

Role of noise

Noise plays an important role in the bacterial world. The cell swims along curly trajectories rather than straight paths because of the Brownian motion causing rotational diffusion (Berg, 1993). The network itself is affected by the noise from receptor-ligand binding, methylation, and variations in protein concentrations (gene noise). The variety of noise sources that disturb the chemotactic navigation poses a question of how this navigation is possible at all, taking

into account the relative simplicity of the system. Computer simulations and experimental methods resolved this question. Variation of *E. coli* network parameters does not break its property of precise adaptation because of its robustness (Barkai and Leibler, 1997; Alon et al., 1999). The topology of *E. coli* chemotaxis network ensures robustness of output (concentration of CheYp) against concerted variations in protein levels (Kollmann et al., 2005), which is the dominant source of gene expression noise. Uncorrelated variations in protein levels, which arise due to noise in protein translation, are further compensated by the translational coupling of neighbouring chemotaxis genes (Lovdok et al., 2009).

However, noise in concentrations adaptation enzymes CheR and CheB and/or their kinetic parameters does affect the the adaptation time (Alon et al., 1999). This means that even genetically identical cells can have a variability in chemotactic behavior (Berg and Tedesco, 1975; Spudich and Koshland, 1976). However, this can have positive outcome for population as a whole. Computer simulations show that in any fixed gradient, there will be a subpopulation with the optimal memory length for this gradient. Such a population heterogeneity may be evolutionary favorable to ensure co-existence of subpopulations that will be optimally tactic in different gradients (Andrews et al., 2006; Vladimirov et al., 2008).

Another intrinsic source of noise arises from slow reactions of receptors methylation. Interestingly, the cells appear to have been selected to maintain low CheR expression levels, which lead to high noise in methylation events and long-term variations in system output. It was shown experimentally that such a noise provides long-term variations in the cellular behavior, with correlations in motor output spanning up to 20 min (Korobkova et al., 2004). Such variation in motor behavior, and hence run length, can allow the cell to explore the surrounding environment more efficiently, because the runs in adapted state are distributed as Lévy-flights rather than exponentially. In this case, the noise can be beneficial for individual cells to explore new areas, also in the presence of gradient (Emonet and Cluzel, 2008).

The two aforementioned examples of positive noise effect in chemotaxis are the rare exceptions – most of the noise factors decrease the efficiency of chemotactic navigation. But the chemotactic network can cope with that. Simulations of the network input-output response shows that the pathway demonstrates properties of low-pass filter coupled to a differentiator (Block, 1982; Andrews et al., 2006; Tu et al., 2008; Tostevin and Ten Wolde, 2009). In this form, the system averages the signal for a certain time (defined by its memory), and then differentiates it to determine the steepness of the gradient in the current run direction. In this way, bacterial system follows the main signal (gradient) and filters out high-frequency noise.

The optimal memory length depends on the noise sources. The optimal memory is shorter if the noise from rotational diffusion of a cell body is higher. This has an intuitive explanation: high coefficient of rotational diffusion makes the cell to loose its running direction, and ligand concentrations in the past become non-relevant faster. On the contrary, the optimal memory is longer upon higher noise in receptor-ligand binding. In this case, the cell needs longer memory to filter out large variations in noisy signal. As mentioned above, there are several other types

of noise which disturb the system efficiency. However, bacterial signaling system works close to the theoretical limit of precision (Rayleigh limit), demonstrating the characteristics of nearly perfect molecular instrument (Andrews et al., 2006).

Weber-Fechner law

Many natural sensory systems respond proportionally to the relative change of stimulus $\Delta S/S$ rather than absolute change ΔS, the effect known in psychophysics as Weber-Fechner law. The dependence fits visual, smell and acoustical perception. This law, discovered in 19-th century, grounded the basics of modern psychophysics. In more recent studies, the Weber-Fechner (logarithmic) law was shown to be a first approximation of the power law, which provides a better fit of the experimental data (Stevens, 1961). For a recent review, see Johnson et al. (2002).

The Weber-Fechner law was often recalled to demonstrate the similarity of chemotaxis system to sensory systems of higher organisms (Mesibov et al., 1973; Koshland, 1981). Consistent with the Weber-Fechner law, *E. coli* demonstrates approximately constant response to exponentially changing gradients (Block et al., 1983; Tu et al., 2008; Kalinin et al., 2009). Therefore, the bacterial chemotaxis system appears to track the gradient of the logarithm of ligand concentration. Although, computer simulations of the up-to-date chemotaxis models predict that the ’true’ constant response, over several orders of attractant concentrations, can be achieved by stimulation with yet another type of gradient, which has a form of (Vladimirov et al., 2008). This gradient is well fitted by the exponential gradient in a wide concentration range.

In conclusion, due to its relative simplicity, the bacterial sensory system provides a perfect workbench for a detailed analysis of sensory phenomena, and it is far from being fully understood. Even though we know the molecular mechanisms in detail, there is a vast *terra incognita* in our understanding how bacteria interact with their dynamically changing environment. The issues of individual versus collective behavior, as well as noisy versus deterministic environment, come to the foreground of the modern research.

Acknowledgements

The work was supported by the Bioquant graduate program ’Molecular machines: mechanisms and functional interconnections’ and Landesgraduiertenförderung of Land Baden-Württemberg.

References

Adler, J. (1966). Chemotaxis in Bacteria. Science *153*, 708–716.

Adler, J. (1969). Chemoreceptors in Bacteria. Science *166*, 1588–1597.

Adler, J. (1975). Chemotaxis in bacteria. Annu. Rev. Biochem. *44*, 341–356.

Alon, U., Camarena, L., Surette, M. G., Aguera y Arcas, B., Liu, Y., Leibler, S., and Stock, J. B. (1998). Response regulator output in bacterial chemotaxis. EMBO J. *17*, 4238–4248.

Alon, U., Surette, M. G., Barkai, N., and Leibler, S. (1999). Robustness in bacterial chemotaxis. Nature *397*, 168–171.

Andrews, B. W., Yi, T.-M., and Iglesias, P. A. (2006). Optimal noise filtering in the chemotactic response of *Escherichia coli*. PLoS Comput. Biol. *2*, 1407–1418.

Bainer, R., Park, H., and Cluzel, P. (2003). A high-throughput capillary assay for bacterial chemotaxis. J. Microbiol. Methods *55*, 315–319.

Barkai, N. and Leibler, S. (1997). Robustness in simple biochemical networks. Nature *387*, 913–917.

Berg, H. C. (1971). How to track bacteria. Rev. Sci. Instruments *42*, 868–871.

Berg, H. C. (1993). Random Walks in Biology (Princeton, USA: Princeton University Press).

Berg, H. C. and Brown, D. A. (1972). Chemotaxis in *Escherichia coli* analysed by three-dimensional tracking. Nature *239*, 500–504.

Berg, H. C. and Purcell, E. M. (1977). Physics of chemoreception. Biophys. J. *20*, 193–219.

Berg, H. C. and Tedesco, P. M. (1975). Transient response to chemotactic stimuli in *Escherichia coli*. Proc. Natl. Acad. Sci. USA *72*, 3235–3239.

Berg, H. C. and Turner, L. (1990). Chemotaxis of bacteria in glass capillary arrays. *Escherichia coli*, motility, microchannel plate, and light scattering. Biophys. J. *58*, 919–930.

Block, S. (1982). Impulse responses in bacterial chemotaxis. Cell *31*, 215–226.

Block, S. M., Segall, J. E., and Berg, H. C. (1983). Adaptation kinetics in bacterial chemotaxis. J. Bact. *154*, 312–323.

Borkovich, K. A., Alex, L. A., and Simon, M. I. (1992). Attenuation of sensory receptor signaling by covalent modification. Proc. Natl. Acad. Sci. USA *89*, 6756–6760.

Bray, D., Bourret, R. B., and Simon, M. I. (1993). Computer simulation of the phosphorylation cascade controlling bacterial chemotaxis. Mol. Biol. Cell *4*, 469–482.

Bray, D., Levin, M. D., and Lipkow, K. (2007). The chemotactic behavior of computer-based surrogate bacteria. Curr. Biol. *17*, 12–19.

Chung, C. Y., Funamoto, S., and Firtel, R. A. (2001). Signaling pathways controlling cell polarity and chemotaxis. Trends Biochem. Sci. *26*, 557–566.

Cluzel, P., Surette, M., and Leibler, S. (2000). An ultrasensitive bacterial motor revealed by monitoring signaling proteins in single cells. Science *287*, 1652–1655.

Dahlquist, F. W., Lovely, P., and Koshland, D. E. (1972). Quantitative analysis of bacterial

migration in chemotaxis. Nat. New Biol. *236*, 120–123.

Darnton, N. C., Turner, L., Rojevsky, S., and Berg, H. C. (2007). On torque and tumbling in swimming *Escherichia coli*. J. Bacteriol. *189*, 1756–1764.

Emonet, T. and Cluzel, P. (2008). Relationship between cellular response and behavioral variability in bacterial chemotaxis. Proc. Natl. Acad. Sci. USA *105*, 3304–3309.

Emonet, T., Macal, C. M., North, M. J., Wickersham, C. E., and Cluzel, P. (2005). AgentCell: a digital single-cell assay for bacterial chemotaxis. Bioinformatics *21*, 2714–2721.

Ford, R. M., Phillips, B. R., Quinn, J. A., and Lauffenburger, D. A. (1991). Measurement of bacterial random motility and chemotaxis coefficients: I. Stopped-flow diffusion chamber assay. Biotechnol. Bioeng. *37*, 647–660.

Freter, R., O'Brien, P. C., and Halstead, S. A. (1978). Adhesion and chemotaxis as determinants of bacterial association with mucosal surfaces. Adv. Exp. Med. Biol. *107*, 429–437.

Frymier, P. D., Ford, R. M., Berg, H. C., and Cummings, P. T. (1995). Three-dimensional tracking of motile bacteria near a solid planar surface. Proc. Natl. Acad. Sci. USA *92*, 6195–6199.

Hazelbauer, G. L., Falke, J. J., and Parkinson, J. S. (2008). Bacterial chemoreceptors: high-performance signaling in networked arrays. Trends Biochem. Sci. *33*, 9–19.

Johnson, K. O., Hsiao, S. S., and Yoshioka, T. (2002). Neural coding and the basic law of psychophysics. Neuroscientist *8*, 111–121.

Kalinin, Y. V., Jiang, L., Tu, Y., and Wu, M. (2009). Logarithmic sensing in *Escherichia coli* bacterial chemotaxis. Biophys. J. *96*, 2439–2448.

Kaupp, U. B. and Koch, K. W. (1992). Role of cGMP and Ca^{2+} in vertebrate photoreceptor excitation and adaptation. Annu. Rev. Physiol. *54*, 153–175.

Kelly, F. X., Dapsis, K. J., and Lauffenburger, D. A. (1988). Effect of bacterial chemotaxis on dynamics of microbial competition. Microb. Ecol. *16*, 115–131.

Kennedy, M. J. (1987). Role of motility, chemotaxis, and adhesion in microbial ecology. Ann. N.Y. Acad. Sci. *506*, 260–273.

Kennedy, M. J. J. and Lawless, J. G. G. (1985). Role of chemotaxis in the ecology of denitrifiers. Appl. Environ. Microbiol. *49*, 109–114.

Kentner, D. and Sourjik, V. (2006). Spatial organization of the bacterial chemotaxis system. Curr. Opin. Microbiol. *9*, 619–624.

Keymer, J. E., Endres, R. G., Skoge, M., Meir, Y., and Wingreen, N. S. (2006). Chemosensing in *Escherichia coli*: two regimes of two-state receptors. Proc. Natl. Acad. Sci. USA *103*, 1786–1791.

Khan, S., Jain, S., Reid, G. P., and Trentham, D. R. (2004). The fast tumble signal in bacterial chemotaxis. Biophys. J. *86*, 4049–4058.

Kim, C., Jackson, M., Lux, R., and Khan, S. (2001). Determinants of chemotactic signal amplification in *Escherichia coli*. J. Mol. Biol. *307*, 119–135.

Kollmann, M., Lovdok, L., Bartholome, K., Timmer, J., and Sourjik, V. (2005). Design

principles of a bacterial signalling network. Nature *438*, 504–507.

Korobkova, E., Emonet, T., Vilar, J. M., Shimizu, T. S., and Cluzel, P. (2004). From molecular noise to behavioural variability in a single bacterium. Nature *428*, 574–578.

Koshland, D. E. (1974). Chemotaxis as a model for sensory systems. FEBS Lett. *40* (Suppl. 1), S2.

Koshland, D. E. (1980). Bacterial chemotaxis in relation to neurobiology. Annu. Rev. Neurosci. *3*, 43–75.

Koshland, D. E. (1981). Biochemistry of sensing and adaptation in a simple bacterial system. Annu. Rev. Biochem. *50*, 765–782.

Larsen, S. H., Reader, R. W., Kort, E. N., Tso, W. W., and Adler, J. (1974). Change in direction of flagellar rotation is the basis of the chemotactic response in *Escherichia coli*. Nature *249*, 74–77.

Lauffenburger, D. (1991). Quantitative studies of bacterial chemotaxis and microbial population dynamics. Microb. Ecol. *22*, 175–185.

Levit, M. N. and Stock, J. B. (2002). Receptor methylation controls the magnitude of stimulus-response coupling in bacterial chemotaxis. J. Biol. Chem. *277*, 36760–36765.

Lewus, P. and Ford, R. M. (2001). Quantification of random motility and chemotaxis bacterial transport coefficients using individual-cell and population-scale assays. Biotechnol. Bioeng. *75*, 292–304.

Li, G. and Weis, R. M. (2000). Covalent modification regulates ligand binding to receptor complexes in the chemosensory system of *Escherichia coli*. Cell *100*, 357–365.

Lipkow, K., Andrews, S. S., and Bray, D. (2005). Simulated diffusion of phosphorylated CheY through the cytoplasm of *Escherichia coli*. J. Bact. *187*, 45–53.

Lovdok, L., Bentele, K., Vladimirov, N., Müller, A., Pop, F., Lebiedz, D., Kollmann, M., and Sourjik, V. (2009). Role of translational coupling in robustness of bacterial chemotaxis pathway. PLoS Biol., in press.

Macnab, R. M. and Koshland, D. E. (1972). The gradient-sensing mechanism in bacterial chemotaxis. Proc. Natl. Acad. Sci. USA *69*, 2509–2512.

Mao, H., Cremer, P. S., and Manson, M. D. (2003). A sensitive, versatile microfluidic assay for bacterial chemotaxis. Proc. Natl. Acad. Sci. USA *100*, 5449–5454.

Mello, B. A. and Tu, Y. (2003). Quantitative modeling of sensitivity in bacterial chemotaxis: the role of coupling among different chemoreceptor species. Proc. Natl. Acad. Sci. USA *100*, 8223–8228.

Mello, B. A. and Tu, Y. (2005). An allosteric model for heterogeneous receptor complexes: understanding bacterial chemotaxis responses to multiple stimuli. Proc. Natl. Acad. Sci. USA *102*, 17354–17359.

Mesibov, R., Ordal, G. W., and Adler, J. (1973). The range of attractant concentrations for bacterial chemotaxis and the threshold and size of response over this range. Weber law and related phenomena. J. Gen. Physiol. *62*, 203–223.

Monod, J., Wyman, J., and Changeux, J. P. (1965). On the nature of allosteric transitions: a plausible model. J. Mol. Biol. *12*, 88–118.

Park, S., Wolanin, P. M., Yuzbashyan, E. A., Silberzan, P., Stock, J. B., and Austin, R. H. (2003). Motion to form a quorum. Science *301*, 188.

Pilgram, W. K. and Williams, F. D. (1976). Survival value of chemotaxis in mixed cultures. Can. J. Microbiol. *22*, 1771–1773.

Pugh, E. N. and Lamb, T. D. (1990). Cyclic GMP and calcium: the internal messengers of excitation and adaptation in vertebrate photoreceptors. Vision Res. *30*, 1923–1948.

Segall, J. E., Block, S. M., and Berg, H. C. (1986). Temporal comparisons in bacterial chemotaxis. Proc. Natl. Acad. Sci. USA *83*, 8987–8991.

Shimizu, T. S., Aksenov, S. V., and Bray, D. (2003). A spatially extended stochastic model of the bacterial chemotaxis signalling pathway. J. Mol. Biol. *329*, 291–309.

Skoge, M. L., Endres, R. G., and Wingreen, N. S. (2006). Receptor-receptor coupling in bacterial chemotaxis: evidence for strongly coupled clusters. Biophys. J. *90*, 4317–4326.

Sourjik, V. (2004). Receptor clustering and signal processing in *E. coli* chemotaxis. Trends Microbiol. *12*, 569–576.

Sourjik, V. and Berg, H. (2002). Receptor sensitivity in bacterial chemotaxis. Proc. Natl. Acad. Sci. USA *99*, 123–127.

Sourjik, V. and Berg, H. C. (2004). Functional interactions between receptors in bacterial chemotaxis. Nature *428*, 437–441.

Spudich, J. L. and Koshland, D. E. (1975). Quantitation of the sensory response in bacterial chemotaxis. Proc. Natl. Acad. Sci. USA *72*, 710–713.

Spudich, J. L. and Koshland, D. E. (1976). Non-genetic individuality: chance in the single cell. Nature *262*, 467–471.

Stevens, S. S. (1961). To honor Fechner and repeal his law: a power function, not a log function, describes the operating characteristic of a sensory system. Science *133*, 80–86.

Stocker, R., Seymour, J. R., Samadani, A., Hunt, D. E., and Polz, M. F. (2008). Rapid chemotactic response enables marine bacteria to exploit ephemeral microscale nutrient patches. Proc. Natl. Acad. Sci. USA *105*, 4209–4214.

Tindall, M., Maini, P., Porter, S., and Armitage, J. (2008a). Overview of mathematical approaches used to model bacterial chemotaxis II: bacterial populations. Bull. Math. Biol. *70*, 1570–1607.

Tindall, M., Porter, S., Maini, P., Gaglia, G., and Armitage, J. (2008b). Overview of mathematical approaches used to model bacterial chemotaxis I: the single cell. Bull. Math. Biol. *70*, 1525–1569.

Tostevin, F. and Ten Wolde, P. R. (2009). Mutual information between input and output trajectories of biochemical networks. Phys. Rev. Lett. *102*,

Tsang, N., Macnab, R., and Koshland, D. E. (1973). Common mechanism for repellents and attractants in bacterial chemotaxis. Science *181*, 60–63.

Tu, Y., Shimizu, T. S., and Berg, H. C. (2008). Modeling the chemotactic response of *Escherichia coli* to time-varying stimuli. Proc. Natl. Acad. Sci. USA *105*,

Turner, L., Ryu, W. S., and Berg, H. C. (2000). Real-time imaging of fluorescent flagellar filaments. J. Bact. *182*, 2793–2801.

Vladimirov, N., Lovdok, L., Lebiedz, D., and Sourjik, V. (2008). Dependence of bacterial chemotaxis on gradient shape and adaptation rate. PLoS Comput. Biol. *4*, e1000242+.

Wadhams, G. H. and Armitage, J. P. (2004). Making sense of it all: bacterial chemotaxis. Nat. Rev. Mol. Cell Biol. *5*, 1024–1037.

Zufall, F. and Leinders-Zufall, T. (2000). The cellular and molecular basis of odor adaptation. Chem. Senses *25*, 473–481.

Figure legends

Figure 1 *E. coli* chemotaxis.
(A) The cell moves in a random walk, consisting of long runs (about 1 s) and short tumbles (about 0.1 s). The direction of a new run is assumed to be chosen randomly, while the run length is longer if the cell encounters positive change of attractant concentration, or negative change of repellent concentration. This allows to follow attractant and avoid repellent gradients (insets). Longer runs in a favorable direction are shown by '+', normal (unbiased) runs by '-'. (B) Chemotaxis pathway of *E. coli*. Changes in attractant or repellent concentrations are sensed by a protein complex consisting of transmembrane receptors, an adaptor protein CheW, and a histidine kinase CheA. Transmembrane receptors can be of five types (Tar, Tsr, Tap, Trg, Aer). Autophosphorylation activity of CheA is inhibited by attractant binding and enhanced by repellent binding to receptors. The phosphoryl group is rapidly transferred from CheA to the response regulator CheY. Phosphorylated CheY (CheYp) diffuses to the flagellar motors and changes the direction of motor rotation from counterclockwise to clockwise to promote tumbles. CheZ phosphatase, localized to sensory complexes through binding to CheA, ensures a rapid turnover of CheYp, which is essential to quickly re-adjust bacterial behaviour. Adaptation in chemotaxis is mediated by two enzymes, methyltransferase CheR and methylesterase CheB, which add or remove methyl groups at four specific glutamate residues on each receptor monomer. Receptor modification increases CheA activity and decreases sensitivity to attractants. Feedback is provided by CheB phosphorylation through CheA that increases CheB activity. (C) The time course of a typical chemotactic response. Step-wise addition of saturating amount of attractant results in an initial fast (less than 0.1 s) decrease in kinase activity that is followed by a slow CheR-dependent adaptation. Adaptation time is proportional to the change in receptor occupancy. Next, removal of attractant results in an initial fast increase in kinase activity followed by CheB-dependent adaptation. Kinase activity below the steady state causes longer runs, above the steady state – frequent tumbling.

Figure 2 Optimal rate of adaptation in chemotaxis.
(A) Simulations of chemotactic cells in gradient of different steepness. The average drift velocity of population increases in steeper gradient. The optimal navigation in steep gradients requires higher adaptation rate (shorter memory), because excitation arising in steep gradient must be counterbalanced by higher adaptation rate. (B) CCW motor bias as a function of relative CheYp concentration. Gray bands indicate the CheYp interval and the corresponding motor range that ensure optimal drift velocity. The average CheYp must be balanced by counteracting excitation and adaptation, to fit the optimal range of flagellar motor.

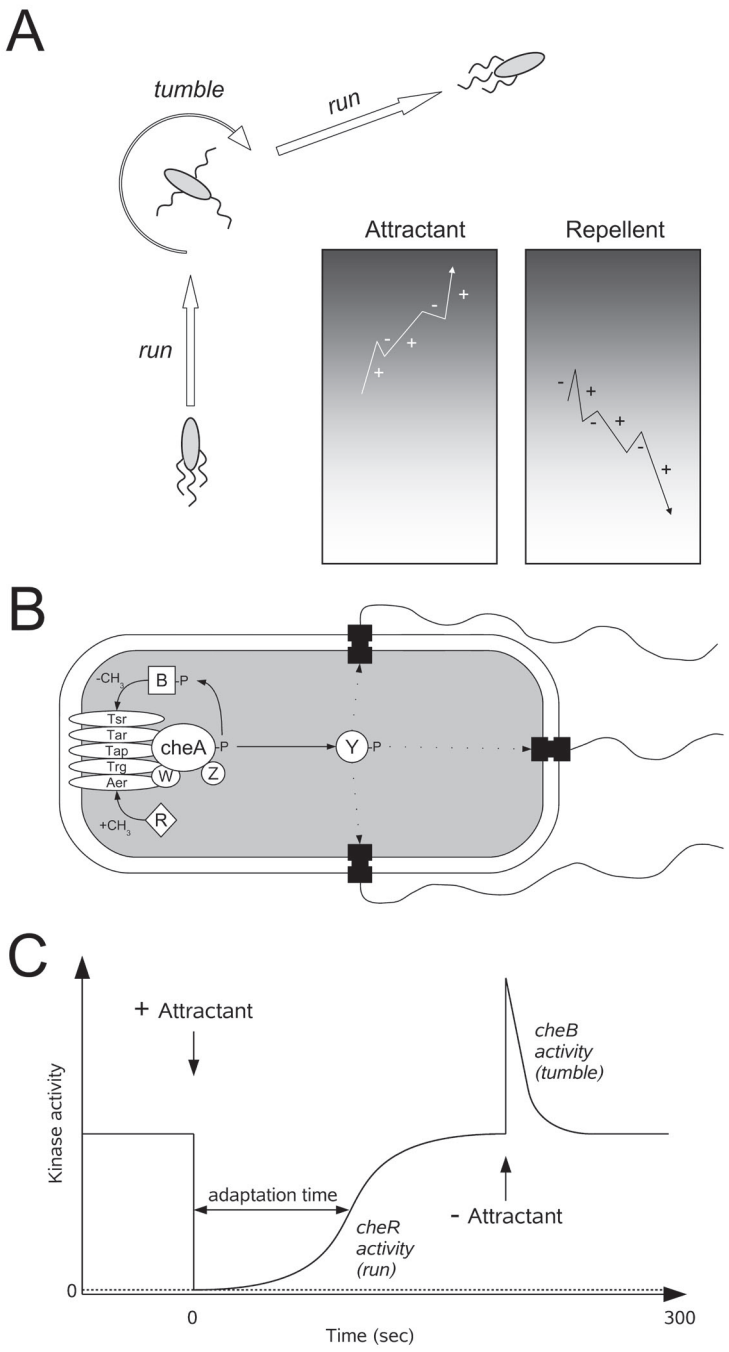
A
tumble
run
Attractant
Repellent
run
B
-CH3
B
-P
Tsr
Tar
Tap
Trg
Aer
cheA
-P
W
Z
Y
-P
+CH3
R
C
+ Attractant
Kinase activity
cheB
activity
(tumble)
adaptation time
- Attractant
cheR
activity
(run)
0
0
300
Time (sec)

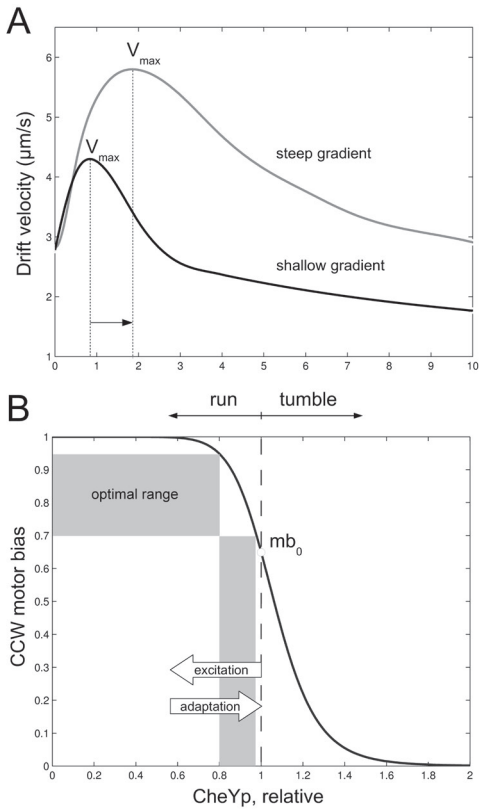
A
V max
V max
steep gradient
shallow gradient
Drift velocity (μm/s)
B
run
tumble
optimal range
mb0
excitation
adaptation
CCW motor bias
CheYp, relative

Auxiliary navigation mechanism of peritrichously flagellated chemotactic bacteria

Nikita Vladimirov [1]
Interdisziplinäres Zentrum für Wissenschaftliches Rechnen
der Universität Heidelberg (IWR),
Im Neuenheimer Feld 368, D-69120 Heidelberg, Germany;

Dirk Lebiedz
Zentrum für Biosystemanalyse der Universität Freiburg (ZBSA),
Habsburger Str. 49, D-79104 Freiburg, Germany;

Victor Sourjik
Zentrum für Molekulare Biologie
der Universität Heidelberg, DKFZ-ZMBH Alliance,
Im Neuenheimer Feld 282, D-69120 Heidelberg, Germany

October 2, 2009

[1]Corresponding author. Address: Interdisziplinäres Zentrum für Wissenschaftliches Rechnen (IWR), Im Neuenheimer Feld 368, 69120 Heidelberg, Germany. Tel.: (+49-6221)54-8889, Fax: (+49-6221)54-8884, e-mail: nikita.vladimirov@gmail.com

Abstract

Chemotactic movement of *Escherichia coli* is one of the most thoroughly studied paradigms of simple behavior. Due to significant competitive advantage conferred by chemotaxis and to high evolution rates in bacteria, the chemotaxis system is expected to be strongly optimized. Bacteria follow gradients by performing temporal comparisons of chemoeffector concentrations along their runs, a strategy which is most efficient given their size and swimming speed. Concentration differences are detected by a sensory system and transmitted to modulate rotation of flagellar motors, decreasing the probability of a tumble and reorientation if the perceived concentration change during a run is positive. Such regulation of tumble probability is on itself sufficient to explain chemotactic drift of a population up the gradient, and is commonly assumed to be the only navigation mechanism of chemotactic bacteria.

We use computer simulations to predict existence of an additional mechanism of gradient navigation in *E. coli* and other peritrichously flagellated bacteria. Based on the experimentally observed dependence of cell tumbling angle on the number of switching motors (Turner et al., 2000, J Bacteriol 182, 2793-2801), we suggest that not only the tumbling probability but also the degree of reorientation during a tumble depend on the swimming direction along the gradient. Although the difference in mean tumbling angles up and down the gradient predicted by our model is small, it results in a dramatic enhancement of the cellular drift velocity along the gradient.

We thus demonstrate a new level of optimization in *E. coli* chemotaxis, which arises from collective switching of several flagellar motors and a resulting fine tuning of tumbling angle. Similar strategy is likely to be used by other peritrichously flagellated bacteria, and indicates a yet another level of evolutionary optimization in bacterial chemotaxis.

Key words: chemotaxis, peritrichously flagellated, Escherichia coli, tumbling angle, RapidCell

Author summary

Chemotaxis of bacteria plays an important role in their life, providing them with the ability to actively search for an optimal growth environment. The chemotaxis system is supposed to be highly optimized, because on the evolutionary time scale even a modest enhancement of its efficiency can give cells a large competitive advantage. For a long time it was believed that the only navigation mechanism of bacteria is increasing the run length toward the preferred direction. The tumble was assumed to be a purely random change of direction between runs.

We analysed recently published experimental data that demonstrate a dependence of tumbling angle on the number of CW-switched motors. We introduced such a dependence into our model of chemotactic *E. coli*, and simulated it in different conditions. Our simulations show that this dependence is an important additional mechanism of bacterial navigation, which was previously unrecognized because it lays below the experimental errors of conventional single-cell tracking. We show that such a fine tuning of tumbling significantly improves efficiency of chemotaxis, and represents a new level of evolutionary optimization of bacteria.

Introduction

Many motile unicellular organisms are known to direct their movement in gradients of specific chemical substances – the process called chemotaxis. Chemotaxis plays an important role in the microbial population dynamics with chemotactic bacteria in a nonmixed environment – that is in presence of nutrient gradients – having significant growth advantage (1–4). Modeling of microbial population dynamics indicates that motility and chemotactic ability can be as important for evolutionary competition as cell growth rate (5, 6). The chemotaxis system is thus expected to be highly optimized, as has been indeed suggested by several studies (7–10).

The best example of such optimization is bacterial chemotaxis strategy itself. While eukaryotic cells are able to sense the gradients by direct comparison of concentrations at the opposite sides of the cell (11), bacteria employ temporal comparisons along their runs (12). Theoretical analysis suggested that such strategy is superior to direct spatial comparisons for objects of bacterial size and swimming speed (7). Adapted bacteria have two swimming modes: runs, which are periods of long straight swimming, and tumbles, when bacterium stops and changes its orientation. The runs of a swimming bacterium are interrupted by tumbles which abruptly change the swimming direction. For cells swimming up an attractant gradient, the runs become longer due to suppression of tumbles, and the cell population migrates up the gradient. The frequency of tumbles is controlled by the chemotaxis network through switching of individual motors. During a run, flagellar motors rotate counter-clockwise (CCW) causing flagella to form a bundle, whereas switching of one or several flagellar motors to clockwise (CW) rotation breaks up the bundle and initiates a tumble. The direction of motor rotation depends on the concentration of phosphorylated CheY molecules, which bind to the motor and switch its direction in a highly cooperative mode. The CheY phosphorylation is controlled by the histidine kinase CheA, which forms sensory clusters together with transmembrane receptors and the adaptor CheW. Each receptor can be either active or inactive, depending on ligand binding and on the methylation level. The active receptor activates CheA, eliciting downstream phosphorylation of the response regulator CheY. Phosphorylated CheY (CheYp) is dephosphorylated by CheZ. Receptors can be methylated by the methyltransferase CheR and demethylated by the methylesterase CheB. Methylation regulates the receptor activity. Because the reaction of receptor methylation is much slower than the initial response, methylation

provides chemical 'memory', which allows the cell to compare the current ligand concentration with the recent past.

Early single-cell tracking experiments reported no dependence of the tumbling angle, i.e. turning angle between consequent runs, on the direction of the gradient and the inclination of a run (12), and it was thus presumed to be random in subsequent modeling of bacterial chemotaxis. However, in recent study that used high-resolution fluorescence video microscopy (13), it was shown that the cell turning angle depends on the number of CW-rotating filaments involved in the tumble, and thereby the turning angle rises proportionally to the number of motors that switched to CW. Because the CW switch probability is set by the chemotaxis system dependent on the cellular swimming direction along the gradient, the tumbling angle can be expected to depend on the swimming direction, too. If the cell swims up a gradient of attractant, the probability of CW rotation is smaller, and fewer motors are likely to change directions. Therefore, even if the cell makes a tumble, the tumbling angle should be small. When the cell swims down the gradient of attractant, the probability of CW rotation is higher and more motors are likely to change directions during a tumble, with the consequence that the tumbling angles will be larger.

The goal of this study was thus to investigate the magnitude of the tumbling angle dependence on the swimming direction and the effect of such dependence on the chemotactic efficiency. We introduced dependence of the turning angle on the number of CW-rotating motors in a recently constructed hybrid model of chemotactic *E. coli*, RapidCell simulator (14). Our simulations demonstrate that although the estimated difference of tumbling angles up and down the gradient is only few degrees, even such a small difference significantly improves the chemotactic efficiency of bacteria. We thus suggest that tuning of tumbling angle depending on swimming direction serves as an additional navigation mechanism for *E. coli* and other peritrichously flagellated bacteria.

Methods

Model of chemotaxis signaling network

We applied the recently proposed MWC model for mixed receptor cluster (15, 16), which accounts for the observed experimental dose-response curves

of adapted cells measured by *in vivo* FRET experiments (15, 17), as shown in (16, 18, 19). According to the MWC model, an individual receptor homodimer is described as a two-state receptor, being either 'on' or 'off', with the free energy being a function of methylation level m and ligand concentration $[S]$

$$f_r(m) = \varepsilon_r(m) - \log\left(\frac{1 + [S]/K_r^{off}}{1 + [S]/K_r^{on}}\right) \tag{1}$$

where $\varepsilon_r(m)$ is the 'offset energy', and K_r^{on}, K_r^{off} are the dissociation constants for the ligand in the 'on' and 'off' state, respectively. Groups of receptors form larger sensory complexes, or signaling teams, with all receptors in a team being either 'on' or 'off' together. The teams are composed of mixtures of Tar ($r = a$) and Tsr ($r = s$) receptors, and the total free energy of the team is given by

$$F = n_a f_a(m) + n_s f_s(m) \tag{2}$$

The probability (A) that a team will be active is a function of its free energy

$$A = \frac{1}{1 + e^F} \tag{3}$$

The adaptation is modeled according to the mean-field theory (20, 21), assuming that the CheB demethylates only active receptors, CheR methylates only inactive receptors, and both enzymes work at saturation

$$\frac{dm}{dt} = a(1 - A)[CheR] - bA[CheB] \tag{4}$$

This equation implies that both enzymes work in the zero-order regime. The linear products $a(1 - A)[CheR]$ and $(bA[CheB])$ mean that a bound CheR (CheB) can only act if the receptor team is inactive (active), with probability $(1 - A)$ and A, respectively.

The average methylation level m is assumed to be a continuously changing variable within the interval $[0, 8]$, with linear interpolation between the key offset energies, $\varepsilon_r(i), i = 0..8$, as suggested in (21, 22). The ODE for methylation (Eqn. 4) is integrated using the Euler method to ensure high computational speed of the program, while the time step is chosen as 0.01 s to keep the simulation error low.

The details of network model were previously described in (14). CheA kinase activity is assumed to be equal to the activity of the receptor complex

(A). The rate of phosphotransfer from active CheA to CheY is much faster than the rate of CheA autophosphorylation (9, 23). Therefore, the relative concentration of CheYp is obtained as a function of active CheA from the steady-state equation

$$[CheYp] = 3\frac{k_Y k_s A}{k_Y k_s A + k_Z Z + \gamma_Y} \tag{5}$$

where $k_s = 0.45$ is a scaling coefficient, $k_y = 100\mu M^{-1}s^{-1}$, $k_Z = 30/[CheZ]s^{-1}$, $\gamma_Y = 0.1$ are the rate constants according to (9, 24, 25).

The relative concentration of CheYp is converted into the CCW-motor bias using a Hill function (26):

$$mb(CheYp) = (1 + (1/mb_0 - 1)(CheYp)^H)^{-1} \tag{6}$$

where $H = 10.3$ (26), $mb_0 = 0.65$ (26, 27).

Model of bacterial swimming

To simulate the experimentally observed hydrodynamics of bacterial swimming and tumbling (13, 28) in simple terms, we introduce a *distortion* factor d_{cw} which reflects how one CW-rotating flagellum influences the cellular speed and angular deviation

$$d_{cw} = \begin{cases} t_{cw}/t^0_{cw}, & t_{cw} \le t^0_{cw} \\ e^{-20(t_{cw} - t^0_{cw})}, & t_{cw} > t^0_{cw} \end{cases} \tag{7}$$

This functional form implies that the distortion rises proportionally to the CW rotation time t_{cw} as long as it is below the threshold t^0_{cw} (the first period). After this threshold is reached, the distortion exponentially decays (the second period). The first period corresponds to unwinding of a flagellum from the bundle and its rotation in the right-handed semicoiled form, which initiates a tumble. In the second period, when the flagellum rotates CW longer than the threshold time, a rapid transformation from semicoiled to curly 1 form occurs, and the flagellum twists around the bundle during the new run, due to high flexibility of the latter form (28).

The collective influence of several simultaneously CW-rotating motors is assumed to be proportional to the sum of their distortion factors

$$D_{cw} = \sum_{i=1}^{n_{cw}} d^i_{cw} \tag{8}$$

This implies that the tumble can occur if a single motor rotates CW for at least t^0_{cw} period, or if two or more motors rotate CW together for a shorter time. Formally, a tumble occurs when $D_{cw} \geq D^0_{cw}$, where D^0_{cw} is a threshold value. In principle, the threshold depends on the total number of motors: the larger N, the higher D^0_{cw} is required to generate a tumble. This is consistent with experimental data of (13), Fig. 12 therein, where switching of 1 motor is sufficient for a tumble at $N = 2 - 4$, but for $N = 5$ at least 2 motors are necessary for a tumble. However, we keep the same $D^0_{cw} = 1$ for $N = 2, 3, 4, 5$ for simplicity, to avoid additional arbitrarily chosen thresholds. The simulated run lengths in a ligand-free medium have distribution close to exponential.

The cellular swimming speed depends on the distortion in a piece-wise linear form

$$v = \begin{cases} V_{max}(D^0_{cw} - D_{cw}), & D_{cw} < D^0_{cw} \\ 0, & D_{cw} \geq D_{cw} \end{cases} \quad (9)$$

In our model, we considered only 'complete' tumbles, which occur when D_{cw} reaches D^0_{cw} and the swimming speed falls to zero: at this time point the cell instantly changes its orientation by the tumbling angle Θ, which is determined by two alternative models, isotropic and anisotropic. For simplicity, we assumed that if the distortion D_{cw} does not reach D^0_{cw}, it causes only a drop of speed, without a change of the swimming direction.

During a run, the direction of cellular swimming is affected by the rotational diffusion (12, 29). After each time step, the swimming direction is changed by adding a stochastic component with normal distribution $N(m, \sigma) = N(0, \sqrt{2D_r\Delta t})$, where the diffusion coefficient D_r equals $0.062\, rad^2 s^{-1}$ (29).

Isotropic tumbling. The tumbling angle Θ is distributed according to the continuous probability density function $f(\Theta) = 0.5(1 + cos\Theta)sin\Theta$, $0 < \Theta < \pi$, as suggested in (30). The mean $M(\Theta)$ of this angle distribution, 67.5^o, is close to experimental measurement of 68^o (12), and shapes of the simulated and experimental distributions are simular. The angle distribution does not depend on any external factors.

Anisotropic tumbling. The tumbling angle Θ is determined by number of CW-rotating motors n_{cw} involved in the tumble, and the total number of motors N. For each pair of (n_{cw}, N), we simulated the cell swimming in a ligand-free medium and calculated the frequency p_i of the tumbles which are caused by n_{cw} CW-rotating motors. Using the frequency p_i, we chose the turning angle Θ_i close to the experimental values (13), while keeping the

average turning angle constant in all models,

$$\sum_{i=1}^{N} p_i \Theta_i = 67.5^o \tag{10}$$

Constant-activity gradient

In order to measure the chemotactic efficiency accurately and to avoid the effects of receptors saturation, we simulated the cells in an artificial constant-activity gradient, which ensures a constant chemotactic response CheYp and a constant cell drift velocity over a wide range of ligand concentrations, in contrast to commonly used Gaussian and linear gradients (14). Drift velocity in constant-activity gradient was measured by a linear fit of $\langle X(t) \rangle$ in the time interval from 200 to 500 s. The constant-activity gradient has the following form:

$$S(x) = K^* \frac{Cx}{\frac{K^{on} - K^{off}}{K_D} - Cx} \tag{11}$$

where $S(x)$ is the ligand concentration in position x, and $K_D = \sqrt{K^{on} K^{off}}$ is the geometric mean of the dissociation constants. C is a free parameter which determines the steepness of the gradient, and thereby the drift velocity of cells up the gradient. We compare the drift velocities in three constant-activity gradients of aspartate, with relative steepness changing two-fold from one to another, and designate them as N0, N1 and N2. The corresponding gradient functions are

$$S(x) = K^* \frac{Cx}{\frac{K^{on} - K^{off}}{K^*} - Cx}, \; C = \frac{K^{on} - K^{off}}{K^*} \cdot \frac{0.999}{x_{max}} \tag{12}$$

with $x_{max} = 40, 20, 10$ mm for N0, N1 and N2, respectively. Here x_{max} is the size of square 2D domain, where cells were simulated starting from the left wall $x = 0$.

Results and Discussion

Dependence of tumbling angle on the number of CW-rotating motors. The tumbling angle dependence on the number of switching motors was investigated by extending the recently published hybrid model of chemotactic *E. coli* (14). First, a more detailed model of tumbling was developed to

bring the model in a closer agreement with the tracking experiments of (12). While previous version of the model relied on a simple voting model of tumbling, which started the tumble as soon as the majority of motors rotate CW, our new model takes into account the duration of CW-rotation of every motor (Fig. 1A). The complex hydrodynamics of multiple flagella is described in simplified form, through a distortion factor which is a function of t_{cw} of each motor (see Methods). Despite this simplification, the simulated swimming of *E. coli* is in a very good agreement with the original tracking experiments (12). The model realistically reproduces nearly all data provided by tracking experiments: mean cellular speed, run times, tumbling angles (Table 2), as well as individual motor switching and graduate recovery of cellular speed after a tumble.

Second, we introduced a dependence of tumbling angle on the number of CW-rotating motors that cause the tumble (Fig. 1B). This was done by fitting the experimental data of (13) with a realistic choice of discrete tumbling angles at each number of CW-switched motors (Fig. 1C). To ensure consistency with experimental data, we further assumed dependence of tumbling angle on the total number of motors. This model was called anisotropic, and it was compared to a conventional model of isotropic tumble, which chooses the tumbling angle stochastically. In simulations without a gradient, both models produce equal cellular drift velocities, with the accuracy of estimation error. To keep the mean angles of both models consistent, we defined the frequencies of the discrete angles in the anisotropic model as shown in Fig. 1D.

Dependence of tumbling angle on swimming direction. For anisotropic model, the tumbling angles depend on the swimming direction prior to tumbles (Fig. 2A). This dependence naturally arises from the dependence of tumbling angle on the number of CW-rotating motors. The cells which turned with the smallest n_{cw} were swimming in slightly skewed directions up the gradient before the tumble, whereas the cells which turned with the highest n_{cw} were swimming with even smaller skew down the gradient before the tumble. A more detailed analysis shows that the total angular difference between tumbling angles that correspond to the movement up and down a gradient is only about 3^o (Fig. 2B). Such a small difference is within the error of the early tracking experiments, about 5^o (31), which explains why it remained undetected.

Effect of anisotropic model on cell drift velocity. Despite such a small difference of mean angles, it can significantly increase the chemotactic

performance, with the mean drift velocity being up to two times higher for anisotropically tumbling cells (Fig. 2C). The positive effect of anisotropic tumble becomes more visible in steeper gradients and for higher number of motors, which suggests that highly flagellated cells can adjust their tumbling angle more precisely.

In the case of $N = 3$ motors and moderate gradient (N1), the mean tumbling angle is $M(\Theta) = 67.0^o$. This value is only 0.5^o smaller than the angle in ligand-free simulations, so the increase of the drift velocity in the anisotropic model cannot be attributed to the change of the total mean tumbling angle. The mean tumbling angle up the gradient $\Theta(cos(\alpha > 0)) = 66.4^o$, while down the gradient it is $\Theta(cos(\alpha < 0)) = 67.6^o$. Therefore, the 1.2^o difference in mean tumbling angles causes a 52% increase in the population drift velocity, from 0.92 to 1.4 $\mu m s^{-1}$ (Fig. 2C).

Dependence of anisotropic model effect on the magnitude of angle adjustment and on rotational diffusion. As a control, we simulated chemotactic cells that tumble with a constant angle (67.5 deg.), and compared them to cells that tumble with slightly higher angle (67.5-Δ), when they swim up the gradient, and with slightly lower angle (67.5+Δ), when they swim down the gradient. Here, the Δ was a constant parameter changed from 1 to 5 deg. A difference of $\Delta = 5$ degrees increased the drift velocity by about 100% in the gradient N1, and by $\sim 50\%$ in the gradient N2 (Fig. 3A). This confirms that the observed increase in drift velocity shown in Fig. 2C is due to small changes in tumbling angles of up- and down-swimming cells, and does not arise from model-specific parameters.

Bacterial movement in gradients is further affected by the Brownian motion for both isotropic and anisotropic tumbling models (Fig. 3B). In our simulations we used $D_r = 0.062\, rad^2 s^{-1}$ (Table 1). At lower coefficients of rotational diffusion, both models demonstrate better chemotaxis, and the advantage of the anisotropic tumbling is most pronounced, which is due to lower noise factor arising from rotational diffusion (32). Since rotational diffusion depends on the cells size, flagellar length, media viscosity and temperature (29, 33), predicted effects of anisotropic tumbling can be even more pronounced for other bacteria or under different environmental conditions.

Conclusions. Taken together, our results suggest that in addition to extending the run length while swimming up the gradient, *E. coli* uses an auxiliary mechanism of tumbling angle tuning according to the swimming direction. This fine tuning of tumble is mediated by the same adjustment of tumbling frequency that underlies the conventional chemotaxis strategy

of bacteria (Fig. 4). This previously unrecognized feature is expected to be shared by other peritrichously flagellated bacteria and seems to represent yet another level of evolutionary optimization of the chemotaxis system.

Acknowledgements

We thank Howard C. Berg and Yuhai Tu for their valuable suggestions regarding the manuscript. The work is supported by the Bioquant graduate program 'Molecular machines: mechanisms and functional interconnections' and Landesgraduiertenförderung of Land Baden-Württemberg.

References

1. Kennedy MJ (1987) Role of motility, chemotaxis, and adhesion in microbial ecology. Annals of the New York Academy of Sciences 506:260–273.

2. Kennedy MJJ, Lawless JGG (1985) Role of chemotaxis in the ecology of denitrifiers. Applied and Environmental Microbiology 49:109–114.

3. Pilgram WK, Williams FD (1976) Survival value of chemotaxis in mixed cultures. Canadian journal of microbiology 22:1771–1773.

4. Freter R, O'Brien PC, Halstead SA (1978) Adhesion and chemotaxis as determinants of bacterial association with mucosal surfaces. Advances in Experimental Medicine and Biology 107:429–437.

5. Lauffenburger D (1991) Quantitative studies of bacterial chemotaxis and microbial population dynamics. Microbial Ecology 22:175–185.

6. Kelly FX, Dapsis KJ, Lauffenburger DA (1988) Effect of bacterial chemotaxis on dynamics of microbial competition. Microbial Ecology 16:115–131.

7. Berg HC, Purcell EM (1977) Physics of chemoreception. Biophysical Journal 20:193–219.

8. Bialek W, Setayeshgar S (2005) Physical limits to biochemical signaling. Proc Natl Acad Sci USA 102:10040–10045.

9. Kollmann M, Lovdok L, Bartholome K, Timmer J, Sourjik V (2005) Design principles of a bacterial signalling network. Nature 438:504–507.

10. Endres RG, Wingreen NS (2008) Accuracy of direct gradient sensing by single cells. Proc Natl Acad Sci USA 105:15749–15754.

11. Chung CY, Funamoto S, Firtel RA (2001) Signaling pathways controlling cell polarity and chemotaxis. Trends in Biochemical Sciences 26:557–566.

12. Berg HC, Brown DA (1972) Chemotaxis in Escherichia coli analysed by three-dimensional tracking. Nature 239:500–504.

13. Turner L, Ryu WS, Berg HC (2000) Real-time imaging of fluorescent flagellar filaments. Journal of Bacteriology 182:2793–2801.

14. Vladimirov N, Lovdok L, Lebiedz D, Sourjik V (2008) Dependence of bacterial chemotaxis on gradient shape and adaptation rate. PLoS Computational Biology 4:e1000242+.

15. Sourjik V, Berg HC (2004) Functional interactions between receptors in bacterial chemotaxis. Nature 428:437–441.

16. Mello BA, Tu Y (2005) An allosteric model for heterogeneous receptor complexes: understanding bacterial chemotaxis responses to multiple stimuli. Proc Natl Acad Sci USA 102:17354–17359.

17. Sourjik V, Berg H (2002) Receptor sensitivity in bacterial chemotaxis. Proc Natl Acad Sci USA 99:123–127.

18. Keymer JE, Endres RG, Skoge M, Meir Y, Wingreen NS (2006) Chemosensing in escherichia coli: two regimes of two-state receptors. Proc Natl Acad Sci USA 103:1786–1791.

19. Skoge ML, Endres RG, Wingreen NS (2006) Receptor-receptor coupling in bacterial chemotaxis: evidence for strongly coupled clusters. Biophysical Journal 90:4317–4326.

20. Mello BA, Shaw L, Tu Y (2004) Effects of receptor interaction in bacterial chemotaxis. Biophysical Journal 87:1578–1595.

21. Endres RG, Wingreen NS (2006) Precise adaptation in bacterial chemotaxis through "assistance neighborhoods". Proc Natl Acad Sci USA 103:13040–13044.

22. Hansen CH, Endres RG, Wingreen NS (2008) Chemotaxis in escherichia coli: a molecular model for robust precise adaptation. PLoS Computational Biology 4:14–27.

23. Emonet T, Cluzel P (2008) Relationship between cellular response and behavioral variability in bacterial chemotaxis. Proc Natl Acad Sci USA 105:3304–3309.

24. Stewart RC, Jahreis K, Parkinson JS (2000) Rapid phosphotransfer to chey from a chea protein lacking the chey-binding domain. Biochemistry 39:13157–13165.

25. Sourjik V, Berg HC (2002) Binding of the escherichia coli response regulator chey to its target measured in vivo by fluorescence resonance energy transfer. Proc Natl Acad Sci USA 99:12669–12674.

26. Cluzel P, Surette M, Leibler S (2000) An ultrasensitive bacterial motor revealed by monitoring signaling proteins in single cells. Science 287:1652–1655.

27. Segall JE, Block SM, Berg HC (1986) Temporal comparisons in bacterial chemotaxis. Proc Natl Acad Sci USA 83:8987–8991.

28. Darnton NC, Turner L, Rojevsky S, Berg HC (2007) On torque and tumbling in swimming Escherichia coli. Journal of Bacteriology 189:1756–1764.

29. Berg HC (1993) Random Walks in Biology. Princeton University Press.

30. Chen KC, Ford RM, Cummings PT (1998) The global turning probability density function for motile bacteria and its applications. Journal of Theoretical Biology 195:139–155.

31. Brown DA (1974) Chemotaxis in Escherichia coli: a biased random walk. Ph.D. Thesis. Dissertation, University of Colorado, Department of Physics and Astrophysics.

32. Andrews BW, Yi TM, Iglesias PA (2006) Optimal noise filtering in the chemotactic response of Escherichia coli. PLoS Computational Biology 2:1407–1418.

33. Mitchell J (1991) The influence of cell size on marine bacterial motility and energetics. Microbial Ecology 22:227–238.

34. Block SM, Segall JE, Berg HC (1983) Adaptation kinetics in bacterial chemotaxis. Journal of Bacteriology 154:312–323.

35. Staropoli JF, Alon U (2000) Computerized analysis of chemotaxis at different stages of bacterial growth. Biophysical Journal 78:513–519.

36. Morton-Firth CJ, Shimizu TS, Bray D (1999) A free-energy-based stochastic simulation of the tar receptor complex. Journal of Molecular Biology 286:1059–1074.

37. Shimizu TS, Aksenov SV, Bray D (2003) A spatially extended stochastic model of the bacterial chemotaxis signalling pathway. Journal of Molecular Biology 329:291–309.

Figure Legends

Figure 1.

Anisotropic model of *E. coli* tumbling. (A) The output series for a single swimming cell (from bottom to top): switching of a single motor (blue), its distortion d_{cw} (green), the sum of distortions of 3 motors D_{cw} (red), the resulting falls of swimming speed during tumbles (black). (B) The schematic illustration of tumbling angle (green arrow) dependence on the number of CW-rotating motors (green circles). (C) Anisotropic model of tumbling. The tumbling angle Θ_i at different number of CW-rotating motors n_{cw}. *Inset.* Experimental data sets reproduced from Fig. 12 of (13). Solid lines show means, errorbars show standard deviations, circles correspond to individual tumbles. Color code of the inset is the same as in the main panel. (D) Frequencies p_i of tumbles which involve n_{cw} CW-rotating motors out of the total number of motors $N = 2..5$.

Figure 2.

Behavior of cells with anisotropic tumbling model. (A) Distribution of cellular orientations prior to tumbles. The tumbling events are divided into 3 groups, by the number of CW-rotating motors involved in a tumble. The rose histograms are normalized by the number of counts. The inner black circle shows unbiased (isotropic) distribution as a reference. Cell orientation is given relative to the gradient. The gradient steepness is N1. (B) Average tumbling angle as a function of orientation along the gradient prior to tumbles. (C) Chemotactic drift velocity of cells in gradients of different steepness. Bars show the drift velocities of cells with 3 motors (left group) or 5 motors (right group) in the medium without a gradient (gray), in gradient N0 (blue), N1 (green) and N2 (red). Left bars show the isotropic model, right (hatched) bars – anisotropic model of tumbling. In the absence of gradient, the difference is within the error of estimation. Standard error of the mean is about 0.03. Cells in (A) and (B) have 3 motors, other parameters are as described in Tab. 1. The number of simulated cells is 10^3 in each case.

Figure 3.

Effects of tumbling angle adjustment and rotational diffusion on chemotactic efficiency. (A) Dependence of chemotactic drift velocity on fixed tumbling

angle deviation Δ in a simplified tumbling model. The cells swimming up the gradient tumble with a smaller angle $67.5-\Delta$, while cells swimming down the gradient tumble with higher angle $67.5+\Delta$. Cells with $\Delta = 0$ tumble with a fixed angle 67.5^o, i.e. isotropically. (B) Dependence of chemotactic drift on rotational diffusion coefficient for cells with isotropic (blue) and anisotropic (green) models of tumbling. The number of simulated cells is 10^3 in each case, the gradient is N1. Cells in (A) and (B) have 3 motors, other parameters are as described in Tab. 1.

Figure 4.

Enhancement of chemotactic efficiency by anisotropic tumbling. In the isotropic model (top), cells have lower CW bias and tumble less frequently up the gradient, but their average tumbling angle is the same in all directions. In the anisotropic model (bottom), the same lowering of CW motor bias additionally leads to the reduction of tumbling angles below average for cells swimming up the gradient. Cells swimming down the gradient have tumbling angles larger than the average. Directional dependence of the tumbling angle enhances average drift up the gradient. The difference of tumbling angles is exaggerated for illustration purposes.

Table 1: Parameters used in *E. coli* model

Parameter	Value	Reference
mb_0^{ccw}	0.65	Steady-state CCW motor bias (26, 27)
T_{ccw}	1.20 s	Av. CCW rotation time of a motor (34)
T_{cw}	0.65 s	Av. CW rotation time, given that $mb_0^{ccw} = \frac{T_{ccw}}{T_{ccw}+T_{cw}}$
t_{cw}^0	0.15 s	Max. time the flagellum rotates CW in semicoiled form (13)
D_{cw}^0	1.0	Threshold of total distortion to initiate a tumble (13)
V_{max}	$20\,\mu m s^{-1}$	Maximum swimming speed (12, 35)
D_r	$0.062\,rad^2 s^{-1}$	Rotational diffusion coefficient (29)
H	10.3	Hill coefficient of motor response to [CheYp] (26)
Δt	0.01 s	Time step in simulations (this work)
K_a^{on}	$12\,\mu M$	Diss. constant of Tar to Asp (36)
K_a^{off}	$1.7\,\mu M$	Diss. constant of Tar to Asp (36)
K^*	$4.52\,\mu M$	Apparent diss. constant of Tar to Asp (37)

Table 2: Comparison of the RapidCell output and the tracking data from (Berg and Brown, 1972). The model parameters are as in Table 1, the number of motors $N = 3$, the aspartate gradient is N1. Values are estimated from 1000 cells simulated for 500 s. Controls correspond to a ligand-free medium. Means and std (where relevant) are shown.

Parameter	Isotropic model	Anisotropic model	Experiment
Tumbling angle, control (^{o})	67.5	67.5	68
Run length, control (s)	0.81 ± 0.63	0.81 ± 0.63	0.86 ± 1.18
Run length, gradient (s)	0.89 ± 0.77	0.92 ± 0.86	0.90 ± 1.56
Run length, up gradient (s)	0.93 ± 0.83	0.98 ± 0.95	1.07 ± 1.80
Run length, down gradient (s)	0.83 ± 0.69	0.86 ± 0.75	0.80 ± 1.38
Swimming speed, control ($\mu m s^{-1}$)	17 ± 5.4	17 ± 5.4	14.2 ± 3.4
Drift velocity, control ($\mu m s^{-1}$)	0.36 ± 0.03	0.39 ± 0.03	–
Drift velocity, gradient ($\mu m s^{-1}$)	0.92	1.40	0.90

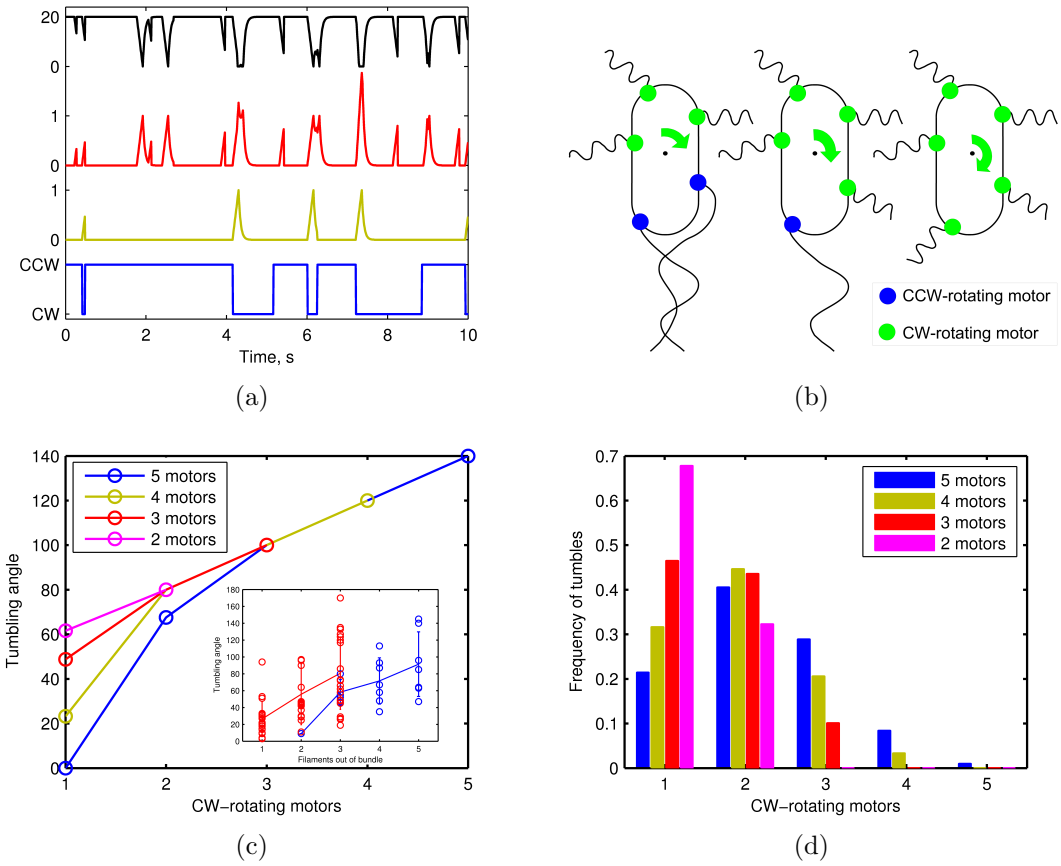
20
0
1
0
1
0
CCW
CW
0
2
4
6
8
10
Time, s
(a)
CCW-rotating motor
CW-rotating motor
(b)
140
120
100
80
60
40
20
0
Tumbling angle
5 motors
4 motors
3 motors
2 motors
1
2
3
4
5
CW−rotating motors
Filaments out of bundle
(c)
0.7
0.6
0.5
0.4
0.3
0.2
0.1
0
Frequency of tumbles
5 motors
4 motors
3 motors
2 motors
1
2
3
4
5
CW−rotating motors
(d)

Figure 1:

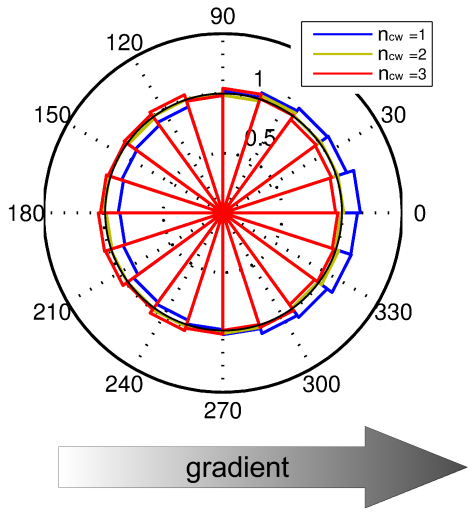
90
120
150
180
210
240
270
300
330
30
0
1
0.5
n_{cw} =1
n_{cw} =2
n_{cw} =3
gradient

(a)

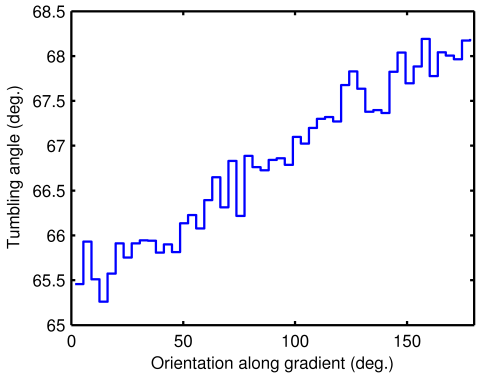
Tumbling angle (deg.)
Orientation along gradient (deg.)
68.5
68
67.5
67
66.5
66
65.5
65
0
50
100
150

(b)

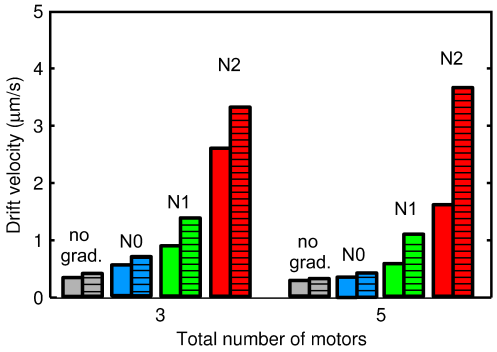
Drift velocity (μm/s)
Total number of motors
no grad.
N0
N1
N2
3
5

(c)

Figure 2:

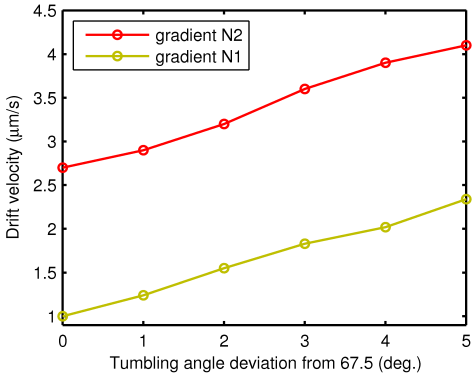
gradient N2
gradient N1
Drift velocity (μm/s)
Tumbling angle deviation from 67.5 (deg.)
4.5
4
3.5
3
2.5
2
1.5
1
0
1
2
3
4
5

(a)

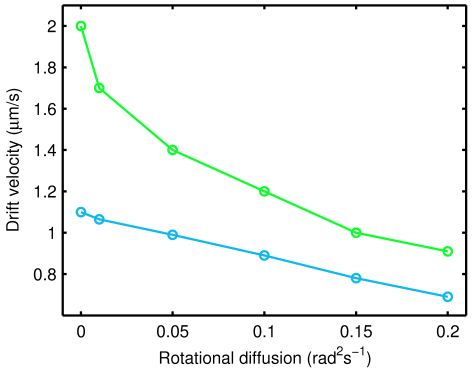
Drift velocity (μm/s)
Rotational diffusion (rad^{2}s^{-1})
2
1.8
1.6
1.4
1.2
1
0.8
0
0.05
0.1
0.15
0.2

(b)

Figure 3:

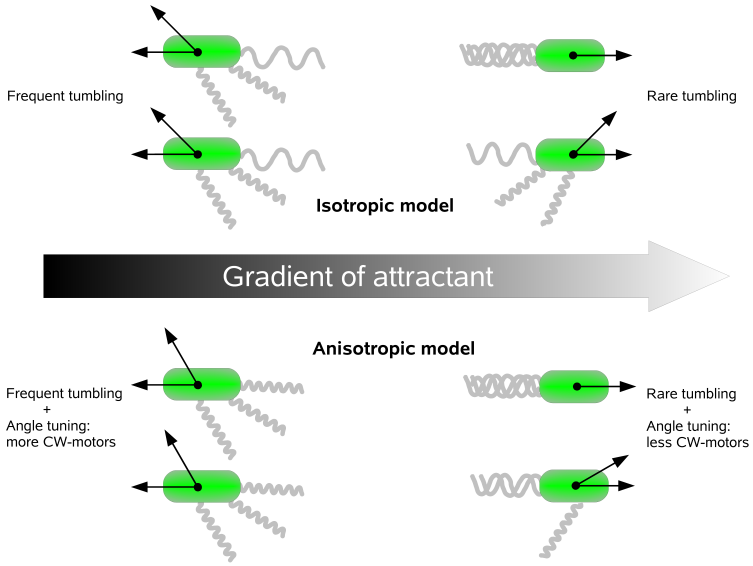
Frequent tumbling
Rare tumbling
Isotropic model
Gradient of attractant
Anisotropic model
Frequent tumbling
+
Angle tuning:
more CW-motors
Rare tumbling
+
Angle tuning:
less CW-motors

(a)

Figure 4: